

Université de Caen Normandie

Ecole doctorale SIMEM

Thèse de doctorat

présentée et soutenue le : 09/12/2015

par

Bérenger CABY

pour obtenir le

Doctorat de l'Université de Caen Normandie

Spécialité : Milieux denses et matériaux

Développement de l'analyse combinée par Réflectométrie de rayons X (XRR) et Fluorescence des rayons X en Incidence Rasante (GIXRF) pour des applications micro et nano-électroniques.

Directeur de thèse : Magali Morales
Co-directeur de thèse : Daniel Chateigner

Composition du Jury

Marie-Christine Lépy	Directrice de Recherches, Laboratoire National Henri Becquerel , CEA-Saclay (Rapporteur)
Philippe Jonnard	Directeur de Recherches CNRS, Laboratoire de Chimie Physique - Matière et Rayonnements, UPMC, Sorbonne Universités (Rapporteur)
Christina Strelt	Professeure des Universités, Vienna University of Technology, Institute of Atomic and Subatomic Physics, Vienne, Autriche
Giancarlo Pepponi	Chercheur, Center for Materials and Microsystems, Fondazione Bruno Kessler, Trento, Italie
Luca Lutterotti	Professeur des Universités, HDR, Department of Industrial Engineering, Università di Trento, Italie
Emmanuel Nolot	Ingénieur, CEA-Leti, MINATEC, Grenoble
Magali Morales	Maître de conférences, Laboratoire CIMAP, Caen (Directeur de thèse)
Daniel Chateigner	Professeur des universités, Laboratoire CRISMAT, Caen (Co-directeur de thèse)

Depuis l'apparition du transistor en 1947, l'industrie microélectronique n'a eu de cesse de chercher à développer des méthodes d'innovations technologiques toujours plus efficaces. Cette hausse quasi-exponentielle de la demande d'appareils toujours plus puissants et plus miniaturisés a été accompagnée d'un besoin croissant de nouvelles techniques de caractérisation de surfaces. La démocratisation des dispositifs micro- et nano-métriques ont mis en évidence certaines limites des techniques de caractérisation classiques comme la Spectrométrie de masse à ionisation secondaire (SIMS) ou la spectroscopie de rétrodiffusion de Rutherford (RBS). La Fluorescence de rayons X en Incidence Rasante (GIXRF) est alors apparue comme une technique alternative prometteuse.

La GIXRF est une variation de la Fluorescence de rayons X en Réflexion Totale (TXRF), une technique déjà bien connue et établie pour l'étude de la contamination de surface de couches minces. La GIXRF consiste à irradier un échantillon avec un faisceau primaire de rayons X à des faibles angles d'incidence (généralement entre 0 et 5°), afin de réduire la zone excitée à quelques nanomètres. Comme cette profondeur sondée varie avec l'angle d'incidence, la distribution en profondeur des atomes peut être obtenue. La GIXRF permet ainsi de réaliser des mesures de profil de composition et de densité de façon non-destructive avec une bonne résolution.

Depuis une dizaine d'années, des expériences GIXRF ont été réalisées dans différents laboratoires ou installations de rayonnement synchrotron afin d'étudier des profils en profondeur de dopants ou pour caractériser des empilements multicouches. Le nombre croissant de montages expérimentaux disponibles ainsi que le récent développement de logiciels d'analyse indique un intérêt croissant de la communauté scientifique pour cette technique de caractérisation. De plus, avec la réduction des temps d'analyse, grâce à l'augmentation de la puissance de calcul, les possibilités pour la GIXRF de réaliser des profils de distribution en profondeur ont été améliorées. En effet, donner une meilleure interprétation des données mesurées ainsi qu'extraire des informations quantitatives sur la composition de l'échantillon est devenue récemment possible.

Un des autres avantages de la GIXRF est la possibilité de la combiner avec d'autres techniques d'analyse comme la réflectométrie de rayons X (XRR), une méthode de caractérisation bien connue qui permet de déterminer le profil de densité électronique de divers échantillons. En combinant ces deux techniques, les informations complémentaires ainsi obtenues permettent de réduire les incertitudes que présentent chacune des méthodes individuellement. Une caractérisation en profondeur avec un niveau de confiance considérablement augmenté est donc possible.

Dans ce cadre, un groupe international de collaboration a été mis en place récemment entre différents laboratoires: la Fondazione Bruno Kessler (FBK, Trento, Italie), l'Université de Technologie de Vienne (VUT, Vienne, Autriche), le CEA-Leti (Grenoble, France) ainsi que deux laboratoires de l'ENSICAEN, CRISMAT et CIMAP (Caen, France). La mise en place de cette collaboration internationale vise à partager à la fois l'expertise, les équipements et les logiciels d'analyse de ces groupes pour accélérer le développement de la technique d'analyse combinée XRR et GIXRF. C'est dans ce contexte général international que cette thèse a été écrite en langue anglaise, avec comme objectif principal l'établissement, pour la première fois, de méthodologies quantitatives et de protocoles pour l'acquisition et l'analyse des mesures combinées XRR et GIXRF. La compréhension des principes physique sous-jacents à la GIXRF, des capacités, des limitations de la technique combinée ou non, ainsi que des différentes approches pour la quantification a également été nécessaire.

Le premier chapitre de ce travail de thèse a pour objectifs de présenter les généralités de la technique GIXRF. Un intérêt particulier a été apporté à la description des algorithmes nécessaires pour l'analyse quantitative ainsi que les principes physiques et mathématiques sous-jacents. Une première introduction à la problématique de cette analyse quantitative sera présentée. Le deuxième chapitre est quant à lui consacré à la présentation du contexte scientifique sur lequel est basé ce travail. Une description approfondie de l'état de l'art de la TXRF sera faite. La description des dispositifs expérimentaux nécessaires, des applications connues et maîtrisées ainsi que des diverses méthodes de quantification sera réalisée. En se fondant sur ces observations, un rapport préliminaire sur les récents développements de la GIXRF sera fait. La troisième partie de ce manuscrit concerne l'étude des logiciels d'analyse combinée XRR et GIXRF. La description, la comparaison et le test de quatre logiciels d'analyse combinée sera réalisée. Un intérêt tout particulier sera apporté à l'étude de la fonction instrumentale. L'influence de certains effets instrumentaux sur les mesures ainsi que différentes solutions pour corriger avec précision ces effets parasites sera présentée. Ce chapitre se terminera par une discussion sur les méthodes de quantification, leurs avantages et leurs limites.

Ces trois premiers chapitres font office de guide pour le lecteur afin de réaliser avec précision des acquisitions et analyses combinées XRR et GIXRF avec peu ou pas de connaissance a priori sur la technique de caractérisation. C'est pourquoi, la dernière partie de ce manuscrit sera consacrée aux mesures expérimentales réalisées sur des échantillons ayant des potentialités d'applications dans le domaine de la micro-électronique ou du photovoltaïque. Tout d'abord, l'étude en profondeur d'un profil de dopants sera présentée. Les problématiques liées au processus d'implantation que rencontrent les méthodes de caractérisation standard (SIMS) et les solutions que la GIXRF peut apporter seront évoquées. De plus, le profil d'implantation ainsi que

la dose totale de dopants implantés ont été déterminées avec une bonne résolution. Ensuite, les potentialités de la technique d'analyse combinée XRR et GIXRF pour la caractérisation qualitative et quantitative en profondeur seront testées avec des empilements de couches fines $\text{In}_2\text{O}_3/\text{Ag}/\text{In}_2\text{O}_3$. Enfin, des mesures quantitatives seront effectuées sur des échantillons $\text{Ta}_2\text{O}_5/\text{NiCo}$. Les effets du processus de dépôt sur la structure de ces empilements seront démontrés. Les difficultés rencontrées et les perspectives possibles seront ensuite discutées.

Ce travail de thèse a donc permis de montrer que la GIXRF, couplée ou non à la XRR, est une technique quantitative de caractérisation en profondeur non destructive avec une bonne résolution. En effet, par des mesures sur des équipements commerciaux, expérimentaux ou dans des installations synchrotron, les méthodologies, les possibilités et les limites de l'analyse combinée ont été présentées. Dans un premier temps, nous avons pu conclure que malgré certaines limitations quant à la caractérisation en profondeur complète des profils de concentration, la GIXRF permet d'observer des différences structurales entre différents échantillons. De plus, dans un second temps, nous avons démontré que les méthodes de quantification standard n'étaient pas adaptées à la plupart des situations et que par conséquent, une méthode simple qui nécessite moins de connaissances sur le dispositif expérimental est nécessaire. Cette nouvelle méthode présente aussi ses propres limitations, ainsi de nouvelles solutions sont envisagées et développées aujourd'hui dans les différents laboratoires de notre groupe international de collaboration. Enfin, dans ce manuscrit, nous avons aussi montré que la combinaison de deux techniques de caractérisation réduisait fortement les incertitudes sur les méthodes individuelles. La combinaison de la XRR et la GIXRF avec d'autres techniques de caractérisation (comme par exemple la XRD) a également été réalisée. Toutefois, si ces premiers résultats sont encourageants, des travaux supplémentaires dans ce sens doivent être poursuivis dans le cadre de la collaboration internationale mise en place.

Remerciements

Je tiens à remercier en tout premier lieu le directeur du CIMAP monsieur Amine Cassimi et du CEA-LETI SDEP monsieur Laurent Vandroux pour m'avoir accueilli au sein de leur laboratoire.

Un très grand merci va aussi tout naturellement à Magali Morales et Daniel Chateigner qui ont dirigé ce travail de thèse. Tout au long de ces années, ils ont su orienter mes recherches et trouver les bons mots pour me remotiver dans les moments plus difficiles. Je les remercie pour leur disponibilité, leur engagement total et leur confiance.

Je remercie les rapporteurs de cette thèse Marie-Christine Lépy et Philippe Jonnard pour avoir accepté de relire mon manuscrit ainsi que pour l'intérêt et l'attention qu'ils ont porté à mon travail. Merci également aux autres membres du jury qui ont accepté d'assister à ma soutenance et de juger mon travail : Luca Lutterotti, Giancarlo Peponi, Christina Strelj chacun ayant également participé très activement à ce travail de thèse. Merci donc pour l'aide qu'ils m'ont apporté depuis trois ans.

Je tiens à relever le plaisir que j'ai eu à travailler au sein du laboratoire CEA-LETI Service Dépôt et plus particulièrement dans l'équipe de métrologie, j'en remercie ici tous les membres. Je remercie aussi Emmanuel Nolot pour l'encadrement de ce travail ainsi que pour sa contribution dans ma compréhension de certains aspects de la physique et du milieu scientifique ainsi que Patrice Gergaud pour la confiance et les opportunités qu'il a pu me donner.

Cette thèse n'aurait pas pu se faire sans le soutien sans faille des différents collaborateurs, en particulier Giancarlo Peponi et Christina Strelj ainsi que leurs étudiants respectifs Fabio Brigidi et Dieter Ingerle. Je les remercie de m'avoir accueilli dans leurs laboratoires et d'avoir su trouver du temps pour me former, m'accompagner et m'épauler malgré leur emploi du temps chargé.

J'ai eu un grand plaisir à partager l'open-space et mon bureau avec de nombreuses personnes toutes avec des profils différents. Un merci tout particulier à Agathe André, Blanka Detlefs, Hélène Rotella, Larissa Djomeni qui ont su m'aider à la fois professionnellement et personnellement tout au long de cette thèse. Je pense aussi à Laëtitia, Cyril, Christopher,

Philippe, Cédric et Gaël ; merci pour toutes ces discussions que nous avons eu autour d'une table ou d'un café.

Je remercie aussi tous mes amis qui m'ont soutenu de diverses manières dans cette aventure. En premier lieu, les anciens de Phelma: Bastien Bonef, Simon Borgniet, Simon Joret, Sylvain Pouch et Jocelyn Berthoz. Je remercie aussi Marc Tinois et toute sa famille pour leur soutien et leur gentillesse. Un merci tout particulier à Edouard *Glerek* Moinard, Méлина *Nowdle* Auer et Matthieu *PKLugar* Dermendjian pour leur présence et leur soutien continu. Merci enfin à tous ceux rencontrés sur différents sites communautaires. Nos diverses rencontres et discussions hors du cadre scientifique m'ont souvent fait le plus grand bien.

Cette thèse n'aurait pas été possible sans le soutien et l'aide de ma famille. Je suis reconnaissant pour le soutien moral, la patience et les attentions dont ils ont fait preuve tout au long de ces années.

Acknowledgments

I would like to thank first and foremost the director of CIMAP Mr. Amine Cassimi and CEA-LETI SDEP Mr. Laurent VANDROUX for hosting me in their laboratory.

A large thank you also goes naturally to Magali Morales and Daniel Chateigner who led this thesis. Throughout these last three years, they have been able to direct my research and find the correct words to motivate me in the most difficult moments. I want to thank them for their availability, total commitment and trust.

I also would like to thank Marie-Christine Lepy and Philippe Jonnard for agreeing to read my manuscript as well as for the interest and attention they have shown in my work. Thank you too to the other jury members who have agreed to attend my PhD defense and judge my work: Luca Lutterotti, Giancarlo Pepponi and Christina Strela which have been also very active and at my side in this thesis. I would like to thank them for the help they have given me during these work.

I want to note the pleasure I had to work in the laboratory CEA-LETI in the deposition service and especially with the metrology team; I want to thank all the members and colleagues here. I also thank Emmanuel Nolot for his supervision of my work as well as for his contribution in my understanding of certain aspects of physics and scientific community. I thank Patrice Gergaud for the trust and the opportunities he has been able to give me.

This thesis would not have been possible without the unfailing support of various collaborators, especially Giancarlo Pepponi and Christina Strela as well as their respective students Fabio Brigidi and Dieter Ingerle. I want to thank them deeply for welcoming me in their laboratories and managing to find time to train me, accompany me and support me despite their busy schedule.

I had a great pleasure to share the open space and my office with many people all with different profiles. I want to give a special thank you to Agathe André, Blanka Detlefs, Hélène Rotella, and Larissa Djomeni who have helped me both professionally and personally throughout this thesis. I cannot forget Laëtitia, Cyril, Christopher, Philippe, Cédric and Gaël; thank you for all the discussions we had around a table or coffee.

I also thank all my friends who supported me in various ways in this adventure. First, the old friends of Phelma: Bastien Bonef, Simon Borgniet, Simon Joret, Sylvain Pouch and Jocelyn Berthoz. I also thank Marc Tinois and his family for their support and kindness. I want to give a special thank you to Edouard *Glerek* Moinard, Mélina *Nowdle* Auer and Matthieu *PKLugar* Dermendjian for their presence and their continuous support. Finally, thank you to all those encountered on various community sites. Our various meetings and discussions outside the scientific framework have been more than welcome.

This thesis would not have been possible without the support and help of my family. I am grateful for the moral support, patience and attention they have shown throughout the years.

Contents

1. Theoretical background	12
1.1. Basics of X-ray fluorescence	12
1.1.1. X-ray emission	12
1.1.2. Interaction of radiation with matter	13
1.1.3. Emission of characteristic X-rays	16
1.2. Refraction of X-rays	19
1.2.1. Total external reflection of X-rays	19
1.2.2. Critical angle for total external reflection	21
1.2.3. Characterization of X-ray standing wave (XSW) pattern	22
1.2.4. X-ray Standing Wave (XSW) field within a thin layer	24
1.3. X-ray fluorescence signals	25
1.3.1. Reflection at the surface of a flat surface	25
1.3.2. Reflection within a multilayer with sharp interfaces	26
1.3.3. GIXRF of a single layer with a flat surface	28
1.3.4. GIXRF within a multilayer with sharp interfaces	31
1.3.5. Reflection and fluorescence from rough surfaces	34
1.4. Quantitative analysis	35
1.4.1. Matrix effects	36
1.4.2. Disturbing effects	37
1.4.3. Mathematical models	37
1.4.4. Geometrical factor correction	40
1.5. Bibliography	42
2. From TXRF to GIXRF	44
2.1. TXRF	44
2.1.1. TXRF instrumentation	44
2.1.2. Applications of TXRF	51
2.1.3. Quantitative analysis	58
2.2. GIXRF	62
2.2.1. TXRF combined with etching	62
2.2.2. GIXRF	63
2.3. Bibliography	69

3. Data analysis	73
3.1. GIXRF and XRR combined analysis	73
3.1.1. Advantages of the combined analysis	73
3.1.2. Available software	75
3.2. Software comparison	76
3.2.1. X-ray database	76
3.2.2. Sample definition	78
3.2.3. Instrumental function	80
3.3. Validation on simulated data	88
3.3.1. X-ray database effect	89
3.3.2. Roughness effect	91
3.3.3. Effect of the divergence	92
3.4. Instrumental correction function	93
3.4.1. Using Maud program	93
3.4.2. Using jGIXA program	94
3.4.3. Using GIMPy and Medepy programs	95
3.5. Validation on experimental data	100
3.5.1. Full parameter approach	100
3.5.2. Combined XRR and GIXRF modeling	102
3.6. Bibliography	105
4. GIXRF applications	107
4.1. Depth profiling characterization of implanted samples	107
4.1.1. Case study	107
4.1.2. First experiments and analysis	109
4.1.3. Second experiments and analysis	118
4.1.4. Results and discussion	121
4.2. Study of annealing induced diffusion in $\text{In}_2\text{O}_3/\text{Ag}/\text{In}_2\text{O}_3$ structures	124
4.2.1. Case of study	124
4.2.2. Experiments	125
4.2.3. Results and discussion	130
4.3. Depth profiling characterization of multilayered structures	136
4.3.1. Case of study	136
4.3.2. Experimental	137
4.3.3. Results and discussions	140
4.4. Bibliography	146

Introduction

Since the apparition of the transistor in 1947, microelectronics has steadily grown to provide the public with more efficient technological innovations. This rising and quasi-exponential demand of the computer and electronic industries for devices always more powerful and more miniaturized has been accompanied with a rising need for surface or near-surface in-depth characterization techniques. Recent developments and the democratization of nanometric devices have highlighted some of the limitations of classic techniques such as the Secondary Ion Mass Spectroscopy (SIMS) or the Rutherford Backscattering Spectroscopy (RBS) and the Grazing Incidence X-Ray Fluorescence (GIXRF) appeared as a promising alternative.

GIXRF is an angle dependent variation of the Total Reflection X-ray Fluorescence (TXRF) analysis, a well-established technique for the study of surface contamination. It consists in irradiating a sample with a primary monochromatic X-ray beam at shallow incidence angles (generally from 0° to 5°) in order to confine the X-ray fluorescence production to a surface-near region (on a nanometer scale). As the probed depth region varies with the incidence angle, the in-depth distribution of the atoms can be obtained and GIXRF thus allows non-destructive depth-profiling experiments.

In the last decade, GIXRF experiments have been performed in various laboratories and synchrotron facilities for the study of in-depth doping profiles and for the characterization of multilayered structures. However, the increasing number of available and functioning GIXRF experimental setups as well as the recent development of analysis software indicates an increasing interest of the scientific community in the technique. As the time consumption of the analyses is reduced with the always increasing computational power, the depth-profiling potential of GIXRF has been pushed further. Indeed, the chance to give a better interpretation of measured data and extract quantitative information about the sample composition becomes possible.

One of the other strength of the GIXRF is the possibility to combine it with other glancing incidence analysis techniques such as X-ray Reflectivity (XRR), a well-known characterization method for the determination of the electronic density depth-profile of the material. By combining these two techniques, the additional information can be used to reduce the uncertainties of the individual methods and allows an in-depth characterization with drastically increased confidence level.

A collaborative international group has been set up between different laboratories: Fondazione Bruno Kessler (FBK, Trento, Italy), Vienna University of Technology (VUT, Vienna, Austria), CEA-Leti (Grenoble, France) and Ensicaen (Caen, France). Its goal was to share expertise, equipments and analysis software on combined XRR and GIXRF to accelerate the development of the technique. It is in this general context that this thesis has been written. The main objective consists in establishing methodologies and protocols for the acquisition and the analysis of combined XRR and GIXRF measurements. Assessing the physical principle behind GIXRF, the capabilities, the limitations of the technique, as well as the different approaches for the elemental quantification was also necessary. Thus, this manuscript is divided in four chapters.

The first chapter has for objectives to present the generalities of grazing incidence X-ray fluorescence. A particular interest was made on the description of the algorithms necessary for GIXRF analysis as well as the underlying physical and mathematical principles. A first introduction to the quantitative analysis problematics will be presented.

The second chapter is dedicated to the presentation of the scientific context on which is based this work. A deep description of the Total Reflection X-ray Fluorescence (TXRF) work of art will be made especially on the required experimental setup, the known and mastered applications of TXRF and the various quantification methods. Based on these observations, a preliminary report on recent GIXRF developments will be shown.

The third part of this manuscript concerns the GIXRF analysis software. In this chapter, I will describe, compare and test the validity of four different combined XRR and GIXRF analysis software. After a comparison of the implementation differences, a large description of the instrumental function correction will be made. The influence of some instrumental effects on the fluorescence intensities as well as various solutions to accurately correct these parasite effects will be presented. I will conclude this chapter by a discussion on the quantification methods, their advantages and their limits.

These first three chapters act as a guide to perform accurately combined XRR and GIXRF acquisitions and analysis with no or little a priori knowledge on the characterization technique. Therefore, the last part of this manuscript will be dedicated to experimental combined XRR and GIXRF measurements performed on samples for micro-electronic or photovoltaic applications. Firstly, the study of arsenic dopants implemented via Plasma Ion Immersion Implantation (PIII) will be presented. I will talk about the problematics linked to the implantation process for standard characterization method such as SIMS and about the solutions that GIXRF can bring to overcome the difficulties. The profile of implantation and the total dose of dopants implanted have been determined. Then, the qualitative in-depth characterization capabilities of GIXRF will

be tested with $\text{In}_2\text{O}_3/\text{Ag}/\text{In}_2\text{O}_3$ thin layered samples as I highlighted the effects of an annealing on the stack structure. Finally, quantitative GIXRF measurements have been performed on $\text{Ta}_2\text{O}_5/\text{NiCo}$ samples. The effects of the Atomic Layer Deposition (ALD) process on the structure of the multilayer will be demonstrated. The difficulties we are currently facing and the possible outlooks will be discussed.

1. Theoretical background

1.1. Basics of X-ray fluorescence

1.1.1. X-ray emission

X-rays were discovered by W.C Röntgen in 1895 and correspond to a radiation of energy in the kilo electron-Volt (keV) range (generally from 0.1 to 100 keV) and wavelength between the wavelengths of UV radiation and gamma rays. The energy (E) and the wavelength (λ) of the radiation of frequency (ν) can directly be linked by a linear law

$$E = h\nu = \frac{hc}{\lambda} \quad (1.1)$$

with h the Planck constant and c the velocity of light in vacuum.

X-ray emission is generated by two mechanisms. On the one hand, X-rays are produced when high-energy charged particles (*e.g.* electrons) are decelerated in the field of a target atom's electron or nucleus (in standard X-ray tubes) or accelerated using bending magnets, undulators or wigglers (in synchrotrons). The deceleration or acceleration of the initial particle produces a continuous spectrum (also called "Bremsstrahlung"), ranging from zero up to the particles incident energies. On the other hand, X-rays are produced via the de-excitation of ionized atoms (Section 1.1.3). The energy of the emitted X-ray radiation is characteristic of the energy levels of core electrons of the target elements.

In standard X-ray tubes, both X-ray emission phenomena occur as the electrons will firstly be decelerated at the impact with the anode material and secondly the atoms of the anode material will de-excite. The produced X-ray spectrum is therefore composed of two distinct components: the continuous Bremsstrahlung and the characteristic X-ray lines which are superimposed (Figure 1).

However, only the first X-ray emission mechanism (*i.e.* the deceleration of the electrons) takes place for synchrotron radiation. Indeed, synchrotron radiation occurs when electrons in the storage ring are constrained into a circular trajectory. The radiation produced possesses a characteristic polarization and the energies generated can range over the entire electromagnetic spectrum.

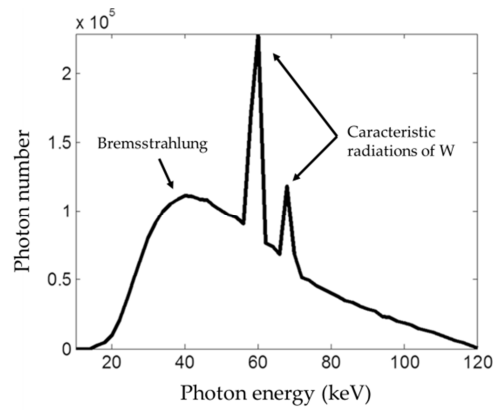


Figure 1 : Spectrum of a tungsten (W) tube.

1.1.2. Interaction of radiation with matter

When a parallel beam of X-ray photons of energy E_0 and intensity I_0 penetrates with normal incident angle a homogeneous material, some photons interact with the medium through absorption and/or scattering processes. The intensity $I(x)$ of the emerging beam after a distance x in the medium is given by the Beer-Lambert law:

$$I(x) = I_0 e^{-\mu x} \tag{1.2}$$

where μ is the linear attenuation coefficient characteristic of the material irradiated by the incident beam.

The linear absorption coefficient expresses the photon interaction probability per unit path length. The total linear absorption coefficient is the sum of the linear absorption coefficients for individual interaction mechanisms as

$$\begin{matrix} \mu_{tot} & = & \mu_{PP} & + & \mu_{CS} & + & \mu_{RS} & + & \mu_{PE} & & (1.3) \\ \text{Total} & & \text{Pair} & & \text{Compton} & & \text{Rayleigh} & & \text{Photoelectric} & & \\ & & \text{production} & & \text{scattering} & & \text{scattering} & & \text{effect} & & \end{matrix}$$

1.1.2.1. Pair production

Pair production can only occur for incident photons with an energy larger than 1.022 MeV, which represents the rest-mass energy equivalent of 2 electrons (as $E = 2m_e c^2$ where m_e is the rest-mass of the electron = 9.11×10^{-31} kg). The interaction of the incident photon with the electric field of the nucleus might result in the production of an electron (e^-) and a positron (e^+) pair, with any photon energy in excess of 1.022 MeV being transferred to the kinetic energy of the e^-/e^+ pair equally. Eventually, the positron will combine with any available electron and produce two annihilation radiations of 511 keV travelling with opposite directions (Figure 2).

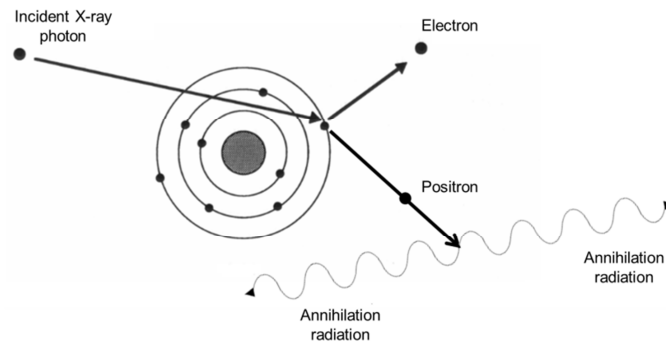


Figure 2 : Mechanism of pair production.

1.1.2.2. Rayleigh scattering

An incident X-ray photon can interact with an electron and be deflected or scattered with no loss of energy (elastic scattering). The Rayleigh scattering occurs by temporarily raising the energy of the electron although the electron will not leave its shell. The electron returns to its initial energy level by re-emitting an X-ray photon after absorption with a negligible change in energy and a slightly different direction. Therefore the atom is neither excited nor ionized and no energy is lost. This type of scattering is dependent approximately on Z^2 .

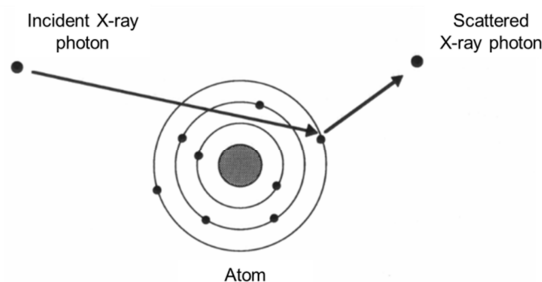


Figure 3 : Coherent scattering of an X-ray photon by an atom.

1.1.2.3. Compton scattering

Compton scattering is an inelastic interaction between an X-ray photon of energy E_0 that is much larger than the binding energy of an atomic electron. Partial energy transfer to the electron causes a recoil and removal from the atom at an angle ϕ . The rest of the energy is transferred to a scattered X-ray photon with a trajectory of angle θ relative to the trajectory of the incident photon (Figure 4). The scattered photon may travel in any direction with any angle θ from 0° to 180° . The recoil electron may only be directed forward relative to the incident X-ray photon (*i.e.* with ϕ from 0° to 90°).

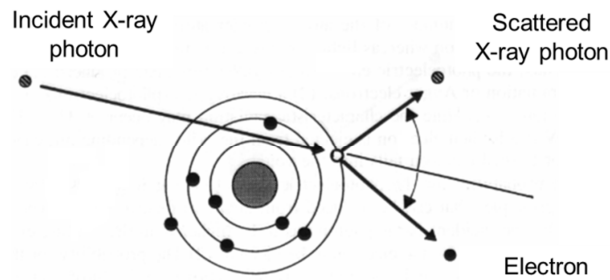


Figure 4 : The Compton scattering process.

Compton scattering is independent of the atomic number and decreases with an increase of the incident energy. The most important consequence of Compton scattering is the appearance of scattered photons of lower energy than the incident photon beam which may cause overlap and high background effects in the XRF spectra.

1.1.2.4. Photoelectric absorption

In this absorption process, an incident photon undergoes an interaction with an inner electron shell in the absorbing atom that has a binding energy similar to but smaller than the energy of the incident photon. If the binding energy is larger than the energy of the incident X-ray photon, the photoelectric process cannot occur. This interaction is possible only when the photon has sufficient energy to overcome the binding energy and extract the electron from the atom. Nevertheless, if the incident X-ray energy (E_0) is equal to the electronic binding energy (E_{BE}), the photoelectric effect becomes energetically feasible and a large increase in attenuation occurs. Energies at which these discontinuities occur are called absorption edges (Figure 5). The probability of photoelectric interactions also depends on the atomic number of the irradiated material as the probability of photoelectric interactions is proportional to $Z^{4.5}/E^3$.

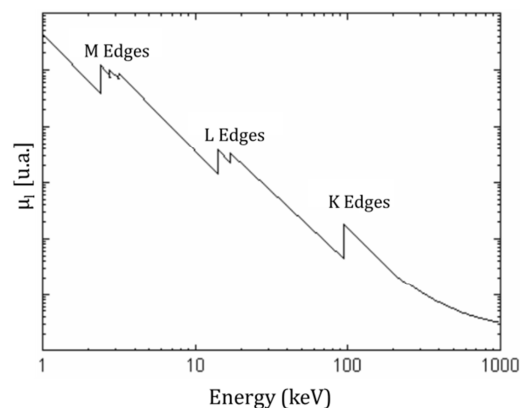


Figure 5 : Plot of the mass attenuation coefficients versus the primary energy. It highlights the absorption edges of the different shells of a high Z element [3].

The incident X-ray photon transfers its energy to the electron. It results in the ejection of the electron from its initial shell with a kinetic energy equal to $(E_0 - E_{BE})$. The atom, which is left in an excited state, will shortly after return to a stable state through one of two possible mechanisms: X-ray fluorescence or Auger effect.

For fluorescence emission, the vacated electron shell is subsequently filled by an electron from an outer shell with less binding energy (e.g. in the case of a vacancy on a K shell, with an electron coming from the L or the M shell) producing a characteristic X-ray. Its energy will be equal to the difference in electron binding energies of the source electron shell and the final electron shell.

$$E_{\text{photon}} = E_{\text{outer shell}} - E_{\text{inner shell}} \quad (1.4)$$

Alternatively, the energy released by an electron hopping from the L shell to the hole in the K shell can be used to expel another electron from one of the outer shells. This secondary emitted electron is called an Auger electron.

In the following work, as we will only consider primary X-ray radiation in the kilo electron-Volt range, the dominant effect will be the photoelectric absorption as shown in the Figure 6.

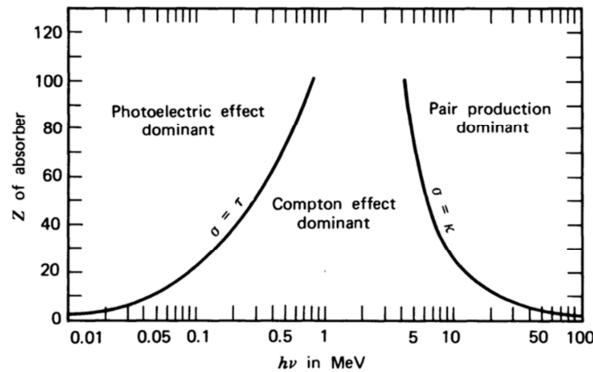


Figure 6 : Relative importance of the three major interactions. Solid lines show the boundary where the two neighboring effects are equal [1].

1.1.3. Emission of characteristic X-rays

1.1.3.1. Characteristic lines and selection rules

As we have seen in Section 1.1.2, fluorescence can occur when a target is irradiated by a radiation of electrons, ions or in our case X-ray photons of a sufficient energy. The atoms constituting the material may undergo ionization meaning that according to Niels Bohr's atomic model [2], one or more electrons can be ejected from the atomic orbitals of each of these atoms. The atom is then in an excited and unstable state as a vacancy is created within the inner electron

shell. For the atom to regain its stable ground state, an electron from a higher level fills the vacancy (Figure 8). In such electronic transitions, the loss of potential energy is transferred to an emitted photon.

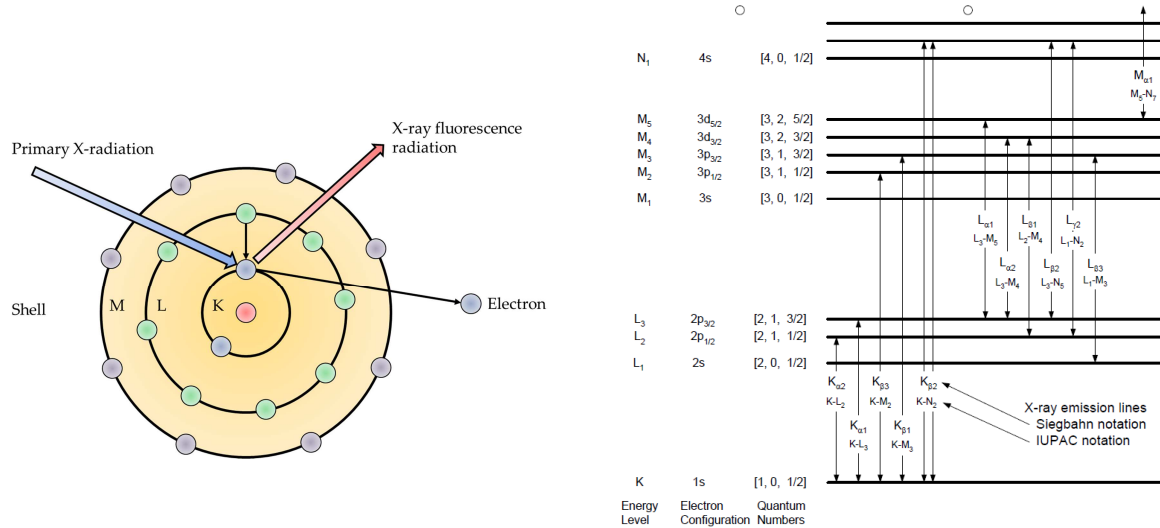


Figure 7: Schematic principle of X-ray fluorescence. **Figure 8:** Atomic allowed electronic transitions.

The production of X-rays involves transitions of the orbital electrons between allowed energy states, associated with ionization of the inner atomic shell. The possible transitions that electrons can undergo from initial to final state are specified by three quantum selection rules.

- $\Delta n \geq 1$
- $\Delta l = \pm 1$
- $\Delta j = \pm 1$ or 0 (with $j = 0 \rightarrow 0$ forbidden)

where n is the principal quantum number (associated to the electron shells K, L, M, etc), l the azimuthal (or angular, orbital) quantum number (associated to s, p, d, f, ... orbitals) and j the total angular moment (angular plus spin).

When an electron is ejected from the K-shell by photoabsorption, the atom becomes ionized. If the corresponding electron vacancy is filled by an electron coming from an L-shell, the transition is accompanied by the emission of an X-ray line known as K-line. A new vacancy is created in the L-shell, which can be filled by an electron from the M-shell. It is accompanied by the emission of a L-line. Therefore, the characteristic X-ray lines are labelled K, L or M to denote the shells they originate from. The designations $\alpha, \beta, \gamma, etc$ added to the line name identify the corresponding emitted X-rays: $K\alpha$ X-rays are produced from a L->K electron transition whereas $K\beta$ for M-> transition, $L\alpha$ for M->L transition, etc.

Furthermore, due to shells degeneracy, several electron transitions can occur between two given shells, with equal or closeby emitted photon energies. An additional designation is made as α_1, α_2 or β_1, β_2 to assign them.

Another nomenclature has been created by the IUPAC (International Union of Pure and Applied Chemistry) and is based solely on the shell designation. Table 1 compares Sieghban and IUPAC notations.

Siegbahn	IUPAC	Siegbahn	IUPAC
$K\alpha_1$	K-L ₃	$L\alpha_1$	L ₃ -M ₅
$K\alpha_2$	K-L ₂	$L\alpha_2$	L ₃ -M ₄
$K\beta_1$	K-M ₃	$L\beta_1$	L ₂ -M ₄
		$L\beta_2$	L ₃ -N ₅

Table 1 : K and L X-ray lines in Siegbahn and IUPAC notations.

The electron cascade phenomenon can continue toward the outermost shells, by emission of X-ray photons (or not) with progressively smaller energies. The process stops when the atom reaches its original state.

1.1.3.2. Fluorescence yield

When an electron is ejected from an atomic orbital by a photoelectric process, two mechanisms can occur: X-ray emission or Auger electron ejection (see Subsection 1.1.2.4). One of these two events occurs for each excited atom but not both. Therefore, Auger electron production is a process which is competitive with X-ray photon emission. The probability that the filling of a hole in a K, L, *etc* shell results in the emission of an X-ray is called fluorescence yield and can be defined as

$$\omega_K = \frac{N_{X-K}}{N_0} \quad (1.5)$$

where N_{X-K} is the number of X-ray photons filling a K shell and N_0 is the number of K-shell vacancies.

Figure 9 shows a plot of the X-ray fluorescence yield versus the atomic number of elements for the K and the L shells. In the following work, we will have to take into account that low atomic number elements (generally $Z < 10$) have a low fluorescence yield. Moreover, the L-fluorescence yield is always inferior compared to the K-fluorescence yield for the same element.

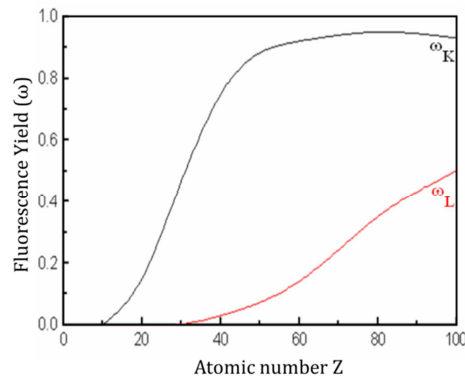


Figure 9 : Fluorescence yield versus atomic number for K and L.

1.2. Refraction of X-rays

Usually, the efficiency of surface or interfaces analysis using X-ray analysis methods is limited due to the large penetration of the incident primary beam into the sample. Therefore, in order to enhance near-surface probing using X-ray scattering, we will use in this work very low incidence angles between the surface of the probed material and the primary incoming X-rays, for which total reflection of X-rays occurs. Since our interest will concentrate on the fluorescence signal, such a technique is called the Total Reflection X-ray Fluorescence (TXRF). In TXRF, the reflected beam superpose coherently with the incident beam above the surface of the sample resulting in an X-ray Standing Wave (XSW) field which does not penetrate significantly into the material bulk and allows to probe near-surface atoms only.

1.2.1. Total external reflection of X-rays

As X-rays are electromagnetic propagating waves, reflection and transmission laws at the interface between different media apply. The TXRF characterization method is based on the total external reflection of the incident X-ray beam. Total reflection occurs at very low incidence angle when the incident beam is completely reflected at the surface of the irradiated material and no refracted beam penetrates deep into the sample.

In order to observe total external reflection of X-rays, different conditions must be satisfied. First, the refractive index n_1 of the medium in which the primary beam is initially propagating must be larger than the refractive index n_2 of the reflecting medium. Moreover, the primary X-ray beam should be propagating towards the interface with an incidence angle smaller than the critical angle for total reflection θ_c . These two conditions can be derived from the Snell-Descartes law (1.6) which can be obtained from the continuity condition for the incident, reflected and refracted waves at the interface.

$$n_1 \sin \theta_i = n_2 \sin \theta_t \quad (1.6)$$

This law shows that if $n_1 > n_2$ (i.e. if the first condition for total external reflection is verified), the refraction angle θ_t must be smaller than the incident angle θ_i . It means that when the incidence angle is getting smaller, the refracted wave inside the material becomes more parallel to the interface (Figure 10). Therefore, it exists a minimum incidence angle for which $\theta_t = 0^\circ$ meaning that the refracted wave propagates along the interface between the media. This angle is called the critical angle for total reflection and can be expressed $\theta_c = \arcsin(n_2/n_1)$. The incident beam cannot be further refracted towards the interface for angles of incidence smaller than θ_c because below this value $\sin(\theta_t)$ has no real solution for θ_t . The incident beam is then reflected with a reflection angle θ_r equal to θ_i . The incident and reflected beams will then superpose and interfere above the region where the incident beam hits the sample surface creating an X-ray standing wave (XSW) pattern.

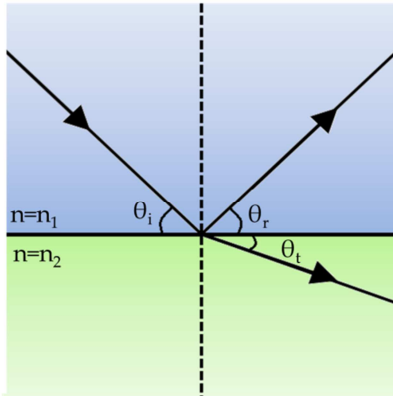


Figure 10 : Incident, reflected and refracted beam at an interface between two media with different refractive index.

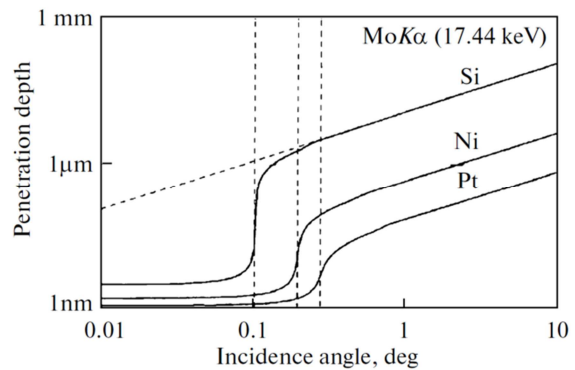


Figure 11 : Penetration depth of Mo-K α X-ray radiation for silicon, nickel and platinum versus the incidence angle. It depends strongly on the incidence angle. Penetration depth is defined as the depth at which the intensity of the radiation inside the material falls to about 37%. Below the critical angle θ_c only a shallow surface is penetrated [3].

The total external X-ray reflection improves the quality of fluorescence analysis from the near-surface region thanks to two factors. First, the excitation efficiency for fluorescence radiation will be improved by the XSW field. In addition, it will prevent any fluorescence excitation from the bulk as incidence angles θ_i will be smaller than the critical angle θ_c . Due to the small angles of incidence, the evanescent wave is in practice not probing the bulk of the material and the entire TXRF signal comes from the near-surface (Figure 11).

1.2.2. Critical angle for total external reflection

Let's take a wave of incident X-rays with an electric field form: $E(\mathbf{r}) = E_0 \exp(i\mathbf{k} \cdot \mathbf{r})$. This wave penetrates the medium of refractive index $n(\mathbf{r})$ and propagates according to the Helmholtz equation.

$$\Delta_r E(\mathbf{r}) + k^2 n(\mathbf{r})^2 E(\mathbf{r}) = 0 \quad (1.7)$$

where $k = 2\pi/\lambda$ is the modulus of the wave vector \mathbf{k} ; and λ denotes the X-ray wavelength.

Conventionally, the refractive index of solid samples in the X-ray domain is a complex quantity [3].

$$n(\mathbf{r}) = 1 - \delta(\mathbf{r}) + i\beta(\mathbf{r}) \quad (1.8)$$

where δ is the refractive index and β the absorption index being positive quantities related to scattering and absorption properties [4].

$$\delta(\mathbf{r}) = \frac{N_A}{2\pi} r_e \rho(\mathbf{r}) \frac{1}{A} [f_0 + f(\lambda)] \lambda^2 \quad (1.9)$$

$$\beta(\mathbf{r}) = \frac{\lambda}{4\pi} \mu(\mathbf{r}) \quad (1.10)$$

where N_A is the Avogadro's number = 6.022×10^{23} atoms/mol; r_e the classical electron radius = 2.818×10^{-13} cm; ρ the density (in g/cm³) of the respective element of the medium; A the atomic mass (in g/mol); f_0 is a quantity that for X-rays is equal to the atomic number Z ; and $f(\lambda)$ is a correction term that is only decisive at and below the absorption edges and is generally negative and $\mu(\mathbf{r})$ is the linear absorption coefficient.

For compounds, solutions or mixtures δ and β have to be calculated using an additive law.

$$\delta_{total} = \sum c_i \delta_i$$

$$\beta_{total} = \sum c_i \beta_i$$

where the c_i terms are the different mass fractions of the individual elements i with respective values δ_i and β_i .

The dispersion δ is a positive number of the order 10^{-6} for hard X-rays. The absorption β is typically one or two order of magnitude smaller ($10^{-7} - 10^{-8}$). In the hard X-ray domain, as the refractive index of all materials is slightly inferior to 1, the first condition for total external reflection will always be validated at the interface between air and the sample interface.

The condition for total external reflection of an X-ray beam targeting a sample with refractive index n_2 can be rewritten

$$\cos \theta_c = n_2 = 1 - \delta \quad (1.11)$$

Representing the cosine function by its first terms of a Taylor series, we can obtain:

$$\theta_c \sim \sqrt{2\delta} \sim \frac{\lambda_i}{\sqrt{\pi}} \sqrt{N_A r_e \frac{\rho Z}{A}} \quad (1.12)$$

The latter approximation is for X-ray wavelengths shorter than wavelengths corresponding to the absorption edges of the sample's element. The critical angle for total reflection θ_c is usually inferior to 1° and decreases for larger incident X-ray energies and for heavier elements.

1.2.3. Characterization of X-ray standing wave (XSW) pattern

Whenever an electromagnetic wave travels towards a boundary separating two materials with different refractive index, a part of the energy is reflected and another part is transmitted through the medium. The incident and reflected wave planes (with respective wave vectors k_o and k_r) will interfere and generate an XSW pattern with planes of maximum intensity parallel to the surface and with a period $D = \lambda/(2 \sin\theta)$ [5].

Interferences result from the superposition of two beams. In the region of superposition, the total displacement is equal to the sum of the individual displacement of each wave. The fluctuation of the displacement will be distinct if the two waves are monochromatic and coherent (*i.e.* the waves have the same wavelengths and a fixed phase difference). If the phase difference between the two superposing waves is an even multiple of π , then the crest of the first wave is superimposed with the crest of the other wave. Therefore, the magnitude of the total displacement is the sum of the individual magnitudes and sums up to a maximum. The interference is defined as constructive. On the contrary, if the phase difference between the two superposing waves is an odd multiple of π , the maxima of one wave will correspond to the minima of the other. The amplitudes are then subtracted to a minimum and this kind of interference is called destructive.

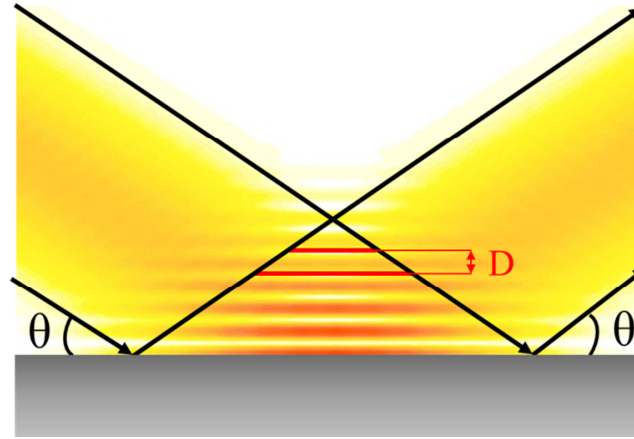


Figure 12 : Illustration of the X-ray standing wave field (XSW) created by the interference between the incident and the reflected wave. The planes in which constructive interference takes place are parallel to the sample surface. The periodicity varies with the incidence angle.

For a flat substrate, in the case of hard X-rays, the value of the electric field intensity above its surface is [6]:

$$I_{int}(\theta, z) = I_0 \left[1 + R(\theta) + 2\sqrt{R(\theta)} \cos\left(\frac{2\pi z}{D} - \phi(\theta)\right) \right] \quad (1.13)$$

where $I_0 = |E_0|^2$ is a measure of the intensity of the incident beam which is supposed to be constant and $R(\theta)$ the reflectivity = $|E_0^r/E_0|^2$ where E_0^r is the amplitude of the reflected beam and E_0 the amplitude of the incident beam. $\Phi(\theta)$ is the relative phase between the reflected and incident electric field amplitudes. This phase shift only occurs in the region of total reflection.

$$\phi(\theta) = \arccos[2(\theta/\theta_{crit})^2 - 1] \quad (1.14)$$

The value of $\Phi(\theta)$ varies from π to 0 if the angle of incidence is smaller than θ_c . Above the critical angle, it is constant and equal to 0.

Within the substrate, it is worth mentioning that the intensity is exponentially decreasing with the depth and is expressed [3]:

$$I_{int}(\theta, z) = I_0 \left[1 + R(\theta) + 2\sqrt{R(\theta)} \cos(\phi(\theta)) \right] \exp(-z/z_n) \quad (1.15)$$

where z_n is the penetration depth of the incident X-ray wave inside the sample.

The dependence of the intensity above and below the surface of a Silicon substrate irradiated by a Mo-K α radiation is shown on Figure 13. It is noticeable that for $\theta_i = 0.1^\circ = \theta_c$, the maximum is located exactly on the surface and due to the surface reflectance value, the intensity of the antinode is 3.6 time larger than that of the primary beam. At angles smaller than the critical angle, the position of the first antinode moves away from the surface of the sample and the

intensity inside the sample falls to 0 in a few nanometers. At incidence angles larger than the critical angle, the oscillations intensity diminish and the intensity value goes towards 1. Inside the sample, the intensity value is almost constant within a distance of several microns [7].

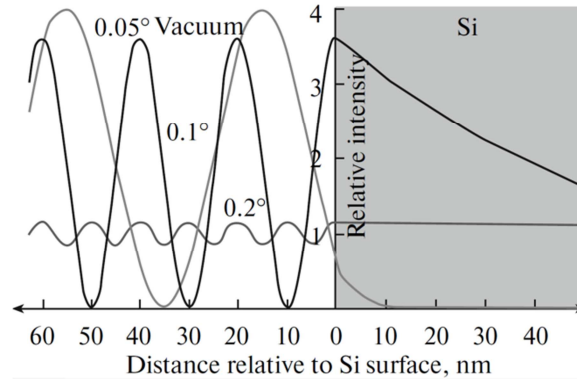


Figure 13 : Intensity above and below the interface between the air and a thick Si substrate considering a Mo-K α striking the sample with different glancing angles [3].

1.2.4. X-ray Standing Wave (XSW) field within a thin layer

Both the intensities of XSW field above the sample surface and penetration depth into the sample strongly depend on the incidence angle. Consequently, depth dependent elemental concentration distributions close to the sample surface can be probed. For the lowest angles (lower than the critical angle of reflection), the beam is totally reflected, and only the first few nanometers below the surface are excited, this excitation being dependent on the XSW field strength. Only the evanescent field penetrates the sample. For incidence angles larger than the critical angle, the incident beam starts to penetrate strongly the material and the XSW field vanishes. Near the critical angle the XSW field is maximal at the sample surface and the penetration depth varies strongly. Thanks to such variations, Grazing Incidence X-ray Fluorescence (GIXRF) is a well suited technique for elemental depth profiling. Around the critical angle, the GIXRF signal allows near surface investigations. Figure 14 illustrates GIXRF angular profiles for two model samples, *i.e.* a bulk with infinite thickness, and a thin layer of the same composition. For both samples, below θ_c , only weak fluorescence intensity is observed coming from the evanescent field excitation (fluorescence signal in this range is magnified for the layer case in Figure 14). Above θ_c , the beam penetrates the sample and fluorescence excitation progressively rises. For the bulk sample the fluorescence intensity consequently increases, reaching an asymptotic behavior due to full incident field absorption in the infinite medium. For the thin layer, an increasing part of the incident wave exits the sample by its back surface, and the fluorescence intensity simultaneously decreases, reaching another asymptotic behavior. For a

layer supported by a substrate, part of this latter wave is back reflected at the substrate interface and the two reflected beams interfere, giving rise to oscillations in the GIXRF spectrum, similarly as in specular reflectivity and as described by De Boer.

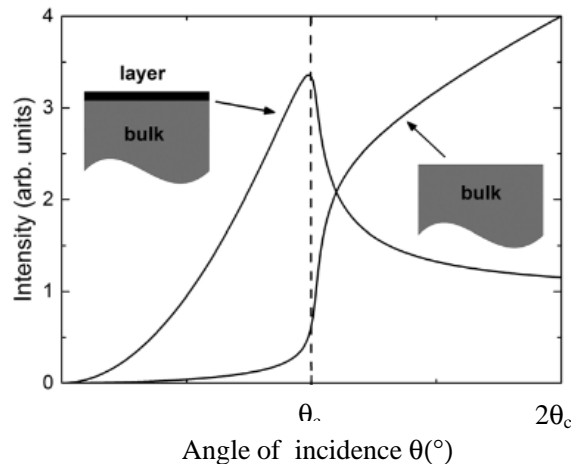


Figure 14 : Angular dependence of X-ray fluorescence intensity for different types of samples [8].

As the modulations of the electric field intensity are in general difficult to predict [8], simulations of these latter by using proper data analysis software appear then necessary.

1.3. X-ray fluorescence signals

1.3.1. Reflection at the surface of a flat surface

When an electromagnetic plane wave $\Psi(z) = \exp(ikz)$ with unit amplitude and wave vector of the radiation normal to the interface $k = 2\pi \sin\theta/\lambda$ hits the sharp surface of a medium with an index of refraction n_s at the angle θ , it splits into a reflected and a refracted wave [9]–[11]. The reflected and refracted waves with respective amplitudes R (the reflection coefficient or reflectivity) and T (the transmission coefficient or transmissivity) are characterized by wave functions.

$$\Psi(z) = R \exp(-ik z) \tag{1.16}$$

$$\Psi(z) = T \exp(in_s k z) = T \exp(ik_s z) \tag{1.17}$$

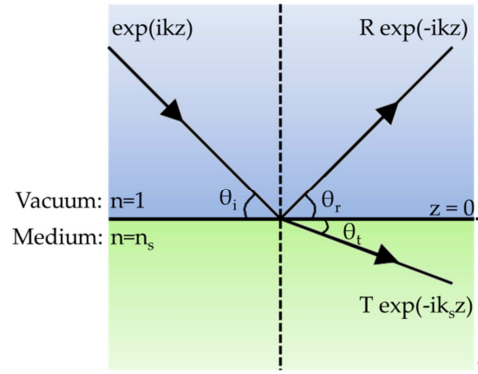


Figure 15: Reflectance and transmittance of the electromagnetic radiation on a substrate.

According to Figure 15, the wave equations to be solved are:

$$\Psi''(z) + k^2\Psi(z) = 0, \quad z \leq 0 \text{ in air} \quad (1.18)$$

$$\Psi''(z) + k_s^2\Psi(z) = 0, \quad z \geq 0 \text{ in the medium} \quad (1.19)$$

At the interface between the vacuum and the considered medium, the boundary conditions must express the continuity of the parallel components of the magnetic and electric field. These boundary conditions can be expressed at the interface $z=0$, $\Psi(0^+) = \Psi(0^-)$ and $\Psi'(0^+) = \Psi'(0^-)$. The general solutions of the wave equations are:

$$\Psi(z) = \exp(ikz) + R \exp(-ikz), \quad z \leq 0 \text{ in air}, \quad (1.20)$$

$$\Psi(z) = T \exp(-k_s z), \quad z \geq 0 \text{ in the medium}, \quad (1.21)$$

Using these solutions and the boundary equations described above, we can find that

$$R = \frac{k - k_s}{k + k_s} \quad T = \frac{2k}{k + k_s} \quad (1.22)$$

The squared modulus of the reflectance $|R|^2$ gives us the intensity of the reflected radiation (the Fresnel reflectivity) and can be measured in a specular reflectivity experiment. This formalism has been extended to systems consisting of a higher number of layers with sharp interfaces. Abelès [12] connected the transmission and reflection coefficients of consecutive layers via matrices. Parrat [13] developed a recursive formalism that provides equivalent results.

1.3.2. Reflection within a multilayer with sharp interfaces

1.3.2.1. Abelès matrix method

The basis of the calculation of the reflectivity using the optical matrix method is that the system is divided into as many uniform layers as necessary to describe accurately the refractive-

index profile normal to the surface. By applying Maxwell's equations at each interface, it is possible to describe each layer by a 2×2 matrix [14, 15]. The characteristic matrix for each layer is called the transfer matrix.

$$M_j = \begin{bmatrix} \cos \beta_j & -(i/k_j) \sin \beta_j \\ ik_j \sin \beta_j & \cos \beta_j \end{bmatrix} \quad (1.23)$$

with k_j the wave vector normal to the interface in the layer j and β_j is the phase shift on traversing the layer j once.

For a system with N different layers, each layer j has a transfer matrix M_j . The complete system transfer matrix is then

$$M_s = M_N \cdot \dots \cdot M_2 \cdot M_1 \quad (1.24)$$

By respecting the boundary conditions at the interfaces, the expression of the reflected amplitude can be obtained

$$R = \frac{(M_{11} + M_{12}k_N)k_0 - (M_{21} + M_{22})k_N}{(M_{11} + M_{12}k_N)k_0 + (M_{21} + M_{22})k_N} \quad (1.25)$$

where M_{ij} are the elements of the 2×2 complete system matrix M_s . The two equations above are not the most convenient way of computing the reflectivity. The recurrence relations between Fresnel coefficients are usually used for the calculation.

1.3.2.2. Parrat's recursive method

Parrat's recursive method is the most widely used method for calculating the reflectivity. Similarly as what has been done with the Abelès method, the sample has to be divided into uniform (*i.e.* with constant refractive index) sub-layers of various thicknesses (Figure 16).

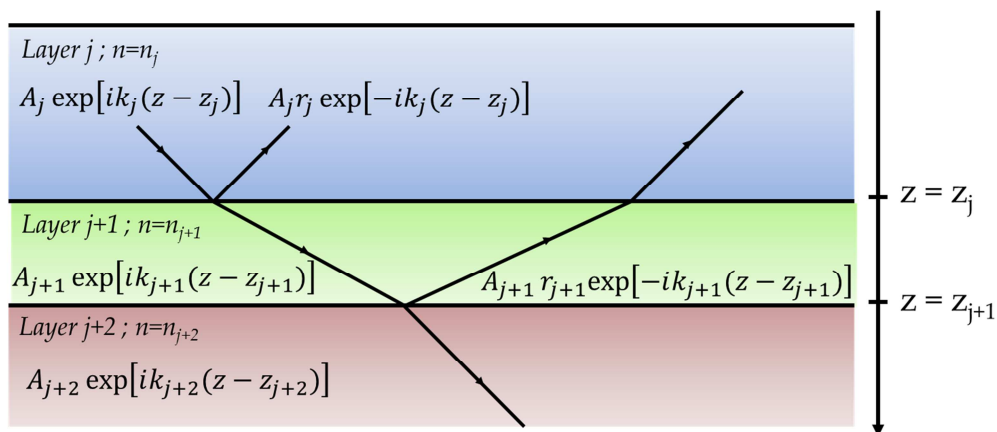


Figure 16: Reflectance and transmittance of electromagnetic radiation through a layer within a stack of N layers.

The calculation method for a substrate has been presented in the Section 1.3.1. Therefore, by deriving the equation for a general multilayer of N uniform layers stacked along the z -axis with thickness Δz_j and wave numbers k_j , we have:

$$\Psi''(z) + k^2\Psi(z) = 0, \quad z \leq 0 \quad (1.26)$$

$$\Psi''(z) + k_{j+1}^2\Psi(z) = 0, \quad z_j \geq z \geq z_{j+1}, \quad (1.27)$$

$$\Psi''(z) + k_N^2\Psi(z) = 0, \quad z \geq z_N, \quad (1.28)$$

By respecting the boundary conditions at each interface (*i.e.* $\Psi(z_j^+) = \Psi(z_j^-)$ and $\Psi'(z_j^+) = \Psi'(z_j^-)$), Parrat obtained [9]:

$$R_j = \frac{F_{j+1} + R_{j+1} \exp(2ik_{j+1}\Delta z_{j+1})}{1 + F_{j+1}R_{j+1} \exp(2ik_{j+1}\Delta z_{j+1})} \quad (1.29)$$

with F_j the Fresnel coefficients for each individual layer j defined by

$$F_j = \frac{k_{j-1} - k_j}{k_{j-1} + k_j} \quad (1.30)$$

If all the structural elements (k_j and Δz_j) are given for $j = 1, 2, 3, \dots, N$, the value R_j can be calculated for all j starting with the layer at the interface with the substrate. Proceeding step by step, we can obtain the value of the reflectance of the complete system which is given by R_0 . The reflectivity measured during the experiment is then the squared modulus of the reflectance of the system $|R_0|^2$.

1.3.3. GIXRF of a single layer with a flat surface

In order to calculate the X-ray fluorescence intensities emitted by a sample irradiated with a primary X-ray beam at glancing angles, the electromagnetic field inside the material has to be known for every incidence angle of the primary radiation. In order to do so, some new constants must be defined [16]:

$$\alpha = 2\delta - \delta^2 + \beta^2 \quad (1.31)$$

$$\gamma = 2\beta(1 - \delta) \quad (1.32)$$

$$N_j = N'_j - iN''_j \quad (1.33)$$

$$\varepsilon_j = \varepsilon'_j - i\varepsilon''_j = 1 - \alpha - i\gamma \quad (1.34)$$

where N_j is the complex vector of refraction and ε_j the complex dielectric constant of the material j . δ and β are the respective dispersion and absorption coefficients defined before. The z -component of N_j perpendicular to the interface considered can be written [17]:

$$N_{jz} = (\varepsilon_j - \cos^2\theta)^{1/2} \quad (1.35)$$

where θ is the angle of incidence of the primary radiation.

The following calculation of X-ray fluorescence intensities is only valid in the case of an s-polarized primary radiation (electric field parallel to the interface). The case of a p-polarization (magnetic field parallel to the interface) can be found in the literature [18]. The effect of the polarization of the primary X-ray beam will be discussed later. Then, for an s-polarization, the complex refraction and transmission coefficients can be defined by the Fresnel coefficients.

$$r_j = \frac{N_{jz} - N_{j+1,z}}{N_{jz} + N_{j+1,z}} \quad t_j = \frac{2N_{jz}}{N_{jz} + N_{j+1,z}} \quad (1.36)$$

Let's consider the case of a single layer with a flat surface deposited on a flat substrate. It is known [19] that the time-averaged flux (*i.e.* the energy flowing through a unit surface area per unit time) is given by the Poynting vector. Therefore, we have:

$$\mathbf{P}_j = \frac{1}{2} \text{Re}(\mathbf{E}_j \times \mathbf{H}_j^*) = \frac{1}{2} \text{Re}(\mathbf{E}_j^* \times \mathbf{H}_j) \quad (1.37)$$

$$\mathbf{P}_j = \frac{|E_j|^2}{2Z_0} \mathbf{N}'_j \quad (1.38)$$

where $Z_0 = (\mu_0/\epsilon_0)^{1/2}$ is the impedance of vacuum.

The position dependence of \mathbf{P}_j is found by substituting the plane-wave expression in (1.38):

$$\mathbf{P}_j = \frac{|E_j^t|^2 \mathbf{N}'_j}{2Z_0} \exp\left(-\frac{4\pi N''_{jz} z}{\lambda}\right) \quad (1.39)$$

where E_j^t is the electric field at the top of the layer j and z is the depth position inside the material (with $z = 0$ representing the surface of the sample).

The absorption of the radiation must be taken into account. According to Poynting theorem, the amount of electromagnetic energy absorbed per unit of time within a volume bounded by a surface S can be written

$$A = - \iint_S \mathbf{P}_j \cdot \mathbf{u} \, ds \quad (1.40)$$

where ds is an area element of S .

From that, we can directly deduce that the amount of energy absorbed by a slice of material at depth z with infinitesimal thickness dz is

$$dA = -S_1 \frac{\partial P_{jz}}{\partial z} dz \quad (1.41)$$

where S_1 is both the bottom and the top surface area.

We can conclude that the amount of absorbed radiation is proportional to $\partial P_{jz}/\partial z$ and from (1.35) and (1.39), we have directly

$$-\frac{\partial P_{jz}}{\partial z} = \frac{|E_j^t|^2 2\pi\epsilon_j''}{2Z_0 \lambda} \exp\left(-\frac{4\pi N_{jz}'' z}{\lambda}\right) \quad (1.42)$$

From then, the X-ray fluorescence intensity (I_{aj}) (the number of photons emitted per unit of time by atoms of a particular element a in the layer j) of a multi-structure can be expressed by

$$I_{aj} = \frac{\lambda}{hc} C_{aj} \frac{\tau_{a\lambda}}{\mu_{j\lambda}/\rho_j} J_{a\lambda} \omega_a g_a \exp\left(-\sum_{n=1}^{j-1} \frac{\mu_{na} d_n}{\sin \psi_d}\right) S_1 \int_0^{d_j} dz \left(-\frac{\partial P_{jz}}{\partial z}\right) \exp\left(-\frac{\mu_{ja} z}{\sin \psi_d}\right) \quad (1.43)$$

with C_{aj} the mass fraction of element a in layer j , ρ_j the density of material j , $\tau_{a\lambda}$ is the photoelectric part of the mass absorption coefficient for element a at wavelength λ , $J_{a\lambda}$ is the absorption jump factor at wavelength λ for the creation of holes in the considered shell of element a , ω_a is the fluorescence yield for the decay of holes in the considered shell of a , g_a is the relative emission rate for the considered XRF line in preference to other lines originating from the same hole in a , and μ_{na} the linear absorption coefficient of the considered fluorescence radiation from element a in layer n , ψ_d is the detection angle and S_1 is the irradiated detected sample area.

The sample area is generally equal to the detected area. However, depending on the size of the sample or the experimental setup we are using, the size of the detected area may not be the limiting factor. This particular point will be addressed in the following subsections. The equation for the calculation of the primary XRF (1.43) takes into account different factors as explained on Figure 17. The attenuation of the primary radiation is taken into account in the $\partial P_{jz}/\partial z$ factor. The fraction of absorbed radiation which is used for photoionization of the considered shell of atom a , the probability of emission of the considered radiation and the absorption factor for the outgoing radiation are also taken into account. These factors are multiplied by the absorption of the emitted X-ray fluorescence by the layer itself (via an integration on z the position of the atom) and the system above the considered layer (in the case of a multilayered structure).

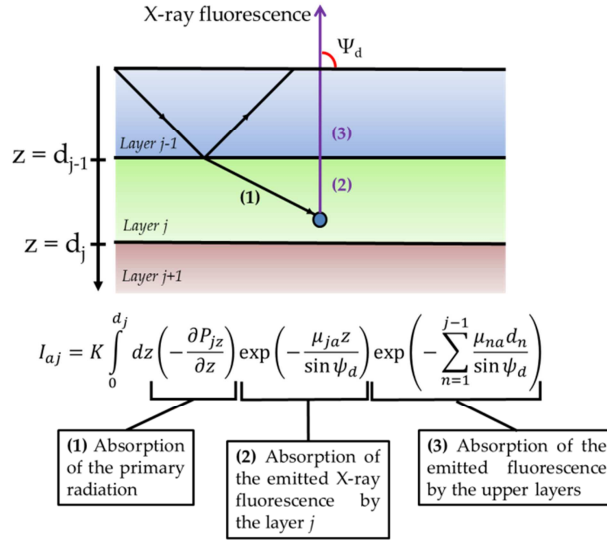


Figure 17 : Calculation of the primary X-ray fluorescence intensity from an atom in a layer j .

1.3.4. GIXRF within a multilayer with sharp interfaces

Considering the equation (1.43), we see that the only difference for the XRF intensity calculation between a single layer deposited on a substrate and a multilayered structure is the value of the absorption of the incident radiation $\partial P_{jz}/\partial z$. Indeed, the probability of fluorescence of the considered atom and the absorption of the emitted X-ray fluorescence are already taken into account. Therefore, a formula for the derivative of the Poynting vector is necessary.

As before, the calculation has been operated considering a primary s-polarized radiation. The total electric field at a point in a layer j is the sum of two contributions: the transmitted contribution \mathbf{E}_j^\downarrow and the reflected contribution \mathbf{E}_j^\uparrow :

$$\mathbf{E}_j = \mathbf{E}_j^\downarrow + \mathbf{E}_j^\uparrow \quad (1.44)$$

Using Maxwell's equation,

$$\nabla \times \mathbf{E}_j = -\mu_0 \partial \mathbf{H}_j / \partial t \quad (1.45)$$

and re-injecting it in (1.37), we obtain

$$P_{jz} = \frac{1}{4Z_0} (\mathbf{E}_j^\downarrow + \mathbf{E}_j^\uparrow)^* (\mathbf{E}_j^\downarrow - \mathbf{E}_j^\uparrow) N_{jz} \quad (1.46)$$

$$P_{jz} = \left\{ N_{jz}' |E_j^t|^2 \exp\left(-\frac{4\pi N_{jz}'' z}{\lambda}\right) - N_{jz}' |E_j^r|^2 \exp\left(\frac{4\pi N_{jz}'' z}{\lambda}\right) + N_{jz}'' \left[i E_j^{t*} E_j^r \exp\left(\frac{4\pi i N_{jz}' z}{\lambda}\right) \right] \right\} \quad (1.47)$$

with E_j^r the reflected field at the top of the surface j and E_j^t the transmitted field at the top of the layer j .

As we have stated previously, the amount of absorbed radiation is proportional to $\partial P_{jz}/\partial z$, and we have

$$-\frac{\partial P_{jz}}{\partial z} = \frac{1}{2Z_0} \frac{4\pi}{\lambda} N'_{jz} N''_{jz} \left\{ |E_j^t|^2 \exp\left(-\frac{4\pi N''_{jz} z}{\lambda}\right) + |E_j^r|^2 \exp\left(\frac{4\pi N''_{jz} z}{\lambda}\right) + E_j^{t*} E_j^r \exp\left(\frac{4\pi i N'_{jz} z}{\lambda}\right) \right\} \quad (1.48)$$

Defining

$$A_{j1} = \frac{2\pi\epsilon_j'' |E_j^t|^2}{\lambda\mu_{j\lambda} |E_0|^2} \quad (1.49)$$

$$A_{j2} = \frac{2\pi\epsilon_j'' |E_j^r|^2}{\lambda\mu_{j\lambda} |E_0|^2} \quad (1.50)$$

$$A_{j3} = \frac{2\pi\epsilon_j'' 2E_j^t * E_j^r}{\lambda\mu_{j\lambda} |E_0|^2} \quad (1.51)$$

$$b_{j1} = 4\pi N''_{jz}/\lambda \quad (1.52)$$

$$b_{j2} = -b_{j1} \quad (1.53)$$

$$b_{j3} = -4\pi N'_{jz}/\lambda \quad (1.54)$$

Therefore, we have

$$-\frac{\partial P_{jz}}{\partial z} = \frac{|E_0|^2}{2Z_0} \mu_{j\lambda} \text{Re} \left(\sum_{m=1}^3 A_{jm} \exp(-b_{jm} z) \right) \quad (1.55)$$

By injecting the new expression for the attenuation of the incident radiation and doing the integration, we finally obtain

$$I_{aj} = I_0 C_{aj} \rho_j \tau_{\lambda j} J_{a\lambda} \omega_a g_a S_1 \exp\left(-\sum_{n=1}^{j-1} \frac{\mu_{na} d_n}{\sin \psi_a}\right) \times \text{Re} \left(\sum_{m=1}^3 A_{jm} \frac{1 - \exp[-(b_{jm} + \mu_{ja}/\sin \psi_a) d_j]}{b_{jm} + \mu_{ja}/\sin \psi_a} \right) \quad (1.56)$$

where $I_0 = |E_0| \lambda / (2Z_0 h c)$ is the number of incident photons per unit surface area per unit time and the other constants are the same as defined on (1.43).

1.3.4.1. Via recursive method

The expression of A_{jm} ((1.49) to (1.51)) contains the value of the transmitted and reflected electric fields throughout the material irradiated by a primary radiation with an incidence angle θ . These electric fields can be determined from a recursive relation similar to the Parrat's method described earlier. Therefore, in the recursive method E_j^r and E_j^t can be determined from [18]

$$E_j^r = a_j^2 X_j E_j^t \quad (1.57)$$

$$E_{j+1}^t = \frac{a_j E_j^t t_j}{1 + a_{j+1}^2 X_{j+1} r_j} \quad (1.58)$$

$$a_j = \exp\left(-\frac{2\pi i d_j N_{jz}}{\lambda}\right) \quad (1.59)$$

$$X_j = \frac{r_j + a_{j+1}^2 X_{j+1}}{1 + a_{j+1}^2 X_{j+1} r_j} \quad (1.60)$$

with d_j the thickness of the layer j , r_j and t_j are respectively the complex coefficients of reflection and transmission has defined in Section 1.3.2.

1.3.4.2. Via transfer matrix

De Boer's formalism is based on the Parrat's relation in order to obtain the expression for the electromagnetic fields. Identically as the reflectivity, some other approaches are possible. One can use an approach closer to Abelès formalism and connect the different electric-field vectors by two transfer matrixes [3]. Therefore, the relation between the electric fields can be written

$$\begin{bmatrix} E_j^t \\ E_j^r \end{bmatrix} = M_{j,j+1} \begin{bmatrix} E_{j+1}^t \\ E_{j+1}^r \end{bmatrix} \quad (1.61)$$

with

$$M_{j,j+1} = \begin{bmatrix} m_{1,j+1} & m_{2,j+1} \\ m_{3,j+1} & m_{4,j+1} \end{bmatrix} \quad (1.62)$$

with $j = 0$ for the vacuum and $j = N+1$ for the substrate.

A unique solution for E_j^t and E_j^r can be found by connecting the two amplitudes E_0^r and E_{N+1}^t by a matrix multiplication

$$\begin{bmatrix} 1 \\ E_0^r \end{bmatrix} = \prod_{j=0}^N M_{j,j+1} \begin{bmatrix} E_{N+1}^t \\ 0 \end{bmatrix} \quad (1.63)$$

Supposing that the detection angle $\Psi_d = 90^\circ$, Klockenkämper obtains a new expression for the X-ray fluorescence intensity which is equal to the formula obtain via the De Boer formalism (1.55)

$$\begin{aligned}
 I_{x,j}(\alpha_0) = & I_0 c_{x,j} S_{x,E0} \varepsilon_{det} T_{air} \exp\left(\sum_{i=1}^{j-1} (\mu/\rho)_{i,E} \rho_i d_i\right) \left\{ |E_j^i|^2 \frac{1 - \exp\left(-\left[\frac{(\mu/\rho)_{j,E0}}{\alpha_j} + (\mu/\rho)_{j,E}\right] \rho_j d_j\right)}{\frac{(\mu/\rho)_{j,E0}}{\alpha_j} + (\mu/\rho)_{j,E}} \right. \\
 & + |E_j^r|^2 \frac{1 - \exp\left(-\left[-\frac{(\mu/\rho)_{j,E0}}{\alpha_j} + (\mu/\rho)_{j,E}\right] \rho_j d_j\right)}{-\frac{(\mu/\rho)_{j,E0}}{\alpha_j} + (\mu/\rho)_{j,E}} \\
 & \left. + 2Re \left[E_j^i E_j^r \frac{1 - \exp\left(-\left[-\frac{2ik_0 \alpha_j}{\rho_j} + (\mu/\rho)_{j,E}\right] \rho_j d_j\right)}{-\frac{2ik_0 \alpha_j}{\rho_j} + (\mu/\rho)_{j,E}} \right] \right\}
 \end{aligned}$$

For both calculations, some approximations have been made. Only the primary intensity coming from the X-ray source has been taken into account. It is well known that the secondary fluorescence occurs due to the excitation by fluorescence radiation emitted by other atoms in the sample (with respect to the elements present in the samples and the values of the energy edges). Taking into account the secondary fluorescence complicates the calculation of the fluorescence intensity because in a multilayer we have to consider all the atoms present in the structure (above and under the probed layer). Moreover, no reflection and refraction of the fluorescence emitted by an element is taken into account. As the measurements are realized at grazing incidences, these effects can be neglected [18].

1.3.5. Reflection and fluorescence from rough surfaces

In most cases, sharp interfaces cannot be considered. Therefore, it is necessary to take into account the effect of the surface and interfacial roughness on the reflection of X-rays. Among all the possibilities to define a roughness, σ can be defined as the mean-square amplitude of fluctuations with respect to a reference level z_0

$$\sigma = \sqrt{(z - z_0)^2} \quad (1.64)$$

The introduction of the roughness is usually done via the introduction of a roughness factor Q_j in the Fresnel reflection coefficients. Different models and expressions for this roughness factor can be used [23]

$$Q_j = 1 \text{ (for ideally smooth surfaces)} \quad (1.65)$$

$$Q_j = \exp(-2k_j^2 \sigma_j^2) \text{ (Debye-Waller-like factor)} \quad (1.66)$$

$$Q_j = \exp(-2k_j k_{j+1} \sigma_j^2) \text{ (Nevot-Croce factor)} \quad (1.67)$$

It has been shown [25, 26] that for a small roughness correlation length (*i.e.* high spatial frequencies), the Nevot-Croce coefficients can be used. If in the considered system, the roughness

cannot be considered as small (<10 nm according to the relation that $k_j\sigma_j < 1$), one can use the Debye-Waller factor.

Samples with interfaces with a composition profile are common. Indeed, in some cases often due to inter-diffusion, there is a grading of the electron density and the interface between two layers is not clearly defined. If we define the interface by a Gaussian profile with a width of σ , it can be shown that [28]

$$Q = \exp(-2k^2\sigma^2) \quad (1.68)$$

This expression of the roughness factor Q is similar to the expressions described above (Equation 1.66). Therefore, it makes impossible for the techniques to distinguish between composition grading and interfacial roughness.

1.4. Quantitative analysis

The observed X-ray photon beam intensity from an element a in a sample is in fact a function of many factors including the concentration (weight fraction) of the element, the matrix, the experimental set-up, the detection system, the spectral distribution of the exciting radiation, and the size of the sample. This is illustrated in Figure 18 where (computed) relative count rates for Fe-K α photons, R_{Fe} , are drawn versus the iron (Fe) concentration in FeNiCr alloys with different concentrations of chromium (Cr) and nickel (Ni). One can note that the data points scatter randomly within non-linear enveloping curves representing the system Fe $_x$ Ni $_{1-x}$ and the system Fe $_x$ Cr $_{1-x}$.

Theoretical as well as empirical approaches are thus necessary to determine concentrations from fluorescent intensities.

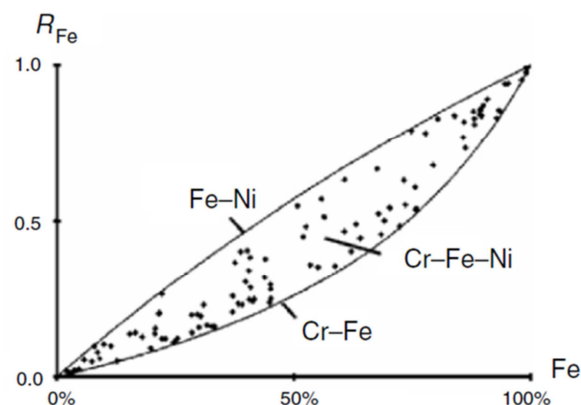


Figure 18 : Counts versus concentration from various matrix compositions of a FeNiCr alloy [29].

1.4.1. Matrix effects

In X-ray fluorescence analysis, the matrix effects result from the influence of the chemical composition environment of the considered atom on the fluorescence intensity. These effects can either be a difference in the absorption of both the primary and the emitted X-ray fluorescence in samples of different matrix composition (*i.e.* the absorption effect) or an increase of the fluorescence intensity (*i.e.* the enhancement effect).

1.4.1.1. Absorption effect

This effect occurs when the variations in the matrix chemical composition result in changes of the mean absorption coefficient of both the primary and the fluorescence radiations. Indeed, the primary X-ray beam penetrating in the sample undergoes attenuation due to various effects (Section 1.1.2) which may occur not only in the atoms of the studied element but also in the atoms of all the other matrix constituents.

Depending on the matrix composition, the absorption effect may either decrease or increase the intensity of the fluorescence radiation of interest. In GIXRF formalism (Equation 1.43), absorption effects are already taken into account and corrected as the absorption of both the primary X-ray radiation and the fluorescence emitted are modelled.

1.4.1.2. Enhancement effect

This effect occurs when the variations in the matrix chemical composition result in additional excitation of the atoms [30]. Enhancement effects constitute a cascade of events, each one involving the excitation of lighter atoms by the fluorescence radiation emitted by heavier ones (Figure 19). Therefore, the intensity of the fluorescence line of interest will depend on the concentration of the matrix element as well as their atomic number. If the energy of the radiation emitted by the matrix elements is just slightly above the absorption edge of the element of interest, the enhancement effect is augmented. Indeed, the studied atom will be more efficiently excited by the fluorescence radiation emitted by the matrix element than by the primary beam whose energy is further from the absorption edge.

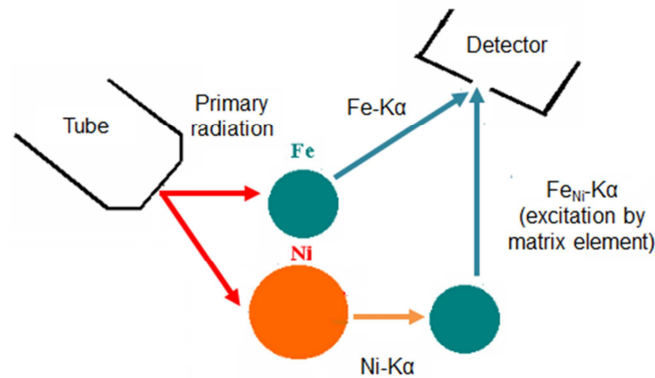


Figure 19 : Schematic illustration of secondary excitation in a sample containing Fe and Ni.

Contrary to the absorption effect, the contributions to the enhancement of a given X-ray line due to the individual matrix elements cannot be expressed quantitatively by some adapted additive coefficients. The total intensity of the fluorescence radiation of an element may be expressed in the most general manner by the formula

$$I_f = I_f^0(1 + S) \quad (1.69)$$

where I_f^0 is the intensity of the fluorescence radiation of the atom excited by the primary radiation and S is the enhancement factor dependent on the atomic number and concentration of the matrix elements.

1.4.2. Disturbing effects

Other effects can be taken into account in order to quantify precisely the composition of a sample. Particle size effects (*i.e.* influence of the grain size or granulation effects) on the fluorescence intensity of powders have been studied [30, 31]. On solid samples, such as alloys, the effects due to surface irregularities have also been observed. These effects are caused by the presence of micro irregularities (*i.e.* micro protuberances and micro cavities) at the sample surface and have been studied by Gunn (1961) and Michaelis and Kilday (1962).

1.4.3. Mathematical models

Numerous methods, both empirical and theoretical, have been proposed for quantitative XRF analysis. Due to the increasing power of computers during the past few years, theoretical methods such as fundamental parameters and theoretical influence coefficients became the most popular in routine XRF analysis.

1.4.3.1. Fundamental parameter method

The concept of deriving algorithms to compensate for matrix effects in quantitative XRF analysis and defining influence coefficients to be used in mathematical expressions was contemplated very early in the development of analytical methods. The Fundamental Parameter (FP) method is based on Sherman equation and enables the calculation the fluorescence intensity of an analyte in a sample of known composition by considering both primary and secondary fluorescence. This calculation is possible if all physical constants are known: photoelectric absorption coefficients, mass-attenuation coefficients, Cöster–Kronig transition probabilities, fluorescence yields, weight of analytical line within the series, absorption jump ratios, whose values can be found in updated databases. In practice, the application of fundamental parameter method consists of two steps: calibration and analysis of unknown sample.

Calibration is a crucial issue in assuring high quality results of quantitative analysis. In FP method, calibration can be performed in different ways using any standard specimen for calibration: pure-element thick or thin standard, one standard similar to unknown sample, series of standards similar to unknown sample, etc. Moreover, standardless analysis can also be performed as the fluorescence intensities can be calculated from theory considering that all elements are evenly distributed. A factor J_{RXi} proportional to the concentration of the element i will be calculated by taking into account the absorption and the enhancement effects of the matrix elements and will depend on the instrumental setup configuration.

Sherman later developed his theory to express the emitted fluorescence X-ray intensity from a multi-element specimen subjected to a polychromatic radiation. The theory was later refined by Shiraiwa and Fujino [33].

The Sherman equation sets the stage for modern X-ray fluorescence spectroscopy but in the early days, the computing power necessary to resolve the equation was not available. Therefore, mathematical models based on empirical approximations have been developed.

1.4.3.2. Empirical influence coefficients

Many influence coefficients algorithms have been developed. The algorithms can be divided in different ways. The influence coefficients can be calculated from theory (using Sherman equation) or from measurements. Therefore the algorithms are generally divided into two groups: theoretical and empirical influence coefficients algorithms.

Beattie and Brissey showed that by taking the ratio between the peak intensity measured for element i in an unknown sample and the peak intensity measured from a pure specimen of element i , the concentration of element i could be determined. Despite the limited accuracy, the

measurement of intensity ratios for a set of standards was an attractive method in the days before inexpensive laboratory computers.

A problem with the formulation of Beattie and Brissey is that the system of equations has no constant terms and so was over determined. In 1966, Lachance and Traill [34] proposed a new expression removing the over determination of the system in order to determine the alpha coefficients α_{ij} . This equation became the basis for empirical alpha equations.

$$C_i = R_i \left(1 + \sum_{j \neq i} \alpha_{ij} C_j \right) \quad (1.70)$$

where R_i is the ratio of the measured net intensity I_i to the measured net intensity of the pure analyte i and C_i the concentration of element i in the specimen.

Other attempts were made to find an empirical equation that more accurately describes the relation between measured X-ray intensity and concentration. One can note that Claisse and Quintin [35] addressed the definition of absorption influence coefficients in the case of a polychromatic source. Moreover, Rasberry and Heinrich [36] proposed a modified form of the Lachance and Traill equation where a new alpha term was defined in order to take into account the secondary enhancement.

1.4.3.3. Fundamental algorithm

The complex Sherman equation can be rewritten more simply, after some algebraic manipulations as:

$$R_i = C_i \frac{1 + \sum_j C_j \varepsilon_{ij}}{1 + \sum_j C_j \beta_{ij}} \quad (1.71)$$

where the ε_{ij} coefficient is the weighted mean of all the enhancement effects caused by matrix element j on analyte i in a given specimen and the β_{ij} coefficient is the weighted mean of all absorption effects caused by matrix element j on analyte i in a given specimen.

In this form, the Sherman equation shows that the relative intensity R_i is proportional to the concentration C_i but also to the ratio on the right-hand side of it. The numerator contains all the enhancement coefficients of each element j of the matrix and the denominator contains all the absorption coefficients of each element j . Thus, R_i will increase with the enhancement effects and decrease with the absorption effects. Since in practice XRF analysts are interested in calculating concentrations rather than intensities (which are measured), one can reverse the equation (1.71) and obtain:

$$C_i = R_i \frac{1 + \sum_j C_j \beta_{ij}}{1 + \sum_j C_j \varepsilon_{ij}} \quad (1.72)$$

This direct use of Sherman equation is called the fundamental algorithm (FA) method. Rousseau [36, 37] proposed the fundamental algorithm to correct for all matrix effects that modify the measured net intensity emitted by an element i in a given specimen. It considers direct and secondary excitations by a polychromatic radiation, calculates influence coefficients for each sample to be analyzed and separately takes into account both matrix effects (*i.e.* absorption and enhancement).

This method has some clear advantages. Indeed, it deduces the concept of influence coefficients directly from Sherman equation without any approximation and empirical coefficients are no longer required. The FA uses only theoretical influence coefficients that are calculated for each sample composition, increasing the accuracy in doing so.

Many other methods, both empirical and theoretical, have been proposed for quantitative XRF analysis each with diverse advantages and drawbacks. Fundamental parameter methods are generally considered to be less accurate than the influence coefficient algorithms. This results from the fact that the FP methods are usually used with only a few standards (or no standard). However, the accuracy of FP methods becomes very similar to that of influence coefficient algorithms when the same standards (*i.e.* many standards similar to the unknown) are used in both cases.

1.4.4. Geometrical factor correction

The measured fluorescence intensities are instrument dependent and a geometrical factor should be taken into account when comparing the theoretical calculation and the experimental data. De Boer [37] first investigated the effects of geometrical factor versus the incidence and detection angles. He showed that the geometrical factor has a great effect on the results (Figure 20). However, the spatial intensity distribution of the incident radiation (*i.e.* the shape of the beam: Gaussian, rectangular, etc.) was not considered in the geometrical factor. Few other analyses of the geometrical factor correction have been reported [38], [39].

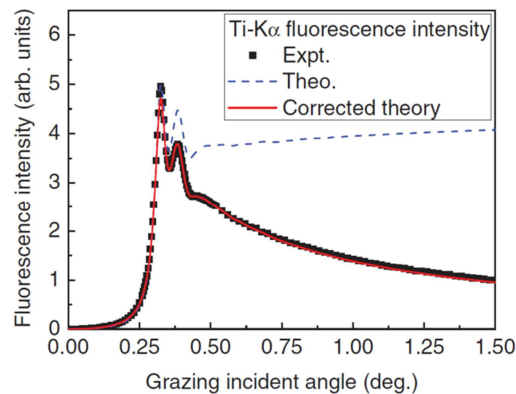


Figure 20 : The Ti-K α fluorescence intensity for a Si/Ti/Ni/Ti/Si (sub) multilayer sample as a function of incident angle [40].

In 2012, Li et al. [40] have presented a geometrical factor correction $G(\theta)$ which takes into account both the spatial intensity distribution of the primary X-ray beam and the instrumental geometry (such as the collimator geometry of the fluorescence detector, the size of the X-ray source, the imprint beam size on the sample and the size of the sample).

More discussion about this expression for the geometrical factor and the management and the correction of the instrumental function will be found in the Chapter 3.

1.5. Bibliography

- [1] R. D. Evans, *The Atomic Nucleus*, McGraw-Hill Book Company Inc., 1955.
- [2] N. Bohr, "On the Constitution of Atoms and Molecules, Part I," *Philos. Mag.*, vol. 26, pp. 1–25, 1913.
- [3] R. Klockenkämper, *Total-Reflection X-ray Fluorescence Analysis*, Wiley Interscience, 1997.
- [4] K. Sakurai and A. Iida, "Layer thickness determination of thin films by grazing incidence X-ray experiments using interference effect," *Adv. X-Ray Anal.*, vol. 35, pp. 813–818, 1992.
- [5] M. J. Bedzyk, G. M. Bommarito, and J. S. Schildkraut, "X-ray standing waves at a reflecting mirror surface," *Phys. Rev. Lett.*, vol. 62, no. 12, pp. 1376–1379, Mar. 1989.
- [6] S. K. Ghose and B. N. Dev, "X-ray standing wave and reflectometric characterization of multilayer structures," *Phys. Rev. B*, vol. 63, no. 24, Jun. 2001.
- [7] N. V. Alov, "Total reflection X-ray fluorescence analysis: Physical foundations and analytical application (A review)," *Inorg. Mater.*, vol. 47, no. 14, pp. 1487–1499, Dec. 2011.
- [8] A. Lesnik, J. Bläsing, J. Hennig, A. Dadgar, and A. Krost, "Characterization of AlInN/AlN/GaN FET structures using x-ray diffraction, x-ray reflectometry and grazing incidence x-ray fluorescence analysis," *J. Phys. Appl. Phys.*, vol. 47, no. 35, p. 355106, Sep. 2014.
- [9] A. van der Lee, "Grazing incidence specular reflectivity: theory, experiment, and applications," *Solid State Sci.*, vol. 2, no. 2, pp. 257–278, May 2000.
- [10] K. M. Zimmermann, *Advanced analysis techniques for x-ray reflectivities theory and application*, Dortmund Techn. University, Dissertation, 2005.
- [11] I. W. Hamley and J. S. Pedersen, "Analysis of neutron and X-ray reflectivity data. I. Theory," *J. Appl. Crystallogr.*, vol. 27, no. 1, pp. 29–35, Feb. 1994.
- [12] A. Abelès, *Recherches sur la propagation des ondes électromagnétiques sinusoidales dans les milieux stratifiés*, Masson, 1950.
- [13] L. G. Parratt, "Surface Studies of Solids by Total Reflection of X-Rays," *Phys. Rev.*, vol. 95, no. 2, pp. 359–369, Jul. 1954.
- [14] D. Chateigner, X-ray Reflectivity, pp235-254, in "Combined Analysis", 2010, Wiley-STE
- [15] J. R. Lu, E. M. Lee, and R. K. Thomas, "The Analysis and Interpretation of Neutron and X-ray Specular Reflection," *Acta Crystallogr. A*, vol. 52, no. 1, pp. 11–41, Jan. 1996.
- [16] B. L. Henke, P. Lee, T. J. Tanaka, R. L. Shimabukuro, and B. K. Fujikawa, "Low-energy x-ray interaction coefficients: Photoabsorption, scattering, and reflection: $E = 100\text{--}2000$ eV $Z = 1\text{--}94$," *At. Data Nucl. Data Tables*, vol. 27, no. 1, pp. 1–144, Jan. 1982.
- [17] D. K. G. de Boer, A. J. G. Leenaers, and W. W. van den Hoogenhof, "The profile of layered materials reflected by glancing-incidence X-ray analysis," *Appl. Phys. A*, vol. 58, no. 3, pp. 169–172, 1994.
- [18] D. K. G. de Boer, "Glancing-incidence x-ray fluorescence of layered materials," *Phys. Rev. B Condens. Matter*, vol. 44, no. 2, pp. 498–511, 1991.
- [19] M. Born and W. Wolf, *Principles of Optics*, Cambridge University Press, 1975.
- [20] R. M. Rousseau, "Corrections for matrix effects in X-ray fluorescence analysis—A tutorial," *Spectrochim. Acta Part B At. Spectrosc.*, vol. 61, no. 7, pp. 759–777, juillet 2006.
- [21] R. M. Rousseau, "Concept of the influence coefficient," *Rigaku J.*, vol. 18, no. 1, 2001.
- [22] K. N. Stoev and K. Sakurai, "Review on grazing incidence X-ray spectrometry and reflectometry," *Spectrochim. Acta Part B At. Spectrosc.*, vol. 54, no. 1, pp. 41–82, 1999.
- [23] P. Croce and L. Névoit, "Caractérisation des surfaces par réflexion rasante de rayons X," *Rev. Phys Appl*, vol. 15, pp. 761–779, 1980.
- [24] D. K. G. de Boer, "X-ray scattering and x-ray fluorescence from materials with rough interfaces," *Phys. Rev. B*, vol. 53, no. 10, pp. 6048–6064, Mar. 1996.

-
- [27] S. K. Sinha, E. B. Sirota, S. Garoff, and H. B. Stanley, "X-ray and neutron scattering from rough surfaces," *Phys. Rev. B*, vol. 38, no. 4, pp. 2297–2311, Aug. 1988.
- [28] R. J. Matyi, "High Resolution X-ray Scattering Methods For ULSI Materials Characterization," *AIP Conf. Proc.*, vol. 683, no. 1, pp. 634–645, 2003.
- [29] B. Beckhoff, B. Kanngieer, N. Langhoff, R. Wedell, H. Wolff, and M. Mantler, *Handbook of Practical X-ray Fluorescence Analysis*, Springer. 2005.
- [30] R. M. Rousseau, "Corrections for matrix effects in X-ray fluorescence analysis—A tutorial," *Spectrochim. Acta Part B At. Spectrosc.*, vol. 61, no. 7, pp. 759–777, juillet 2006.
- [31] R. O. Müller, "Grain Size and Surface Roughness Effects," in *Spectrochemical Analysis by X-Ray Fluorescence*, Springer US, 1972, pp. 72–83.
- [32] Y. Maruyama, K. Ogawa, T. Okada, and M. Kato, "Laboratory experiments of particle size effect in X-ray fluorescence and implications to remote X-ray spectrometry of lunar regolith surface," *Earth Planets Space*, vol. 60, no. 4, pp. 293–297, 2008.
- [33] A. Kuczumow, "The concentration correction equations as a consequence of the shiraiwa and fujino equation," *X-Ray Spectrom.*, vol. 11, no. 3, pp. 112–116, Jul. 1982.
- [34] G. Lachance and R. J. Trail, "A practical solution to the matrix problem in X-ray analysis," *Can Spectrosc.*, vol. 11, pp. 43–48, 1966.
- [35] F. Claisse and M. Quintin, "Generalization of the lachance-Trail method for the correction of matrix effect in X-ray fluorescence analysis," *Can Spectr.*, vol. 12, pp. 129–134, 1967.
- [36] S. D. Rasberry and K. F. J. Heinrich, "Calibration for interelement effects in x-ray fluorescence analysis," *Anal. Chem.*, vol. 46, no. 1, pp. 81–89, Jan. 1974.
- [37] D. K. G. De Boer, "Angular dependence of X-ray fluorescence intensities," *X-Ray Spectrom.*, vol. 18, no. 3, pp. 119–129, Jun. 1989.
- [38] Y. Mori, K. Uemura, and K. Shimano, "A depth profile fitting model for a commercial total reflection X-ray fluorescence spectrometer," *Spectrochim. Acta Part B At. Spectrosc.*, vol. 52, no. 7, pp. 823–828, Jul. 1997.
- [39] J. Boman, "Sample area dependence in quantitative EDXRF analysis," *X-Ray Spectrom.*, vol. 20, no. 6, pp. 321–324, Dec. 1991.
- [40] W.-B. Li, X.-Y. Yang, J.-T. Zhu, Y.-C. Tu, B.-Z. Mu, H.-S. Yu, X.-J. Wei, Y.-Y. Huang, and Z.-S. Wang, "Correction method for the self-absorption effects in fluorescence extended X-ray absorption fine structure on multilayer samples," *J. Synchrotron Radiat.*, vol. 21, no. 3, pp. 561–567, May 2014.

2. From TXRF to GIXRF

As stated in Section 1.2, Total Reflection X-ray Fluorescence (TXRF) consists in impinging an X-ray beam with a very small angle of incidence (smaller than the critical angle of the considered material) on a sample surface and collecting the fluorescence response. One of the main advantages of TXRF compared to energy-dispersive X-ray fluorescence (ED-XRF) is that the radiation excites mainly the near-surface region of a sample as it is totally reflected by its surface. This improves the detection limits (DL) to nanograms or picograms.

Moreover, to prevent matrix effects encountered for standard XRF analyses (*cf.* Section 1.4), TXRF measurements are generally performed on thin samples (ranging from few nanometers to few micrometers depending on the material). Thus, for contamination quantification, element detection and concentration calculation can be performed automatically by commercial and laboratory instruments. However, TXRF profiling capabilities are limited. Alternative solutions such as grazing incidence X-ray fluorescence (GIXRF) have then been developed.

2.1. TXRF

2.1.1. TXRF instrumentation

Total reflection X-ray fluorescence is a special case of ED-XRF and was discovered by Yoneda and Horiuchi in 1971 [1] when they developed a set-up to significantly reduce the spectral background of conventional XRF experiments. Therefore, the instrumentation of the two techniques is similar and consists of an X-ray source (generally monochromatic), a beam modulation unit, a sample carrier and an energy-dispersive detector (Figure 21). However, some improvements have been applied to standard ED-XRF setups. Indeed, contrary to the common 45° geometry, in TXRF experiments the fluorescence detector is usually placed perpendicular to the sample surface in order to be exposed to less scattered intensity and reduce the background in the fluorescence acquisitions. The surface on which the sample is disposed has also to meet some requirements. The sample carrier material must be highly reflective to reduce scattered background radiation. Moreover, its mean roughness should be in the range of only a few nanometers and have a small overall flatness in order to meet the requirements of being optically flat and smooth. Furthermore, it should be free of impurities to eliminate contamination peaks and the carrier material should not have fluorescence peaks in the spectral region of interest. In

addition, it must be chemically inert (*i.e.* resistant against strong chemicals which are often used for sample preparation). Generally, the sample carrier material chosen is quartz glass.

In order to perform optimal TXRF measurements, some other specific experimental setup improvements presented below must be respected.

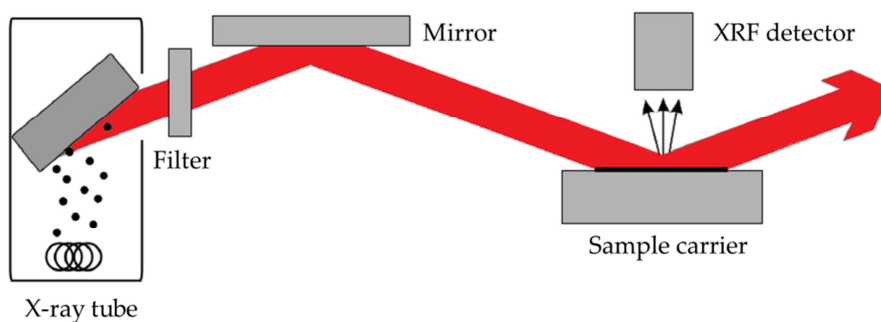


Figure 21 : Schematic set-up of a TXRF experiment. Radiation emitted from the X-ray tube passes a filter and a mirror that act as a bandpass to eliminate radiation of undesired wavelengths. Fluorescence radiation is detected by an ED-XRF detector located at 90° above the sample.

2.1.1.1. The X-ray source

Different types of X-ray sources are available and adapted for TXRF experiments depending on the applications and the work environment.

In stationary spectrometers for XRF analysis, X-ray diffractometry (XRD) or investigation of surfaces, high-power X-ray tubes (1-5 kW) are generally used. The tubes are metallic anodes which are usually water-cooled to keep the tube at temperatures below 55°C [2]. Indeed, the energy of the electrons in the electron beam is mostly converted into heat. The X-rays produced at the anode thus comprise of less than one percent of the energy of the electrons in the electron beam. These fine focus X-ray tubes are available with several different target materials that can sustain such high temperatures and therefore have a high melting point such as Au, W, Ag, Mo, or Cu. For XRF analyses, a small focal spot (generally around $0.5\text{ mm} \times 1.0\text{ mm}$) is required in order to produce a narrow beam. However, immense heat dissipation on the anode is the main problem in achieving small focal spot while preserving the power of the X-ray tube. As the heat accumulates and dissipates within the area of focal spot, a large focal spot could thus be useful to protect the anode. The solution comes from the fact that the optical focal spot at the exit of the tube differs from the electronic focal spot on the anode. Indeed, according to the line focus principle, thanks to a 6° tilt of the anode, the length of the optical spot is approximately ten times

smaller than the length of the electronic spot. X-ray tubes are also composed of an exit window made of beryllium (Be) which is highly transparent for X-rays.

Generally, single element anodes are used in laboratory tools but the use of a Mo/W alloy anode in combination with a tunable monochromator is reported by Knoth *et al.* [3]. It allows the detection of a larger number of elements with optimum detection limits (Figure 22 and Figure 23). The possibility to tune the energy of the radiation outgoing from this experimental setup (9.7, 7.5, or 32 keV) overcomes some of the limitations of standard X-ray tubes and brings some of the advantages of synchrotron experiments into the laboratories.

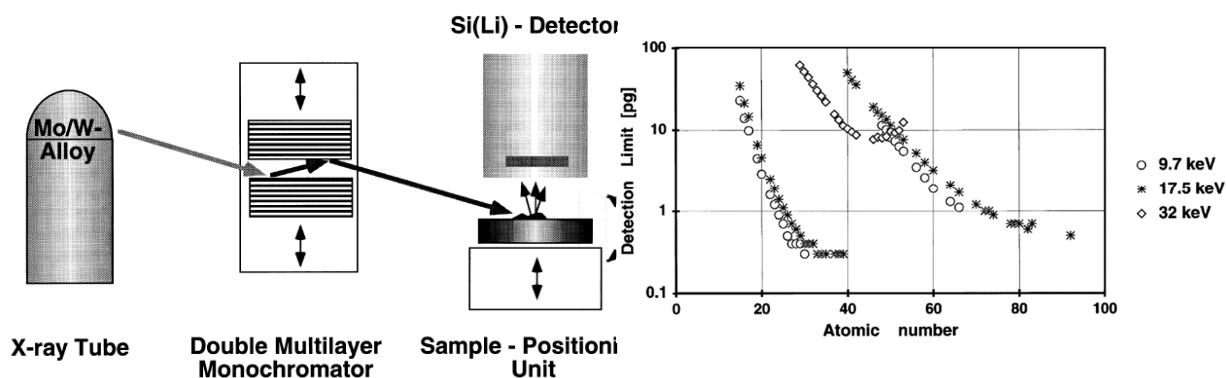


Figure 22: Schematic configuration of a TXRF setup using a Mo/W alloy anode emitting variable excitation energies [3].

Figure 23: Detection limits of the TXRF instrument using a Mo/W alloy anode and a tunable double multilayer monochromator [3].

A higher photon flux on the sample can be achieved using rotating anodes. In contrast to conventional X-ray tubes, the emitted electrons hit the rotating sidewall surface on the anode. These tubes can produce 5 to 20 times more intense X-ray beams than standard X-ray tubes.

In his work [4], Ladisich uses an X-ray tube with two different (Cu and Mo) rotating anodes as primary radiation source (Rigaku 200B generator with 12 kW, 60 kV and 200 mA maximum power, voltage and tube current respectively) mounted in a vacuum chamber. It was equipped with a cathode for a line focus of $10 \times 0.5 \text{ mm}^2$ for TXRF experiments. He shows that rotating anode X-ray tubes are well suited as primary radiation for TXRF experiments concerning the intensity, the beam stability and available focus size.

These observations have been confirmed by Wobruschek *et al.* [5]. He compared the detection limits values for different elements achievable by several TXRF experimental setups. They were operated with various X-ray sources (*i.e.* standard anodes or rotating anodes) and configurations (Figure 24). Extrapolated detection limits of 0.17 pg for Mn according to 1000 s counting time with a Cu rotating anode source have been reached.

Anode	Operating conditions (kV/mA)	Focus (μm)	Spectrometer model	Element	DL (pg)
Standing	Cu/40/35	40	Direct	Mn	0.7
	Cu/40/35	40	MLS	Mn	0.7
	Mo/50/40	40	Direct	Sr	1.5
	Mo/50/40	40	Direct	Sr	1.5
Rotating	Cu/40/190	50	Direct	Mn	0.17
	Cu/50/190	50	MLS	Mn	0.22
	Mo/50/200	50	Direct	Sr	0.70
	Mo/50/200	50	MLS	Sr	0.70

Figure 24: Comparison of detection limits reached with various excitation and spectral modification devices. Values are extrapolated to 1000s and obtained from aqueous solutions pipetted on the sample then evaporated [5].

Another approach to increase the intensity of the primary X-ray beam is to use optics that modify and focus the emitted beam. Indeed, low-power (<1 kW), high brilliance X-ray tubes combined with a poly-capillary concentrator can be used for TXRF experiments. The importance of micro-focus X-ray tubes has grown since new developments in X-ray optics and particularly on capillary optics. It allows the focusing of X-ray beams onto small spots at the sample surface and brilliances that are normally only obtained with high-power X-ray sources can be attained within these spots.

Waldschlaeger [6] introduced a micro-focus X-ray tube in TXRF experiments to increase the excitation power and provide better analytical performances. He showed the difference between a 50 kV/1.0 mA (50 W) standard X-ray tube and a 50 kV/0.75 mA (37.5 W) micro-focus X-ray tube. The excitation spot on the target sample of the line focus tube is round with a diameter of 1.2 mm resulting in a power density of 35 W/mm², whereas the spot of the micro-focus tube is just 0.05 × 0.25 mm² resulting in a power density of 4000 W/mm² (Figure 25). The distinctly higher brilliance of the micro-focus tube causes a 60% increase of fluorescence intensity. However, due to the size of the spot, micro focus X-ray tubes may not be adapted to all TXRF applications such as the study of metal contamination at the surface of a wafer.

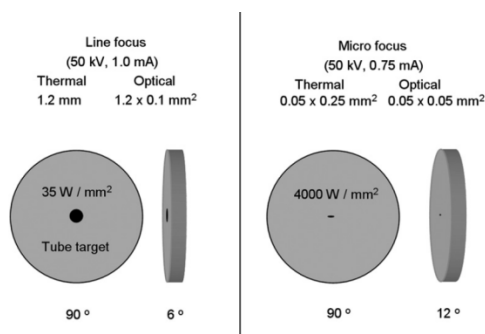


Figure 25: Power density and optical properties of a line-focus and a micro-focus X-ray tube [6].

Finally, one of the approaches for improving the detection limits is to use more powerful X-ray sources such as synchrotron radiation (SR) sources. Because of its importance, synchrotron radiation excited TXRF analysis (SR-TXRF) will be discussed in section 2.1.2.2.

2.1.1.2. The beam modulation unit

In order to perform optimal TXRF experiments, specificities on both the spatial shape and the spectral distribution of the X-ray beam need to be respected. Indeed, TXRF analysis requires excitation with a very narrow beam with an angular divergence in the vertical plane of less than 1 mrad.

A first improvement of the geometrical beam shape can be realized with collimator slits or metallic edges acting as diaphragms. They are generally in metallic silver, steel or platinum and can be fixed in entirely contained devices or have to be adjusted in modular components. However, the alteration of the spectral distribution is not as easy as shaping the beam.

In the case of elemental quantification, the high energy part of the continuous Bremsstrahlung has to be removed in order to induce fluorescence excitation preferably by the characteristic radiation of the anode material. Indeed, as the critical angle θ_c depends inversely on the X-ray energy, the conditions for total reflection are more difficult to realize for high X-ray energies. The high-energy photons could not be totally reflected at the surface of the sample and could be partly scattered causing a significant background. To avoid this effect, the high-energy photons must be eliminated and a low-pass filter is generally used. A low-pass filter can be either a metallic mirror or a perfect crystal or glass upon which the primary X-ray beam impinges with an angle θ_{cut} (*i.e.* the cut-off angle) which depends on the selected cut-off energy E_{cut} . X-ray photons with an energy higher than the cut-off energy will not be totally reflected from the low-pass filter and thus removed from the beam by absorption.

Another way to improve the detection limits of TXRF experiments is to monochromatize the excitation radiation and monochromators constitute nowadays an important part of many modern X-ray fluorescence analysis experimental tools. Indeed, for a quantitative analysis of elemental concentrations, monochromatic excitations are preferred for multiple reasons [7], [8]. First, X-rays can interact with the matter in a lot of different ways (Section 1.1.2). Therefore, just removing the high-energy part of the spectrum via low-pass filters is not sufficient as the scattering in the surface layer can form a considerable background below the energy of the considered fluorescence radiation. Then, because of the count-rate limitations of solid state detectors (SSD; *cf.* below), a high background even far away from the fluorescence peaks of interest decreases the sensitivity. The use of a monochromatic radiation will reduce the total fluorescence counts received by the detector. An improvement of the DL of the experiment can

then be achieved by increasing the primary intensity. Finally, monochromatic X-rays have a well-defined penetration depth in the sample. Particularly for in-depth resolving X-ray fluorescence analysis, the correct management of the penetration depth of the primary beam inside the sample is necessary.

To conclude, even if the presence of a monochromator in the experimental setup goes with a reduction of the primary intensity, it is required in a TXRF setup as it also reduces greatly the spectral background and improves the peak to background ratio.

The monochromatization of the excitation radiation can be achieved using different element such as a combination of crystal monochromators, X-ray mirrors or multilayers. Different filter elements of the primary beam have been compared by Knoth [9]. He concludes that solution (d) (Figure 26) consisting of a tunable double multilayer is the best solution. Indeed, it offers the best compromise between detection limits and multi-element capability. Moreover, it allows the tunability of the primary radiation therefore allowing the analysis of a wide range of elements. The most commonly used multilayered structures for the monochromatization of a primary Mo-K α X-ray radiation are W-Si, Ni-C and W-C multilayers.

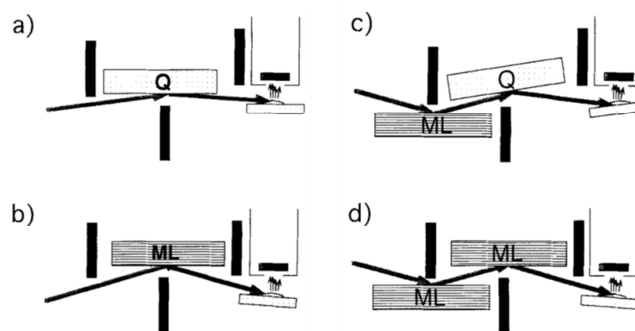


Figure 26 : Different excitation schemes for TXRF analysis;(a) Low-pass filter using a quartz mirror; (b) bandpass filter using a single multilayer mirror; (c) combination of a multilayer and quartz mirror; (d) double multilayer arrangement [9].

2.1.1.3. The X-ray fluorescence detector

In order to identify the chemical elements in the studied sample, it is necessary to resolve the spectral lines emitted by the various elements into separate components. This process requires energy dispersive (ED) or wavelength dispersive (WD) devices. Generally for TXRF experiments, ED detectors are used. An ED detector in combination with a multi-channel analyzer is used to simultaneously collect the fluorescence radiation emitted from the sample and then separate the characteristic X-rays of the different sample elements into an energy

spectrum. Different types of ED detectors have been employed, semiconductor detectors (SD) being the most common. Currently, two types of SD are used in TXRF spectrometers.

Solid state detectors

The most common solid state detector (SSD), the lithium-drifted silicon detector, Si(Li)-SD, was developed and applied to X-ray detection in the 1960's. By the early 1970's, this detector was firmly established in the field of X-ray spectrometry. The main advantage of the Si(Li) detector is its excellent energy resolution and its short measuring time for all elements.

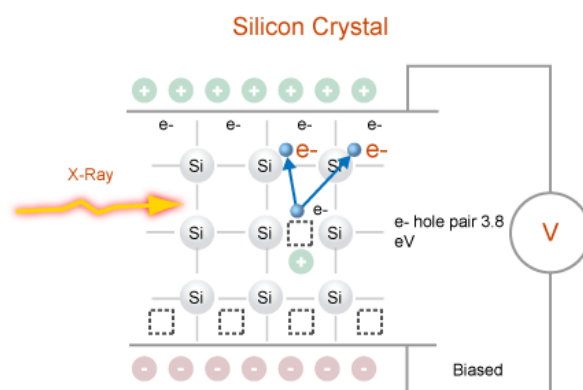


Figure 27 : Working principle of a Si(Li) detector. The voltage applied to the device allows the drift and collection of the charge carriers created by the ionizing radiation.

The basic principle of a simple Si(Li) detector, based on a junction between one p and n semiconductors materials, is shown in Figure 27. When an X-ray photon enters the active region of the detector, photoionization occurs resulting in the ejection of an electron (called photoelectron). This electron then loses its energy creating an electron-hole pair created for each 3.8 eV of photon energy. The carriers (respectively electrons and holes) produced can then be suitably collected at the electrodes (respectively positive and negative) by means of the applied field. The Si(Li) detectors must always be kept cold at liquid nitrogen temperature even when not operated in order to prevent an undesired redistribution of the lithium dopants. Ideally, the detector should completely collect the charge created by the X-ray photon entry and give a specific response depending of the photon energy. In reality, some background counts appear because of some energy loss inside the detector.

The Si(Li) detector is currently the most popular X-ray detector for TXRF experiments in the energy range from a few hundred electron-volt up to about 40 keV. To compare the effectiveness and capabilities of X-ray detectors, the energy resolution of ED-XRF spectrometers is generally expressed as the full width at half maximum (FWHM) of the Mn-K α X-ray at 5.9 keV

[10]. The typical energy resolution of commercial SSD detectors is of the order of 135 eV at 5.9 keV.

Silicon drift detectors

The Silicon drift detector (SDD) has been introduced by E. Gatti and P. Rehak in 1983 [11]. Since its invention, it has been developed for a large variety of applications in the field of X-ray spectroscopy.

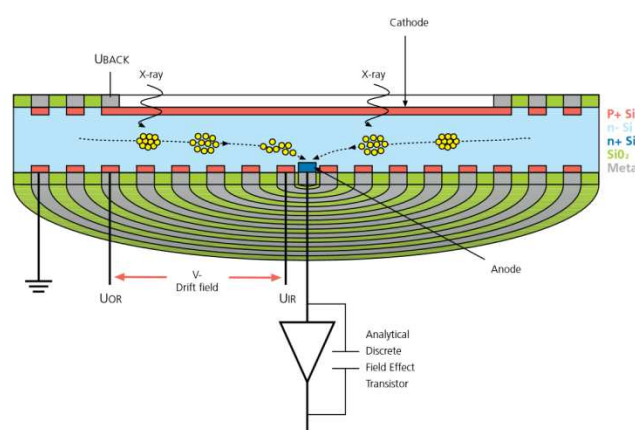


Figure 28 : Working principle of a SSD detector [12].

The SDD sensor is fabricated from high purity silicon disc and consists in a *p* doped large cathode in the entrance side facing the incoming X-rays. On the opposite side, a central and small anode surrounded by a number of concentric drift electrodes can be found (Figure 28). Similarly to SSD, when the junction is exposed to X-rays, it converts, via photoionization and Auger emission, each entry photon into a number of electron-hole pairs proportional to the characteristic energy of the X-ray photon. The transversal field generated by the ring electrodes causes charge carriers to be drifted down to the collection anode. The drift concept of SDD combined with the extremely small value of the anode capacitance allows significantly higher count rates than Si(Li) detectors [13]. Moreover, the SDD's energy resolution is similar to that of a SSD as the FWHM is generally inferior to 145 eV at Mn-K α . The high purity of the material allows for the use of Peltier cooling instead of the liquid nitrogen cooling and therefore allows an easier integration in laboratories.

2.1.2. Applications of TXRF

The first experiment on the total reflection X-ray fluorescence analysis has been carried out by Compton [14] in 1923. By discovering that the reflectivity of a flat and smooth surface rises drastically under an X-ray irradiation at grazing angles (around 0.1°), he launched a new trend in the development of X-rays total reflection technique. In 1963, the variation of X-ray diffuse

scattering with the incidence angle was reported by Yoneda [15]. This modulation of the reflectivity intensity will be afterwards named Yoneda wings. In 1971, Yoneda and Horiuchi performed the analysis of particulate samples with an excitation radiation reaching the surface at an angle below the critical angle of total reflection, therefore creating the first experiment on total reflection X-ray fluorescence spectrometry (TXRF) [1].

Due to its high sensitivity, wide linear range, the relatively easy deconvolution of the fluorescence spectra and the simplicity of its calibration control, TXRF has been widely used to study surface contamination and chemical cleaning procedure efficiency. The aim of these analyses is to detect contaminants on semiconductors wafers that are detrimental to the functioning of the devices to be produced and sort out contaminated wafers before further processing.

2.1.2.1. Laboratory and production tools

TXRF setups are operated in many cleanrooms via industrial monitoring tools and the trace contaminations to be tracked are generally metallic elements [16]. The use of industrial equipment for TXRF experiments has been reported in Shibaya's work [17] where measurements were performed using a TECHNOS TREX 610. This equipment is composed of a rotating anode with a tungsten (W) target operated at 30 kV and 150 mA. A LiF(200) monochromator was used to select the W-L β line as excitation source. Cl, Cu and Zn surface contamination of GaAs wafers down to $1-8 \times 10^{10}$ atoms/cm² have been quantified. On the other hand, Verdonck *et al.* [18] used an Atomica XSA 8000 system equipped with a Mo X-ray tube to study surface contamination induced by plasma etching and more specifically reactive ion etching (RIE). The detection limit of this equipment for the investigated elements is around 10^{11} atoms/cm². However, this TXRF setup is unable to detect aluminum (or any other low-Z elements) on silicon wafers.

Indeed, standard and industrial equipment are not adapted to observe low-Z contaminants as the background originating from the bulk Si may interfere with the fluorescence peaks of low-Z contaminants. One could choose to operate at an energy below the K absorption edge of Si (at 1.840 keV) to get rid of the strong Si-K α fluorescence peak. This can be achieved with an energy-tunable X-ray source or by selecting the W-M α line of a tube with a tungsten anode. However, TXRF measurements performed at low excitation energy raise some difficulties. First, the resonant Raman scattering (RS) from Si will overlap with the fluorescence lines of elements lighter than silicon [19]. Moreover, the poor efficiency of the detector for low X-ray energies and their limited resolution are not helpful in this perspective.

The detection efficiency can be improved by performing TXRF measurements in a vacuum chamber and by diminishing the thickness or removing the windows in front of the X-ray tube and the detector. With these considerations, Hoefler *et al.* [20] have developed a TXRF spectrometer for the study of low-Z elements. The equipment uses a Cr-anode tube (5414 eV), a multilayer monochromator and a Si(Li) detector with an ultrathin window embedded in a vacuum chamber. In order to get rid of Auger and photoelectrons that could get into the sensitive volume of the detector due to the presence of the ultrathin window, permanent magnets have been installed in front of the entrance window of the detector (Figure 29). Biofilms with low-Z elemental masses down to 28 ng/cm² (for magnesium) have been measured (Figure 30).

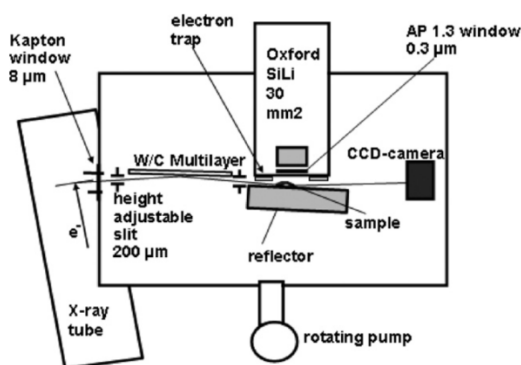


Figure 29 : Scheme of Hoefler TXRF spectrometer for low-Z elements [20].

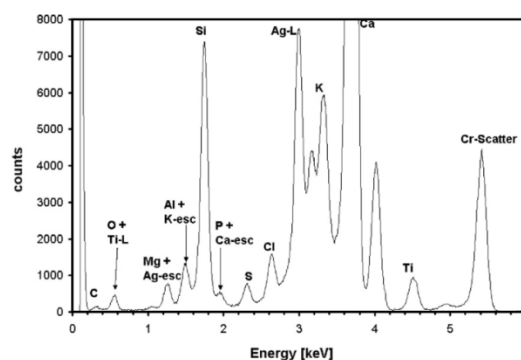


Figure 30 : XRF spectrum of the studied biofilm. Excitation conditions: Cr tube at 30 kV and 20 mA [20].

To further enhance the sensitivity to surface contaminants, TXRF can be combined with vapor phase decomposition (VPD) [21], [22]. The idea consists in collecting all the contaminants dispersed over the whole surface of the sample and concentrate them into a small droplet that will be irradiated. The contaminants are firstly decomposed all together with the surface silicon oxide by exposition to a high purity hydrofluoric (HF) vapor. Finally, all the impurities are collected with a sampling solution, dried naturally and analyzed by TXRF (Figure 31).

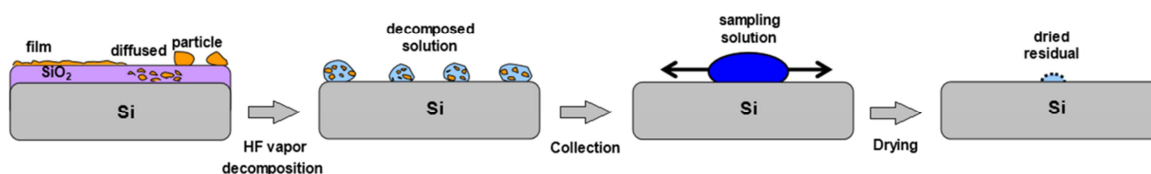


Figure 31 : Pre-treatment process for TXRF measurements [21].

For standard contamination quantification by TXRF measurements, the detection limit (DL) is limited by the fact that the illuminated area seen by the detector is small compared to the size of the wafer. However, for VPD-TXRF, the whole residue is irradiated during the experiment

as the primary beam height is generally larger than the size of the droplet. Therefore, VPD-TXRF offers a large improvement of the DL compared to standard TXRF. Improvement of the detection limit by two to three orders of magnitude can be achieved [23] as the order of magnitude of the improvement factor is given by the ratio of the wafer size to the irradiated spot size seen by the X-ray detector. Thus, compared to standard TXRF where detection limits are generally 10^{10} atoms/cm² for the considered elements, DL of 4×10^8 atoms/cm² have been reached for VPD-TXRF.

However, one of the main disadvantages of VPD-TXRF is that it is a destructive technique and removes the possibility to perform spatially resolved analysis of the wafer surface. Therefore, this solution may not be adapted for industrial purposes.

2.1.2.2. Synchrotron radiation TXRF (SR-TXRF)

Another way to improve the detection limits is to perform TXRF measurements at synchrotron facilities. The synchrotron radiation (SR) has unique properties such as high intensity and a very low angular divergence. The use of a highly polarized radiation also decreases the scattered radiation and reduces the background. Synchrotron radiation is therefore an ideal excitation source for TXRF experiments. Moreover, SR-TXRF allows achieving very low detection limit for low-Z as well as high-Z elements. Indeed, another advantage of SR is the possibility to tune the excitation energy. One can thus operate TXRF experiments with an excitation energy below the absorption edge of a matrix element with high concentration but above the absorption edge of the element of interest. This selective excitation allows to get rid of the majority of matrix effects and inspect low-Z elements without any contribution from the bulk.

If the experiments are performed in air, the scattering of the exciting radiation can contribute to the background. Therefore, all SR-TXRF measurements are operated in a vacuum chamber [24]. As shown by Wobrauschek *et al.* [5], the application of TXRF using synchrotron radiation can be performed with various geometrical arrangements for sample position and detector (Figure 32).

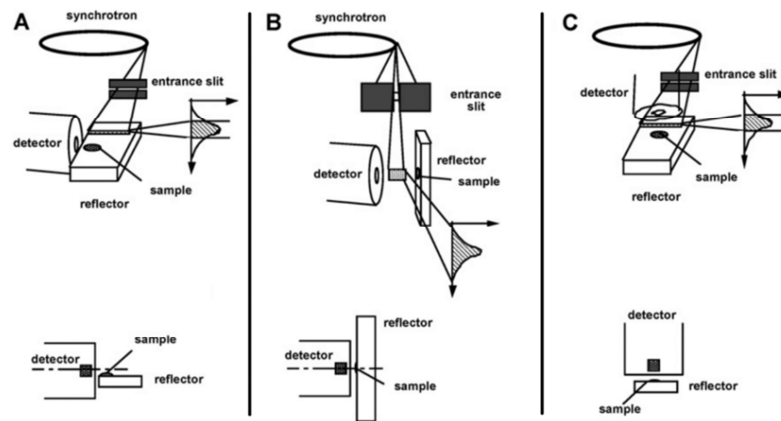


Figure 32 : Three possibilities of arranging wafer and detector for SR-TXRF [5].

With a similar geometry as the one used for standard TXRF measurements, the arrangement C described in Figure 32 (*i.e.* excitation using SR with a horizontal sample reflector and detection performed by placing the detector at the vertical above the sample) will achieve an excellent excitation and detection. However, this combination of sample and detector position will result in a complete loss of the use of the polarization effect of the synchrotron radiation. For geometry A (*i.e.* excitation using SR with a horizontal sample reflector and detection performed by positioning the detector axis in the plane of the orbit), as the X-ray detector is side-looking, the polarization effect is fully utilized. However, even if the sample is excited efficiently, the detection of the fluorescence is not optimized as the fluorescence radiation has a longer path in the sample to reach the detector giving rise to more absorption effects. Finally, configuration B has been obtained by rotating the sample reflector of geometry A to a vertical position without moving the slits. This configuration is not optimal as the excitation conditions are poor. Indeed, most of the photons in the horizontal plane are absorbed by the collimation system. However, the detection efficiency is high as the small distance between the sample and the detector leads to a large solid angle of detection.

Various SR-TXRF setups are accessible around the world and are fully functioning. For example, the synchrotron radiation from SSRL (Stanford Synchrotron Radiation Laboratory, Menlo Park, California) Beam Line III-4 was used as a excitation source for TXRF analysis of light elements [25]. The experimental setup is mounted in the arrangement C described above and equipped with an ultra-thin window high purity Ge detector and a horizontally deflecting toroidal Au mirror to cut off photons with an energy higher than 3 keV. It is therefore perfectly designed to detect and measure light elements ($Z < 14$). TXRF spectra of a sample containing a 5 nm Mg layer excited with a Cr anode fine focus X-ray tube (Figure 33-a) and a sample containing 500 pg Mg measured at SSRL beam line III-4 with a monochromatic beam of 1.77 keV

(Figure 33-b) have been acquired. Table 2 compares the detection limits (DL) and sensitivities (S) obtained at SSRL and with a standard X-ray tube. By using a synchrotron radiation as the excitation source for the analysis of light elements in total reflection geometry, very small detection limits of a few hundred femtograms are obtained. An improvement of 3 orders of magnitude has been achieved compared to a standard laboratory Cr anode X-ray tube. Detection limit of 2 pg for Mg is obtained with synchrotron radiation, whereas 100 times more Mg is necessary with an X-ray tube.

	SSRL 3 GeV 100 mA, BL III-4		X-ray tubes optimized conditions	
	DL (pg)	S (cps/ng)	DL (pg)	S (cps/ng)
F	9	20	1400	0.13
Mg	2	100	200	0.8
Al	0.5	200	100	1.2

Table 2 : Detection limits and sensitivities at SSRL BL III-4 and with a standard X-ray tube (Cr fine focus X-ray tube) with 1000 s of counting time [25].

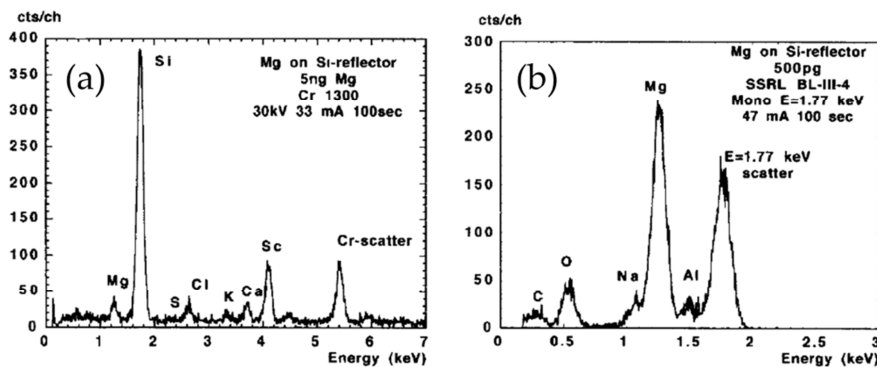


Figure 33 : Comparison of TXRF spectra of (a) a 5 nm Mg layer excited with a standard Cr fine focus X-ray tube and (b) 500 pg Mg sample excited with a 1.77 keV synchrotron excitation [25].

A vacuum SR-TXRF setup is also available at the HASYLAB synchrotron facility in Germany [26]. On this experimental setup, the vacuum chamber is equipped with a Ni/C multilayer monochromator. The fluorescence radiation is measured by a Vortex silicon drift detector (SDD) with a 50 mm² active area. Figure 34 shows a SR-TXRF spectrum obtained from a Ni sample [27]. With a 17 keV monochromatic excitation radiation, a detection limit of 8 fg for Ni has been obtained.

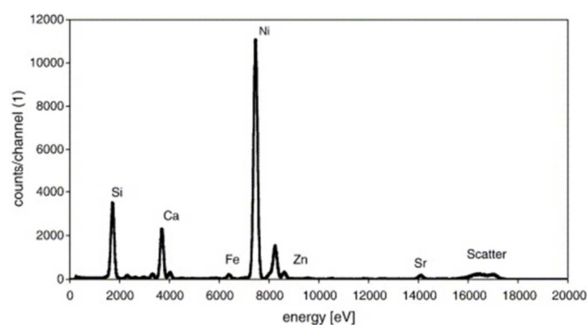


Figure 34 : Spectrum of 100 pg of Ni on a Si wafer excited with a 17 keV radiation during 60 s. The DL was found to be 8 fg [27].

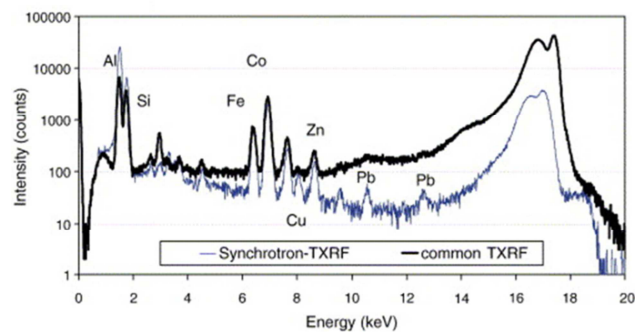


Figure 35 : Comparison of Al_2O_3 powder fluorescence spectra measured with laboratory TXRF (Atomika 8030C) and SR-TXRF [27].

Using the same optic elements and geometry, a comparison of spectra between SR-TXRF and standard TXRF (Atomika 8030C) of alumina (Al_2O_3) powders has been performed (Figure 35). SR-TXRF has been shown to provide very good sensitivity which is crucial for the determination of trace elements such as Cr and Mn in Al_2O_3 powders. The accuracy and precision of these determinations, however, is limited by the inhomogeneity of the samples, which was found to be problematic for analyses with very small quantities.

Another SR-TXRF setup for wafer surface analysis is available at the Physikalisch-Technische Bundesanstalt (PTB) beamline at BESSY2 in Germany. The facility contains two different fluorescence beamlines. First, the four-crystal monochromator (FCM) beamline provides monochromatized radiation in the energy range from 1.75 keV to 10.5 keV. Then, the plane-grating monochromator (PGM) beamline extends the available spectral range down to 78 eV, this latter being then particularly adapted for the study of low-Z elements. This SR-TXRF experimental setup has been used to investigate various samples with a top nano-layer of high-k materials. They consist of a Si substrate with a silicon oxide (SiO_2) layer covered by a hafnium oxide layer with a thickness varying from 2 nm to 5 nm [28]. Both beamlines and thus complementary excitation energies have been used. The first measurement has been performed at 10.5 keV (Figure 36-a). This photon energy is between the energies of the L3 and L2 absorption edges of Hf and therefore allows for the selected excitation of the fluorescence lines of the L3 edge only. The second measurement was carried with a photon energy of 1750 eV in order to excite only the Hf M4 and M5 subshells (Figure 36-b). At a higher energy, the fluorescence of the silicon substrate would have been excited which would have dominated the spectral distribution.

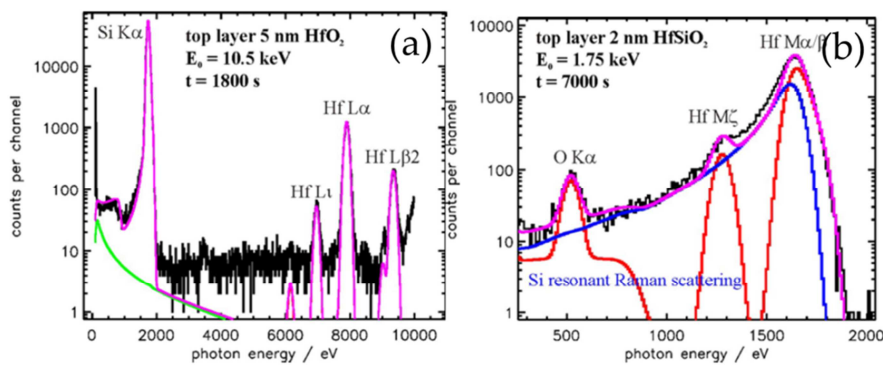


Figure 36: Spectra of Hf containing high-k layers taken in different energy regions. (a) Excitation energy = 10.5 keV and (b) Excitation energy = 1.75 keV. The green and the blue line show background components (green: Bremsstrahlung, blue: resonant Raman scattering of silicon), the red lines are the fluorescence lines convolved with the detector response function to deduce their intensity and the purple line shows the fit to the experimental spectrum [28].

2.1.3. Quantitative analysis

As described above, as TXRF is mainly used to study surface contamination or measure trace elements, TXRF experiments are generally performed on samples thin enough to prevent the matrix effects described in Section 1.4.1. A linear concentration-signal counts relation can be then defined. Therefore, element detection and concentration quantification of surface elements can nowadays be performed automatically by commercial instruments and software.

2.1.3.1. Spectrum evaluation

The spectrum evaluation is the first step required to perform quantitative analysis. The goal of spectrum evaluation is the extraction of the analytically relevant information (*i.e.* the net number of counts under a peak) from experimental data. This step has to be carried out in a consistent way for the different fluorescence peaks as the signal counts will be directly linked to the elemental concentration. Different methods can be used to perform an accurate spectrum evaluation.

The most straightforward method to obtain the net area under a fluorescence peak of interest consists in interpolating the background under the peak and summing the background-corrected channel contents in a region of interest (ROI) over the peak. However, in practice, this method is limited by the curvature of the background or by the presence of other peaks. These other peaks can be fluorescence peaks (as seen in Figure 37 where Ag-L3 peaks are convoluted with In-L3 peaks) or detector artefact peaks such as escape peaks and pile-up peaks.

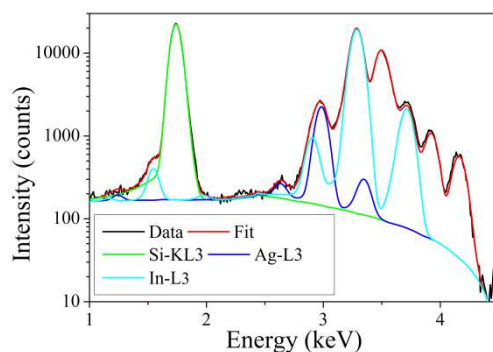


Figure 37: TXRF spectrum of $\text{In}_2\text{O}_3/\text{Ag}/\text{In}_2\text{O}_3$ sample excited by a standard Cu tube. The energy of Ag-L3 and In-L3 lines cannot be separated by ED-XRF detectors.

Escape peaks are consecutive to photoionization followed by electronic shells rearrangement of the detector material (generally Si) through X-ray emission. Part of these rearrangement X-rays are produced close to the detector material fluorescence edge and thus can exit from the active part of the detector and the relevant energy is lost. The energy measured for the incoming X-ray is thus reduced by the magnitude of the Si- $K\alpha$ X-ray and an escape peak (of energy $E_{esc} = E - E_{K\alpha}$) is detected. Generally, less than 2% of incoming X-ray photons will fluoresce Si- $K\alpha$ X-rays from the detector junction. Sum peaks (or pile-up peaks) are produced when the X-ray detector cannot distinguish between two X-ray photons that penetrate the active region of the detector almost simultaneously. Instead of recording two X-rays with either the same or different energies, only one X-ray with an energy equal to the sum of the two incoming photons will be recorded.

Consequently, the integration over a ROI cannot be used as a general method for spectrum evaluation in TXRF. In order to obtain the net areas of the fluorescent lines of interest, a widely used method for spectrum evaluation is the fitting of the spectral data with a model. This model takes into account the contribution from all peaks (*i.e.* both fluorescence peaks and detector artefacts) within a certain ROI and the background.

The background can be calculated via two different ways. The first approach consists in calculating the background only with mathematical functions (generally linear function or exponential polynomials). This method is implemented in spectrum evaluation programs such as PyMCA [29]. The other approach consists in calculating a physical background which takes into account the incident radiant power, the efficiency of the X-ray fluorescence detector employed and the effective solid angle of detection [30]. This fundamental parameter (FP, *cf.* Section 1.4.3) approach thus requires a perfect knowledge of the instrumental setup. As this kind of information is not always easy to collect on standard laboratory tools, this method is mainly developed and implemented at synchrotron facilities. However, the spectrum evaluation of TXRF

analysis of low-Z elements requires the use of the FP method. Indeed, in this low energy region, Bremsstrahlung and Raman scattering are prominent (Figure 38) their correct description are required in order to obtain an accurate TXRF spectrum evaluation.

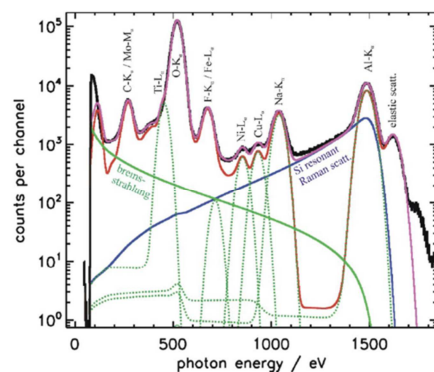


Figure 38 : TXRF spectrum of a wafer containing 10^{12} cm⁻² of various transition metals and 10^{13} cm⁻² of Na and Al (low-Z elements). The spectrum is fitted by detector response functions at the energies of fluorescence lines. The background includes Bremsstrahlung and resonant Raman scattering contributions [30].

2.1.3.2. Calibration

Various effects disturbing the X-ray fluorescence quantification have been described in Section 1.4.1. However, one of the inherent advantages of TXRF experiments is that one deals with thin samples thus enabling a linear relation between the fluorescent intensities and the concentration [31]. In general, the quantitative TXRF analysis can be done using two different methods.

The first approach consists in creating a calibration curve by measuring several standard samples with a known element concentration and finding the relation between the X-ray fluorescence intensity of the measured element and the concentration. After establishing the calibration curve, the conversion from intensity to concentration is easily performed. As the use of proper standards is very important for all trace analysis techniques, a technical committee on surface analysis has been organized at the International Organization of Standardization (ISO) [32]. It includes a working group on TXRF and aims at developing international standards. Different methods to create reliable standards have been considered such as, for example, using a dried residue of an acid solution containing 13 elements of equal concentration [33].

Figure 39 shows a TXRF spectrum of such a standard sample. Single element sensitivities can be calculated from these measurements. The result of a systematic determination of element sensitivities is represented in Figure 40. This calibration curve was obtained by using two different X-ray sources (Mo and W X-ray tubes) in order to excite all elements with an atomic

number $Z > 13$ (Aluminum). The elements with lower atomic numbers cannot be detected because their characteristic X-ray fluorescence radiation is absorbed by the air gap between the sample and the detector.

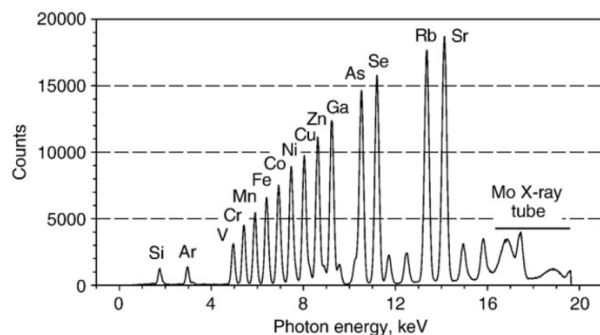


Figure 39 : TXRF spectrum of the residue of a multi-element standard solution containing equal concentrations excited by Mo-K radiation.

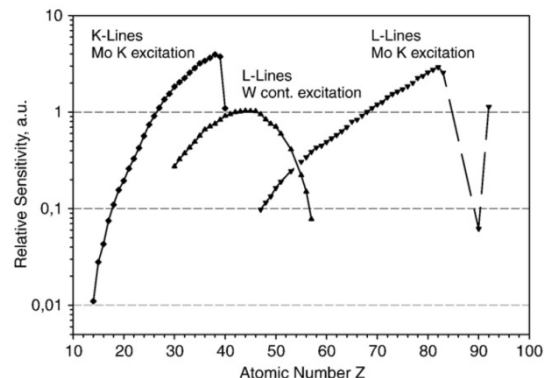


Figure 40 : Set of relative element sensitivities measured under total reflection of X-rays.

The use of this type of calibration curve allows a relative simple quantification. However, the addition of one element as internal standard of known concentration into the sample is recommended to improve the accuracy of the results. Indeed, in this case, volumetric errors will cancel. Then, the concentration of the unknown sample can be given:

$$C_x = \frac{I_x}{S_x} \cdot \frac{S_{std.}}{I_{std.}} \cdot C_{std.} \quad (2.1)$$

where C_x and $C_{std.}$ are respectively the concentration of the unknown and standard sample. I_x and $I_{std.}$ the measured fluorescence intensity of respectively the element of interest and the internal standard. S_x and $S_{std.}$ are the detector sensitivity to respectively the element of interest intensity and the internal standard.

Many relevant information for trace analysis of surface contamination on Si wafers and non-Si (eg. Ge [34]) substrates and layers using standard samples are available and a reliable quantification is possible and done daily in industrial clean rooms. Nevertheless, Hellin *et al.* have shown that in particular cases such as the study of VPD-TXRF (Section 2.1.2.1) calibration curves are not sufficient and sample effects have to be taken into account [35]. Indeed, to avoid TXRF saturation effects, the surface concentration for metallic elements must not exceed an upper limit of 10^{11} atoms.cm⁻².

The other method is known as the Fundamental Parameter (FP) method which is based on theoretical calculations. As evoked in Section 1.4.3.1, considering the type and properties (such as the photoelectric absorption coefficients, mass-attenuation coefficients, Cöster-Kronig

transition probabilities, fluorescence yields, weight of analytical line within the series, absorption jump ratio of all elements), the fluorescence intensity of each line can be derived theoretically without requiring a standard sample. Using this method, the composition of an unknown sample can be directly extrapolated from the fluorescent intensity of each element. One example of theoretical calculations and considerations has been exposed in Shin *et al.* [36]. This quantification method allows circumventing problems related to deviations from the expected linear response between the contamination concentration and the X-ray fluorescence intensity.

A reference-free quantification method has been realized by Beckhoff *et al.* at BESSY facility [37]. The FP method is based on calibrated detectors and calibrated light sources and requires sophisticated computer programs as well as a perfect knowledge of the instrumental parameters and the atomic fundamental parameters. It is often applied in synchrotron facilities as one of the advantages of synchrotron radiation is the absolute calculability of all its properties. Therefore, the fundamental parameter quantification method may be non-adapted for industrial or laboratory experiments on which all experimental parts may not be totally controllable.

2.2. GIXRF

TXRF is an efficient technique for surface analysis. However, new developments in microelectronics require performing depth-profiling analyses to reveal the sequence of layer and their partial inter-diffusion at the interfaces or to obtain the profile of a dopant inside a bulk material. Therefore, some alternative TXRF techniques such as grazing incidence X-ray fluorescence analysis (GIXRF) have been developed.

2.2.1. TXRF combined with etching

The in-depth characterization of a sample is not possible with a single TXRF measurement performed at a unique incidence angle. Consecutive TXRF measurements of different sample layers have thus to be performed. Klockenkämper *et al.* have described two different approaches to realize depth-resolving TXRF. First, similarly to VPD-TXRF, the sample surface is decomposed by an acid droplet, collected in a sampling solution and then dried by evaporation. The residue are analyzed by TXRF [38], [39]. These steps are reproduced a sufficient number of time to obtain the in-depth composition and concentration profile. The quantification is not straightforward and based on the assumption that the chemical processes do not change the oxidation state of the sample. Indeed, in order to determine the total etched quantity, the wafer has to be weighted before and after each step. A mass modification of the sample during

the measurements could lead to inaccurate quantification. The second approach described by Klockenkämper *et al.* consists in etching the sample surface by ion sputtering and then perform a TXRF analysis of the etched surface [40], [41].

The depth-resolution of these techniques is correlated to the thickness of etched material as well as the penetration of the incident X-ray beam inside the material. Generally, it is determined to be around one nanometer. It can be easily noted that the profiling capabilities of sequential TXRF are limited. Added to the fact that it requires numerous steps and resources, it is a destructive technique therefore removing one of the main advantages of standard TXRF.

2.2.2. GIXRF

Grazing incidence X-ray fluorescence (GIXRF) is a total reflection XRF-based method adapted for depth-profiling. As stated in Chapter One, it is based on the fact that the penetration depth of the incident X-ray beam depends significantly on the incidence angle. Different depth regions are thus accessible by varying the incidence angle. Moreover, GIXRF can be applied to a wide range of samples to determine their elemental composition as well as their near-surface structure. GIXRF measurements allow distinguishing between different types of samples (*i.e.* bulk samples, multilayers, implanted samples or residual grains) as the fluorescence intensity varies with the incidence angle. Indeed, the modulation of the X-ray standing wave (XSW) pattern above the sample surface with incidence angles coupled to the increasing penetration depth influence significantly the detected X-ray fluorescence intensity.

GIXRF requires similar instrumental setup and optic elements as the ones presented for standard TXRF experiments. The advantages of synchrotron radiation such as the improvement of the detection limits and the possibility to analyze low-Z elements are unchanged. However, as the incidence angle varies during a GIXRF experiment (generally from $\theta = 0^\circ$ to 5°), the position of the sample compared to the incident beam needs to be known precisely and controlled accurately. Generally, a 5-axis motorized sample positioning system with 3 translational and 2 rotational displacements is necessary to position the sample adequately [42] and align it with the X-ray source.

One of the first applications of GIXRF is the qualitative analysis of multilayered structures. To illustrate this approach, buried boron-carbon layers with nominal thicknesses of 1, 3 and 5 nm and capped with 2.5 nm silicon oxide have been studied using a monochromatized synchrotron radiation of the PTB at the BESSY II facility [43]. GIXRF measurements (from $\theta = 0^\circ$ to 4.5°) at 1060 eV have been performed. The normalized count rates of boron, carbon and oxygen $K\alpha$ as well as the silicon L-2,3 fluorescence signals are shown in Figure 41. The shape of the O- $K\alpha$, C- $K\alpha$ and B- $K\alpha$ curves allows identifying deposited thin films of oxygen, carbon, and boron,

whereas the Si-LI curve is characteristic of a bulk GIXRF signals. Moreover, the position of the GIXRF signals can reveal the sequence of the layers. Indeed, as the penetration depth of the primary radiation increases with the incidence angle, a shift of the angle at half-maximum of the GIXRF peak (1.19° for oxygen, 1.28° for carbon, and 1.39° for boron) can indicate the position of the layers in the stacking.

The qualitative analysis of GIXRF measurements has also been used in the study of $\text{Cu}(\text{In}_{1-x}\text{Ga}_x)\text{Se}_2$ samples synthesized at two different temperatures: 430°C and 530°C [44]. The differences of the fluorescence intensities (Figure 42) between the two different samples are larger than the total error limits of the measurement. Therefore, it indicates that the two samples have different depth distributions distinguishable by GIXRF. These results confirm that GIXRF can give qualitative information on the layer composition and sequence.

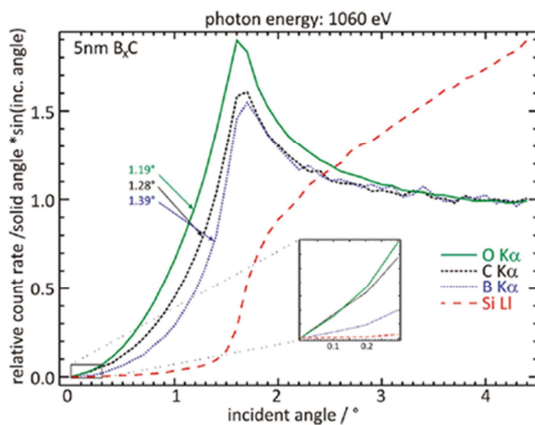


Figure 41 : Relative fluorescence count rate as a function of the incident angle. The shift of GIXRF signals towards larger angles indicates the position of the layers in the stacking [43]

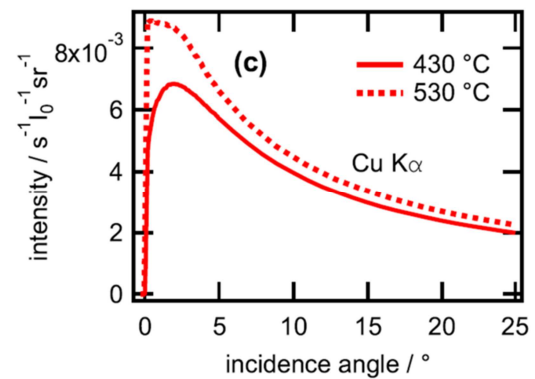


Figure 42 : Cu-K α GIXRF intensities of two different $\text{Cu}(\text{In,Ga})\text{Se}_2$ films synthesized by three-stage co-evaporation process at 430 °C and 530 °C [44].

The depth profiling capabilities of GIXRF measurements has been used for the in-depth characterization of ion-implanted samples [45] and more recently in combination with secondary ion mass spectrometry (SIMS) for ultra-shallow implantation profiles in silicon substrates [46]. As shown on Figure 43, the depth-profile of the implanted ions may be retrieved by inverse modeling. Starting from a reasonable assumption on the depth-profile obtained by SIMS, the standing wave-pattern and the primary beam penetration into the sample are then simulated and the expected fluorescence intensity at the different incidence angles is calculated. Finally, the GIXRF simulations are compared to the experimental fluorescence intensity profile in order to improve the initial assumption and converge to a final result.

An improvement of this inverse modeling problem has been developed on arsenic (As) implants [47]. In his work, with no a priori information, Hönicke used a sample model that takes into account a dopant profile and calculated the resulting GIXRF intensity. He then compared this simulated curve with experimental measurements. The agreement between the simulated and experimental data has been improved by directly fitting the dopant profile. Windt's IMD software package was used to perform the necessary XSW field calculations [48]. The in-depth doping profiles determined with various characterization techniques are shown in Figure 44. These techniques include medium energy ion scattering (MEIS) and Z-contrast tilted sample annular dark field scanning transmission electron microscopy (TSADF-STEM). The comparison of the depth profiles indicates that differences are only observed in the first few nanometers close to the sample surface. In this region, the sputtering rate of SIMS is known to be non-constant. Hönicke demonstrated that for the characterization of ultra-shallow junctions, GIXRF can be a nondestructive, alternative and efficient characterization technique.

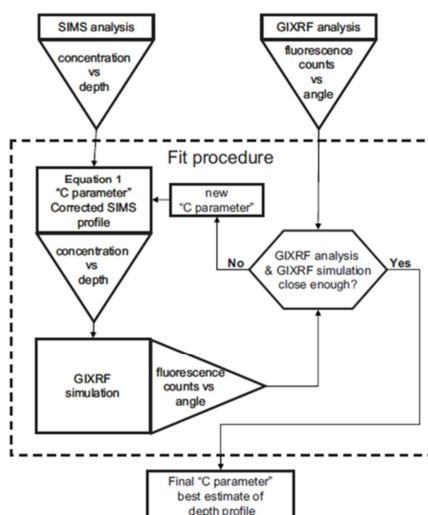


Figure 43: Flow chart depicting the algorithm implemented for fitting GIXRF experimental data by correcting the SIMS profile given as initial best estimate [46].

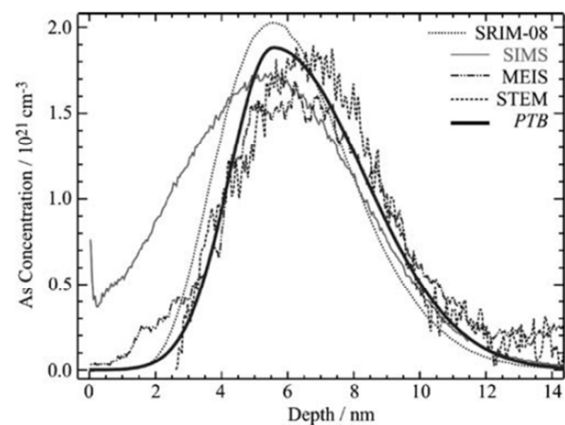


Figure 44: Comparison of the implantation profile for one of the As wafers (3 keV, $1.0 \times 10^{15} \text{ cm}^{-2}$) determined with various techniques and the respective SRIM profile [47].

GIXRF also allows quantitative depth-profiling characterization of multilayers or thin films deposited on a surface [49]–[52]. The thickness, the density and the roughness of each layer as well as the elemental quantity of deposited material are assessed via De Boer's formalism (presented in Equation 1.12). The determination of the thickness of a Pd layer on a Si substrate as well as the in-depth profiling of a Fe/Ti/Fe tri-layer is represented in Figures 45 and 46.

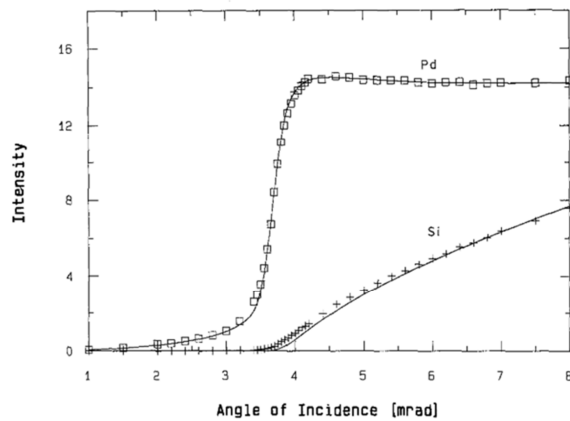


Figure 45 : Determination of the layer thickness of a Pd layer on a silicon substrate. Measured fluorescence intensities of Pd and Si as a function of the incident angle result in a layer thickness of 132 nm. The manufacturer's value is 133 ± 3 nm [50].

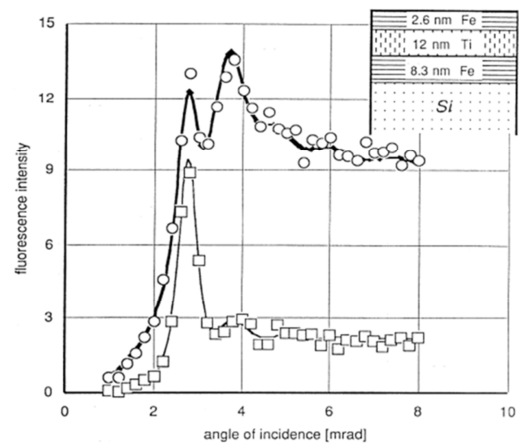


Figure 46 : Analysis of a three-layer system by angle-resolved TXRF measurements. Both the thickness and the density of the layers have been determined [51].

The problematics of quantitative GIXRF are similar to the one explained for TXRF as two approaches are possible (*i.e.* using reference samples or by via FP method). However, due to the variation of the incidence angle, several additional factors have to be taken into account for quantitative GIXRF. It includes instrumental parameters such as the size of the illuminated sample area (dependent on the incidence angle), the spatial intensity distribution of the primary X-ray beam and the angular divergence of the beam. These parameters and the solutions to manage them will be described more thoroughly in Chapter 3.

Recently in 2014, Ingerle D. [53] showed that an unambiguous deconvolution of the angle dependent fluorescence signal in order to determine the layer thickness as well as the density is not possible. The GIXRF results of the fluorescence radiation from the fluorescence Hf-L3M5 and Si-KL3 from a nominal 2 nm thick $\text{Hf}_{0.6}\text{Si}_{0.4}\text{O}_2$ layer on a Si substrate are shown in Figure 47. By fitting the thickness and the density, the results are ambiguous. Indeed, a set of combination density-thickness can be found resulting in good fitting. For demonstration, two combinations were selected and very good fitting results are obtained with the combination of a thickness of 2.25 nm and a density of 6.1 g/cm^3 but also with the other combination of a thickness of 2.05 nm and a density of 6.7 g/cm^3 .

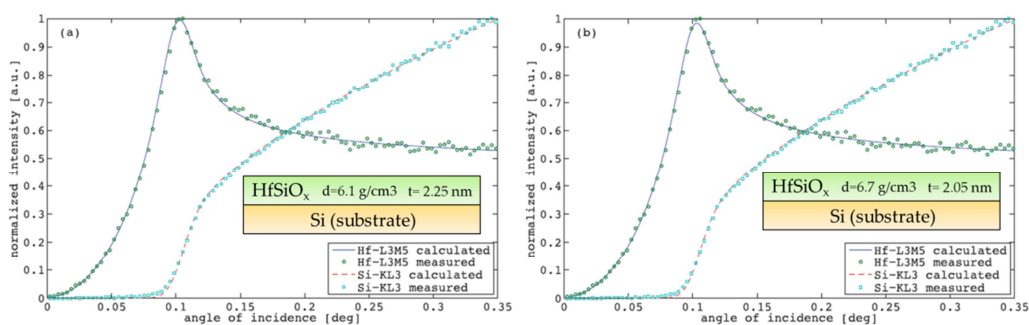


Figure 47 : GIXRF fluorescence signal from Hf and Si from a HfSiO_x layer. The calculation was performed using only the GIXRF signal. Good fit results are obtained for a density of 6.1 g/cm³ using a thickness of 2.25 nm (a) as well as a density of 6.7 g/cm³ using a thickness of 2.05 nm (b), thus showing the ambiguity of the GIXRF data [53].

Due to these GIXRF limitations, a new approach has been considered. Indeed, in 2013, Holfelder *et al.* [54] showed that by combining complementary X-ray fluorescence techniques, one could reduce the uncertainties of the individual techniques and obtain a more reliable characterization (Figure 48). As stated previously, as the thickness and the density of the layers are correlated in the De Boer's formalism, the accurate determination of these two parameters by GIXRF is not possible. The use of an adapted complementary X-ray technique is therefore required.

The best choice to overcome this problem is to combined X-ray reflectivity (XRR) with GIXRF. XRR is a well-known characterization method for the determination of thickness and in-depth electronic profiles of multilayered structures. The thickness values determined by XRR could then be used for GIXRF.

One of the other advantages of combining XRR and GIXRF is that they are both grazing characterization techniques. It is possible to measure simultaneously the specular reflected beam and the fluorescence radiation on a unique experimental setup. Using adapted analysis software, it is also possible to evaluate the data and perform combined fitting of the experimental data. Such a technique, the experimental setup and the analysis software required will be detailed in the next chapter.

2. FROM TXRF TO GIXRF

Methods	TXRF	GIXRF	XRF	XRR	XRD	GISAXS
TXRF	↑	surface contamination	information on surface contamination	information on surface contamination	information on surface contamination	nanoparticle composition
GIXRF	absolute angle calibration	↑	validation measurands	near surface depth profiles	near surface depth profiles	nanoparticle composition
XRF	validation measurands	validation measurands	↑	information on material composition	information on material composition	nanoparticle composition
XRR	layer thickness and roughness for modelling	layer thickness and roughness for modelling	contaminations/ spectral diffraction artefact	↑	layer thickness, roughness, density	substrate surface layer
XRD	information on material morphology, artefacts	information on material morphology, artefacts	information on material morphology, artefacts	information on material morphology	↑	information on material morphology
GISAXS	particle size distribution	particle size distribution	—	particle size distribution	particle size distribution	↑

Figure 48 : How can a method (rows) help another method (columns) to improve or complement the results [54] ?

2.3. Bibliography

- [1] Y. Yoneda and T. Horiuchi, "Optical flats for use in x-ray spectrochemical microanalysis," *Rev. Sci. Instrum.*, vol. 42, no. 7, pp. 169–170, Jul. 1971.
- [2] R. E. Ayala Jiménez, "Total reflection X-ray fluorescence spectrometers for multielement analysis: status of equipment," *Spectrochim. Acta Part B At. Spectrosc.*, vol. 56, no. 11, pp. 2331–2336, Nov. 2001.
- [3] J. Knoth, A. Prange, H. Schneider, and H. Schwenke, "Variable X-ray excitation for total reflection X-ray fluorescence spectrometry using an Mo/W alloy anode and a tunable double multilayer monochromator," *Spectrochim. Acta Part B At. Spectrosc.*, vol. 52, no. 7, pp. 907–913, Jul. 1997.
- [4] W. Ladisich, R. Rieder, P. Wobrauschek, and H. Aiginger, "Total reflection X-ray fluorescence analysis with monoenergetic excitation and full spectrum excitation using rotating anode X-ray tubes," *Nucl. Instrum. Methods Phys. Res. Sect. Accel. Spectrometers Detect. Assoc. Equip.*, vol. 330, no. 3, pp. 501–506, Jun. 1993.
- [5] P. Wobrauschek, P. Kregsamer, W. Ladisich, R. Rieder, and C. Streltli, "Total-reflection X-ray fluorescence analysis using special X-ray sources," *Spectrochim. Acta Part B At. Spectrosc.*, vol. 48, no. 2, pp. 143–151, Feb. 1993.
- [6] U. Waldschlaeger, "Recent and future developments in low power total reflection X-ray fluorescence spectroscopy," *Spectrochim. Acta Part B At. Spectrosc.*, vol. 61, no. 10–11, pp. 1115–1118, Nov. 2006.
- [7] B. Beckhoff, B. Kanngießner, N. Langhoff, R. Wedell, and H. Wolff, *Handbook of practical X-ray fluorescence analysis*, Springer. 2006.
- [8] M. Schuster, "A total reflection X-ray fluorescence spectrometer with monochromatic excitation," *Spectrochim. Acta Part B At. Spectrosc.*, vol. 46, no. 10, pp. 1341–1349, 1991.
- [9] J. Knoth, H. Schneider, and H. Schwenke, "Tunable exciting energies for total reflection X-ray fluorescence spectrometry using a tungsten anode and bandpass filtering," *X-Ray Spectrom.*, vol. 23, no. 6, pp. 261–266, Nov. 1994.
- [10] R. Redus, T. Pantazis, J. Pantazis, A. Huber, and B. Cross, "Benefits of improved resolution for ED-XRF" *Powder Diffr.*, vol. 23, no. 2, p. 180, 2008.
- [11] E. Gatti and P. Rehak, "Semiconductor Drift Chamber - An Application of a Novel Charge Transport Scheme," *Nucl Instr Meth*, vol. A, no. 225, pp. 608–614, 1984.
- [12] "Silicon Drift Detectors explained." Oxford Instruments, 2012.
- [13] L. Strüder and H. S. (invited), "High Resolution Silicon Detectors for Photons and Particles," *Radiat. Prot. Dosimetry*, vol. 61, no. 1–3, pp. 39–46, Aug. 1995.
- [14] A. Compton, "The Total Reflection of X-Rays," *Phi Mag*, vol. 45, pp. 1121–1131, 1923.
- [15] Y. Yoneda, "Anomalous Surface Reflection of X Rays," *Phys. Rev.*, vol. 131, no. 5, pp. 2010–2013, Sep. 1963.
- [16] R. Klockenkamper and A. von Bohlen, "Total-reflection X-ray fluorescence moving towards nanoanalysis: a survey," *Spectrochim. Acta Part B At. Spectrosc.*, vol. 56, no. 11, pp. 2005–2018, Nov. 2001.
- [17] H. Shibaya, "Behavior of Cu and Zn Impurities on GaAs Wafer Surfaces," *Jpn. J. Appl. Phys.*, vol. 34, no. 8A, p. L962, Aug. 1995.
- [18] P. Verdonck, C. M. Hasenack, and R. D. Mansano, "Metal contamination of silicon wafers induced by reactive ion etching plasmas and its behavior upon subsequent cleaning procedures," *J. Vac. Sci. Technol. B*, vol. 14, no. 1, pp. 538–542, Jan. 1996.

- [19] J. Szlachetko, J.-C. Dousse, J. Hoszowska, M. Pajek, R. Barrett, M. Berset, K. Fennane, A. Kubal-Kukus, and M. Szlachetko, "High-resolution study of x-ray resonant Raman scattering at the K edge of silicon," *Phys. Rev. Lett.*, vol. 97, no. 7, p. 073001, Aug. 2006.
- [20] H. Hoefler, C. Strel, P. Wobrauschek, M. Óvári, and G. Záray, "Analysis of low Z elements in various environmental samples with total reflection X-ray fluorescence (TXRF) spectrometry," *Spectrochim. Acta Part B At. Spectrosc.*, vol. 61, no. 10–11, pp. 1135–1140, Nov. 2006.
- [21] Y. Mori and K. Uemura, "Total-reflection X-ray fluorescence analysis for semiconductor process characterization," *Spectrochim. Acta Part B At. Spectrosc.*, vol. 58, no. 12, pp. 2085–2092, Dec. 2003.
- [22] G. Buhner, "Application of vapor phase decomposition/total reflection X-ray fluorescence in the silicon semiconductor manufacturing environment," *Spectrochim. Acta Part B At. Spectrosc.*, vol. 54, no. 10, pp. 1399–1407, Oct. 1999.
- [23] C. Strel, G. Pepponi, P. Wobrauschek, N. Zöger, P. Pianetta, K. Baur, S. Pahlke, L. Fabry, C. Mantler, B. Kanngießler, and W. Malzer, "Analysis of low Z elements on Si wafer surfaces with synchrotron radiation induced total reflection X-ray fluorescence at SSRL, Beamline 3-3: comparison of droplets with spin coated wafers," *Spectrochim. Acta Part B At. Spectrosc.*, vol. 58, no. 12, pp. 2105–2112, décembre 2003.
- [24] C. Strel, P. Wobrauschek, F. Meirer, and G. Pepponi, "Synchrotron radiation induced TXRF," *J. Anal. At. Spectrom.*, vol. 23, no. 6, p. 792, 2008.
- [25] C. Strel, P. Wobrauschek, W. Ladisich, R. Rieder, H. Aiginger, R. W. Ryon, and P. Pianetta, "Total reflection X-ray fluorescence analysis of light elements using synchrotron radiation," *Nucl. Instrum. Methods Phys. Res. Sect. Accel. Spectrometers Detect. Assoc. Equip.*, vol. 345, no. 2, pp. 399–403, Jun. 1994.
- [26] C. Strel, G. Pepponi, P. Wobrauschek, C. Jokubonis, G. Falkenberg, and G. Záray, "A new SR-TXRF vacuum chamber for ultra-trace analysis at HASYLAB, Beamline L," *X-Ray Spectrom.*, vol. 34, no. 5, pp. 451–455, Sep. 2005.
- [27] C. Strel, G. Pepponi, P. Wobrauschek, C. Jokubonis, G. Falkenberg, G. Záray, J. Broekaert, U. Fittschen, and B. Peschel, "Recent results of synchrotron radiation induced total reflection X-ray fluorescence analysis at HASYLAB, beamline L," *Spectrochim. Acta Part B At. Spectrosc.*, vol. 61, no. 10–11, pp. 1129–1134, Nov. 2006.
- [28] M. Kolbe, B. Beckhoff, M. Krumrey, M. A. Reading, J. V. den Berg, T. Conard, and S. D. Gendt, "Characterisation of High-k Containing Nanolayers by Reference-Free X-Ray Fluorescence Analysis with Synchrotron Radiation," *ECS Trans.*, vol. 25, no. 3, pp. 293–300, Sep. 2009.
- [29] V. A. Solé, E. Papillon, M. Cotte, P. Walter, and J. Susini, "A multiplatform code for the analysis of energy-dispersive X-ray fluorescence spectra," *Spectrochim. Acta*, vol. 62, pp. 63–68, Jan. 2007.
- [30] B. Beckhoff, A. Gottwald, R. Klein, M. Krumrey, R. Müller, M. Richter, F. Scholze, R. Thornagel, and G. Ulm, "A quarter-century of metrology using synchrotron radiation by PTB in Berlin," *Phys. Status Solidi B*, vol. 246, no. 7, pp. 1415–1434, Jul. 2009.
- [31] R. Klockenkämper and A. von Bohlen, "Determination of the critical thickness and the sensitivity for thin-film analysis by total reflection X-ray fluorescence spectrometry," *Spectrochim. Acta Part B At. Spectrosc.*, vol. 44, no. 5, pp. 461–469, 1989.
- [32] C. J. Powell and R. Shimizu, "Formation of Technical Committee 201 on Surface Chemical Analysis by the International Organization for Standardization," *Surf. Interface Anal.*, vol. 20, no. 4, pp. 322–325, avril 1993.
- [33] A. von Bohlen, "Total reflection X-ray fluorescence and grazing incidence X-ray spectrometry — Tools for micro- and surface analysis. A review," *Spectrochim. Acta Part B At. Spectrosc.*, vol. 64, no. 9, pp. 821–832, Sep. 2009.
- [34] D. Hellin, V. Geens, I. Teerlinck, J. Van Steenberghe, J. Rip, W. Laureyn, G. Raskin, P. W. Mertens, S. De Gendt, and C. Vinckier, "Vapor phase decomposition–droplet collection–total reflection X-ray fluorescence spectrometry for metallic contamination analysis on Ge wafers," *Spectrochim. Acta Part B At. Spectrosc.*, vol. 60, no. 2, pp. 209–213, février 2005.

- [35] D. Hellin, J. Rip, V. Geens, T. Delande, T. Conard, S. D. Gendt, and C. Vinckier, "Remediation for TXRF saturation effects on microdroplet residues from preconcentration methods on semiconductor wafers," *J. Anal. At. Spectrom.*, vol. 20, no. 7, pp. 652–658, Jun. 2005.
- [36] N. S. Shin, C. H. Chang, Y. M. Koo, and H. Padmore, "Synchrotron radiation excited total reflection X-ray fluorescence quantitative analysis of Si wafer by absolute fluorescence intensity calculation," *Mater. Lett.*, vol. 49, no. 1, pp. 38–42, May 2001.
- [37] B. Beckhoff, R. Fliegau, M. Kolbe, M. Müller, J. Weser, and G. Ulm, "Reference-Free Total Reflection X-ray Fluorescence Analysis of Semiconductor Surfaces with Synchrotron Radiation," *Anal. Chem.*, vol. 79, no. 20, pp. 7873–7882, Oct. 2007.
- [38] R. Klockenkämper, A. von Bohlen, H. W. Becker, and L. Palmetshofer, "Comparison of shallow depth profiles of cobalt-implanted Si wafers determined by total reflection x-ray fluorescence analysis after repeated stratified etching and by rutherford backscattering spectrometry," *Surf. Interface Anal.*, vol. 27, no. 11, pp. 1003–1008, Nov. 1999.
- [39] R. Klockenkämper and A. von Bohlen, "A new method for depth-profiling of shallow layers in silicon wafers by repeated chemical etching and total-reflection X-ray fluorescence analysis," *Spectrochim. Acta Part B At. Spectrosc.*, vol. 54, no. 10, pp. 1385–1392, Oct. 1999.
- [40] R. Klockenkämper, H. Krzyżanowska, and A. von Bohlen, "Density–depth profiles of an As-implanted Si wafer studied by repeated planar sputter etching and total reflection x-ray fluorescence analysis," *Surf. Interface Anal.*, vol. 35, no. 10, pp. 829–834, Oct. 2003.
- [41] M. B. R. Klockenkämper, "Near-surface density of ion-implanted Si studied by Rutherford backscattering and total-reflection x-ray fluorescence," *J. Appl. Phys.*, vol. 98, no. 3, pp. 033517–033517–5, 2005.
- [42] Y. Mori, K. Uemura, and K. Shimano, "A depth profile fitting model for a commercial total reflection X-ray fluorescence spectrometer," in *Spectrochimica acta. Part B: Atomic spectroscopy*, 1997, vol. 52, pp. 823–828.
- [43] R. Unterumsberger, B. Pollakowski, M. Müller, and B. Beckhoff, "Complementary Characterization of Buried Nanolayers by Quantitative X-ray Fluorescence Spectrometry under Conventional and Grazing Incidence Conditions," *Anal. Chem.*, vol. 83, no. 22, pp. 8623–8628, 2011.
- [44] C. Streeck, S. Brunken, M. Gerlach, C. Herzog, P. Hönicke, C. A. Kaufmann, J. Lubeck, B. Pollakowski, R. Unterumsberger, A. Weber, B. Beckhoff, B. Kanngießler, H.-W. Schock, and R. Mainz, "Grazing-incidence x-ray fluorescence analysis for non-destructive determination of In and Ga depth profiles in Cu(In,Ga)Se₂ absorber films," *Appl. Phys. Lett.*, vol. 103, no. 11, p. 113904, 2013.
- [45] K. Iltgen, B. MacDonald, O. Brox, A. Benninghoven, C. Weiss, T. Hossain, and E. Zschech, "Ultra-shallow junction depth profile analysis using TOF-SIMS and TXRF," *AIP Conf. Proc.* 449, pp. 777–781, 1998.
- [46] G. Pepponi, D. Giubertoni, M. Bersani, F. Meirer, D. Ingerle, G. Steinhauser, C. Strelti, P. Hoenicke, and B. Beckhoff, "Grazing incidence x-ray fluorescence and secondary ion mass spectrometry combined approach for the characterization of ultrashallow arsenic distribution in silicon," *J. Vac. Sci. Technol. B Microelectron. Nanometer Struct.*, vol. 28, no. 1, p. C1C59, 2010.
- [47] P. Hönicke, B. Beckhoff, M. Kolbe, D. Giubertoni, J. van den Berg, and G. Pepponi, "Depth profile characterization of ultra shallow junction implants," *Anal. Bioanal. Chem.*, vol. 396, no. 8, pp. 2825–2832, Apr. 2010.
- [48] D. L. Windt, "IMD—Software for modeling the optical properties of multilayer films," *Comput. Phys.*, vol. 12, no. 4, p. 360, 1998.
- [49] J. Knoth, R. Bormann, R. Gutschke, C. Michaelsen, and H. Schwenke, "Examination of layered structures by total-reflection X-ray fluorescence analysis," *Spectrochim. Acta Part B At. Spectrosc.*, vol. 48, no. 2, pp. 285–292, Feb. 1993.

- [50] U. Weisbrod, R. Gutschke, J. Knoth, and H. Schwenke, "Total reflection X-ray fluorescence spectrometry for quantitative surface and layer analysis," *Appl. Phys. Solids Surf.*, vol. 53, no. 5, pp. 449–456, Nov. 1991.
- [51] S. I. Zheludeva, M. V. Kovalchuk, N. N. Novikova, I. V. Bashelhanov, N. N. Salaschenko, A. D. Akhsakhalyan, and Y. Y. Platonov, "Thickness and density determination of ultrathin solid films comprising multilayer x-ray mirrors by x-ray reflection and fluorescence study," *Rev. Sci. Instrum.*, vol. 63, no. 1, p. 1519, 1992.
- [52] H. Schwenke and J. Knoth, *Anal Sci*, vol. 11, no. 3, pp. 533–537, 1995.
- [53] D. Ingerle, F. Meirer, G. Pepponi, E. Demenev, D. Giubertoni, P. Wobrauschek, and C. Strelt, "Combined evaluation of grazing incidence X-ray fluorescence and X-ray reflectivity data for improved profiling of ultra-shallow depth distributions," *Spectrochim. Acta Part B At. Spectrosc.*, vol. 99, pp. 121–128, Sep. 2014.
- [54] I. Holfelder, B. Beckhoff, R. Fliegau, P. Hönicke, A. Nutsch, P. Petrik, G. Roeder, and J. Weser, "Complementary methodologies for thin film characterization in one tool – a novel instrument for 450 mm wafers," *J. Anal. At. Spectrom.*, vol. 28, no. 4, p. 549, 2013.

3. Data analysis

3.1. GIXRF and XRR combined analysis

3.1.1. Advantages of the combined analysis

Grazing incidence X-ray fluorescence (GIXRF) is a powerful non-destructive technique for depth-profiling and characterization of thin layers or thin films [1], [2]. It provides information on the depth distribution and the total dose of elements in depths of a few nanometers as well as information on the thickness, densities and roughness of thin films. GIXRF is based on the fact that an X-ray standing wave field (XSW) is created above and inside the material due to interferences between the incoming and the reflected beam which occur at incidence angles close to the critical angle of total external reflection θ_{crit} [3]. By increasing the incidence angle (resulting in an increase of the penetration depth of the primary beam), the wave field intensity inside the sample distribution varies and the X-ray fluorescence signal is affected. This angular dependency of the fluorescence signals provides information on the elemental composition and material properties of the layers and the substrate material. On the other hand, X-ray reflectivity (XRR) is a non-destructive, highly accurate method based on the reflection in the specular direction of X-rays at the surface and interfaces of the sample [3]. XRR is a well-known and used method for the determination of the thickness, in-depth electronic density and roughness of thin layers [4]–[7].

Both techniques use a similar measurement procedure (*i.e.* increasing the incidence angle and collecting data at various angles) and XRR experimental requirements are close to the ones for GIXRF experiments (Section 2.2.2). Indeed, the experimental setup required to perform XRR measurements requires various elements such as a monochromatized and well collimated X-ray beam (with preferably a divergence smaller than 0.01° in the propagation direction), a X-ray detector with a high dynamic range (*i.e.* the ability to detect counting rates from 0 to more than 10^6 counts per second) and finally a motor system that allows having an accurate knowledge and control of the sample position and the incidence angle of the primary beam. Both methods can therefore be realized on a unique experimental setup using the same primary X-ray radiation (Figure 49).

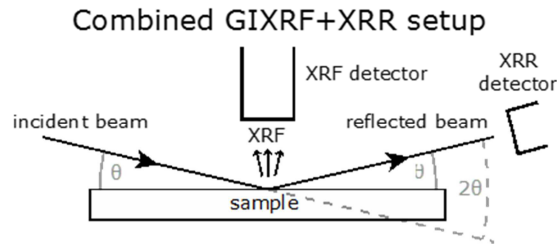


Figure 49 : Experimental setup for combined XRR and GIXRF analysis.

Finally, for both techniques, part of the information is left unused. By combining them, the additional information can be used to reduce the uncertainties of the individual methods and allows a determination of dose and depth profile of the implanted elements with drastically increased confidence level [8]. To overcome the limitations of each technique, the intensity of the specular reflectivity and the fluorescence can be measured simultaneously and the data evaluated using a combined fitting software.

In chapter One, we have shown that for GIXRF analysis, the X-ray fluorescence intensity I_{aj} of an element a in a layer j can be expressed according to De Boer formalism [9]:

$$I_{aj} = \frac{\lambda}{hc} C_{aj} \frac{\tau_{a\lambda}}{\mu_{j\lambda}/\rho_j} J_{a\lambda} \omega_a g_a \exp\left(-\sum_{n=1}^{j-1} \frac{\mu_{na} d_n}{\sin \psi_d}\right) S_1 \int_0^{d_j} dz \left(-\frac{\partial P_{jz}}{\partial z}\right) \exp\left(-\frac{\mu_{ja} z}{\sin \psi_d}\right) \quad (3.1)$$

with C_{aj} the mass fraction of element a in layer j , ρ_j the density of material j , $\tau_{a\lambda}$ is the photoelectric absorption coefficient for element a at wavelength λ , $J_{a\lambda}$ is the absorption jump factor at wavelength λ for the creation of holes in the considered shell of element a , ω_a is the fluorescence yield for the decay of holes in the considered shell of a , g_a is the relative emission rate for the considered XRF line in preference to other lines originating from the same hole in a , and μ_{na} the linear attenuation coefficient of the considered fluorescence radiation from element a in layer n , ψ_d is the detection angle and S_1 is the irradiated detected sample area.

As shown in Section 1.4.4, the measured fluorescence intensities are instrument dependent and a geometrical function should be taken into account when comparing the theoretical calculation and the experimental data. In De Boer's formalism, all the instrumental effects are corrected by the introduction of the irradiated detected sample area S_1 , however some recent developments have shown that a more complex function is required. The method to describe this correction function $G(\theta)$ as well as the impact of the formalism implementation and the choice of the database will be described and compared on four different combined XRR-GIXRF data analysis software.

3.1.2. Available software

Data analysis methods specifically for XRR have been developed over the years and various performant software already exist. In 2007, Van der Lee [10] even described diverse modern XRR data analysis methods and compared them with respect to their performance in a variety of situations. We had at our disposal several well-known XRR analysis software such as Leptos (developed by Brüker), GenX [11] and Maud (developed by L. Lutterotti [12]).

However, at the moment this thesis is written, a reference analysis software widely recognized by the GIXRF community does not exist and several groups are developing their own. A round-robin including different software developers has been created to topple this problem. This collaboration group was organized together with the Vienna University of Technology (Vienna, Austria) developing the software jGixa [13], the engineering department of the University of Trento (Trento, Italy) developing a XRF module for the Maud program [12], the Fondazione Bruno Kessler (FBK) (Trento, Italy) developing the software GIMPy and the Cea-Leti (Grenoble, France) developing the software Medepy. Even if not many of these software have been publicly released yet and their development stage varies, all of them are designed to perform combined XRR and GIXRF analysis and therefore in-depth characterization and elemental quantification of multilayers.

- **Maud** (Material Analysis Using diffraction) by L. Lutterotti has originally been developed for X-ray diffraction (XRD) and a XRR, GIXRF simulation modules have been added in order to perform a combined XRR-GIXRF-XRD analysis. The GIXRF module is intended to be a fundamental parameter (FP) analytical method designed to simulate the entire fluorescence spectrum at each incidence and outgoing angles.
- **Medepy** (Material Elemental DEpth profiling using Python) by B. Detlefs, G. Picot, E. Nolot, H. Rotella, B. Caby is also based of the FP approach for the GIXRF quantification. However, its goal is to simulate integrated fluorescence intensities. A spectrum evaluation (Section 2.1.3) third party software such as AXIL [14] or PyMCA [15] is then necessary to deconvolute and extract the intensity of the different fluorescence lines of interest.
- **GIMPy** (Grazing Incidence Material analysis with Python) by G. Pepponi and F. Brigidi is sensibly similar to Medepy. However, one characteristic of GIMPy is being able to perform both operations of signal deconvolution and fluorescence simulation fitting inside the same environment.
- **jGIXA** (Grazing Incidence X-ray Analysis using Java) by D. Ingerle is designed to perform elemental quantification via the simulation of integrated fluorescence intensities

and the use of standard samples. Similarly to Medepy, a third party software is necessary to extract the fluorescence intensities.

The second stage of the round-robin consisted in testing these data analysis software and evaluate their performances. The validation mission has been performed in two distinctive steps. Firstly, the XRR and GIXRF calculations have been compared with data obtained from a reference software (available for XRR) or using simple and simulated reference samples. Secondly, the fitting capabilities of the software have been tested on XRR and GIXRF acquisitions. This second approach is more complicated to perform as it requires a high control over all the parameters involved and a good knowledge of the sample structure and composition.

3.2. Software comparison

In a fundamental parameter approach, the first limitation to the reliability of the elemental quantification that every program has to face is the not completely trustworthiness of the available X-ray databases. Even accepting the errors that might come from the parameters contained in the databases, further errors can be introduced from a wrong implementation of the calculations or a wrong modelling. Therefore, the following work will point out some of the implementation differences between the four analysis software described above and check their impact on both the XRR and the GIXRF simulations.

3.2.1. X-ray database

Having access to reliable information about the material parameters (photoelectric cross-section, mass attenuation, fluorescent yield, etc...) is of primary importance for an analytical software. The acquisition of these parameters has been the subject of extensive research in the last decades and several databases and tabulation on scientific publications are now available, some of which are based on experimental measurements and other on theoretical calculations. Even if it is safe to say that the information concerning the most common measured fluorescence lines (generally the K lines) are nowadays extremely reliable, this is not the case for some of the L and most of the M lines. The problem of distinguishing the most reliable data among the high quantity of databases available has already been tackled and the answer is not straightforward [16]. It is known from the literature [17] that differences exist between the databases. For example, in Figure 50 are represented the absorption cross sections μ/ρ of Ag around the L edges. One can note that around the fluorescence edge, the various databases do not return the same values.

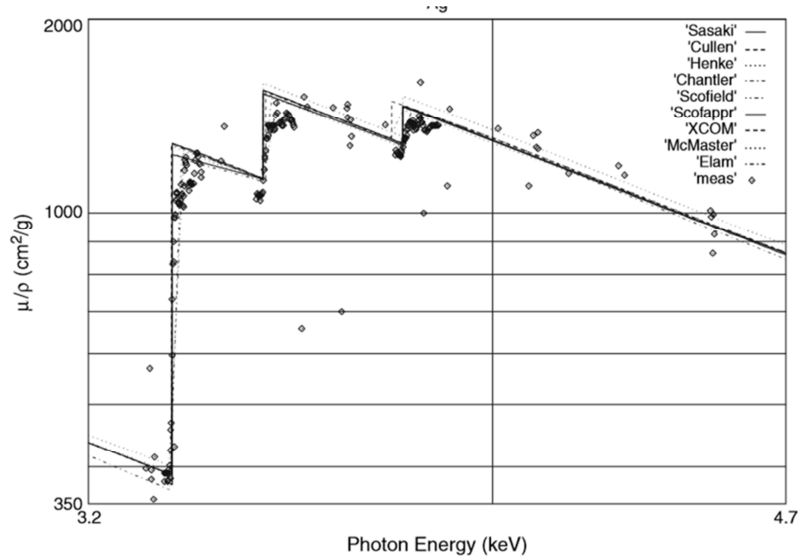


Figure 50 : Magnification of the L-edge range of silver [17].

In GIMPy, jGixa and Maud a combined database has been created combining the following available sources:

- **Standard Atomic Weight (A)** : International Union of Pure and Applied Chemistry (IUPAC) recommended values [18]
- **Elemental densities (ρ)** : Reporting values used in reference [19]
- **Electron binding energies (X-ray absorption edges)**
Edge Jump (extent of discontinuities in the photoelectric absorption cross section at absorption edges = $J_{a\lambda}$)
X-Ray lines (radiative electronic transitions in the X-ray regions)
Transition probabilities (radiative transition decay relative probability for a certain electron vacancy)
Fluorescence yield (probability of a fluorescence decay, as opposed to Auger, for a certain electron vacancy)
Cöster-Kronig transition probabilities (non-radiative inner L-shell transitions, redistribution of vacancies in the L-(sub) shells)
 have all been extracted from the following publications [20, 21]
- **Atomic scattering factors (f_1 and f_2)** in the range from 150 eV to 30000 eV [22]
- **Atomic scattering factors** in the range from 30 keV to 300 keV [23]
- **Photoelectric, elastic and inelastic scattering cross sections (μ/ρ)** [17]

Other X-ray databases are available. For example, T. Schoonjans combined several databases together, which in this case led to the creation of the very broad and exhaustive xraylib [24]

which is used in Medepy. The simulation differences induced by the choice of the database will be discussed in Section 3.3.

3.2.2. Sample definition

All software are built around De Boer's formalism [9] based on Parrat's recursive method [25] for the calculation of X-ray reflectivity and fluorescence. This calculation approach requires the considered multilayer to be divided into a small number of parallel sublayers each with parameters such as the scattering density, the thickness and the interfacial roughness that can vary independently. The way a multi-layered sample has to be simulated is represented in Figure 3. This particular construction is adapted for combined analysis as it is possible to separate the contributions of all parameters and to combine different simulation strategies to the data fitting.

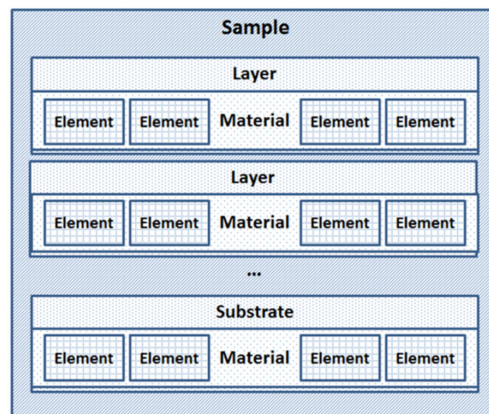


Figure 51 : Conceptual scheme of the modeling of a multi-layered structure in the four used combined analysis software [31].

In all four combined analysis software (GIMPY, jGIXA, Medepy and Maud), the top level object (*i.e.* the "Sample") is split in a series of "Layers" which in turn consist of a "Material" composed of different "Elements". From this constructed "Sample" object, it is possible to start the fluorescence calculation that will return the expected fluorescence recorded for this sample. However, the way the sample and the material parameters are described in the software is different.

3.2.2.1. Material parameters described from densities

In GIMPY and jGIXA, the input for the object "Material" is the mass density of the considered material (expressed in $\text{g}\cdot\text{cm}^{-3}$) and the input for the object "Element" is its stoichiometry in the material. As stated previously, one of the main features of this sample construction is the possibility to fit each parameter independently such as mass densities and the elemental stoichiometry. Indeed, the mass densities of each layer are then not calculated from the

input stoichiometry and vice versa. This non correlated relationship between the mass density and the stoichiometry can lead to some uncertainties on the parameters of the analyzed sample. Thus, an alternative method has been developed in Medepy.

In Medepy, the input necessary for the object “Element” is still its stoichiometry in the material. However, the input for the object “Material” is the numerical density (ρ_{num}) of the considered material (*i.e.* the number of atom per lattice in \AA^3). The mass density (ρ_{mass}) can then be calculated with the stoichiometry input via

$$\rho_{mass} = \rho_{num} \frac{xM_A + (1-x)M_B}{N_A} \quad (3.2)$$

where N_A is the number of Avogadro and M_A , M_B are respectively the molar mass of the element A and B of a material A_xB_{1-x}

By supposing a substitutional process, the user has then the possibility to fit the stoichiometry of the material with a fixed numerical density (*i.e.* substitute the layer’s various elements) and obtain the correspondent mass density value.

3.2.2.2. Material parameters described from crystallographic structure

Maud uses a different approach. Indeed, the input for the object “Material” is the crystal structure of the considered material. The complete and accurate crystal structure of various materials can be found in crystallographic databases [26]. It lists the symmetry, the space group, the cell parameter (in \AA) and the number of atoms in the unit cell (Figure 52). From the last two parameters and by knowing the atom molar mass, the mass density can be calculated using the relation (in the case of a simple cubic lattice)

$$\rho_{mass} = \frac{q_A M_A + q_B M_B}{a^3 N_A} \quad (3.3)$$

where a is the cell parameter and q_A , q_B are respectively the number of atoms A and B in the unit cell.

This use of the crystallographic structure allows avoiding uncertainty problems like the correlation between the atom quantity and the mass density. Indeed, by supposing a substitutional or interstitial process, it is possible to fit the number of atoms in the crystallographic lattice with a fixed cell parameter value and thus obtain the corresponding calculated mass density.

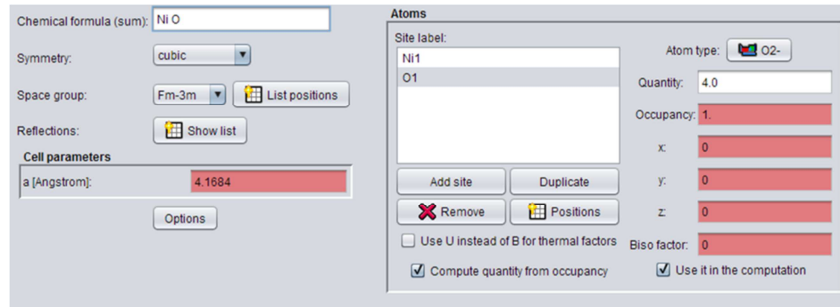


Figure 52 : Maud graphic interface of the material definition (in this case NiO). It lists the symmetry, the space group, the cell parameter, the number of atoms and their position in the crystallographic lattice.

3.2.3. Instrumental function

As stated in Subsection 1.4.4, in GIXRF the measured fluorescence intensities are instrument dependent. A geometrical factor should be taken into account when comparing theoretical calculation with experimental data. In the following sections, the modelling of the instrumental function and the definition of the correction function will be explained. The effect of selected parameters on the outcome of the simulation will also be highlighted.

3.2.3.1. Approximated approach

In 1989, De Boer [27] first investigated the effects of the geometrical factors versus the incidence and detection angle and showed that the geometrical factor had a great effect on the GIXRF acquisitions. However, it is only recently that a new instrumental correction formula has been established. Indeed, in 2012, Li et al. [28] have presented a geometrical factor correction which takes into account both the spatial intensity distribution of the primary X-ray beam (*i.e.* the shape of the beam) and the instrumental geometry (such as the collimator geometry of the fluorescence detector, the size of the X-ray source and the imprint beam size on the sample).

As the detected fluorescence intensity $I_x(\theta)$ depends on the geometrical function $G(\theta)$, it can be expressed by :

$$I_x(\theta) = F_x(\theta)G(\theta) = F_x(\theta) \frac{\Delta\Omega}{4\pi} I_0 S(\theta) \varepsilon_{det} T_{air} \quad (3.4)$$

where $F_x(\theta)$ is the total emitted fluorescence intensity per atoms of element x , $\Delta\Omega$ is the detection solid angle, I_0 is the incident beam intensity which is usually non-uniform along the beam cross-section, $S(\theta)$ is the sample surface area which is illuminated by the incident beam and detected by the fluorescence detector. ε_{det} and T_{air} represent the detector efficiency and the transmission efficiency of the X-ray fluorescence through the air path between the sample and the fluorescence detector respectively. These two last factors are independent of the incident angle and will be considered as constants.

For the rest of this work, we will also define the size of the sample L_s , the size of the detected area L_d , the size of the illuminated area L_i , the distance between the sample and the collimator d_1 , the pinhole height d_2 and finally the diameter of the pinhole holes d_p .

In order to determine the illuminated detected sample area $S(\theta)$, the 2D and 3D schematic representation of a GIXRF experimental setup is shown in Figure 53 and Figure 54. In this particular approach, only the incident beam width b_0 will be considered. Indeed, we assume that W_\perp the incident beam width in the direction perpendicular to the direction of propagation is quite broad, so that the beam intensity can be considered homogeneously distributed along this direction. The illuminated and detected sample area can therefore be rewritten $S(\theta) = W_\perp \times W_{||}(\theta)$.

For the following calculations, other hypotheses have to be assumed. The first one is that the X-ray fluorescence detector has to be placed at 90° above the sample surface. The second one is that only the X-ray source is rotating and the position of the sample is fixed. Finally, we will consider that $\Delta\Omega$ is independent of the incident angle and will be considered as a constant value. Finally, it is also assumed that all the exit fluorescence radiation from the pinhole is collected by the detector, so the distance between the detector entrance to the collimator exit will not be considered. These assumption are limitations mainly because some GIXRF experimental setups do not respect these two conditions. Some alternatives will be presented later in this work.

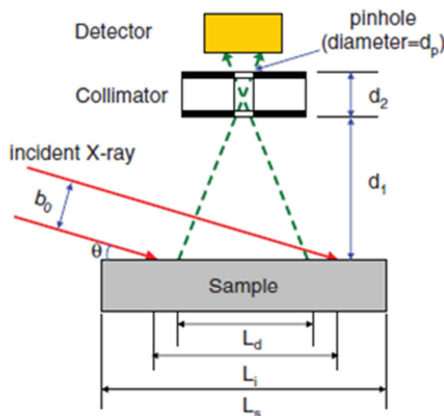


Figure 53: 2D schematic of the X-ray incident beam and the geometry for the fluorescence X-ray detection in a GIXRF experiment [28].

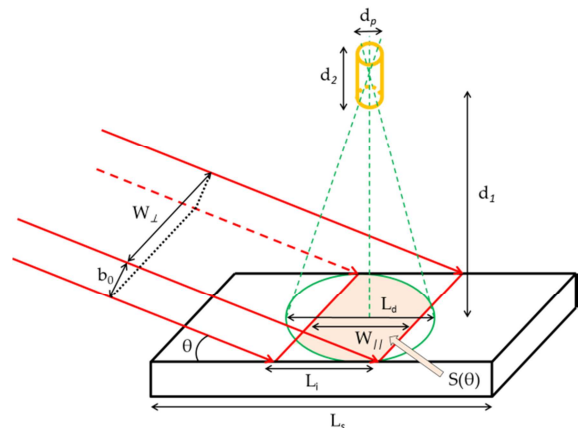


Figure 54: 3D schematic of the X-ray incident beam and the geometry for the fluorescence X-ray detection in a GIXRF experiment.

The X-ray beam is striking the sample surface of size L_s at a grazing incident angle θ . If the beam has a width b_0 near the sample surface, the footprint width L_i of the irradiated area on the sample surface is:

$$L_i(\theta) = b_0 / \sin \theta \quad (3.5)$$

From this geometrical arrangement, the width of the detected surface area L_d can be calculated (via Thales theorem) as:

$$L_d = 2 \frac{d_1 + \frac{d_2}{2}}{\frac{d_2}{d_p}} \quad (3.6)$$

With the suppositions made for this calculation, one can note that L_d is not angle dependent. It can be deduced easily that the detected irradiated width $W_{\parallel}(\theta)$ is dependent on the incidence angle, beam width (or more generally $L_i(\theta)$), the sample size (L_s), and the detected surface width (L_d).

Besides the geometrical setup, the spatial intensity distribution of the incident beam is also needed to be considered in order to correct the effect of the geometrical factor. Generally, the spatial intensity distribution of the incident beam is described by a Gaussian profile $g(\theta, t)$ as a function of the beam width. Therefore, the illuminated detected sample area width $W_{\parallel}(\theta)$ has to be weighted by the beam intensity distribution over the sample surface, which is given by:

$$W_{\parallel}(\theta) = \int_{-L_s/2}^{+L_s/2} g(\theta, t) \Pi_{L_d}(t) dt \quad (3.7)$$

where $\Pi_{L_d}(t)$ is a rectangular function of the detectable area with a width of L_d .

Equation (3.4) can then be rewritten with the following formula to express the geometrical function $G(\theta)$:

$$G(\theta) = \frac{\Delta\Omega}{4\pi} I_0 \varepsilon_{det} T_{air} \times W_{\perp} \times \int_{-L_s/2}^{+L_s/2} g(\theta, t) \Pi_{L_d}(t) dt \quad (3.8)$$

Figure 55 shows the calculated geometrical correction factor for different widths of the detectable area ($L_d = 2, 5, 10, 30$ mm), where the sample width L_s equals to 30 mm and the incident beam of spatial extension $b_0 = 0.15$ mm has Gaussian intensity distribution profile. For the rest of the work, we will also suppose that the intensity of the primary beam I_0 is equal to 1. In order to illustrate the relationship of the factor with the grazing incident angle, the inverse of the geometrical factor (*i.e.* the correction function) $1/G(\theta)$ is presented. It can be seen that the

geometrical factor will have greater effects on the measured fluorescence intensity when the detectable area width is larger. When the width L_d becomes very small such as 2 mm, the geometrical factor increases approximately linearly from 0.94 to 1.0 with the grazing incident angle from 0.0° to 1.5° and the effect of the instrumental function on the fluorescence measurements is small.

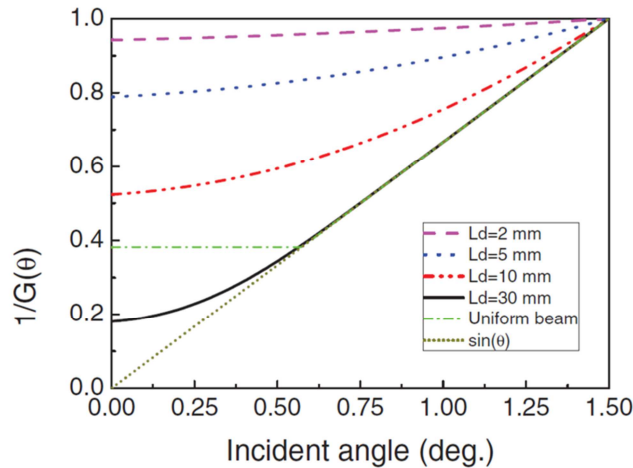


Figure 55 : The inverse of geometrical function (*i.e.* the correction function) calculated for different widths L_d of the detectable area, where $L_s = 30\text{mm}$ and $b_0 = 0.15\text{ mm}$ and $I_0 = 1$. The short dotted line is a $\sin(\theta)$ function for a visual guide [28].

In order to demonstrate the effect of the beam intensity distribution, the correction function $1/G(\theta)$ for a uniform (or square) beam intensity is also given. If the incident beam is uniformly distributed, the Gaussian function $g(\theta, t)$ is replaced in equation (3.7) by a rectangular function defined from $-L_i/2$ to $+L_i/2$. The width $W_{11}(\theta)$ is then the smallest value between the sample size L_s , the footprint width L_i , and the width of the detected area L_d .

In the case of a uniform beam, one can note that a boundary divides the geometrical factor correction function into two distinct regions. The singular point of the curve occurs at the incidence angle for which the footprint width $L_i(\theta)$ has the same value as the smallest value between L_s and L_d . Therefore, in the smaller θ angle range region below the inflexion point, the geometrical factor is a constant value, whereas, after the inflexion point, the correction function $1/G(\theta)$ is a $\sin(\theta)$ function as the width of the detected irradiated area is only determined by the footprint width $L_i(\theta)$ (smaller than the other parameters), which has a $\sin(\theta)$ dependence.

The representation of the correction functions in Figure 55 have been obtained by supposing that the spectrometer is well aligned, the fluorescence detector points at the center of the sample, the solid angle of detection is not dependent on the incidence angle and that the detector is placed at the vertical of a fixed sample. Even L_i 's expression of the geometrical

function needs some refinement, its representation of the correction function $1/G(\theta)$ will be used as a reference for the following work.

3.2.3.2. Correction of the detected illuminated area

The first correction added to Li's expression of the geometrical function is the effect of the position of the X-ray fluorescence detector. Indeed, in some experimental setup or due to inadequate alignment, the detection angle φ_d can be different from 90° . A new expression of the detected area L_d that takes into account the angle of detection has then been developed.

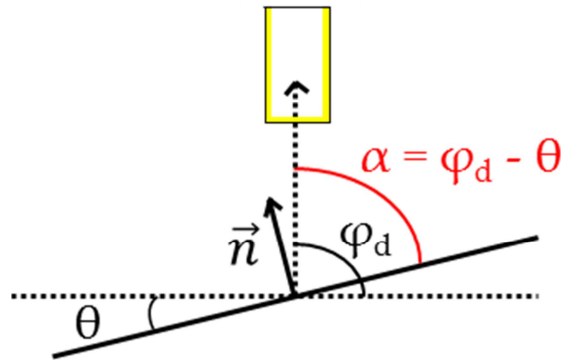


Figure 56 : Definition of the angles used in this work. The incidence angle θ , the detection angle φ_d is the angle between the X-ray detector and the horizontal plane and α is the angle between the detector and the sample will be used.

In a first approach, we have considered a GIXRF experimental setup with a fixed sample. Therefore, the angle between the sample and the X-ray fluorescence detector can be expressed $\alpha = \varphi_d$ and is not dependent of the incidence angle (Figure 56). The schematic of the geometry of the GIXRF experimental setup is represented in Figure 57. It can be seen that the variation of the angle of detection has an effect on the size and the position of the detected area L_d . The detected area can be divided into two distinct regions: A (*i.e.* the area seen by the X-ray detector on the detector side) and B (*i.e.* the area seen by the X-ray detector on the source side). With an angle of detection $\varphi_d \neq 90^\circ$, the detected area is shifted in relation to the center of the sample ($A \neq B$) and its size is different from the expression obtained in equation (3.6).

The expressions of A and B can be obtained via the application of a Thales theorem between the triangles GFE and GCD and therefore we have:

$$\frac{GF}{GC} = \frac{FE}{CD} \quad (3.9)$$

Using the parameters defined previously, it can be rewritten:

$$\frac{\frac{d_p}{2 \tan \alpha} + \frac{d_2}{2}}{d_1 + \frac{d_2}{2}} = \frac{\frac{d_p}{2 \sin \alpha}}{A} \quad (3.10)$$

and we obtain:

$$A = \left(d_1 + \frac{d_2}{2}\right) / \left(\frac{d_2}{d_p} * \sin \alpha + \cos \alpha\right) \quad (3.11)$$

With the same reasoning, one can find that:

$$B = \left(d_1 + \frac{d_2}{2}\right) / \left(\frac{d_2}{d_p} * \sin \alpha - \cos \alpha\right) \quad (3.12)$$

On a second approach, we have considered a tilted X-ray fluorescence detector placed in spectrometer in which the X-ray source is fixed and the sample is rotating. In this particular case, the angle between the sample and the detector depends on the incidence angle and can therefore be expressed $\alpha(\theta) = \varphi_d - \theta$ (Figure 58). As previously, the detected area can be divided into two distinctive regions A and B and their values can be obtained thanks to the use of the Thales theorem:

$$A(\theta) = \left(d_1 + \frac{d_2}{2}\right) / \left(\frac{d_2}{d_p} * \sin \alpha(\theta) + \cos \alpha(\theta)\right)$$

$$B(\theta) = \left(d_1 + \frac{d_2}{2}\right) / \left(\frac{d_2}{d_p} * \sin \alpha(\theta) - \cos \alpha(\theta)\right)$$

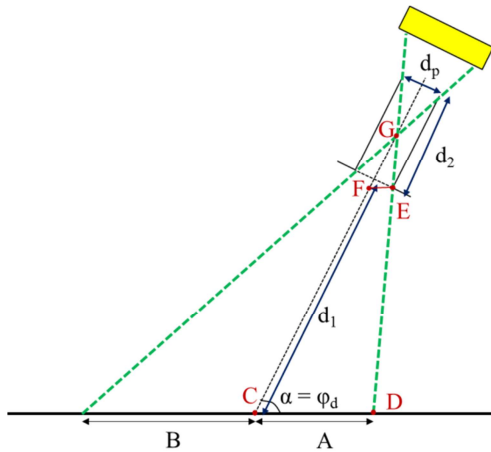


Figure 57: Schematic of the geometry for the fluorescence X-ray detection in a GIXRF experiment with a X-ray fluorescence detector tilted compared to the sample surface.

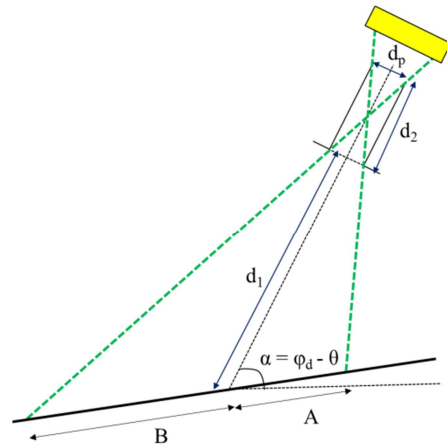


Figure 58: Schematic of the geometry for the fluorescence X-ray detection in a GIXRF experiment with a X-ray fluorescence detector tilted compared to a rotating sample.

After calculations, the expressions for A and B in the case of a tilted X-ray detector with a rotating sample are similar to the ones obtained in (3.11) and (3.12) but are angle-dependent.

Therefore, the size and the position of the detected area have to be recalculated for each angle of incidence.

3.2.3.3. The acceptance function

The second correction brought to Li's instrumental function correction is connected to the solid angle acceptance function $\Delta\Omega$. In his work, it is assumed that the solid angle of detection $\Delta\Omega$ is independent of the incident angle and is considered as a constant. Such limitation can be removed and a more accurate solid angle acceptance function can be defined.

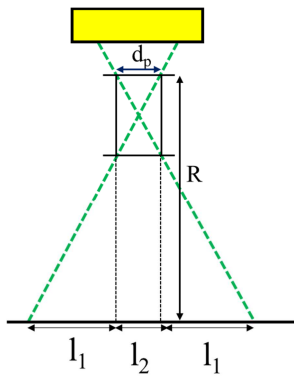


Figure 59 : 2D schematic representation used for the calculation of the solid angle of detection $\Delta\Omega$.

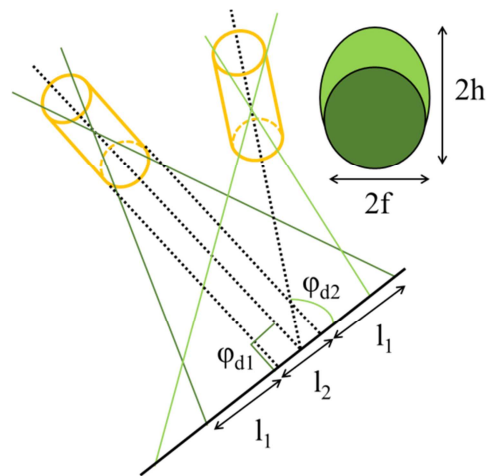


Figure 60 : 3D schematic representation used for the calculation of the solid angle of detection $\Delta\Omega$.

In Figure 59 and Figure 60 is shown the division in characteristic regions for the calculation of the solid angle according to B. Beckhoff et al. [29]. The solid angle calculation has been improved by taking into account the variation of the solid angle collected within the area l_2 and by better describing the behavior in the areas l_1 .

In the region marked as l_2 , the solid angle is subtended by a circle since the whole area of the detector not covered by the collimator is accessible. In the region marked as l_1 , the solid angle is not subtended by a circle any more, but from an ellipse that becomes smaller moving far from the center of the detector. Therefore, the solid angle calculation has been modelled following J.T. Conway paper [30] in which it is stated that:

$$\Delta\Omega = 2\pi(1 - \Lambda_0(\beta, k)) \quad (3.13)$$

with

$$\Lambda_0(\beta, k) = \frac{2}{\pi} [E(k)F(\beta, k') + K(k)E(\beta, k') - K(k)F(\beta, k')] \quad (3.14)$$

where $A_0(\beta, k)$ is the Heuman's Lambda function which is given in terms of E the complete elliptic integral of the second kind, F the incomplete elliptic integral of the first kind and K the complete elliptic integral of the first kind.

And by considering:

$$k = \sqrt{(h^2 - f^2)/(R^2 + h^2)}$$

$$k' = \sqrt{1 - k^2}$$

$$\beta = \arcsin \sqrt{\frac{R^2}{R^2 + f^2}}$$

with R the distance between the sample of the exit of the collimator, and h and f the half axes of the elliptic solid angle of detection.

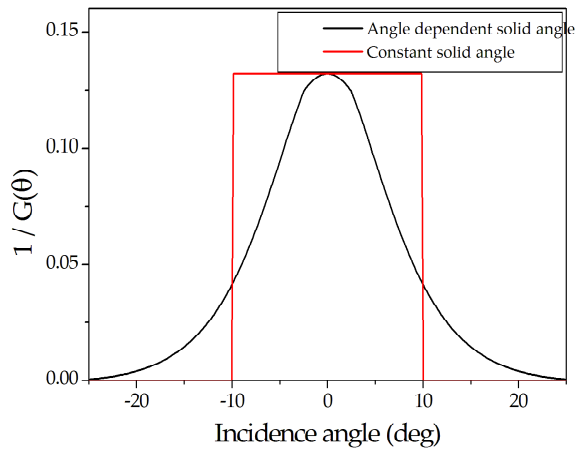


Figure 61 : Comparison of the acceptance function in the case where the solid angle $\Delta\Omega$ is considered constant or not.

The validity of the modeling of the acceptance function has been investigated by Fabio Brigidi [31] by comparing the result of the calculation to one obtained with a Monte Carlo (MC) simulation. The comparison between Li's approximated approach (*i.e.* a constant solid angle) and the calculated solid angle acceptance function is shown in Figure 61.

3.2.3.4. Divergence

The divergence of the primary X-ray beam has an important effect on both XRR and GIXRF measurements and its management in analysis software is not straightforward. Indeed, because of the divergence, for each position of the primary source, it is not possible to consider a unique angle of incidence. We rather have to define an array of angle from $\theta_i + \theta_{div}$ to $\theta_i - \theta_{div}$ (Figure 62). This method multiplies the calculation time by at least the number of angles in the array and therefore is not feasible from a software developer point of view.

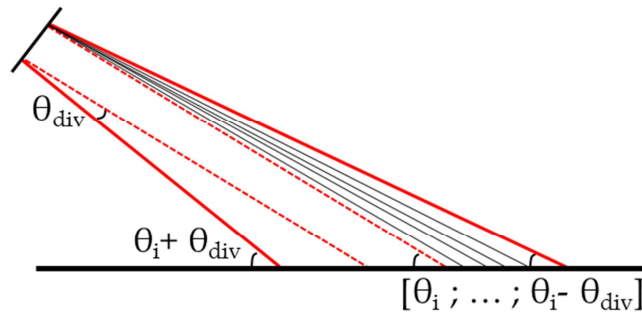


Figure 62 : Schematic of primary X-ray beam divergence.

Another method to take into account the divergence has to be implemented. The method chosen is the one implemented in most of performant XRR analysis software. It consists in evaluating the effect of the divergence as a convolution of the XRR or GIXRF simulation with a Gaussian curve of sigma (σ) equal to the divergence of the primary beam. The effect of this divergence implementation method on the accuracy of the GIXRF results will be discussed in Section 3.5.1. With all these corrections taken into account, equation (3.4) can therefore be written

$$I_x(\theta) = (F_x(\theta)G(\theta)) * h(\theta) \quad (3.15)$$

where $h(\theta)$ is a Gaussian function representing the divergence of the primary X-ray source.

3.3. Validation on simulated data

The first approach for the software evaluation was to compare the XRR and GIXRF calculations with data obtained on simulated reference samples. For each situation, we have decided to represent all the reflectivity and fluorescence curves as well as the difference curve Δ .

For XRR simulations, we have

$$\Delta_X = \log I_X - \log I_{LEPTOS} \quad (3.16)$$

where X is the considered XRR analysis software, I_x is the simulated XRR intensity from software X and I_{LEPTOS} is the reflectivity intensity simulated on Leptos (as it is a well-known and performant XRR analysis software).

For GIXRF simulations, we have

$$\Delta_{GX} = I_{GX} - I_{GIMPY} \quad (3.17)$$

where GX is the considered GIXRF analysis software, I_{GX} is the simulated fluorescence intensity from software X and I_{GIMPY} is the fluorescence intensity simulated by GIMPY.

3.3.1. X-ray database effect

Firstly, the effects of the X-ray database and the sample definition on XRR and GIXRF have been evaluated. A first model sample consisting of a 5 nm Nickel oxide (NiO) deposited on a 50 nm Nickel layer on top of a Si substrate has been created (Table 3). To avoid any other effects, the roughness of each layers have been put to 0 nm. Moreover, no instrumental parameters are being considered (*i.e.* the primary beam is not divergent, the instrumental function $G(\theta) = 1$ for all incidence angles). Moreover, the size of the sample is large enough to avoid edge effects as $L_s = 20$ cm.

In this work, the mass densities (in g.cm^{-3}) will be used as it is commonly done in the GIXRF community. Therefore, in Medepy and Maud, the equivalent values respectively in numerical density and cell parameter have been input (see Section 3.2.2 on the sample definition).

	Thickness (nm)	Density (g.cm^{-3})	Roughness (nm)
NiO	5	6	0
Ni	50	8.9	0
Si	SUB	2.33	0

Table 3 : Model sample used for the simulation comparison.

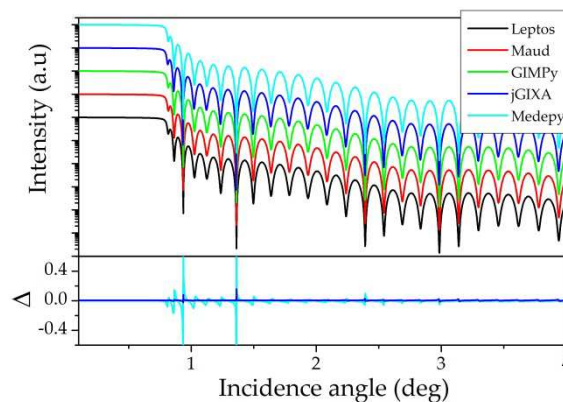


Figure 63 : Comparison of the XRR simulation of a NiO (5nm) / Ni (50nm) / Si (sub) sample irradiated with a Cu-K α radiation.

The XRR simulation has been performed with a Cu-K α radiation (8047 eV) (Figure 63). Medepy simulation give the largest Δ as large spike differences at 0.94° and 1.36° can be noted between Medepy and Leptos. A good agreement among all the other software is observed. These spike differences are due to a 0.001° angular shift between the two simulated curves. We supposed that this shift was due to differences between the databases used by the various software. Indeed, as shown in Section 3.2.1, contrarily to the other analysis software, Medepy

uses the xraylib database on which some parameters (such as the atomic scattering factors f_1 and f_2) are known to differ from the other X-ray database.

We then operated GIXRF simulations using a Mo-K α radiation (17479 eV). The excitation energy is far from the Si-K edge (1839 eV) or the Ni-K edge (8333 eV). The results of the Si-K α and Ni-K α fluorescence lines are represented in the Figure 64 and Figure 65. A good agreement is found between all the simulations as the largest Δ values, spotted around the critical angle, do not exceed 6%.

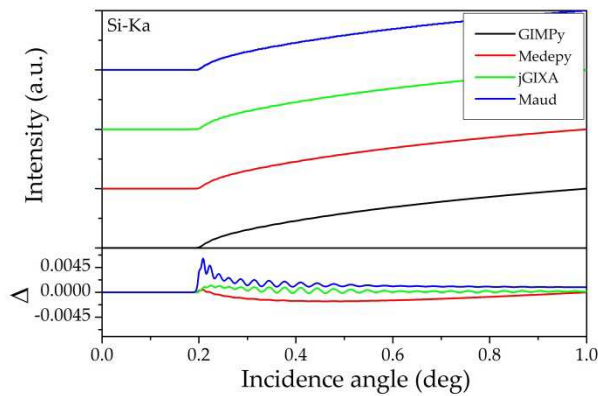


Figure 64: Comparison of the Si-K α GIXRF simulation of a NiO (5nm) / Ni (50nm) / Si (sub) sample irradiated with a Mo-K α radiation.

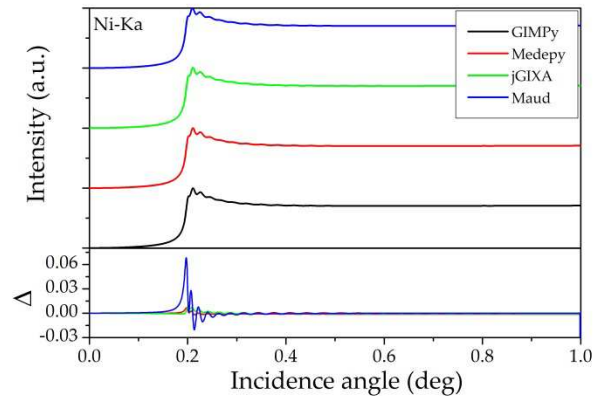


Figure 65: Comparison of the Ni-K α GIXRF simulation of a NiO (5nm) / Ni (50nm) / Si (sub) sample irradiated with a Mo-K α radiation.

Using the same sample, additional simulations have been performed at 8400 eV, close to the Ni-K edge (Figure 66).

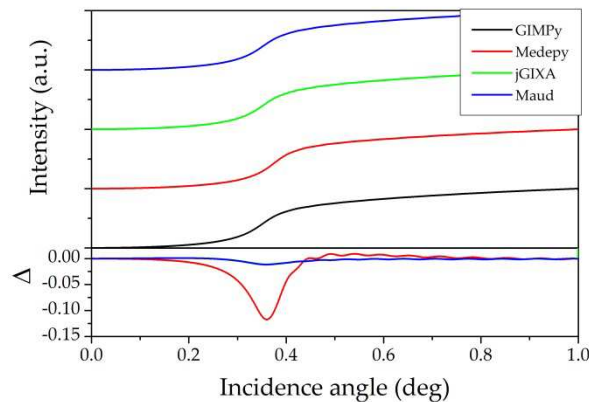


Figure 66: Comparison of the Ni-K α GIXRF simulation of a NiO (5nm) / Ni (50nm) / Si (sub) sample irradiated with a 8400 eV radiation.

A noticeable difference between Medepy and the other three software (approximately 15% around the critical angle) can be seen. Previously in Section 3.2.1, we noted that, close to fluorescence edges, the values of the absorption cross sections (μ/ρ) can vary a lot between different databases. As the 8400 eV excitation is only 67 eV above the Ni-K edge, we conclude that the difference between the GIXRF simulations is mainly due to the database. It allows us to confirm that the large disparities noted in the XRR simulations between Medepy and the other software are also due to database differences.

In conclusion, when working close to the fluorescence edges, the choice of the database is crucial and conditions the quality of the simulations and the quantification. However, for simulations performed at energies far from any fluorescence edge, these problems disappear as a good agreement can be found between all the analysis software.

3.3.2. Roughness effect

A new simulation has been carried out using the same stacking and excitation energies as previously but introducing surface roughness for the two layers and the substrate (Table 4).

	Thickness (nm)	Density (g.cm ⁻³)	Roughness (nm)
NiO	5	6	1
Ni	50	8.9	0.5
Si	SUB	2.33	1

Table 4 : Model sample used for the simulation comparison.

Even if Leptos allows two possible corrections for the roughness (*i.e.* Debye-Waller or Nevot-Croce), GIMPY, Maud, jGIXA and Medepy treat the effect of the roughness following the Nevot-Croce implementation described in Section 1.3.5. Therefore, the latter has been selected in Leptos.

Medepy still presents large spike differences in XRR simulations. We will not consider them as they are database induced differences. Thus, the agreement between the simulations was once more very good with less than 3% differences for GIXRF simulations.

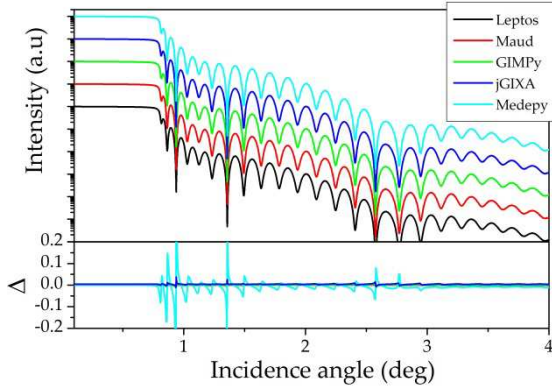


Figure 67 : Comparison of the XRR simulation of Table 4 sample irradiated with a Cu-K α radiation.

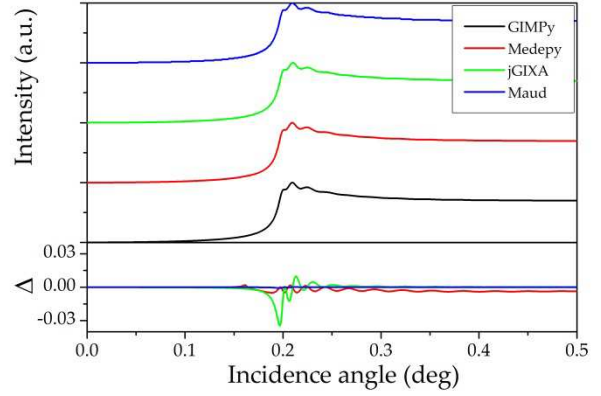


Figure 68 : Comparison of the Ni-K α GIXRF simulation of Table 4 sample irradiated with a Mo-K α radiation.

3.3.3. Effect of the divergence

Another simulation was focused on the effect of the divergence correction, using the same parameters as before (Table 4). All the software implement the divergence in a similar way (*i.e.* via the convolution with a Gaussian function), the only difference being in the unit of measure used for the definition of the Gaussian profile used in the convolution.

In Leptos and jGIXA, the Gaussian function uses the half width at half maximum (HWHM) of the distribution whereas in GIMPy, it is expressed as the standard deviation (*i.e.* σ) of the Gaussian with the relation:

$$H = 2\sqrt{2 \ln 2} \sigma \quad (3.18)$$

where H is the full width at half maximum (FWHM).

In Maud, the Caglioti parameters U, V and W are used and are defined as:

$$H^2 = U(\tan \theta)^2 + V(\tan \theta) + W \quad (3.19)$$

with θ the incidence angle of the primary X-ray radiation and H the FWHM.

In order to harmonize this expression with the other software and not deal with an angle-dependent divergence, we set $U = V = 0$ and input W accordingly. Simulations have been carried out by considering a HWHM of 0.3 mrad for the Gaussian function. Results (Figure 69 and Figure 70) again show a good agreement between the simulations. Less than 3% differences between all GIXRF simulations can be noted and moreover, due to the reduction of the fringes intensity by divergence effect, the XRR errors in Medepy are not predominant anymore and a 6% difference can be found between all the analysis software.

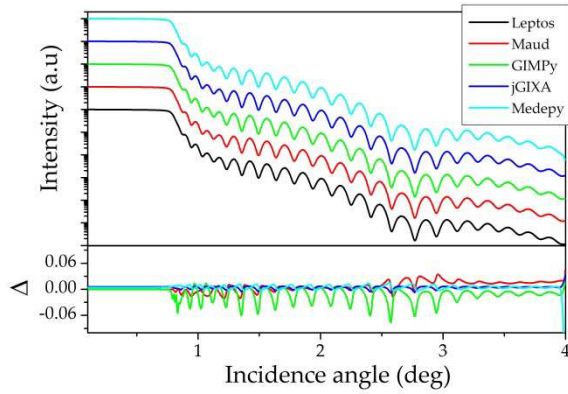


Figure 69 : Comparison of the XRR simulation of a NiO (5nm) / Ni (50nm) / Si (sub) sample with roughness irradiated with a divergent (HWHM = 0.3 mrad) Cu-K α radiation.

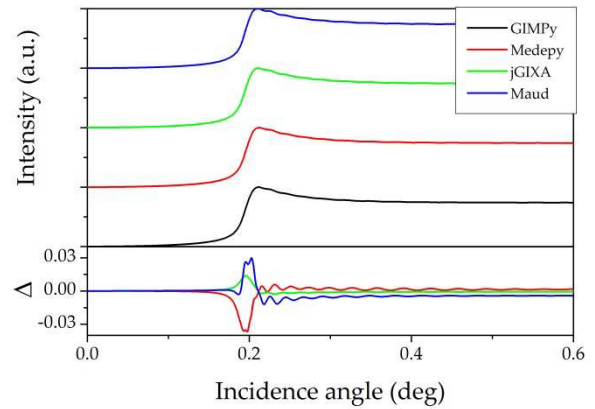


Figure 70 : Comparison of the Ni-K α GIXRF simulation of a NiO (5nm) / Ni (50nm) / Si (sub) sample with roughness irradiated with a divergent (HWHM = 0.3 mrad) Mo-K α radiation.

3.4. Instrumental correction function

The second approach to evaluate the analysis software was to compare the correction function $1/G(\theta)$ and its implementation. To avoid possible correlation problems with the differences shown above, we have decided to only consider the correction function without simulating any stacking. Moreover, for practical reasons, we will consider samples much larger than both the illuminated and the detected area. All other assumptions made for each software will also be listed.

3.4.1. Using Maud program

By supposing that the X-ray fluorescence detector is placed at 90° above the sample in a spectrometer where the sample is fixed, the geometrical function $G(\theta)$ in Maud is defined by:

$$G(\theta) = \left(\frac{1}{\sin \theta} \right)^\alpha \quad (3.20)$$

where θ is the incidence angle of the primary beam.

We can note that for $\alpha = 1$, $1/G(\theta) = \sin \theta$. Thus, it is impossible to dissociate the $\sin(\theta)$ function from the correction function (Figure 71). Compared to the representation of the correction function in the Li's article, the shape of the curve is different with major disparities noted in the angular range inferior to the critical angle. Solutions to this limitation will be considered and developed.

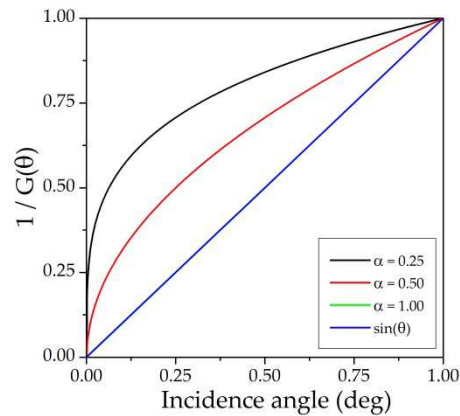


Figure 71 : Correction function $1/G(\theta)$ in Maud.

3.4.2. Using jGIXA program

The correction function implemented in jGIXA is similar to the one described in Li's article. Therefore, all the supposition made in Li's work (*i.e.* X-ray detector placed at 90° above the surface of a fixed sample) also have to be respected in jGIXA. To test the correction function, we have considered a sample length L_s of 20 cm and a $50\mu\text{m}$ beam width b_0 and tested various values of detected area L_d . The results are presented on Figure 72.

By using Li's publication as reference, the shape of the correction function $1/G(\theta)$ is in agreement with our expectations (*cf.* Figure 55). Indeed, as the detected area increases, the geometrical function will have greater effects. When the width L_d becomes small (2 mm), the correction function $1/G(\theta)$ increases approximately linearly from 0.90 to 1.0 with the incident angle from 0.0° to 1.0° and the effect of the instrumental function on the fluorescence measurements is small. However, for a large detected area (30 mm), the correction function $1/G(\theta)$ is, for a large angle range, equal to the $\sin(\theta)$ function and the effect of the geometrical function on the fluorescence measurements will be important.

One simulation using a uniform beam has also been performed and the results concur with Li's publication (*cf.* Figure 55).

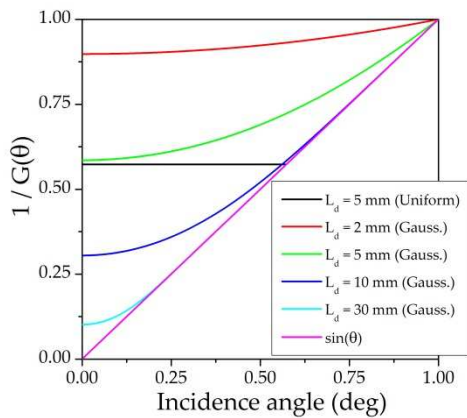


Figure 72 : Correction function $1/G(\theta)$ in jGIXA calculated for different widths L_d of the detectable area, where $L_s = 200\text{mm}$ and $b_0 = 50 \mu\text{m}$.

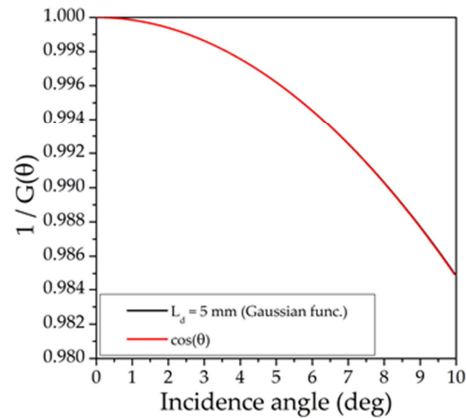


Figure 73 : Correction function $1/G(\theta)$ in the case of a rotating sample in jGIXA.

jGIXA has also the possibility to simulate an experimental setup with a rotating sample and a detector placed at 90° above the sample surface . The other experimental parameters (*i.e.* the sample size and the beam width) have been kept identical to previous simulations and a detected area L_d of 5 mm has been considered. As seen on Figure 73, the correction applied in this case can be expressed:

$$\frac{1}{G(\theta)} = \cos \theta \quad (3.21)$$

It simulates the increase in the detected area due to the rotation of the sample below the X-ray detector by multiplying the instrumental correction function by the inverse of a cosine. In a first approach and for small incidence angles (smaller than three times the critical angle θ_c of the considered sample), this approximated correction implemented in jGIXA is valid. However, as demonstrated above, considering an experimental setup with a rotating sample induces other effects on the size and the position of the detected illuminated area that have to be taken into account.

3.4.3. Using GIMPY and Medepy programs

GIMPY and Medepy both take into account the correction of the detected illuminated area and the acceptance function correction for the different experimental setup geometries described in Section 3.2.3. The way these corrections are implemented in GIMPY and Medepy is strictly identical. The following simulation results and conclusions are valid for both software.

3.4.3.1. Fixed sample and detector at 90°

We only considered the simple case of an X-ray fluorescence detector placed at 90° above the surface of a fixed sample. For the following simulations of the correction function, we considered a beam width b_0 of 50 μm and a sample length L_s of 20 cm (larger than the illuminated area or the detected area) and tested the influence of d_1 , d_2 and d_p .

First, we tested the influence of the distance between the sample and the collimator (d_1) on the correction function and its effect on the fluorescence profile (Figure 74 and Figure 75). The sample used for these simulations is the one described in Table 3.

Using Li's correction function representation as reference, the shape of the correction function $1/G(\theta)$ is as expected. Indeed, when the distance between the sample and the collimator increases, both the area seen by the X-ray fluorescence detector and the geometrical effects also increase. On this first set of simulations, the effect of the beam intensity distribution has not been tested.

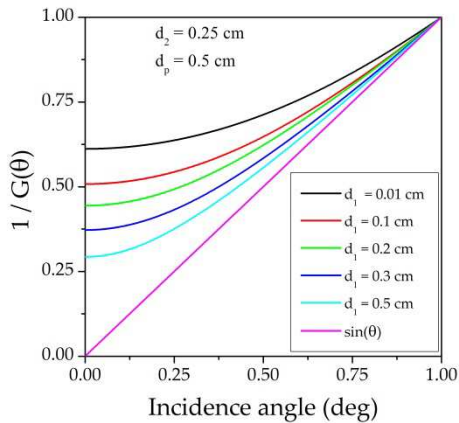


Figure 74: Correction function $1/G(\theta)$ with various distance sample-collimator (d_1) in Medepy and GIMPy.

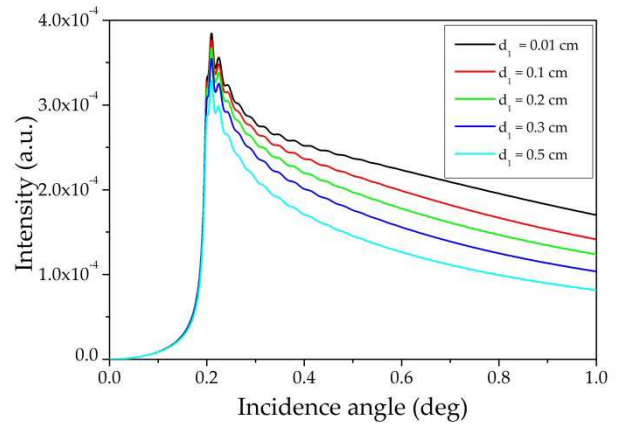


Figure 75: Geometrical function $G(\theta)$ multiplied by the Ni- $K\alpha$ fluorescence intensity.

We then tested the influence of the variation of the pinhole diameter d_p on the correction function $1/G(\theta)$ and its influence on the Ni- $K\alpha$ fluorescence profile (Figure 76 and Figure 77). The shape of the curves agrees with our expectations as an increase in the pinhole diameters will result in an increase in the detected area and thus an increase of the geometrical effects.

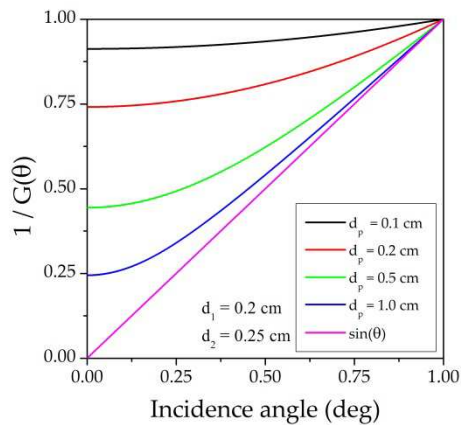


Figure 76: Correction function $1/G(\theta)$ with various pinhole diameters (d_p) in Medepy and GIMPy.

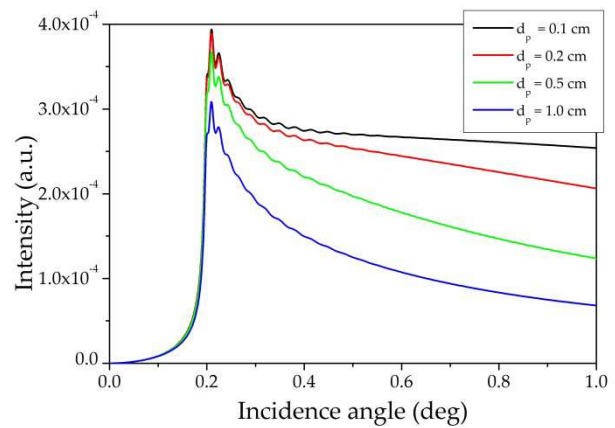


Figure 77: Geometrical function $G(\theta)$ multiplied to the Ni-K α fluorescence intensity.

Finally, the influence of the pinhole height d_2 has been tested (Figure 78 and Figure 79). As expressed in the equation (3.6), contrary to the two previous parameters, an increase of the size of the pinhole height d_2 will result in a decrease of the size of the detected area L_d as well as a decrease of the geometrical effects.

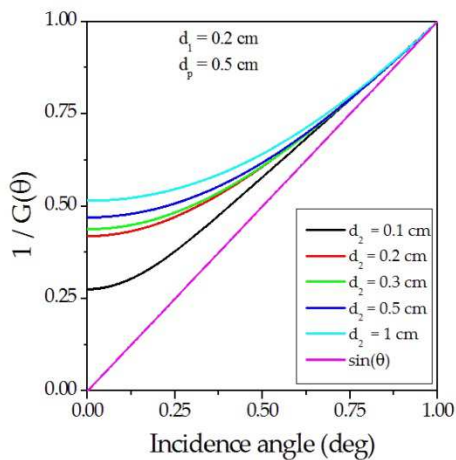


Figure 78: Correction function $1/G(\theta)$ with various pinhole height (d_2) in Medepy and GIMPy.

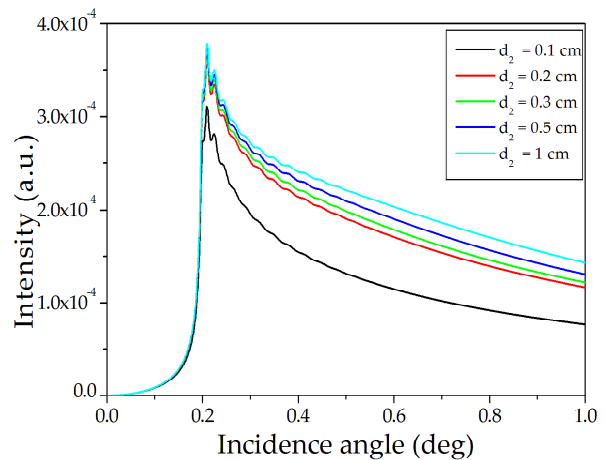


Figure 79: Geometrical function $G(\theta)$ multiplied to the Ni-K α fluorescence intensity.

In conclusion, the simulation of the instrumental function correction in GIMPy and Medepy gives similar results to the ones found in the literature and therefore can be used as a valid work base. Quantification problematics and the management of this instrumental correction for the fitting of XRR and GIXRF acquisitions will be treated in Section 3.5.

3.4.3.2. Tilted detector and rotating sample

The influence of the spectrometer geometry as well as the detection angle on the instrumental function correction has been evaluated in GIMPy and Medepy. In Section 3.2.3, we have already established that, in order to take into account the detection angle as well as the rotation of the illuminated sample, the size of the detected area A and B could be expressed:

$$A(\theta) = \left(d_1 + \frac{d_2}{2}\right) / \left(\frac{d_2}{d_p} * \sin \alpha(\theta) + \cos \alpha(\theta)\right)$$

$$B(\theta) = \left(d_1 + \frac{d_2}{2}\right) / \left(\frac{d_2}{d_p} * \sin \alpha(\theta) - \cos \alpha(\theta)\right)$$

where α is the angle between the detector and the sample, A is the area seen by the X-ray detector on the detector side and B is the area seen by the X-ray detector on the source side.

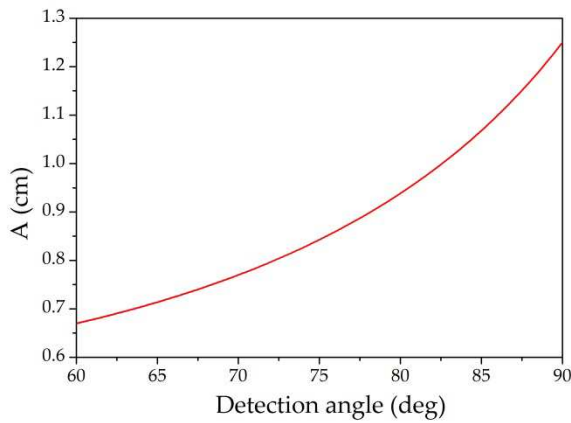


Figure 80 : Variation of the size of A (area seen by the X-ray detector on the detector side) with the incidence angle.

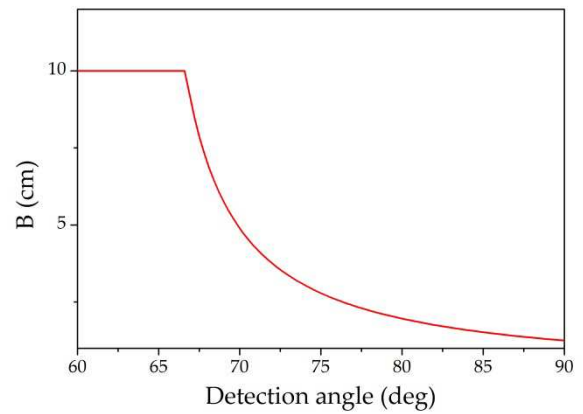


Figure 81 : Variation of the size of B (area seen by the X-ray detector on the source side) with the incidence angle.

The evolution of $A(\theta)$ and $B(\theta)$ are given in Figure 80 and Figure 81 by arbitrary supposing $d_1 = 0.2$ cm, $d_2 = 0.25$ cm and $d_p = 0.5$ cm and a sample length $L_s = 20$ cm. With the modification of the detection angle away from its 90° position, a decrease of the size of A can be noted. On the contrary, an important increase of the length of B is visible and a plateau starting at a specific angle of detection is observed. It represents the fact that below that critical angle of detection, the detected area on the source side by the X-ray fluorescence detector becomes larger than the size of the sample. Therefore, in our simulation, the plateau value of B is at 10 cm (*i.e.* the half of the sample size).

Let's consider the case of GIXRF setup with an X-ray detector placed at the vertical above the surface of a rotating sample. Generally for GIXRF experiments, the incidence angle does not go over 10° and therefore the angle between the detector and the sample $\alpha (= \varphi_d - \theta)$ varies from 90° to 80° . However, if due to misalignments or the geometry of the experimental setup, the

detection angle is different from 90° , large differences in the detected area calculation can be found. It will lead to large differences in the correction function (Figure 82).

In the case of a rotating sample, due to rapid variations of the sizes of A and B with the incidence angle, a misalignment of 5° or 10° of the fluorescence detector lead to important differences in the geometrical function. Therefore, for quantitative GIXRF analysis, the position of the detector must be accurately known and controlled during the entire experiment.

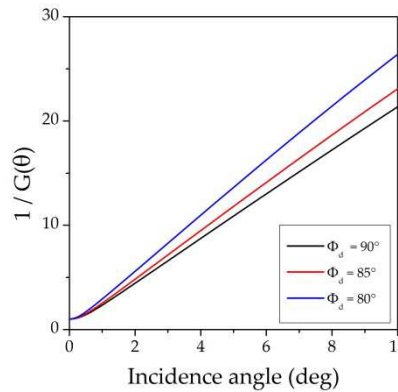


Figure 82 : Comparison of the correction function for different detection angles in the case of an experimental setup with a rotating sample.

Therefore, in order to perform precise GIXRF measurements and limit the effect of the geometric effects, the acquisition should be carried out in specific conditions. The X-ray detector should always be placed at the vertical above the sample surface to avoid the divergence of the size of the detected area B and avoid the limitations due to the sample size that follows. Moreover, to reduce the impact of the geometrical function on the fluorescent intensities and obtain a better resolution on the fluorescent fringes (Figure 83 and Figure 84), the operator should place the collimator close to the sample surface (optimally between 5 and 10 mm).

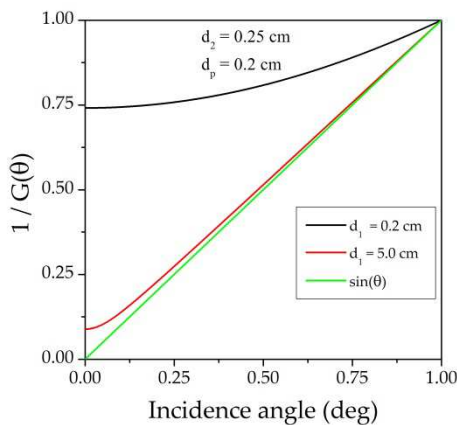


Figure 83 : Correction function $1/G(\theta)$ with various distance sample-collimator (d_1) in Medepy and GIMPy.

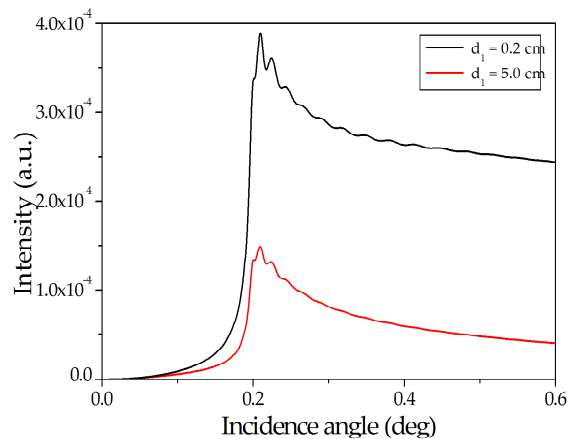


Figure 84 : Geometric function $G(\theta)$ applied to the Ni- $K\alpha$ fluorescence intensity.

3.5. Validation on experimental data

3.5.1. Full parameter approach

As stated previously, GIMPy and Medepy are both based on the FP approach for the GIXRF quantification. The FP approach requires the user to know all the material and instrumental parameters that may affect the fluorescence signal intensities.

The most straightforward parameters to determine are the size b_0 of the beam, the beam intensity I_0 , the detection angle φ_d , the distance between the sample and the collimator d_1 , the pinhole height d_2 and the diameter of the collimator pinholes d_p as defined before.

However, other instrumental parameters have to be known in order to perform a FP quantitative analysis such as the detector sensitivities. Indeed, as stated previously, the most commonly used detectors for ED-XRF measurements are solid state semiconductor detectors. The energy released in the detector material during the radiation interaction is converted into a certain amount of charge which is then collected at an output electrode of the device. The amount of electrons collected is proportional to the energy of the impinging photon. The efficiency of the detection is defined as the fraction of the total number of photons emitted by the source that is completely absorbed. The intrinsic efficiency, defined as the number of photons absorbed in the active volume of the detector sensor, is given by the absorption coefficient of the active crystal material and its thickness. However, this intrinsic efficiency is not equal to the total efficiency of the detection, since this latter is limited by several factors. The first modifications to the total efficiency come from the absorption of the impinging X-rays from those components that do not generate any signal. These are the detector frontal window and the dead layer. The dead layer of the detector is a silicon layer found in the frontal part of the active crystal where the electric charge, if generated, cannot be collected and hence produces no signal. The detector window is a thin cap placed in front of the detector to maintain the vacuum and trap the electrons. The materials typically used are polymers or Beryllium. Both of these two elements are very absorbing in the low energies region, so the dead layer and the window have to be taken into account.

Moreover, the shape of the fluorescence peak has to be precisely determined in order to obtain the fluorescent intensities. The final shape of a fluorescent peak is given by intrinsic effects, directly connected to the relaxation process of the atoms which generated the photons, and extrinsic effects, coming from the recording phase inside the detector. Moreover, the final peak shape is significantly influenced by the effect of the detector and the optic paths. The energy resolution of the detector, (*i.e.* its capability to distinguish photons closely separated in energy)

further modifies the final shape of the peak. The resolution of the detector is limited by different sources of statistical fluctuation such as the statistical noise, the electronic noise and the incomplete charge collection. Therefore, the evaluation of the detector response has to be performed.

Furthermore, as demonstrated previously, the beam intensity distribution has an important effect on the instrumental function correction. In all software, it is assumed that the incident X-ray beam has a Gaussian intensity distribution. By experience, it is known that different optics (such as slits) on the experimental setup may alter the Gaussian profile. Such a modification of the beam intensity distribution cannot be tested on the GIXRF analysis software at the present time.

Finally, the management of the divergence may not be accurate enough. Even if it has shown its efficiency for XRR simulations, some interrogations concerning GIXRF simulations persist. Indeed, different angles of incidence mean different penetration depths as well as different amplification effects due to the X-ray standing wave (XSW) field. The effect of these multiple amplifications on the GIXRF simulations cannot be evaluated.

In conclusion, the fundamental parameter approach for the GIXRF quantification is not straightforward as it requires the knowledge of many parameters values and their effects on the GIXRF simulations. It is therefore not applicable in the case of an unknown or not controlled experimental setup (generally laboratory or production equipment). In order to fit XRR and GIXRF data acquired on experimental setups on which d_1 , d_2 or d_p cannot be determined, a different approach must be defined.

As seen on Figure 85, tests have shown that different $\{ d_1, d_2, d_p \}$ triplets give the same geometrical function $G(\theta)$ and therefore the same fluorescence intensities. One can also note that the variation of the pinhole height d_2 has a limited effect on the simulated fluorescence intensities. As the distance between the sample and the collimator d_1 can be measured on the majority of experimental setups, the only parameter left to define is the pinhole diameter d_p . Therefore, in a simplified approach, in order to model the correction function $1/G(\theta)$, GIMPY and Medepy users could fix the values of d_1 and d_2 and fit the parameter d_p . This simplified approach is similar to one applied in jGIXA where L_d the detected surface is the unique experimental parameter required for fitting GIXRF measurements.

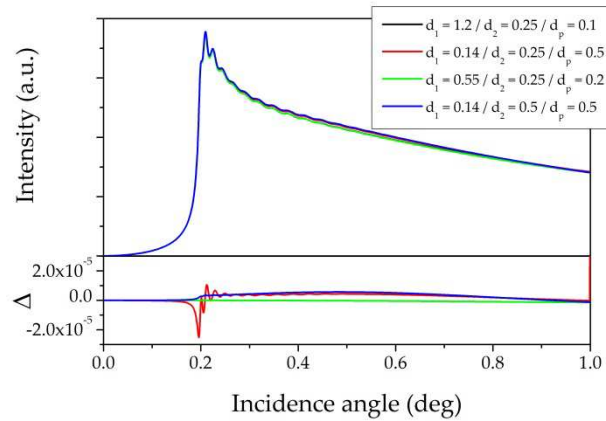


Figure 85 : Comparison of the Ni-K α fluorescence intensity corrected by various geometric functions $G(\theta)$.

In the following work, most of XRR and GIXRF acquisitions have been performed on setups where access to all experimental parameters was not possible. Therefore, the use of the FP method for quantification was impossible. Thus, this simplified method has been chosen. With this approach, in order to quantify the elements present in the studied sample, the use of standard sample is necessary. The steps and methodology required to perform this quantification will be described in Chapter Four.

3.5.2. Combined XRR and GIXRF modeling

The combined modeling of reflectivity and fluorescence measurements has been carried out using jGIXA on a Ni (50 nm) / Si (sub) sample. For the optimization procedure, arbitrary sample and experimental setup parameters have been defined as starting values (see Table 5). Due to existing local minima, a global optimization algorithm has been used to find the global minimum. The fitting of the measured data has been optimized with a differential evolution (DE) algorithm included in the software [32]. More details on the algorithms used and the fitting process will be described in Chapter Four.

$L_d = 5$	Thickness (nm)	Density (g.cm ⁻³)	Roughness (nm)
NiO	5	6	1
Ni	50	8.9	1
Si	SUB	2.33	1

Table 5 : Starting sample model used for the simulation comparison.

The sample has been measured at the Atominstitut (Vienna, Austria). Both XRR and GIXRF measurements have been carried out on a self-developed system with a Mo anode tube

and a multilayer monochromator selecting the Mo-K α line (17479 eV). Both elements are mounted in a vacuum chamber with a rotating sample [33]. An Amptek Silicon Drift Detector (SDD) was used to measure the reflected beam and the fluorescence signal was measured with a Vortex SDD placed at $\varphi_d = 90^\circ$ above the sample.

Both XRR and GIXRF data (open circles) and jGIXA simulations (solid lines) for the as-deposited samples are shown in Figure 38 and Figure 39 respectively. The agreement between the experimental and simulated points is very good as seen on the values of the difference curves Δ .

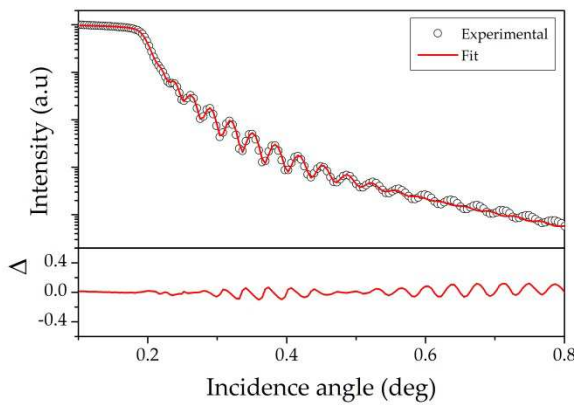


Figure 86: XRR measurements at 17479 eV (open circles) and fits (solid lines) of the Ni / Si sample by jGIXA.

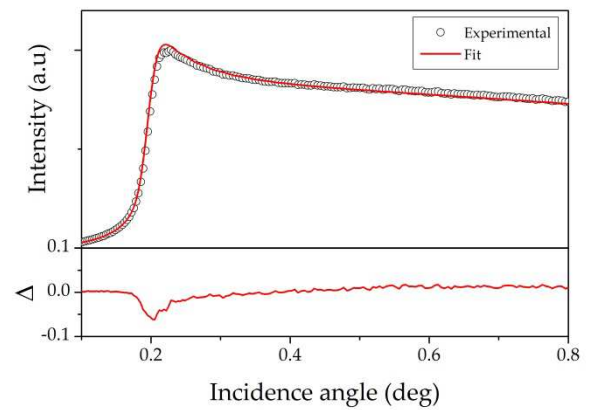


Figure 87: Ni-K α GIXRF measurements at 17479 eV (open circles) and fits (solid lines) of the Ni / Si sample by jGIXA.

A model (Table 6) has been determined by combining the XRR and GIXRF measurements. The incorporation of a top nickel oxide (NiO) layer with a low density is necessary in order to reproduce all the fine details of the reflectivity curves and improve the refinement agreement. A more complex sample model could be tested in order to improve the quality of the fit at incidence angle larger than 0.6° . However, in a first approach, we have shown that this simplified approach that requires only a unique parameter to describe the geometrical function gives satisfactory results.

$L_d = 3$	Thickness (nm)	Density (g.cm $^{-3}$)	Roughness (nm)
NiO	1.8	6.45	1.1
Ni	51	8.90	0.9
Si	SUB	2.33	0.3

Table 6: Refined sample model.

At the moment this thesis is written, a similar approach is being developed and tested in Medepy and the results are encouraging. Its development could bring a more complete and accurate simulation of the instrumental function correction and therefore a good alternative to jGIXA.

We have shown that the simplified approach does not require a large knowledge of the GIXRF experimental setup and can give satisfactory results. Therefore, it has been used to model XRR and GIXRF data as well as to perform the elemental quantification of samples of interest for the microelectronics or the photovoltaic. Combined XRR and GIXRF analyses of doped samples as well as various multilayered structures will be carried out in Chapter Four.

3.6. Bibliography

- [1] A. Lesnik, J. Bläsing, J. Hennig, A. Dadgar, and A. Krost, "Characterization of AlInN/AlN/GaN FET structures using x-ray diffraction, x-ray reflectometry and grazing incidence x-ray fluorescence analysis," *J. Phys. Appl. Phys.*, vol. 47, no. 35, p. 355106, Sep. 2014.
- [2] D. K. G. de Boer, A. J. G. Leenaers, and W. W. van den Hoogenhof, "The profile of layered materials reflected by glancing-incidence X-ray analysis," *Appl. Phys. A*, vol. 58, no. 3, pp. 169–172, Mar. 1994.
- [3] J. Daillant and A. Gibaud, Eds., *X-ray and Neutron Reflectivity*, vol. 770. Berlin, Heidelberg: Springer Berlin Heidelberg, 2009.
- [4] M. Fahland, T. Vogt, W. Schoenberger, and N. Schiller, "Optical properties of metal based transparent electrodes on polymer films," *Thin Solid Films*, vol. 516, no. 17, pp. 5777–5780, 2008.
- [5] L. L. Ren, H. F. Gao, S. T. Gao, J. J. Liu, and W. Zhang, "Determination of multilayer thicknesses of GaAs/AlAs superlattice by grazing incidence X-ray reflectivity," *Int. J. Metrol. Qual. Eng.*, vol. 4, no. 2, pp. 81–86, 2013.
- [6] S. Sintonen, S. Ali, O. M. E. Ylivaara, R. L. Puurunen, and H. Lipsanen, "X-ray reflectivity characterization of atomic layer deposition Al₂O₃/TiO₂ nanolaminates with ultrathin bilayers," *J. Vac. Sci. Technol. Vac. Surf. Films*, vol. 32, no. 1, 2014.
- [7] S.-W. Han, J. A. Pitney, P. F. Miceli, M. Covington, L. H. Greene, M. J. Godbole, and D. H. Lowndes, "X-ray reflectivity study of thin film oxide superconductors," *Phys. B Condens. Matter*, vol. 221, no. 1–4, pp. 235–237, Apr. 1996.
- [8] D. Ingerle, M. Schiebl, C. Strelt, and P. Wobrauschek, "Combination of grazing incidence x-ray fluorescence with x-ray reflectivity in one table-top spectrometer for improved characterization of thin layer and implants on/in silicon wafers," *Rev. Sci. Instrum.*, vol. 85, no. 8, p. 083110, Aug. 2014.
- [9] D. K. G. de Boer, "Glancing-incidence x-ray fluorescence of layered materials," *Phys. Rev. B Condens. Matter*, vol. 44, no. 2, pp. 498–511, 1991.
- [10] A. Van Der Lee, F. Salah, and B. Harzallah, "A comparison of modern data analysis methods for X-ray and neutron specular reflectivity data," *J. Appl. Crystallogr.*, vol. 40, no. 5, pp. 820–833, Oct. 2007.
- [11] M. Björck and G. Andersson, "GenX: an extensible X-ray reflectivity refinement program utilizing differential evolution," *J. Appl. Crystallogr.*, vol. 40, no. 6, pp. 1174–1178, Dec. 2007.
- [12] L. Lutterotti, "Total pattern fitting for the combined size–strain–stress–texture determination in thin film diffraction," *Nucl. Instrum. Methods Phys. Res. Sect. B Beam Interact. Mater. At.*, vol. 268, no. 3–4, pp. 334–340, Feb. 2010.
- [13] D. Ingerle, M. Schiebl, C. Strelt, and P. Wobrauschek, "Combination of grazing incidence x-ray fluorescence with x-ray reflectivity in one table-top spectrometer for improved characterization of thin layer and implants on/in silicon wafers," *Rev. Sci. Instrum.*, vol. 85, no. 8, p. 083110, Aug. 2014.
- [14] P. Van Espen, K. Janssens, and J. Nobels, "AXIL-PC, software for the analysis of complex X-ray spectra," *Chemom. Intell. Lab. Syst.*, vol. 1, no. 1, pp. 109–114, Nov. 1986.
- [15] V. A. Solé, E. Papillon, M. Cotte, P. Walter, and J. Susini, "A multiplatform code for the analysis of energy-dispersive X-ray fluorescence spectra," *Spectrochim. Acta*, vol. 62, pp. 63–68, Jan. 2007.
- [16] B. Beckhoff, "Reference-free X-ray spectrometry based on metrology using synchrotron radiation," *J. Anal. At. Spectrom.*, vol. 23, no. 6, p. 845, 2008.
- [17] H. Ebel, R. Svagera, M. F. Ebel, A. Shaltout, and J. H. Hubbell, "Numerical description of photoelectric absorption coefficients for fundamental parameter programs," *X-Ray Spectrom.*, vol. 32, no. 6, pp. 442–451, Nov. 2003.

-
- [18] M. E. Wieser and M. Berglund, "Atomic weights of the elements 2007 (IUPAC Technical Report)," *Pure Appl. Chem.*, vol. 81, no. 11, Jan. 2009.
- [19] S. M. Seltzer, "Calculation of Photon Mass Energy-Transfer and Mass Energy-Absorption Coefficients," *Rad Res*, vol. 136, pp. 147–170, 1993.
- [20] A. Brunetti, M. Sanchez del Rio, B. Golosio, A. Simionovici, and A. Somogyi, "A library for X-ray-matter interaction cross sections for X-ray fluorescence applications," *Spectrochim. Acta Part B At. Spectrosc.*, vol. 59, no. 10–11, pp. 1725–1731, Oct. 2004.
- [21] M. O. Krause, "Atomic radiative and radiationless yields for K and L shells," *J. Phys. Chem. Ref. Data*, vol. 8, no. 2, p. 307, 1979.
- [22] B. L. Henke, E. M. Gullikson, and J. C. Davis, "X-Ray Interactions: Photoabsorption, Scattering, Transmission, and Reflection at $E = 50\text{--}30,000$ eV, $Z = 1\text{--}92$," *At. Data Nucl. Data Tables*, vol. 54, no. 2, pp. 181–342, Jul. 1993.
- [23] S. Brennan and P. L. Cowan, "A suite of programs for calculating x-ray absorption, reflection, and diffraction performance for a variety of materials at arbitrary wavelengths," *Rev. Sci. Instrum.*, vol. 63, no. 1, p. 850, 1992.
- [24] T. Schoonjans, A. Brunetti, B. Golosio, M. Sanchez del Rio, V. A. Solé, C. Ferrero, and L. Vincze, "The xraylib library for X-ray-matter interactions. Recent developments," *Spectrochim. Acta Part B At. Spectrosc.*, vol. 66, no. 11–12, pp. 776–784, Nov. 2011.
- [25] L. G. Parratt, "Surface Studies of Solids by Total Reflection of X-Rays," *Phys. Rev.*, vol. 95, no. 2, pp. 359–369, Jul. 1954.
- [26] S. Grazulis, A. Daskevicius, A. Merkys, D. Chateigner, L. Lutterotti, M. Quiros, N. R. Serebryanaya, P. Moeck, R. T. Downs, and A. Le Bail, "Crystallography Open Database (COD): an open-access collection of crystal structures and platform for world-wide collaboration," *Nucleic Acids Res.*, vol. 40, no. D1, pp. D420–D427, Jan. 2012.
- [27] D. K. G. de Boer, "Fundamental parameters for X-ray fluorescence analysis," *Spectrochim. Acta Part B At. Spectrosc.*, vol. 44, no. 11, pp. 1171–1190, 1989.
- [28] W. Li, J. Zhu, X. Ma, H. Li, H. Wang, K. J. S. Sawhney, and Z. Wang, "Geometrical factor correction in grazing incident x-ray fluorescence experiment," *Rev. Sci. Instrum.*, vol. 83, no. 5, p. 053114, May 2012.
- [29] B. Beckhoff, R. Fliegau, M. Kolbe, M. Müller, J. Weser, and G. Ulm, "Reference-Free Total Reflection X-ray Fluorescence Analysis of Semiconductor Surfaces with Synchrotron Radiation," *Anal. Chem.*, vol. 79, no. 20, pp. 7873–7882, Oct. 2007.
- [30] J. T. Conway, "Analytical solution for the solid angle subtended at any point by an ellipse via a point source radiation vector potential," *Nucl. Instrum. Methods Phys. Res. Sect. Accel. Spectrometers Detect. Assoc. Equip.*, vol. 614, no. 1, pp. 17–27, Feb. 2010.
- [31] F. Brigidi, "PhD manuscript: 'Modelling of Grazing Incidence X-Ray Fluorescence (GIXRF) for surface layer characterisation.'" 2015.
- [32] R. Storn and K. Price, "Differential Evolution – A Simple and Efficient Heuristic for Global Optimization over Continuous Spaces," *J. Glob. Optim.*, vol. 11, no. 4, pp. 341–359, Dec. 1997.
- [33] D. Ingerle, F. Meirer, N. Zoeger, G. Pepponi, D. Giubertoni, G. Steinhauser, P. Wobrauschek, and C. Streltsov, "A new spectrometer for grazing incidence X-ray fluorescence for the characterization of Arsenic implants and Hf based high-k layers," *Spectrochim. Acta Part B At. Spectrosc.*, vol. 65, no. 6, pp. 429–433, Jun. 2010.

4. GIXRF applications

4.1. Depth profiling characterization of implanted samples

In the following study, grazing incidence X-ray fluorescence (GIXRF) will be applied to the characterization of arsenic (As) doping profiles in silicon (Si). Two different strategies for the characterization of the As profiles have been used: the first one consisting in quantifying the total dose of dopants implanted and a second one aiming to obtain the complete in-depth profiling of Ultra-Shallow Junctions (USJ). For both strategies, preliminary Secondary Ion Mass Spectrometry (SIMS) measurements were used as an input. After a brief introduction about the interest around the analyzed samples, the data treatment procedure and the result of the investigation will be presented.

4.1.1. Case study

4.1.1.1. MOS technology

Continuous developments in the microelectronics field require the integration on a single chip of a large number of miniaturized components such as Metal-Oxide-Semiconductor Field Effect Transistors (MOSFET). Basic logic gates are produced using combinations of n-channel MOSFET (NMOS) (Figure 88) and p-channel MOSFET (PMOS). NMOS is a multilayered structure based on three main terminals (*i.e.* source, drain and gate). Source and drain are two highly n-doped regions (*i.e.* in these regions, electrons are the major carriers) separated by the channel which is a p-doped silicon substrate (*i.e.* holes are the major carriers). A metallic or polysilicon gate terminal is located over the channel, separated by an insulating layer (generally SiO₂ or materials with higher dielectric constant). The point where the doping concentration in the source or the drain equals the doping concentration in the channel is defined as the junction depth (X_j).

Billions of MOSFET can be integrated on a single integrated circuit, and according to Moore's law, the driving force for performance improvements is the continuous miniaturization of MOSFET devices. By integrating more and more transistors in a smaller area, not only the speed of the component will increase but also the energy consumption will decrease [1]. One of the first steps for the miniaturization of MOSFET devices is the reduction of the length of the

junction depth. Therefore, ion implantation technologies with the ability to perform ultra-shallow implantation of a high dose of n-dopants have been developed.

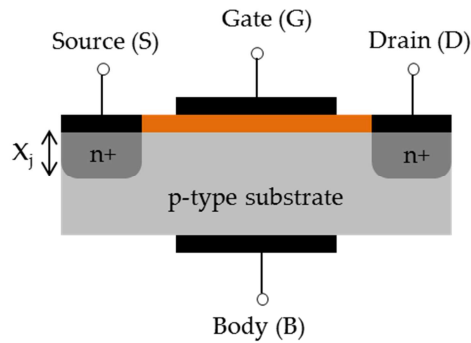


Figure 88 : Schematic representation of a n-channel MOSFET (NMOS).

4.1.1.2. Semiconductor doping

For the past 35 years, ion beam (or beamline) implantation has been a dominant method of semiconductor doping offering unsurpassed advantages such as reproducibility, extremely accurate depth distribution and fluence (*i.e.* the time-integrated flux of particle stream impinging the wafer surface) control [2]. In beamline implantation, an ion source is used to create an ion beam of the element to be implanted. The ion beam is then accelerated through a potential (from 10 to 100 kV) and transported to the wafer surface (Figure 89). Since the beam spot is usually smaller than the wafer size, mechanical and electrostatic scanning are necessary to achieve dose uniformity. As ultra-shallow junctions (USJ) require a high dose of dopants implemented within a few nanometers, this limitation can lead to prohibitive costs.

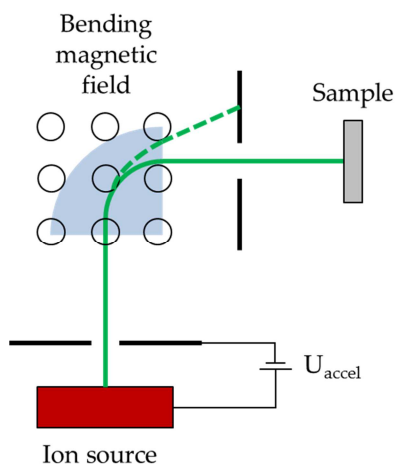


Figure 89 : Schematic representation of the ion beam (or beamline) implantation technique with mass separator.

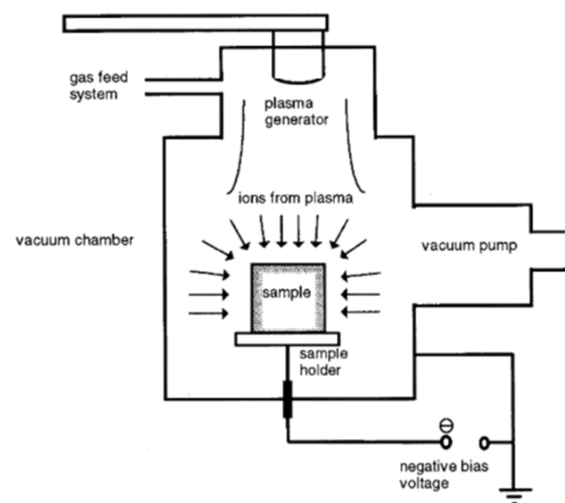


Figure 90 : Schematic representation of the plasma immersion ion implantation (PIII) technique [3].

Plasma Immersion Ion Implantation (PIII) was initially developed by Conrad and Castagna [4] to overcome the beamline implantation limitations. As shown in Figure 90, the sample is entirely immersed in the plasma and then biased to a negative voltage (generally few kV). Due to the negative voltage, the electrons are repelled from the substrate and a plasma sheath [5] depleted from electrons is formed. The negatively biased substrate will therefore accelerate the doping ions towards it (Figure 91). As the sheath completely surrounds the sample, all surfaces are implanted at the same time and production time and cost are reduced.

Since dopant atoms can contribute to the electrical conductivity only when they are in substitutional positions and lattice defects are minimal, an annealing process is required to remove the crystal damage and activate dopant atoms.

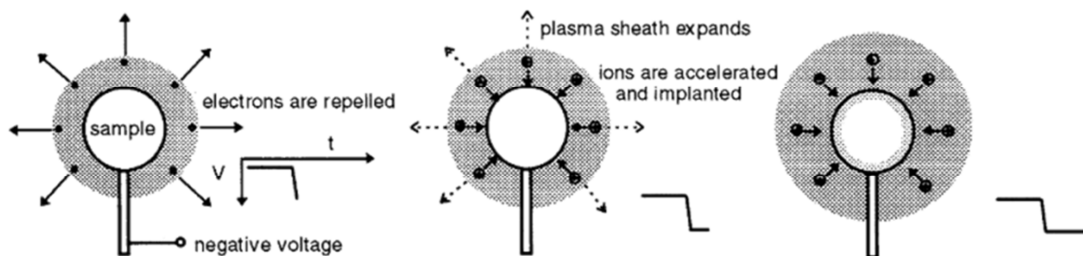


Figure 91 : Evolution of the plasma sheath with time when a negative voltage pulse $V(t)$ is applied to the substrate [3].

In the following work, arsenic (As) has been chosen as the n-type dopant. As the arsenic has an atomic radius similar to the one of silicon, it possesses a high solid solubility and high concentrations can be implanted. Moreover, its diffusivity is about a tenth of phosphorous so it has a lower diffusion during thermal annealing processes. Finally, its higher mass leads to lower penetration depth. Therefore, As is an adapted element for the realization of USJ where well-controlled abrupt boundaries are required.

4.1.2. First experiments and analysis

USJ pose a significant challenge to traditionally used depth-profiling characterization technique such as SIMS. Indeed, these new microelectronics systems have exposed some SIMS limitations because transient [6] and matrix effects [7], uncertainties in the measurements of elemental concentration in the first nanometers can appear.

These problems highlighted the need for complementary depth-profiling analysis techniques. GIXRF appeared as a promising candidate [8, 9] as it is not affected by transient nor matrix effects (*cf.* Section 2.2.2). Moreover, the high sensitivity of GIXRF in the first nanometer is particularly adapted for the study of USJ.

Via a first measurement campaign, combined XRR and GIXRF have been done to quantify the total dose of As implanted in Si and to obtain the in-depth doping profile. The samples measured were already characterized by SIMS and the quantification of the total dose was made. The interest was to test GIXRF when it is used as a complementary technique with SIMS.

4.1.2.1. Sample preparation

The batch of samples studied by combined XRR-GIXRF analysis consists in four 300 mm Si(001) substrate implanted with As ions with a 9 kV pulse voltage. Two different sample holder temperature conditions for the implantation (25°C and 500°C) have been tested. All the samples were implanted with the same nominal fluence of 1×10^{15} at/cm².

In order to simulate the activation of dopant atoms, a thermal budget has been applied to some samples. The annealing consists in a pre-stabilization of the furnace at 650°C for 10 s followed by a spike with a fast ramp-up rate (generally larger than 250°C/s). The temperature spike height was 1050°C. As soon as the peak temperature is reached, the annealing is stopped and the wafer cools down at approximately 80°C/s.

Sample code	Nominal fluence (at/cm ²)	Sample holder T (°C)	Annealing
1	1×10^{15}	25°C	None
2	1×10^{15}	25°C	1050°C spike annealing
3	1×10^{15}	500°C	None
4	1×10^{15}	500°C	1050°C spike annealing

Table 7 : Description of analyzed samples.

4.1.2.2. Secondary Ion Mass Spectroscopy (SIMS)

4.1.2.2.1. SIMS process

SIMS is a well-known technique used to analyze the composition and provide the mass spectrum of solid surfaces and thin films [10, 11]. It consists in bombarding a beam of primary ions (*i.e.* charged heavy particles with energies in the 1-25 keV range) on the surface of a solid. The primary ions collide with the sample atoms, gradually losing their energy and generally stopping a few tenth of nanometers below the surface. Due to the energy released in the collision, particles at and near the surface receive sufficient kinetic energy to be ejected. These secondary particles can be electrons, atoms, molecules, ion, clusters, etc (Figure 92). For most materials, the vast majority of emitted particles are neutral, but approximately 1% is ejected in the form of charged particles (positive or negative). These are known as secondary ions and can be detected and analyzed by mass spectroscopy.

A basic SIMS experimental setup therefore requires a primary ion beam source (generally O₂⁺, O⁻, Cs⁺, Ar⁺, Ga⁺) to supply the bombarding species. As a secondary mass spectrum is

obtained by collecting the secondary ions and subjecting them to mass filtration prior to detection, a method to collect the secondary ions, a mass analyzer (eg. quadrupole, magnetic sector, double focusing magnetic sector or time of flight) to isolate the ions of interest and a ion detection system (eg. photographic plate, Faraday cup, electron multiplier or a CCD camera and image plate) are required (Figure 93).

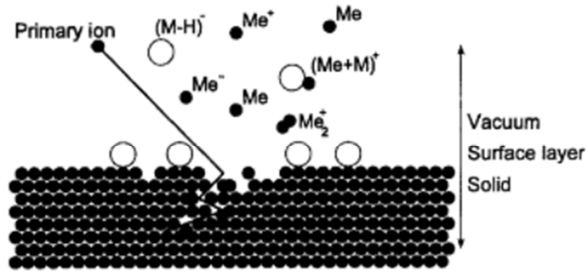


Figure 92 : The sputtering process, as a result of the collision cascade of the impacting primary ions, causes, neutral, positive and negative particles to be released from the surface [12].

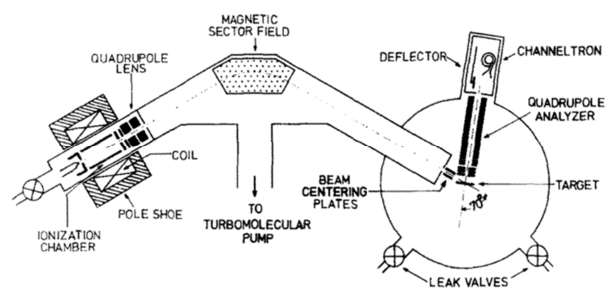


Figure 93 : Schematic of a secondary ion mass spectrometer with mass selected primary ion beam [13].

The secondary ions current $I_s(m)$ for selected ions of mass m is given by the following basic SIMS equation [14]:

$$I_s(m) = I_p Y_m \alpha C(m) T \tag{4.1}$$

where I_p is the primary ion flux, Y_m is the sputter yield, α is the ionization probability, $C(m)$ is the concentration of the detected species in the sputtered volume and T is the overall transmission of the energy and mass filters (*i.e.* the fraction of the sputtered ions of a given mass which are actually detected).

The two fundamental parameters are Y_m and α with Y_m the total number of sputtered particles per incident primary ion impact. It depends on the primary beam parameters as it increases with flux, the primary ions mass and the energy of the beam. Its value is generally between 1 and 10 sputtered particles per ion impact. α is defined as the fraction of secondary particles ejected with a charge (positive or negative). It can range from 0.01 to 10^{-5} and depends on the electronic structure of the species and on their chemical state before ejection.

The dependency of α with the experimental conditions and the chemical state of the sample is complex. Indeed, the secondary ion yield of positive (or negative) ions not only depends on the ionization potential (or the electron affinity) but also on various enhancement

effects such as the presence of electronegative elements (*e.g.*, oxygen) at the surface (Figures 94-95). These matrix effects give rise to extremely complicate quantitative SIMS analyses.

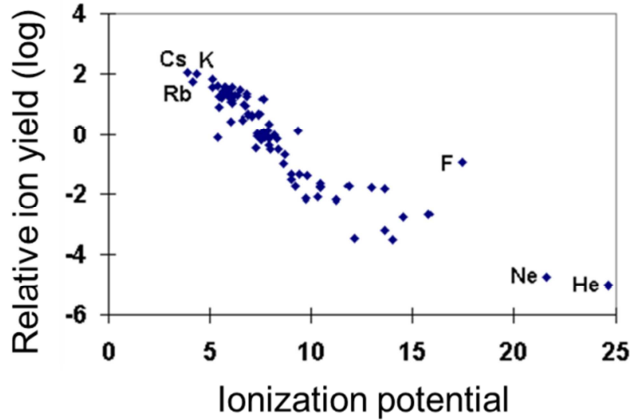


Figure 94 : Logarithm of relative positive ion yields plotted as a function of ionization potential. The ion yields are relative to silicon in a silicon matrix with oxygen sputtering [14].

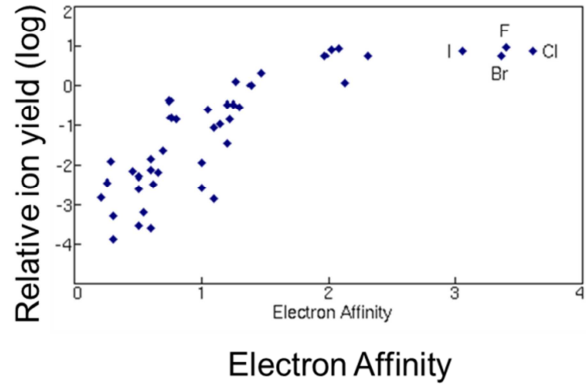


Figure 95 : Logarithm of relative negative ion yields plotted as a function of electron affinities. The ion yields are relative to silicon in a silicon matrix with oxygen sputtering [14].

Moreover, information about the depth position of the ejected atoms can be lost due to the experimental conditions. Indeed, the ion bombardment causes considerable modifications in the near surface region of the sample (*i.e.* displacements of atoms deeper into the sample, degradation of the surface composition, etc). These effects are important if a highly energetic primary ion beam and a fast sputtering rate are used.

Therefore, quantitative measurements are not straightforward as no simple relationship between the atom concentration and the SIMS peak intensity can be made. Therefore, quantitative analysis by SIMS uses relative sensitivity factors (RSF) defined by:

$$\frac{I_R}{C_R} = RSF_E \frac{I_E}{C_E}$$

where I_E is the secondary ion intensity for the element E , I_R is the secondary ion intensity for the reference element R , C_E is the concentration of element E , C_R is the concentration of element R and RSF_E is the relative sensitivity factor for element E . Various tables of RSF values can be found in the literature [15].

This allows composition to be determined if a suitable standard calibration material is available. Such measurements are now routine for dopant elements and are critical to the microelectronics industry.

4.1.2.3. First SIMS measurements

SIMS depth profiling have been performed on the four doped samples using a primary Cs^+ ions beam with an impact energy of 1.0 keV and an intensity of 51 nA. The sputtering rate of the SIMS experiment was 0.3 nm/s. In order to overcome the depth position uncertainties, the depth scale has been calibrated with a reference analyzed at the start of the run. Moreover, the concentration scale has been calibrated in reference to Si using RSF data acquired from As beamline implanted sample using an energy of 160 keV with a nominal fluence of 8×10^{15} at/cm².

Figure 96 and Figure 97 show the As profiles measured on samples implanted at 25°C and 500°C respectively. Table 8 shows the calculated fluence for the different samples compared to the nominal fluence. Even if all the samples have the same nominal fluence of 1×10^{15} at/cm², the measured As fluences on samples implanted at 25°C are larger than the ones measured on samples implanted at 500°C. Moreover, one can note that the spike annealing tends to better homogenize As species throughout the thickness of the implanted sample.

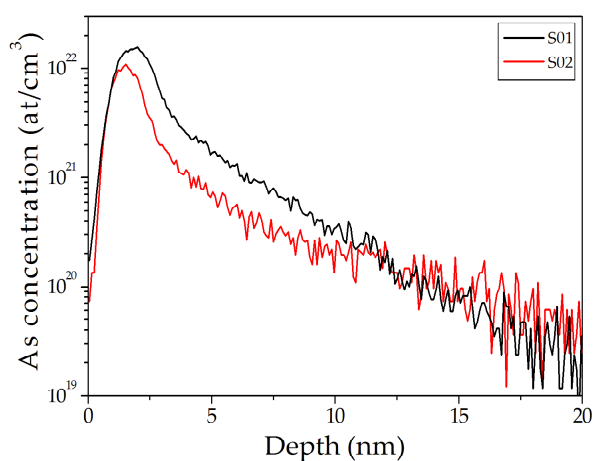


Figure 96 : SIMS results for samples implanted at room temperature (25°C).

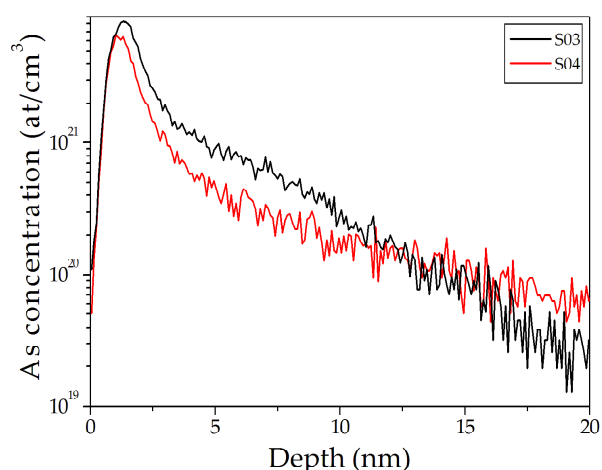


Figure 97 : SIMS results for samples implanted at 500°C).

Sample	Nominal fluence (at/cm ²)	SIMS determined fluence (at/cm ²)
1	1.0×10^{15}	3.7×10^{15}
2	1.0×10^{15}	2.2×10^{15}
3	1.0×10^{15}	1.9×10^{15}
4	1.0×10^{15}	1.3×10^{15}

Table 8 : Comparison between the nominal fluence and the SIMS determined fluence.

We obtained large differences (around four times more) between the nominal fluence and the calculated fluence by SIMS. As plasma ion immersion implantation (PIII) processes are still not as reliable as standard beamline implantation, we were not able to fully explain those differences. Indeed, the hypothesis that the fluence was not reproducible in a PIII experiment could not be

ruled out. Therefore, GIXRF measurements on the same samples have been performed in order to check the validity of these SIMS measurements.

4.1.2.4. Grazing Incidence X-ray Fluorescence (GIXRF)

The GIXRF measurement campaign was performed at the Atominstitut (in Vienna, Austria) on a homemade system with a 3 kW Mo anode tube and a multilayer monochromator (Atomika 8010W) to select the Mo- $K\alpha$ line (17.48 keV). The sample is placed on a rotating sample holder in a vacuum chamber [16]. A tantalum (Ta) 50 μm slit is placed after the multilayer and the fluorescence emitted is detected by a Vortex SDD with a 50 mm^2 active area placed at an angle of detection $\varphi_d = 90^\circ$ (Figure 98 and Figure 99). Fluorescence spectra were acquired from $\theta = 0$ to 0.7° with an angular step of 0.003° for a total count time of approximately 7 hours.

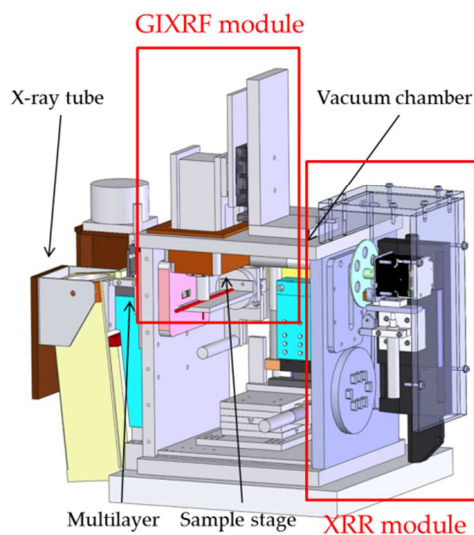


Figure 98: Schematic representation of the homemade GIXRF experimental setup [16].

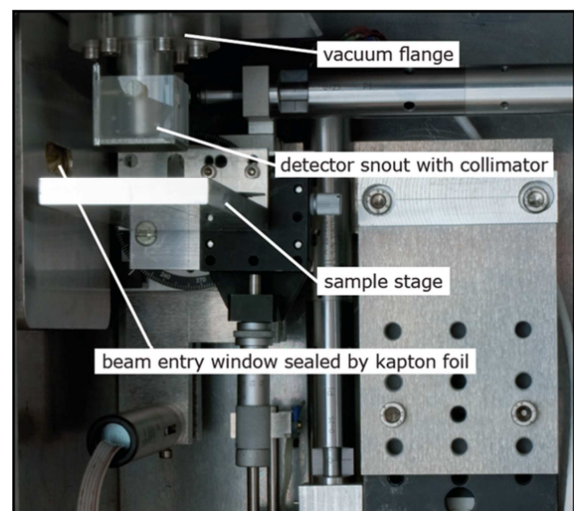


Figure 99: Detailed view of the GIXRF module of the homemade experimental setup [16].

As shown in Figure 100, this excitation energy is optimal as all the K fluorescence lines of interest (*i.e.* Si- $K\alpha$, As- $K\alpha$) are not overlapping. Moreover, as the signal to noise ratio was high, the extraction of the fluorescence intensities has been carried out by directly integrating the fluorescence counts in a region of interest (ROI).

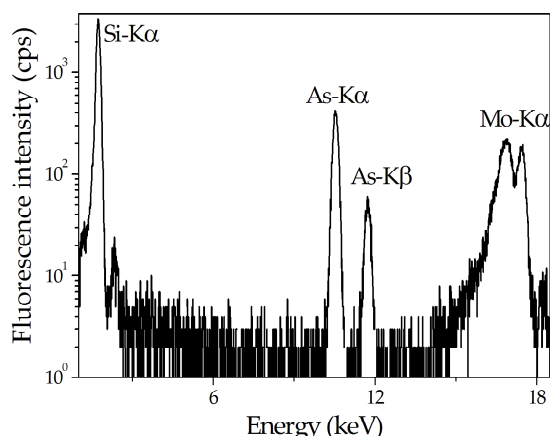


Figure 100 : Fluorescence intensity extraction from a measurement at $\theta = 0.7^\circ$ with a Mo-tube.

This first GIXRF measurement campaign aims at quantifying the total dose of implanted dopants. As explained in Section 3.5.1, in measurements performed on a setup where all the parameters are not known the use of the Fundamental Parameters (FP) method for the elemental quantification is not adapted. A new approach has to be considered.

The new quantification method we adopted is straightforward and is based on standard ED-XRF/WD-XRF experiments. Indeed, as we are working with thin layers, we assumed that at angles of incidence at least three times larger than the critical angle of refraction, the primary X-ray radiation would penetrate and excite completely the sample. In this case, the total number of fluorescence counts of the element would give us information about the total dose of that particular element in the sample. This method has already been tested on simple samples. GIXRF have been performed on multiple samples with various Ti thickness (from 2 to 20 nm) deposited on Si substrate with a standard Cu-tube (Figure 101). A linear relationship between the Ti-K α fluorescence counts at angles larger than the critical angle and the Ti thickness has been confirmed (Figure 102).

Therefore, to quantify the total dose of As dopants implanted, we decided to perform a preliminary GIXRF measurement of a reference sample: a As beamline implant with a nominal fluence of 0.8×10^{15} already characterized by multiple techniques such as SIMS and RBS.

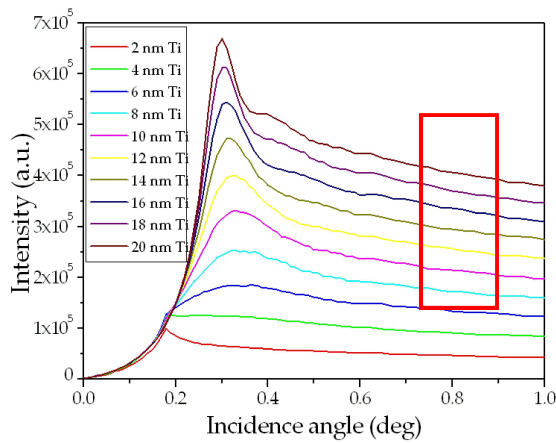


Figure 101 : Ti-K α GIXRF signals of samples with various Ti thickness irradiated with a Cu-K α radiation.

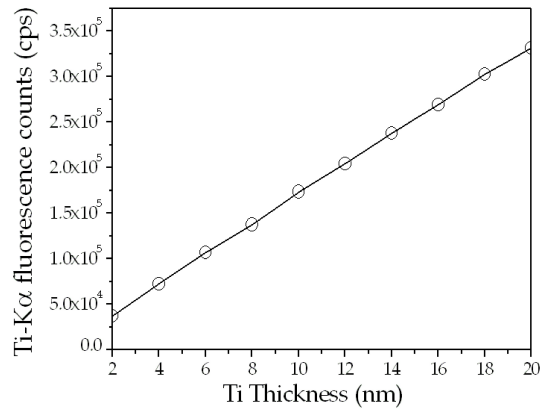


Figure 102 : Linear relation between the expected thickness of Titanium deposited and the total fluorescence counts at angles larger than the critical angle of refraction (in this case 1°).

The comparison of the As-K α fluorescence counts (Figure 103) at 0.7° (*i.e.* larger than the critical angle $\theta_c = 0.12^\circ$) allowed us to determine via GIXRF new values of fluence reported in Table 9. One can note that the Si-K α fluorescence counts at high incidence angles are identical for all four samples (Figure 104). Therefore, this confirms that the causes of the differences in the As-K α fluorescence intensities are not instrumental effects (*i.e.* modification of the intensity of the incident beam, difference in the optics paths, etc) but rather variations of the total dose implanted.

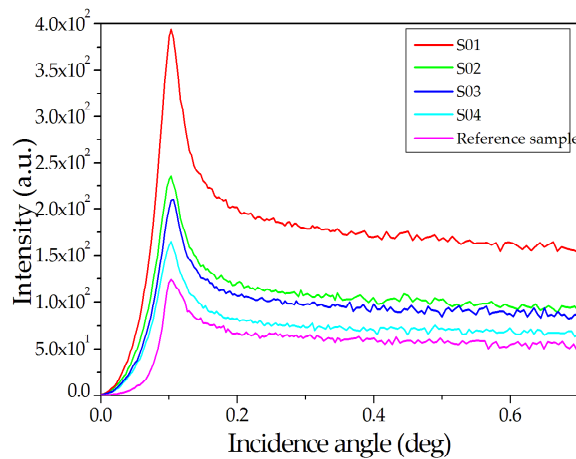


Figure 103 : As-K α GIXRF signals of the implanted samples irradiated with a Mo-K α radiation. The reference sample is a As beamline implant with a nominal fluence of 0.8×10^{15} .

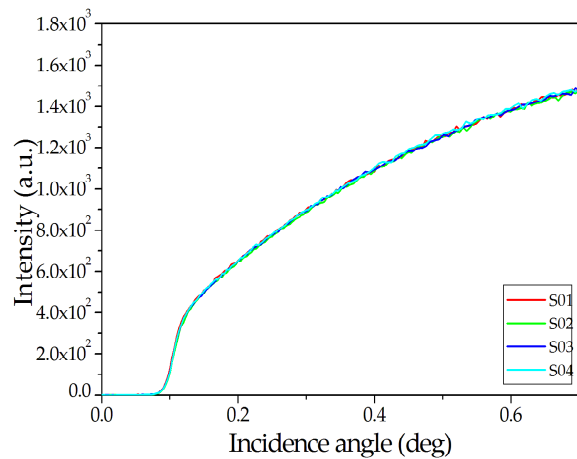


Figure 104 : Si-K α GIXRF signals of the implanted samples irradiated with a Mo-K α radiation.

Sample	Nominal fluence (at/cm ²)	SIMS determined fluence (at/cm ²)	GIXRF determined fluence (at/cm ²)
1	1.0×10^{15}	3.7×10^{15}	2.1×10^{15}
2	1.0×10^{15}	2.2×10^{15}	1.3×10^{15}
3	1.0×10^{15}	1.9×10^{15}	1.2×10^{15}
4	1.0×10^{15}	1.3×10^{15}	1.0×10^{15}

Table 9 : Comparison between nominal, SIMS determined and GIXRF determined fluence.

Even if they follow the same trend (fluences of the annealed samples are smaller than fluences of the as-deposited samples), the fluence determined by GIXRF are noticeably different and smaller (two times smaller) than the ones determined previously by SIMS. These differences have been explained by performing Transmission Electron Microscopy (TEM) on the implanted samples (Figure 105 and Figure 106). These measurements allowed us to detect the presence of a 13 nm amorphous layer on the samples implanted at room temperature. At 500°C, this amorphous layer disappears after crystallization. Amorphisation upon implantation is a well-known phenomenon due to energy deposition along the incident ion paths. To complete amorphisation, strong microstructural changes are involved such as atomic displacements, vacancy creations, grain boundary density increase, porosity, etc. Such microstructure are strongly metastable and rapid annealing eases the recovering of a more stable state with less defects (*i.e.* larger crystallinity). In this case, one can notice that a rapid temperature spike seems quite enough to recover the polycrystalline structure and helps both GIXRF and SIMS to tend to the nominal implanted dose. However, we can conclude that a full annealing at 500°C helps much in the determination of the value of the fluence. Also, GIXRF appears generally less sensitive to microstructural changes compared to SIMS.

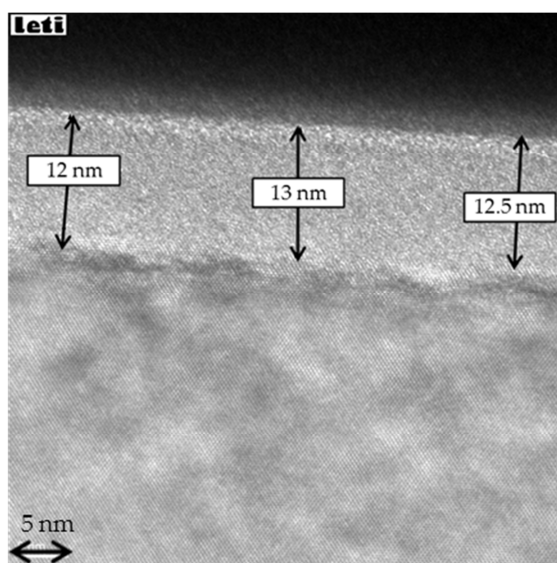


Figure 105 : TEM analysis of samples implanted at room temperature (25°C). The presence of a 13 nm amorphous layer can be noted.

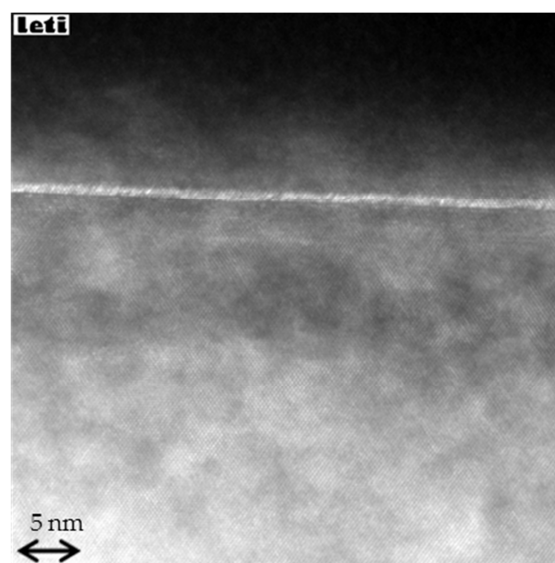


Figure 106 : TEM analysis of samples implanted at 500°C.

Therefore, we concluded that the large disparities between the fluence determined by SIMS and the nominal fluence were due to the creation of a thin amorphous layer. The SIMS experimental conditions may have not been completely adapted for the study of Ultra-Thin Junctions (USJ) and uncertainties about the depth position and the total dose implanted have risen. Moreover, we also determined that GIXRF was an alternative technique for the determination of the fluence of such samples. Additional SIMS experiments with adapted measurements conditions for USJ were necessary to perform the complete characterization of the samples.

4.1.3. Second experiments and analysis

4.1.3.1. SIMS

New SIMS measurements have thus been performed with more adapted experimental conditions in order to overcome the depth position and total dose uncertainties.

SIMS profiles were acquired using a Cs⁺ primary ion beam at 0.34 keV impact energy (compared to 1 keV for the previous measurements). Primary beam intensity and rastered area were set in order to have adequate sputtering rate, point density and secondary ions intensity. Therefore, the sputtering rate was also considerably lowered to 0.027 nm/s (compared to 0.3 nm/s) allowing us to obtain a depth resolution of 0.18 nm. Negative secondary ions were collected from a circular area of 33 μm diameter centered in the 300x300 μm^2 rastered area. ¹⁸O⁻, ³⁰Si⁻ and ⁷⁵As⁻ were the monitored ion species. Mass resolution was set to prevent mass interferences between ⁷⁵As⁻ and several combinations of Si-O ions. Quantification was carried out as described in Demenev *et al.* work [17]. Quantification problematics have been solved by the introduction of RSF obtained after characterized shallow implants of As in either Si or SiO₂.

Figure 107 and Figure 108 show the As profiles measured on samples implanted at 25°C and 500°C respectively. Table 10 shows the calculated fluence for the different samples compared to the nominal fluence. Similarly as what has been observed previously, the measured As fluence on samples implanted at 25°C are larger than the ones measured on samples implanted at 500°C. However, these new determined fluences are closer to the nominal values. Moreover, The annealing induced diffusion can also be noted. Indeed, there is a strong modification of the concentration depth profiles when the samples are subjected to a temperature spike as this latter strongly favors homogenization.

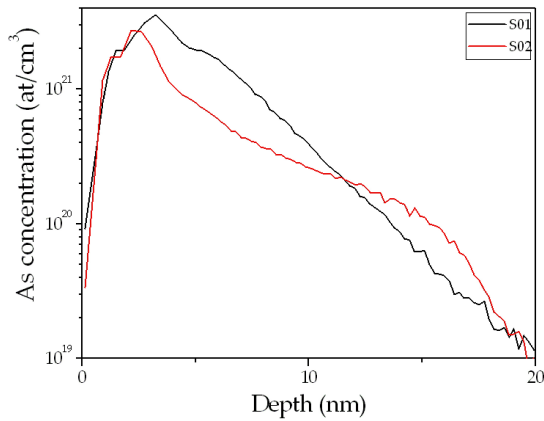


Figure 107 : SIMS-As concentration depth profiles for samples implanted at room temperature (25°C) performed at FBK.

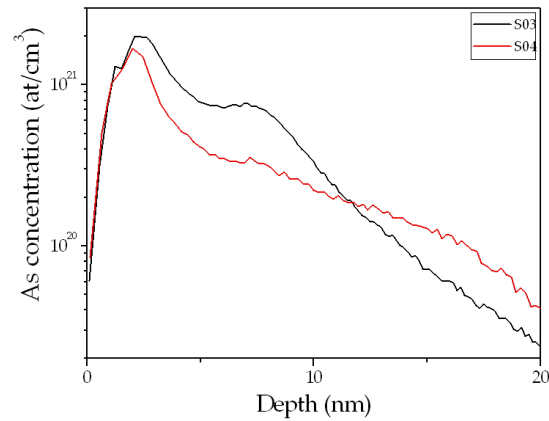


Figure 108 : SIMS-As concentration depth profiles for samples implanted at 500°C performed at FBK.

Sample	Nominal fluence (at/cm ²)	SIMS determined fluence (at:cm ²)
1	1.0×10^{15}	1.7×10^{15}
2	1.0×10^{15}	1.1×10^{15}
3	1.0×10^{15}	1.0×10^{15}
4	1.0×10^{15}	0.73×10^{15}

Table 10 : Comparison between nominal and SIMS determined fluence.

Performed with adapted experimental conditions, SIMS is a powerful technique for the in-depth characterization of implanted samples and precise information about the profile of dopants and the total dose implanted can thus be obtained. Combined X-ray reflectivity (XRR) and grazing incidence X-ray fluorescence (GIXRF) measurements on the four same samples have thus been performed. The results will be compared to the SIMS measurements in order to determine if combining XRR and GIXRF information can be considered as a promising depth-profiling characterization technique.

4.1.3.2. XRR and GIXRF analysis

Along with the fluorescence measurements, the specular reflectivity signals have been recorded. An Amptek SDD was used to measure the reflected beam and was mounted in the experimental setup described in Section 4.1.2. The combined reflectivity and fluorescence spectra have been acquired from $\theta = 0$ to 1.0° with a step of 0.03° for a total count time of approximately 7h.

The As profile has been modeled following a specific methodology. This approach uses no a priori knowledge of the implanted sample but nevertheless requires the measurement of a standard sample. First, the measurement and the fitting of this reference sample will allow us to

obtain the information of the total dose of implanted dopants. The software will record the ratio k of total fluorescence counts versus the nominal dopants dose ($k = C_r/I_r$ with c_i the concentration of element of reference R and I_r the fluorescence intensity at large angle of incidence for the reference element). This calibration k will thus be used to accurately quantify the other samples via

$$C_i = \frac{C_r I_i}{I_r} = k I_i$$

with C_i the concentration of element of interest i and I_i the fluorescence count of the element i at large angle of incidence (three times larger than the critical angle).

This preliminary measurement using a reference sample is also necessary for the determination of the geometrical function. Indeed, as the metrology of the homemade equipment cannot be made completely (as explained in Chapter III), we have decided to use the simplified method to deduce the geometrical parameters. These instrumental parameters have then been fixed during the simulations of the other implanted samples.

The standard chosen is a As beamline implant with a nominal dose of 0.8×10^{15} at/cm³. XRR and GIXRF data measured with the standard laboratory Mo-tube (open circles) and jGIXA simulations (solid lines) for this standard sample are shown in Figure 109 and Figure 110 respectively.

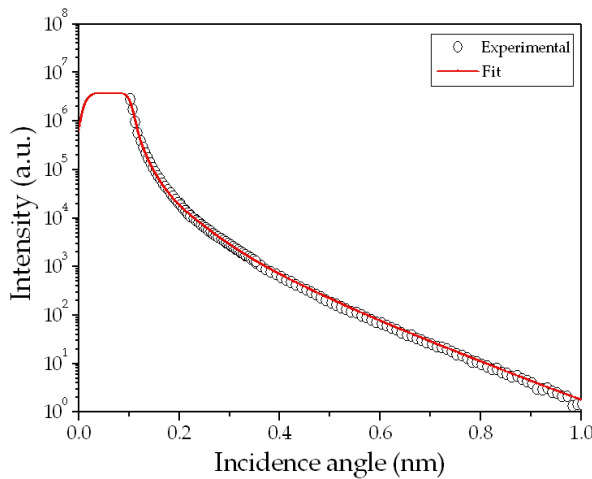


Figure 109: XRR measurements at 17480 eV (open circles) and fit (solid lines) of the reference sample by jGIXA.

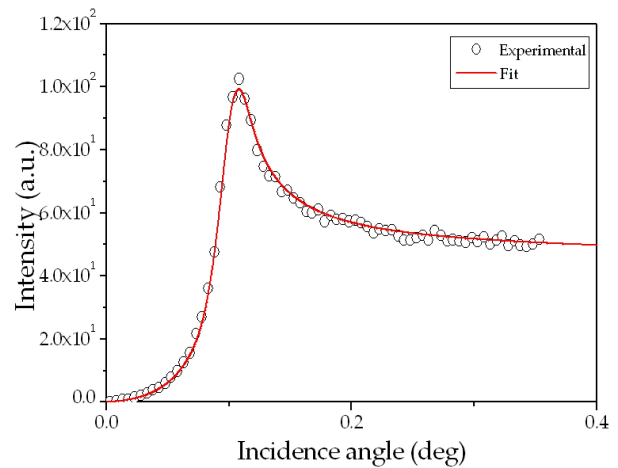


Figure 110: As-K α GIXRF measurements at 17480 eV (open circles) and fit (solid lines) of the reference sample by jGIXA.

In the literature, as ion implanted depth profiles are basically modified Gaussian distributions, or can be described in such terms, the Pearson IV distribution algorithm is used generally to describe ion implanted depth distributions [15]. Indeed, the Pearson algorithms describe generally a statistical distribution in terms of four central moments, μ the mean, σ the

standard deviation, *skew* the skewness and *kurt* the kurtosis, based on a modified or skewed Gaussian distribution. In a Pearson type IV function, the symmetry and the form of a distribution are determined by varying degrees of skewness and kurtosis and for a purely Gaussian distribution $skew = 0$ and $kurt = 3$. As the Pearson distribution is ideally suited to reproduce asymmetric distributions with extensive tails, the modelling of the GIXRF As depth profile have been performed with this distribution. The four central moments have been refined during the simulations as well as the sample parameters (*i.e.* thickness, densities and roughness).

The main advantages of using a mathematical distribution to model the profile of dopants is that only four distinct parameters are required to completely describe the profile. Moreover, thanks to this method, the fitting time is not strongly correlated with the depth resolution and a 0.3-0.5 nm resolution is possible. Indeed, the model construction is fairly straightforward and does not require the user to create a defined number of layers. However, for time consumption related problems, we have limited ourselves to the study of a 10 nm thick implantation with a depth resolution of 0.3 nm. Finally, in this study, the algorithm used for the minimization was the differential evolution (DE) algorithm. A more complete description of this algorithm will be done in Section 4.2.2.

4.1.4. Results and discussion

Data measured with the standard laboratory Mo-tube (open circles) and jGIXA simulations (solid lines) for the implanted sample 1 are shown in Figure 111 and Figure 112 respectively. For both samples, the agreement between the experimental and simulated points is very good.

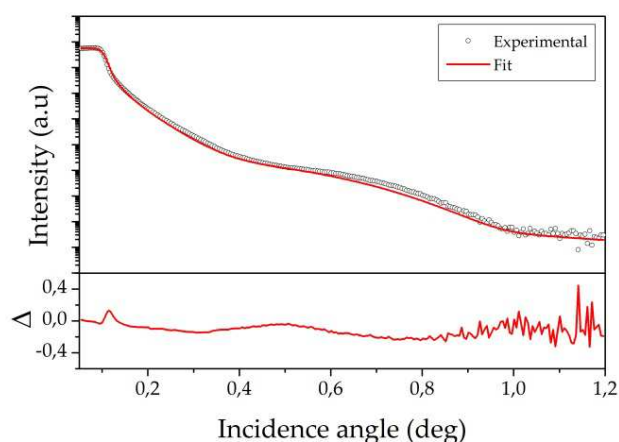


Figure 111 : XRR measurements at 17480 eV (open circles) and jGIXA fit (solid lines) of the implanted sample 1.

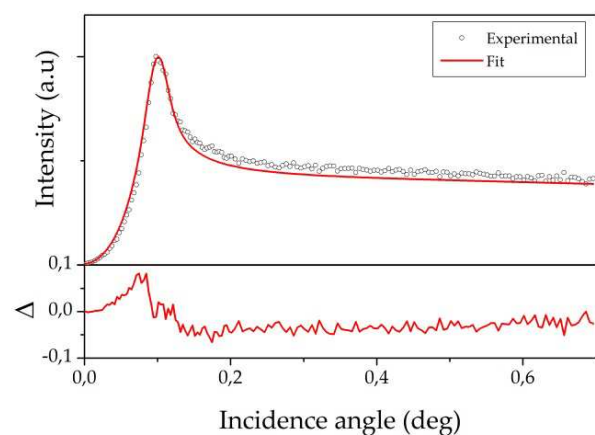


Figure 112 : As-K α GIXRF measurements at 17480 eV (open circles) and jGIXA fit (solid lines) of the implanted sample 1.

Similarly, data measured with the standard laboratory Mo-tube (open circles) and jGIXA simulations (solid lines) for the implanted sample 2 are shown in Figure 113 and Figure 114 respectively.

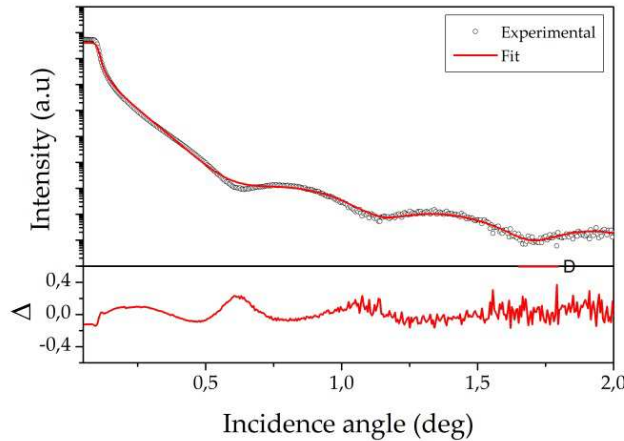


Figure 113 : XRR measurements at 17480 eV (open circles) and jGIXA fit (solid lines) of the implanted sample 2.

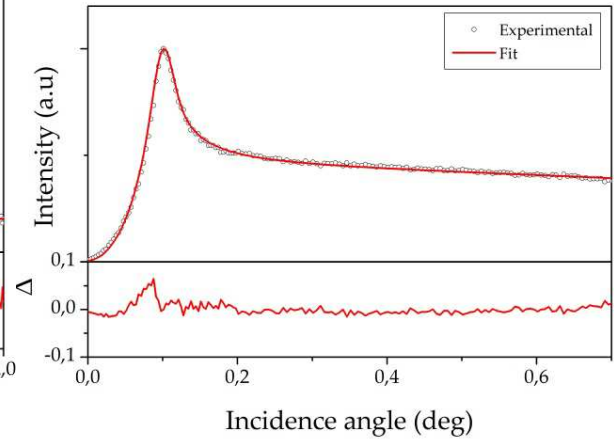


Figure 114 : As-K α GIXRF measurements at 17480 eV (open circles) and jGIXA fit (solid lines) of the implanted sample 2.

By refinement of parameters, the modelling of the depth distribution of As in the Si layer using a Pearson distribution has returned results that can be compared with SIMS (Figure 115 and Figure 116). The noticeable differences (*i.e.* the shift in the position for the annealed sample between GIXRF determined profiles and SIMS determined profiles) highlight the depth-profiling problematics and difficulties linked with GIXRF. These limitations and first solutions to these problems will be largely discussed in Section 4.3.

The values obtained for the fitted dose are reported in Table 11 and the results between the two characterization techniques concur.

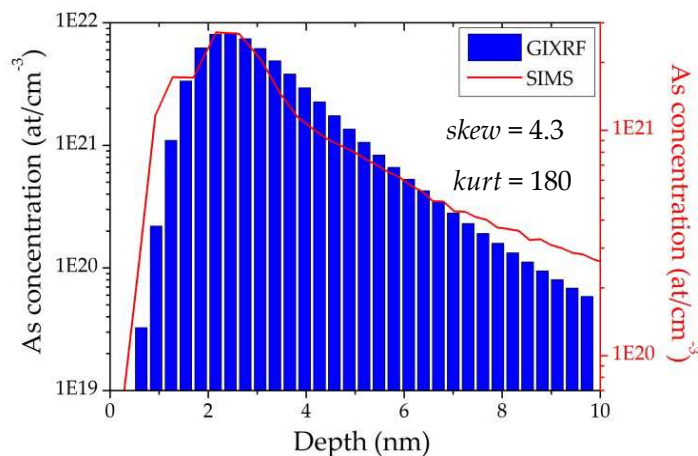


Figure 115 : Comparison of the As concentration depth-profiles obtained by GIXRF and by SIMS for the sample 1.

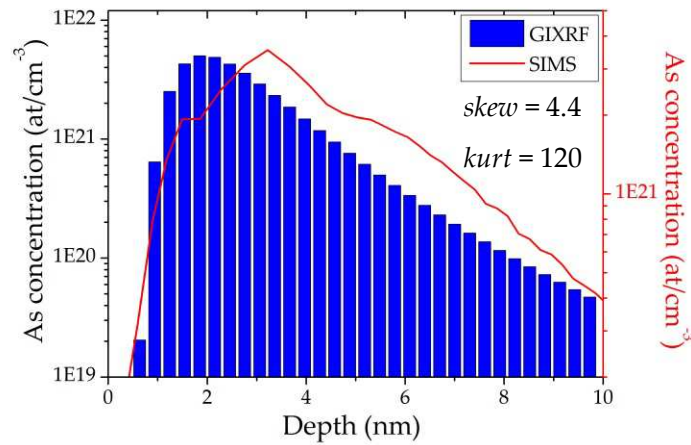


Figure 116 : Comparison of the As concentration depth-profiles obtained by GIXRF and by SIMS for the sample 2.

Sample	Nominal fluence (at/cm ²)	SIMS determined fluence (at/cm ²)	GIXRF determined fluence (at/cm ²)
1	1.0×10^{15}	1.7×10^{15}	1.9×10^{15}
2	1.0×10^{15}	1.1×10^{15}	1.3×10^{15}
3	1.0×10^{15}	1.0×10^{15}	1.2×10^{15}
4	1.0×10^{15}	0.73×10^{15}	0.9×10^{15}

Table 11 : Comparison between the nominal fluence, the SIMS determined fluence and the GIXRF determined fluence.

In conclusion, GIXRF measurements performed on As implants in Si substrates returned information about the total dose implanted into the sample as well as the depth profile of dopants. These results have been obtained on standard laboratory equipment. As synchrotron radiation is not required, combined XRR and GIXRF analysis appears as a promising alternative technique for the characterization of USJ. Indeed, the final values of the fluence determined by GIXRF were in good agreement with the one obtained with adapted SIMS measurements. From the properties point of view, the fact that the As distribution is homogenized throughout the thickness implies that the electronic properties will do so.

Some software development and additional acquisition will be necessary in order to determine accurately the doping profile.

4.2. Study of annealing induced diffusion in $\text{In}_2\text{O}_3/\text{Ag}/\text{In}_2\text{O}_3$ structures

A combination of X-ray reflectivity (XRR) and grazing incidence X-ray fluorescence (GIXRF) measurements have been performed on $\text{In}_2\text{O}_3/\text{Ag}/\text{In}_2\text{O}_3$ structures. This work has been carried out with the idea that the combined XRR and GIXRF analysis would provide more detailed information about the layer structure and its possible modifications due to a thermal annealing than the sum of the individual techniques.

4.2.1. Case of study

Transparent and conductive oxide (TCO) layers are essential components in several emerging photosensitive electronic or optoelectronic technologies. Metal-oxides such as SnO_2 , In_2O_3 or ZnO have widely been used acting as transparent electrical contacts or electrodes in flat panel displays, touch screens and thin film solar cells [18], [19]. However, due to a technological need for large-area photovoltaic devices with improved electrical and optical performances, the development of new structures has been necessary. In this frame, recent investigations have identified TCO/metal/TCO multilayer systems as a good alternative to standard TCO for photovoltaic devices [20], [21].

For photovoltaic applications, a wide range of optic and electrical properties are required. First, the resistivity of the structure needs to be tailored to meet the electrical functionality. For solar cells, the sheet resistance (R_s) must be in the 8-80 Ω/sq range [22]. The other key factor is the optical transmission (T) of the layers as the material must be transparent in the visible spectral range. To achieve the best balance between the optical and electrical properties of the structure, the metal layer has to be a low resistivity material. Therefore, Ag (1.6 $\mu\Omega$ cm at 20°C) is the most common interlayer used for TCO/metal/TCO electrodes [23]. Due to its high transmittance in the visible spectral range, indium oxide (In_2O_3) also referenced as IO is used to embed the conductive layer. The thickness of the layers has also an important effect on the electrical conductivity and optical transmittance. As shown on Figure 117 and by extrapolating from Figure 118, a 6 nm-thick Ag film embedded between two 40 nm-thick IO films gives the best compromise between resistivity and transparency and hence the best performances for photovoltaic applications.

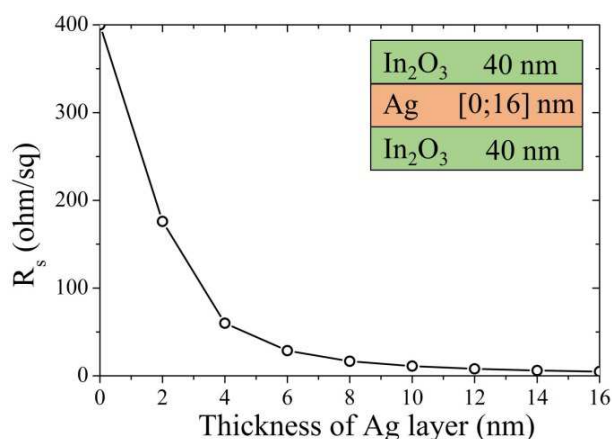


Figure 117 : Sheet resistance for IO/Ag/IO samples for various Ag thicknesses. 0 nm of Ag represents the R_s of a 80 nm In_2O_3 layer. For solar cells, an Ag thickness of 4 nm is required.

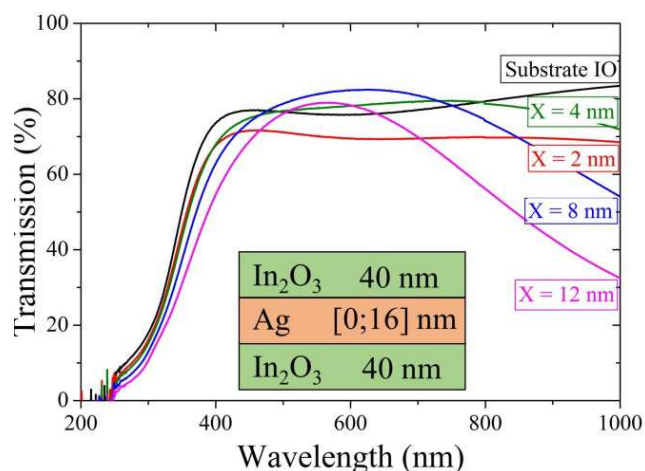


Figure 118 : Optical transmittance for IO/Ag/IO samples for various Ag thicknesses. For photovoltaic applications, an Ag thickness inferior to 8nm is required.

4.2.2. Experiments

4.2.2.1. Sample preparation

The structure of the samples studied in this work consists in a 6 nm Ag layer embedded between two 40 nm In_2O_3 layers deposited on a 500 nm $\text{SiO}_2/\text{Si}(001)$ substrate (Figure 119). Each layer has been deposited via Physical Vapor Deposition (PVD) with a low temperature deposition process.

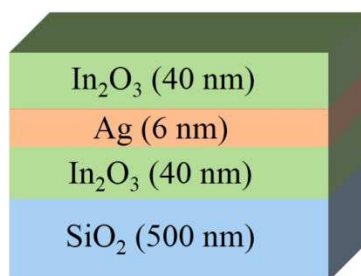


Figure 119 : Layer stack consisting of two 40 nm IO layers and a 6 nm Ag layer. The stack is deposited on a SiO_2 (500 nm)/ $\text{Si}(100)$ substrate.

In order to simulate a realistic technological integration, a thermal budget has been applied to duplicate samples. The annealing has been made in a Tempress furnace system at 200 °C during 1h. To improve the sensitivity at the $\text{In}_2\text{O}_3/\text{Ag}$ interface, the thickness of the top IO layer has been reduced via Chemical Mechanical Polishing (CMP) to a thickness of approximately 15 nm. The same approach was used by Giubertoni et al. to gain sensitivity on buried layers when doing grazing incidence absorption studies [12]. One can note that the CMP

will also greatly reduce the surface roughness of the concerned samples. The list of analyzed samples is reported in Table 12.

Sample	Top layer thickness	Annealing
A	40 nm	
B	40 nm	200°C for 1 h
C	15 nm	
D	15 nm	200°C for 1 h

Table 12 : Description of analyzed samples.

4.2.2.2. Data acquisition

A preliminary measurement campaign was performed at CEA-Leti (Grenoble, France) on a D8-Fabline (Bruker) production tool. Initially designed for standard XRR and energy dispersive XRF (ED-XRF), some improvements have been developed on the experimental setup in order to be able to perform GIXRF. The D8-Fabline is equipped with a Cu anode tube and a third generation Göbel mirror to monochromatize the primary X-ray radiation. The fluorescence emitted by the irradiated sample is collected by a SDD (X-Flash) which offers high count rate capability and an energy resolution better than 129 eV at Mn-K α .

At this excitation energy (*i.e.* 8050 eV), working under vacuum is necessary in order to get rid of Ar-K α lines (2957 eV) and avoid overlaps with the fluorescence lines of interest. As the measurement chamber cannot be brought to vacuum, a continuous He flux has been applied above the sample. Measured fluorescence intensities of Ag-L α and In-L α lines for sample A are presented in Figure 120 and Figure 121 respectively.

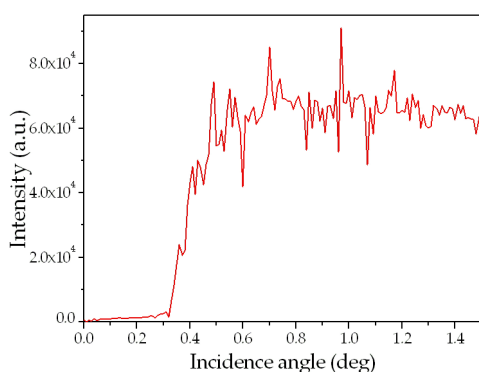


Figure 120 : Ag-L α GIXRF D8-Fabline measurements acquired at 8050 eV (Cu anode tube).

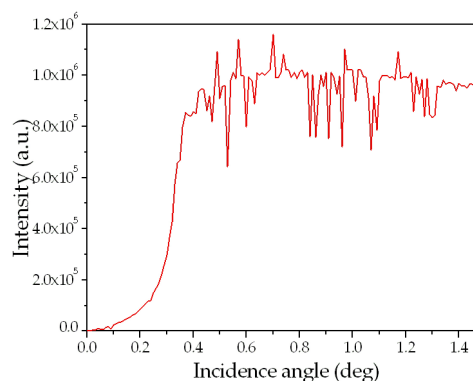


Figure 121 : In-L α GIXRF D8-Fabline measurements acquired at 8050 eV (Cu anode tube).

As explained in Chapter II, GIXRF experiments require some specific elements and configurations in order to perform optimal measurements. As seen on these extremely noisy and inaccurate fluorescence profiles, we can conclude that the D8-Fabline setup does not respect some of these conditions and is therefore not adapted to perform GIXRF measurements. Measurement campaigns on experimental setups designed for combined XRR and GIXRF analysis have been necessary.

The measurement campaign was performed at the Atominstitut (in Vienna, Austria) where both XRR and GIXRF measurements have been carried out on the homemade system described in Section 4.1.2 [16]. A 2 kW fine focus Cu anode tube and a multilayer monochromator selecting the Cu- $K\alpha$ line (8047 eV) have been used to perform the XRR and GIXRF acquisitions. An Amptek Silicon Drift Detector (SDD) was used to measure the reflected beam. A zirconium (Zr) filter was inserted in front of this detector at low angles to reduce the primary beam intensity (Figure 122). XRR and GIXRF spectra were acquired from $\theta = 0^\circ$ to 3° with an angular step of 0.05° for a total counting time of approximately 1 hour.

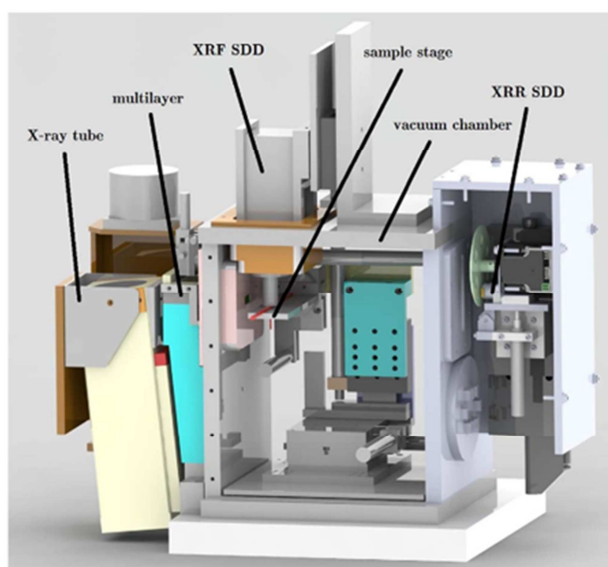


Figure 122: Homemade combined XRR-GIXRF experimental setup (Atominstitut, Vienna, Austria) [16].

As shown in Figure 123, In-L and Ag-L fluorescence lines as well as Si pile-up peak overlap in the 3 keV range. At low incidence angles (typically $< 0.4^\circ$), due to the absorption of the incident beam in the top IO layer, the fluorescence signal of the Ag- $L\alpha$ line is low and completely covered by the In-L fluorescence lines.

In order to overcome signal extraction difficulties due to overlaps and analyze more intense fluorescence K-lines, additional GIXRF measurements have been carried out on the Gilda (BM08) line at ESRF-Grenoble. To improve the sensitivity, the measurements have been realized

at 26400 eV above the Ag-K but below the In-K edge. To avoid sample edge effects during the measurements, the horizontal size of the primary beam was reduced by a 50 μm slit.

A 13-element high purity Ge-Solid state detector (SSD) with a maximum count rate of 80k counts per second was used to measure the fluorescence. Energy dispersive X-ray spectra were acquired from $\theta = 0^\circ$ to 0.6° with an angular step of 0.001° for a total acquisition time of 10 minutes. The energy tunability of the synchrotron source allowed the study of the in-depth Ag- $K\alpha$ line isolated from the indium contributions (Figure 124).

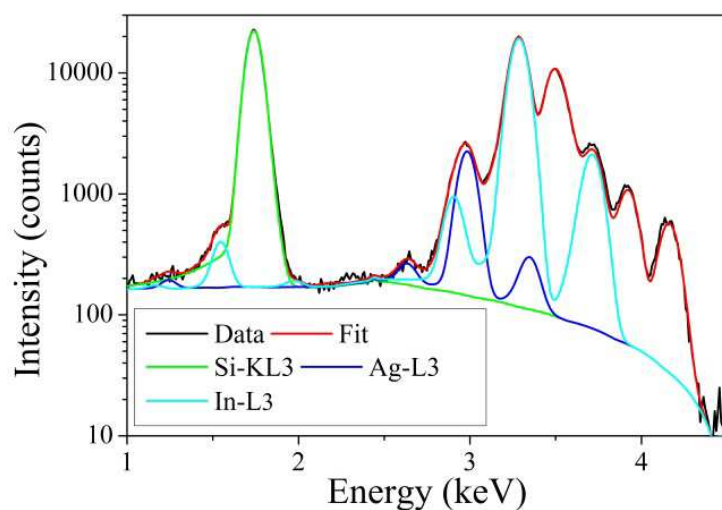


Figure 123 : Fluorescence intensity extraction from a measurement at $\theta = 1.2^\circ$ with a Cu-tube. Due to the correlation of Ag-L3 and In-L3 fluorescence peaks, the use of a third party software like PyMCA [25] is necessary.

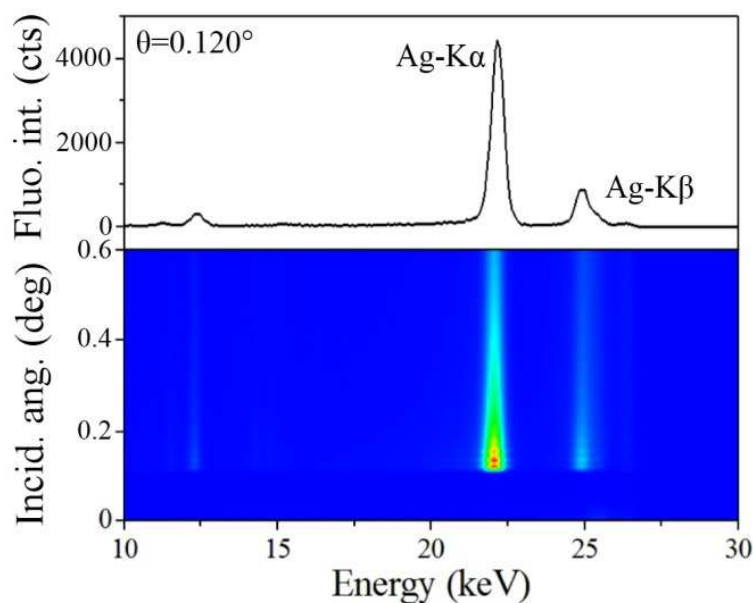


Figure 124 : Fluorescence intensity from a measurement at 26400 eV with a synchrotron radiation at an angle of incidence $\theta = 0.12^\circ$. With this excitation energy, the fluorescence peaks of interest are not overlapping.

4.2.2.3. Data reduction and numerical models

Extraction of fluorescence intensities from data measured with the Cu-tube has been carried out using the software PyMCA [25]. The background has been simulated by the strip background model implemented in the software. For the measurements done at ESRF, as the peaks are not overlapped and the signal to noise ratio is high, the integral of the fluorescence counts in a region of interest (ROI) has been used.

The modeling of reflectivity and fluorescence measurements has been carried out using the jGIXA software [26]. Two approaches have been tested. As GIXRF spectra have been acquired at different excitation energies, the first model consists in combining the fit of XRR and GIXRF spectra acquired at the same excitation energy. On the other hand, the second model aims at combining data acquired at different excitation energies.

As explained fully in Chapter III, the angular profile of GIXRF strongly depends on experimental setup parameters (*i.e.* the divergence of the beam, the width of the beam, the size of the detected area, etc) and a geometrical function has to be defined. As measurements have been performed at a synchrotron facility where the complete metrology of the instrumental chain is not feasible in a short period of time, the Fundamental Parameter (FP) method for GIXRF quantification was not possible. Therefore, the simplified approach has been chosen (*cf.* Section 3.5.1). This simpler method does not require the user to know perfectly the experimental setup parameters but a preliminary measurement of standard samples is required.

The geometrical function has thus been determined by the measurement, on the same experimental setups, of a 50nm Ni layer deposited on a 300nm $\text{SiO}_2/\text{Si}(001)$ substrate. As seen on Figure 125, this well-known reference sample has been used as reference sample for the determination of the geometrical function $G(\theta)$. The deduced geometrical parameters have then been fixed during the simulations of the TCO/metal/TCO samples.

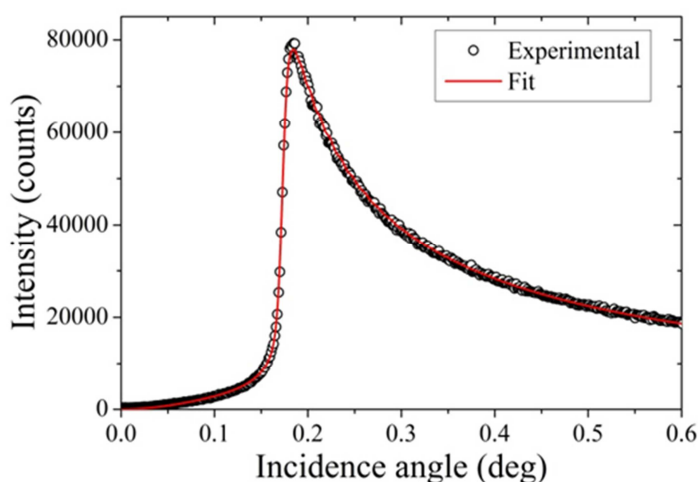


Figure 125 : GIXRF fit on JGIXA of a 50 nm Ni sample measured at 26400 eV at ESRF. Fitting of reference sample allows the determination of geometrical function $G(\theta)$.

Due to existing local minima, global optimization algorithms are required to find the best global minimum. These algorithms reduce the dependency on initial values of the parameters and hence are less relying on a priori knowledge. In jGIXA, several algorithms for the global optimization of the parameters can be used. The fitting of the measured data has been optimized with a differential evolution (DE) algorithm included in the software. DE is a method that optimizes a problem by iteratively trying to improve a candidate solution with regard to a given measure of quality [27]. DE is a parallel direct search method that utilizes a population of parameter vectors for each generation. The initial vector population (called agents) is chosen randomly and should cover the entire parameter space. DE generates new parameter vectors by using simple mathematical formulae to combine the positions of existing agents from the population. If the new position of one of these mutated parameter vectors is an improvement, it is thus accepted and forms part of the population, otherwise the new position is simply discarded. The process is repeated an enough amount of time until a satisfactory solution is discovered. Therefore, in a large time scale, the method grants the minimum solution to be found. However, as the first population is placed randomly in the entire available parameter space, the performances in terms of speed are very poor. For this reason, the selection of proper boundaries using DE algorithms is very important and critical for the data analysis. The use of boundary values for the simulation explains why we do not have standard deviations.

4.2.3. Results and discussion

4.2.3.1. As-deposited samples

Data measured with the standard laboratory Cu-tube (open circles) and jGIXA simulations (solid lines) for the as-deposited samples (Sample A and Sample C) are shown in Figure 126 and Figure 127 respectively. The agreement between the experimental and simulated points is very good.

A first stacking structure (Model 1 in Table 13) resulting from refinement of these data has been obtained. The incorporation of a top indium oxide layer with a low density (LD-In₂O₃) is necessary in order to reproduce all the fine details of the reflectivity curves and improve the refinement agreement (Figure 128).

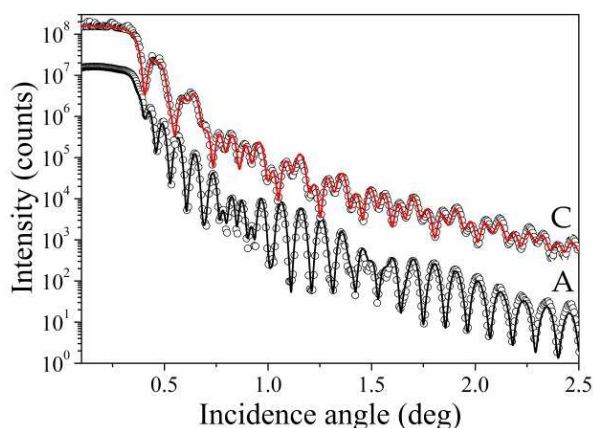


Figure 126 : XRR measurements (open circles) and fits (solid lines) of the as-deposited samples A and C at 8.05 keV.

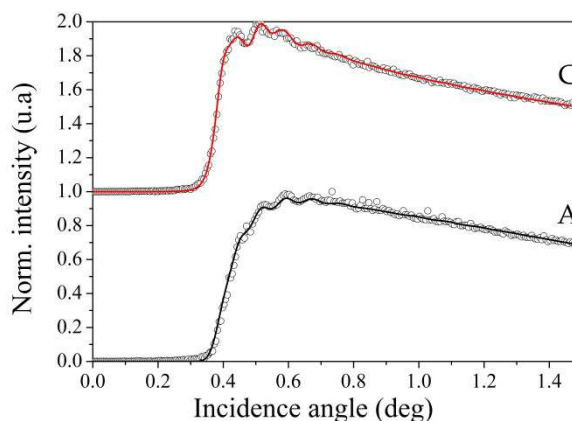


Figure 127 : Ag-L α GIXRF measurements (open circles) and fits (solid lines) of the as-deposited samples A and C at 8.05 keV.

Sample A	Thickness	Density ($\text{g}\cdot\text{cm}^{-3}$)
LD- In_2O_3	1.2 nm	4.04
In_2O_3	40.1 nm	6.91
Ag	6.0 nm	9.83
In_2O_3	40.0 nm	6.95

Sample C	Thickness	Density ($\text{g}\cdot\text{cm}^{-3}$)
LD- In_2O_3	1.4 nm	4.1
In_2O_3	15.0 nm	6.61
Ag	6.0 nm	9.87
In_2O_3	40.0 nm	6.88

Table 13 : Model 1 – Thickness and densities of the as-deposited samples obtained by comparison of jGIXA fitting and experimental results measured with Cu-K α energy.

For both samples, the surface and interfacial roughness ranges from 0.5 to 1.2 nm. The accuracy of XRR for the determination of thickness and roughness is high with uncertainties lower than 5 Å and 1 Å respectively [28]. Thanks to the decoupling of the sample parameters, the determination of the electronic density is reinforced by the use of the XRR and GIXRF curves for a joint fit. This aspect remains sensitive despite weak signal-to-noise ratio and rather smoothed fluorescence fringes.

Compared to the laboratory GIXRF measurements, higher-energy experiments carried out at the Gilda ESRF beam line have both the advantage of non-overlapped fluorescence lines and a much stronger dependence of the fluorescence intensities with the incidence angle. New simulations have been done with this set of data (Figure 129 and Figure 130).

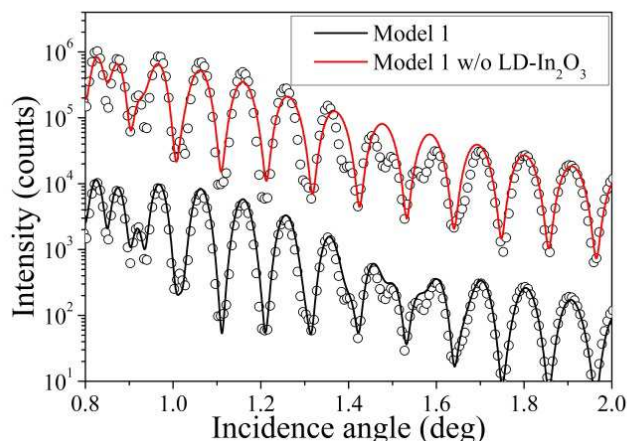


Figure 128 : XRR measurements (open circles) and fits (solid lines) of the as-deposited sample A at 8.05 keV with and without the introduction of the LD-In₂O₃ top layer in the model. This top layer introduction is necessary in order to reproduce the experimental fringes around 1.5°.

By refinement of parameters, an improved model (Model 2 in Table 14) has been obtained by combining the reflectivity measured at Cu-K α energy and the fluorescence measured at the excitation energy of 26.4 keV. The difference curve between calculated and experimental data for the two models compares favorably for model 2, both for XRR and GIXRF experiments via the correction of the densities values. While improving the GIXRF simulations, these density variations (around 5% for each layer) do not have any effects on the reflectivity calculations.

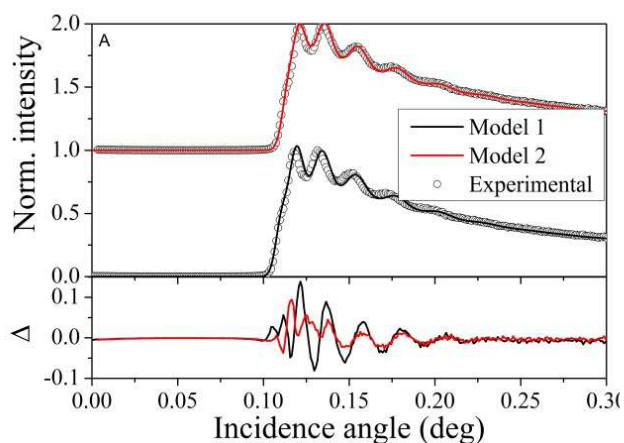


Figure 129 : Ag-K α GIXRF Gilda measurements and fits of Sample A. The difference curve is represented at the bottom of the figure. Model 2 has been obtained by combining sets of data acquired at different excitation energies. It offers smaller differences between experimental and simulated data.

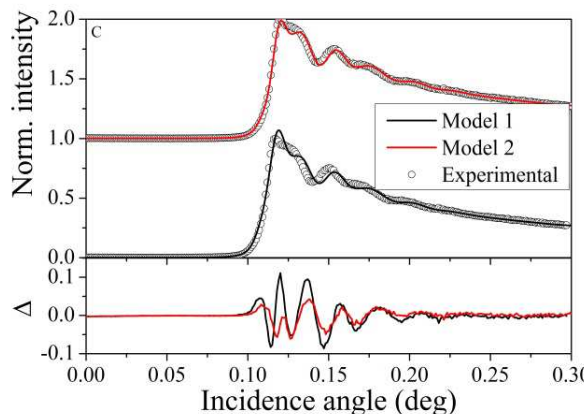


Figure 130 : Ag-K α GIXRF Gilda measurements and fits of Sample C. The difference curve is represented at the bottom of the figure. Model 2 has been obtained by combining sets of data acquired at different excitation energies. It offers smaller differences between experimental and simulated data.

Sample A	Thickness	Density (g.cm^{-3})	Sample C	Thickness	Density (g.cm^{-3})
LD- In_2O_3	0.9 nm	4.44	LD- In_2O_3	1.4 nm	4.31
In_2O_3	40.1 nm	7.28	In_2O_3	15.0 nm	6.95
Ag	6.0 nm	9.80	Ag	6.0 nm	10.40
In_2O_3	40.0 nm	7.10	In_2O_3	40.0 nm	6.99

Table 14 : Model 2 – Thickness and densities of the as-deposited samples obtained from correlating JGIXA fits of the experimental data measured at two different energies (respectively 26.4 and 8.05 keV).

The sensitivity of the combined analysis has been greatly improved by using X-ray measurement done at adapted primary energies. The joint fit of standard laboratory XRR and synchrotron based GIXRF has provided more accurate information about the in-depth profile.

4.2.3.2. Annealed samples

After annealing at 200°C , we tested the efficiency of the combined XRR and GIXRF approach to detect temperature induced modifications of the stack. In Figure 131 and Figure 132, the Ag- $\text{K}\alpha$ fluorescence angular intensities for the four samples are presented. Thinning of the top IO layer has improved the sensitivity of GIXRF to interfaces and reveals differences much more illustrated between samples C and D, than between A and B on which only a slight shift of the whole spectra is being visible. Such behavior was also observed on the Ag- $\text{L}\alpha$ GIXRF profiles measured with laboratory instrument. One could interpret this difference in the GIXRF profile as an annealed-induced inter-diffusion between the Ag and the In_2O_3 layers.

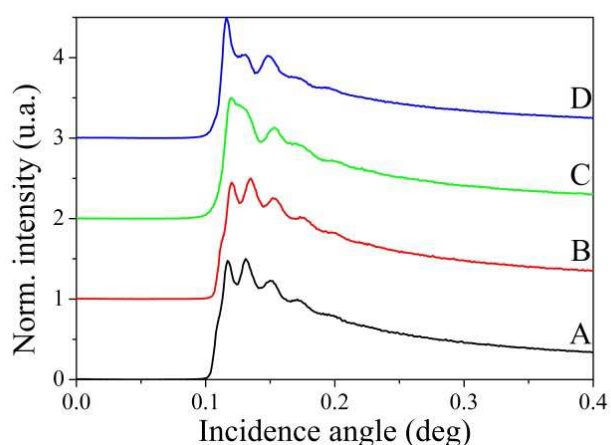


Figure 131 : Ag- $\text{K}\alpha$ GIXRF measurement of the samples at 26400 eV. Differences in the GIXRF profile can be noted between the C (as deposited) and the D (annealed) sample.

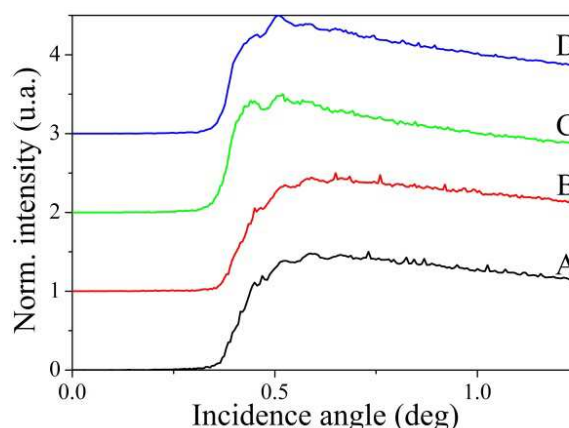


Figure 132 : Ag- $\text{L}\alpha$ GIXRF measurements of the samples at 8050 eV. Differences in the GIXRF profile can be noted between the C (as deposited) and the D (annealed) sample.

GIXRF measurements performed at 26400 eV have been combined with XRR measurements obtained at 8050 eV (Figure 133) and we tested a model for such interdiffusion by modeling this latter with 1 nm thick layers around both Ag/In₂O₃ interfaces.

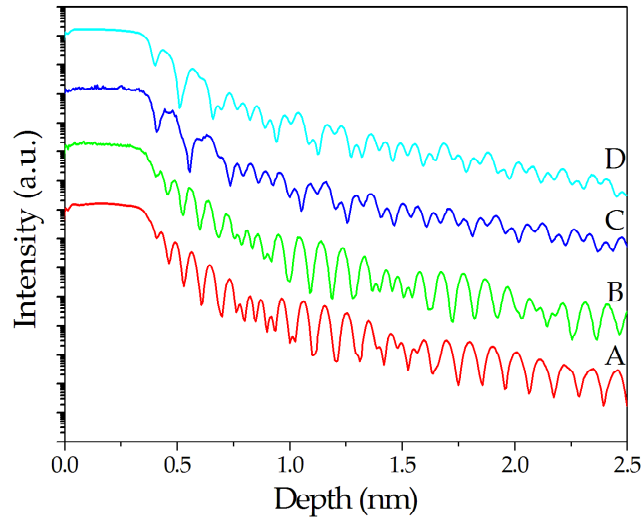


Figure 133 : XRR measurements of the samples at 8050 eV.

The results of the combined fit of the lab based XRR and synchrotron based GIXRF are presented in the Figure 134 and Table 15. The introduction of an intermixing of Ag and IO in the transition layers has been necessary in order to obtain the best fit. Therefore, the simulation highlights the annealing-induced diffusion of the Ag. The surface and interfacial roughness ranges from 4 to 10 Å.

The combination of XRR and GIXRF allows detecting and characterizing a thin diffusion profile at the interface of two layers. Even on non-optimized experimental setup (*i.e.* laboratory Cu-tube), the diffusion induced by thermal annealing is noticeable.

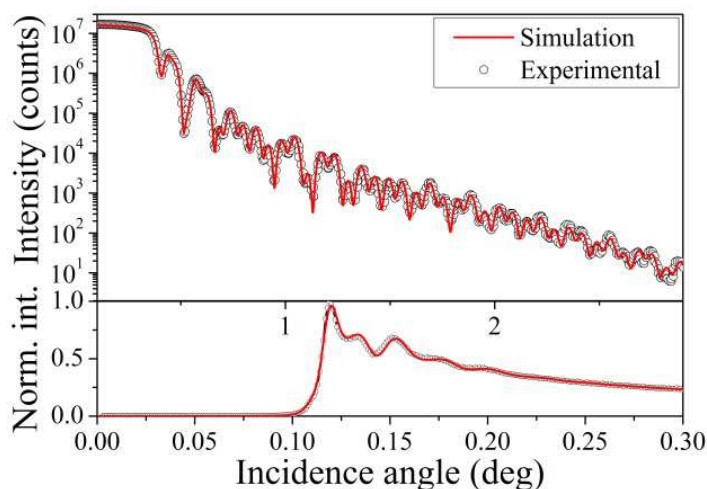


Figure 134 : XRR and GIXRF measurements and fitting of the sample D with reflectivity measured at 8.05 keV and fluorescence at 26.4 keV.

Sample D	Thickness	Density (g.cm^{-3})
LD- In_2O_3	2.0 nm	6.12
In_2O_3	16.3 nm	7.18
$[\text{In}_4\text{O}_6; \text{Ag}]$	1.1 nm	8.36
Ag	5.7 nm	9.90
$[\text{In}_4\text{O}_6; \text{Ag}]$	0.6 nm	7.47
In_2O_3	40.0 nm	7.00

Table 15 : Thickness and densities of the sample D obtained from correlating JGIXA fits of the experimental data measured at two different energies (respectively 26.4 and 8.05 keV).

In conclusion, the combined evaluation of XRR and GIXRF resulted in a non-destructive and precise characterization of the $\text{In}_2\text{O}_3/\text{Ag}/\text{In}_2\text{O}_3$ multilayered structure. It has been shown that the sensitivity of the joint approach can be optimized with the choice of the primary energy. A thin inter diffusion profile induced by annealing has been observed and characterized. Sensitivity to structural changes in the depth of 0.5-1 nm was achieved for measurements performed at a synchrotron facility but also for the ones acquired with the laboratory experimental setup.

The effect of the annealing on material properties such as the crystallographic phase, the size of the crystallites and the residual stress have been observed by X-ray diffraction measurements (XRD). In order to obtain a full characterization of these photovoltaic devices, the combination of XRD, XRR and GIXRF in respect with the models presented in this work is necessary.

4.3. Depth profiling characterization of multilayered structures

4.3.1. Case of study

Non-volatile memory (NVM) technology plays a significant role in the market of electronics products as they can be found in a large number of technologies vastly used in our everyday life such as mobile phone, digital camera, and portal storage devices. Until now, Flash memory has dominated the market of NVM and is integrated in more than 90% of the products. However, with the rapid and non-stopping reduction of the size of microelectronics technology, Flash memory has encountered serious technical challenges. Due to these limitations, various alternatives NVM technologies have been developed such as Magneto resistive Random-Access Memories (MRAM), Phase change RAM (PRAM) and Resistive RAM (ReRAM). In our work, we focused on ReRAM that, compared to the other types of components, has a simple structure and low power consumption with relatively high speed.

A Resistive Random Access Memory (ReRAM) is a simple structure and can be described as a two-terminal passive device based on oxides capable to switch from a High Resistance State (HRS) to a Low Resistance State (LRS) by applying a bias across the device. The ReRAM is a Metal-Insulator-Metal (MIM) multilayered structure (Figure 135). The switching behavior and the switching mechanism are still object of intense research and developments. Therefore, new characterization methods have to be developed in order to fully describe such multilayered structures.

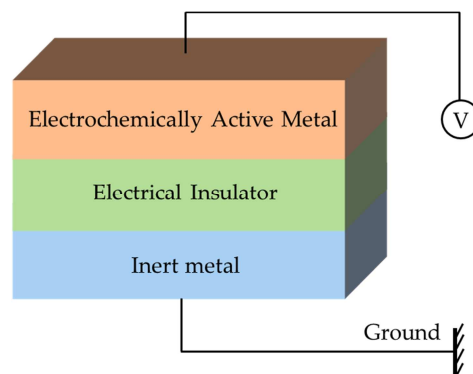


Figure 135 : Metal-Insulator-Metal (MIM) structure of a Resistive RAM (ReRAM) cell. The top electrode is biased and the bottom electrode is grounded during electrical testing.

Binary oxides (Ta_2O_5 , HfO_x , AlO_3 , SiO_x , etc) are generally used in ReRAM technologies. Tantalum oxide (TaO_x) is one of the most promising oxide for ReRAM thanks to its low cost and various material and electrical properties [29, 31]. On the other hand, conductive metals used for the electrodes are generally ruthenium (Ru), iridium (Ir), palladium (Pd), platinum (Pt), titanium

(Ti) and nickel (Ni) and have been used for a large number of ReRAM applications (Figure 136 and Figure 137).

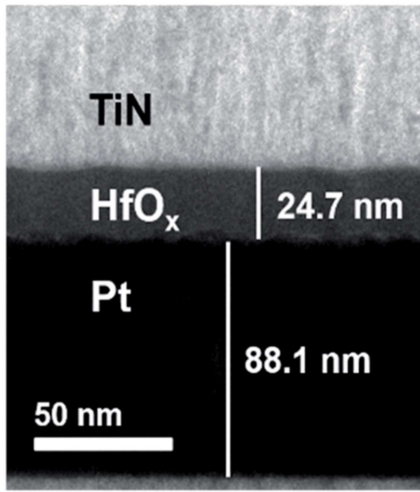


Figure 136 : Cross-sectional TEM image of the fabricated TiN/HfO_x/Pt ReRAM device [32].

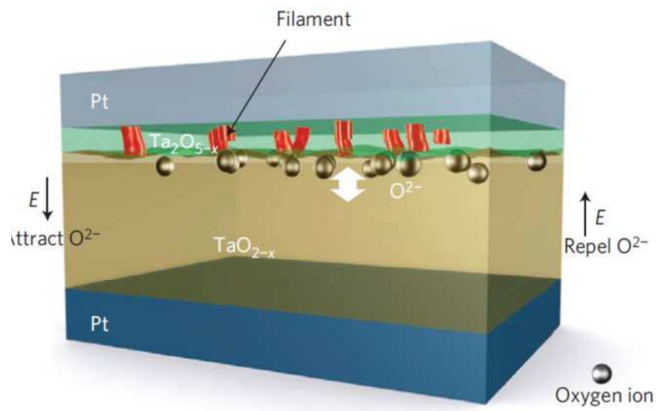


Figure 137 : Schematic representation of the TaO_x device consisting of a thin Ta₂O_{5-x} insulating layer and a TaO_{2-x} base layer. The movement of internal oxygen ions or vacancies is used to model the switching [33].

In the recent years, availability of Ru, Pd, Ir and Pt have diminished a lot. Moreover, as these metals are expensive, ReRAM built around Cobalt (Co), Copper (Cu) and Ni layers have recently been developed. Therefore, with these considerations, in this work, we will only consider a Ta₂O₅/NiCo/Si structure.

4.3.2. Experimental

4.3.2.1. Sample preparation

The structure of the samples studied consists in a 15 nm Ta₂O₅ layer deposited on a 10 nm NiCo layer on top of a Si(011) substrate. The NiCo layer has been deposited via Physical Vapor Deposition (PVD) process. On the other hand, the Ta₂O₅ layer has been deposited by Plasma Enhanced Atomic Layer Deposition (PEALD).

Standard ALD is a thin film deposition technique capable of producing thin films of a variety of materials. It has been introduced in 1974 and has emerged as a powerful tool for many industrial and research applications [34]. An ALD process consists of sequential alternating pulses of chemical gases (called precursors) that will react with the sample surface leaving no more than one monolayer at the surface. Before the next layer is deposited, the reaction chamber is purged to remove any unreacted or passivating atoms in various ways (chemical reactions with gases, thermal spikes, etc). This process is then repeated an enough number of time until the desired film thickness is reached. The particularity of PEALD is to purge the deposition chamber

by using a plasma. The plasma allows breaking the chemical bonds between the deposited and the passivating atoms even at low temperatures. By reducing the deposition thermal budget, PEALD allows reducing diffusion and other annealing-induced effects.

In this work, the precursor used for the deposition of Ta_2O_5 is the TertiaryButylimido,Tris(DiEthylamino)Tantalum (TBTDET) (Figure 138). However, two plasma conditions have been tested and their effects on the multilayer structure have been compared.

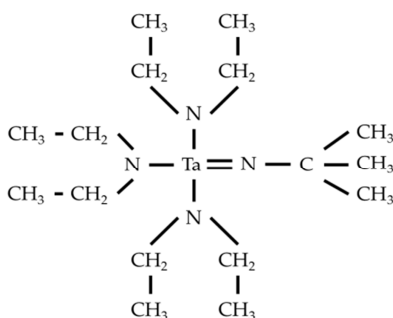


Figure 138 : Chemical representation of the TertiaryButylimido,Tris(DiEthylamino)Tantalum (TBTDET).

The first PEALD experimental condition we considered consists in successive cycling of deposition of TBTDET precursor followed by the use of a O^* plasma (Figure 139). It is known that the plasma O^* has a strong impact on the sample and can often lead to a large oxidation of the substrate or the layer on which the Ta layer is deposited.

Therefore, other experimental conditions have been considered. This new PEALD process consists in adding H^* in the plasma prior to O^* , as this former is supposed to result in a de-oxidation at each deposition cycle (Figure 140).

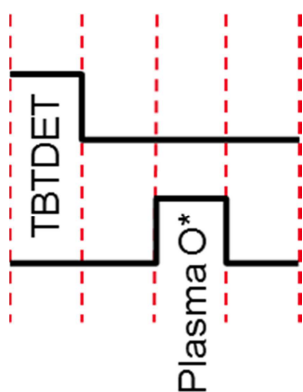


Figure 139 : First PEALD experimental conditions. The precursor used is TBTDET and a O^* plasma is used to remove the passivating atoms.

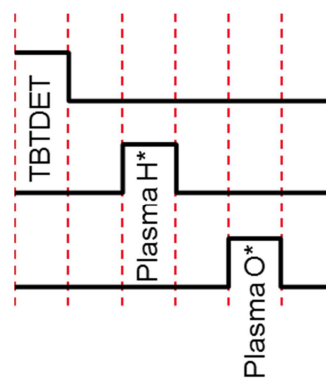


Figure 140 : Second PEALD experimental conditions. The precursor used is TBTDET. A H^* and then a O^* plasma are used to remove the passivating atoms with oxidizing the bottom layer.

4.3.2.2. Data analysis

The combined XRR and GIXRF measurements have been performed on the beamline “X-ray Fluorescence” at Elettra synchrotron facility. The optical path is composed of a monochromator, a toroidal refocusing mirror, a higher order suppressor and exit slits that allow obtaining a $250 \times 50 \mu\text{m}^2$ monochromatic X-ray beam. A solid state detector (SSD) is placed at 90° above a rotating sample in a ultra-high vacuum chamber. In order to measure the fluorescence signals of all the elements of interest (Ni, Co and Ta), the measurements were performed at 10200 eV. Energy dispersive X-ray spectra were acquired from $\theta = 0$ to 1.5° with an angular step of 0.005° for a total count time of approximately 4 hours.

Due to overlaps between the fluorescence lines of interest, extraction of fluorescence intensities has been done using the software PyMCA [25]. As the signal to noise ratio was high, the background has been supposed constant (Figure 141).

Similarly that what has been done previously, the modeling of the XRR and GIXRF measurements has been carried out using the jGIXA software. The simplified approach has been chosen (*cf.* Section 3.5.1) and the geometrical function has been determined by the measurement of a reference sample. As seen on Figure 142, a 10 nm NiCo/Si(001) sample has been used as reference sample for the determination of the geometrical function $G(\theta)$. The deduced geometrical parameters have then been fixed during the simulations of the Ta₂O₅ stacking. The fitting of the measured data has been optimized with the differential evolution (DE) algorithm coded into the software.

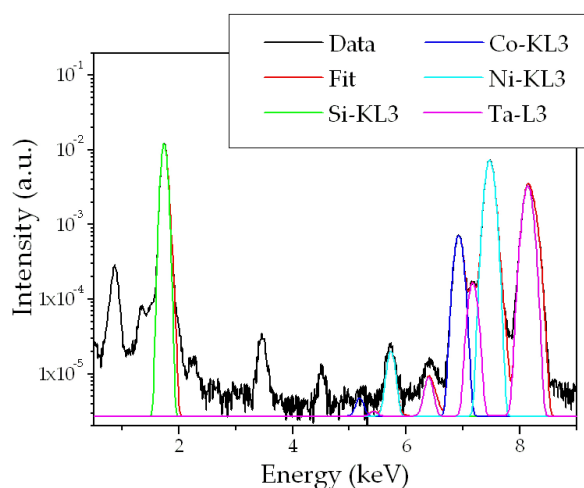


Figure 141 : Fluorescence intensity extraction from a measurement at $\theta = 1^\circ$ at 10200 eV of the sample deposited with the O* plasma. Due to the overlaps of Co-KL3, Ni-KL3 and Ta-L3 fluorescence peaks, the use of a third party software like PyMCA [25] was necessary.

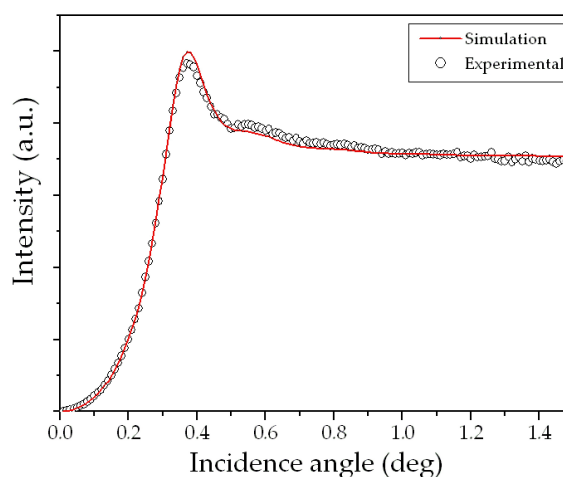


Figure 142 : Ni-K α GIXRF fit on JGIXA of a 10 nm NiCo reference sample measured at 10200 eV at Elettra. Fitting of reference sample allows the determination of geometrical function $G(\theta)$.

4.3.3. Results and discussions

XRR (Figure 143) and GIXRF (Figure 144 to Figure 146) data measured at 10200 eV with the synchrotron X-ray beam are presented below for the two considered samples (*i.e.* one with the O* PEALD process and the other with the H* + O* deposition process). Large differences in the Ni-K α , the Co-K α as well as the Ta-L α GIXRF profiles are noticeable. As explained in Section 2.2, GIXRF allows a simple and straightforward qualitative analysis of multilayered samples. Indeed, by simple observation, we can deduce that the arrangement of the layers and the z-position of the atoms are different between the two samples. Therefore, we are able to confirm that the choice of the PEALD experimental conditions has an important effect on the structure of the stack. However, in Figure 143, we can see that the use of H* species in the plasma modifies the XRR interference fringes considerably. These appear wider when H* is used. Such an effect could allow us to conclude that the sample layers are thinner (via Fourier Transformation), but it is not the case here. Indeed, the fringes appear composed of two or more components. The fringes therefore results from the superposition of phase-shifted waves with different electron densities. This points towards inter-diffusion in the layers composing the stack. We also observe a slightly smaller critical angle θ_c for the H* + O* treated sample indicating a smaller electron density in this latter at the surface.

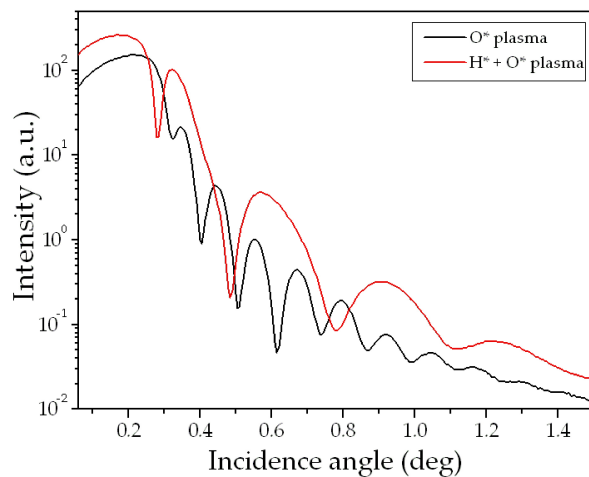


Figure 143 : Comparison of the XRR measurements of the sample processed with O* plasma and the sample processed with the H* + O* plasma. The measurements have been performed at 10200 eV.

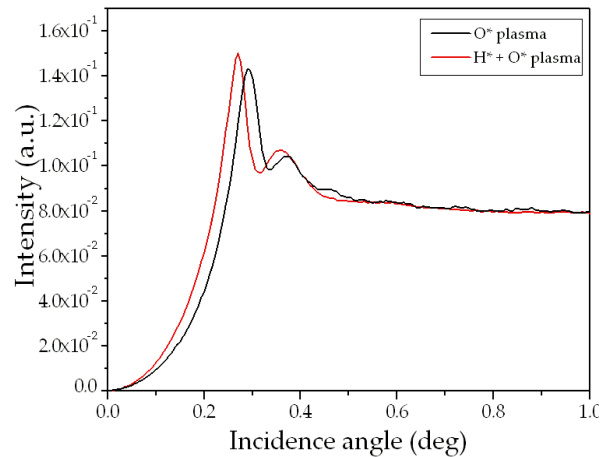


Figure 144 : Comparison of the Ta-L α GIXRF measurements of the sample processed with O* plasma and the sample processed with the H* + O* plasma. The measurements have been performed at 10200 eV.

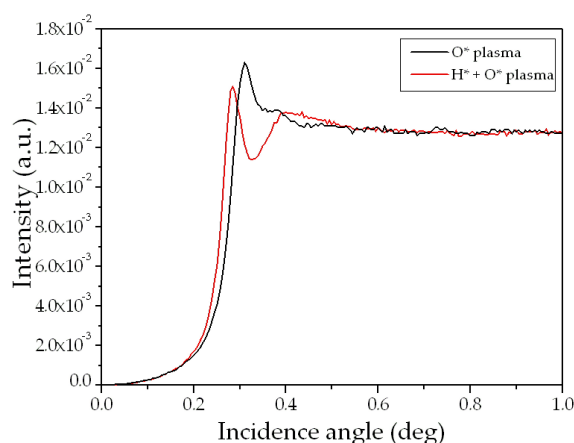


Figure 145 : Comparison of the Ni-K α GIXRF measurements of the sample processed with O* plasma and the sample processed with the H* + O* plasma. The measurements have been performed at 10200 eV.

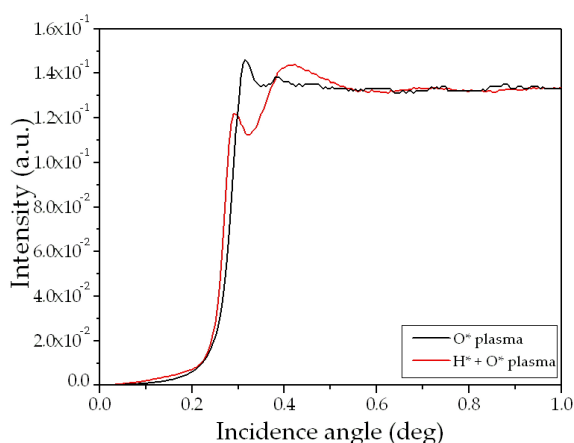


Figure 146 : Comparison of the Co-K α GIXRF measurements of the sample processed with O* plasma and the sample processed with the H* + O* plasma. The measurements have been performed at 10200 eV.

4.3.3.1. First PEALD experimental conditions

XRR and GIXRF data measured at 10200 eV (open circles) and jGIXA simulations (solid lines) for the sample processed with the O* plasma are shown in Figure 147. The agreement between the experimental and simulated points is not really good, and large values of Δ are observed.

The starting multilayered structure for the fitting of the experimental data has been built using our knowledge of the sample. Indeed, we knew that the use of the O* plasma would oxidize the NiCo layer and provoke the diffusion of both Ni and Co towards the surface of the sample. Therefore, a three-layers model with Ta₂O₅ deposited on a diffusion layer (Ta₂O₅ ; NiCo) on top of a NiCo layer has been our starting point for the simulations. The thickness, densities and roughness of each layer have been fitted (Table 16) using a combined refinement of the XRR and GIXRF data.

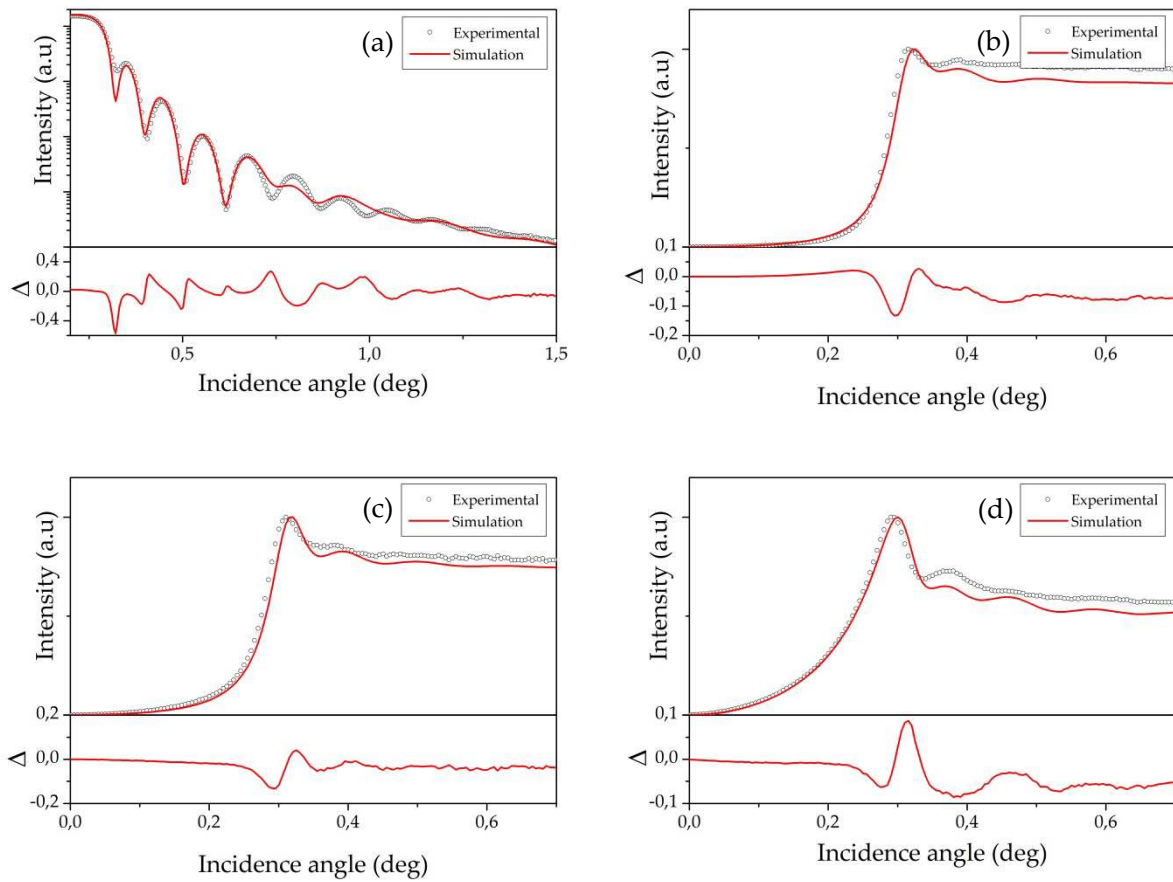


Figure 147 : (a) XRR (b) Ni-K α GIXRF (c) Co-K α GIXRF (d) Ta-L α GIXRF measurements (open circles) and fits (solid lines) of the sample deposited with the O* PEALD process. The measurements were performed at 10200 eV.

Sample	Thickness	Density (g.cm ⁻³)
Ta ₂ O ₅	2.2 nm	8.32
Ta ₂ O ₅ ; NiCo	9.7 nm	6.93
NiCo	13.5 nm	7.34
Si	SUB	2.33

Table 16 : Thickness and densities of the sample deposited with the O* PEALD process obtained from combined XRR and GIXRF fit in jGIXA correlating JGIXA fits.

This model is definitely not perfect and some additional refinements would be necessary in order to characterize fully the sample. However, it has allowed us to confirm the diffusion of NiCo towards the surface of the sample when a O* plasma is solely used for the PEALD deposition process.

4.3.3.2. Second PEALD experimental conditions

We had less to no information or knowledge of the effect of adding a H^* plasma on the layer arrangement. The starting multilayer structure for fitting of experimental data has then been built supposing large $Ta_2O_5/NiCo$ interfacial effects. Therefore, a four-layers model with Ta_2O_5 deposited on two diffusion layers (Ta_2O_5 ; $NiCo$ with different thickness and density) on top of a $NiCo$ layer has been our starting point for the simulations (Table 17).

Using $H^* + O^*$ in the plasma, the agreement between the experimental and simulated points, if potentially good in XRR fits, is not acceptable for XRF data especially for the $Ta-L\alpha$ fluorescence simulation where values of Δ as high as 0.5 can be noted (Figure 148).

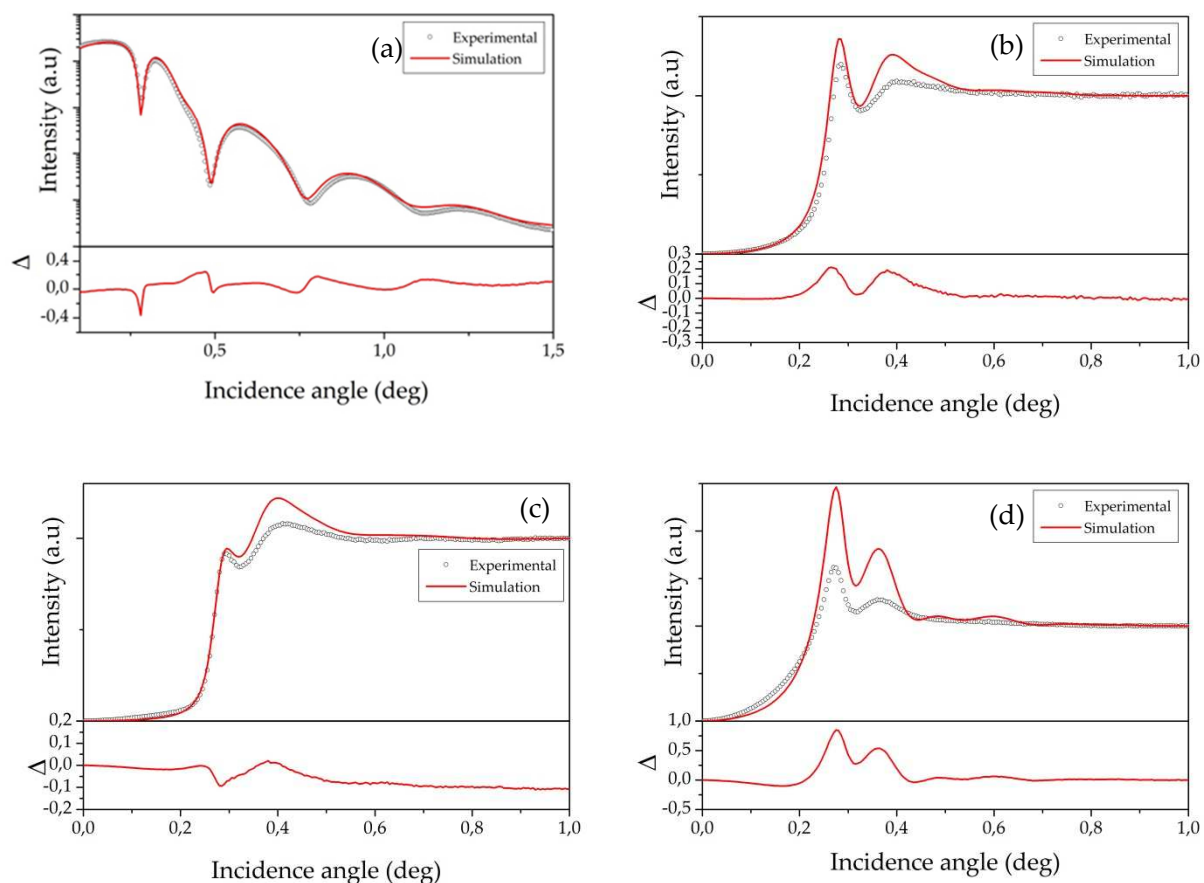


Figure 148 : (a) XRR (b) Ni-K α GIXRF (c) Co-K α GIXRF (d) Ta-L α GIXRF measurements (open circles) and fits (solid lines) of the sample deposited with the $H^* + O^*$ PEALD process. The measurements were performed at 10200 eV.

Sample	Thickness	Density (g.cm ⁻³)
Ta ₂ O ₅	4.0 nm	7.48
Ta ₂ O ₅ ; NiCo	7.3 nm	5.42
Ta ₂ O ₅ ; NiCo	3.1 nm	2.77
NiCo	9.9 nm	8.63
Si	SUB	2.33

Table 17 : Thickness and densities of the sample deposited with the H* + O* PEALD process obtained from correlating JGIXA fits of the experimental data measured at 10200 eV.

From these results, we can conclude that this chosen model is the least perfect. For instance, one can note that one layer has a density of 2.77 g.cm⁻³, a fairly unexpected value. The GIXRF spectra also exhibit large discrepancies between experimental and modelled data. Even if, we can safely assume that the use of a H* + O* plasma does not prevent the diffusion of Ni and Co towards the surface of the sample, the accurate and complete depth-profiling of this sample is impossible with such simple models. Some additional refinements using different starting models (by adding/removing layers, or by testing different stoichiometry) have been performed, but for the moment no acceptable simulation of the experimental data has been obtained. As the shape of the measured fluorescence spectra is much smoother than the simulated one, one further approach could consist in supposing that this smoothness is due to a larger elemental distribution in the sample. One could try to add more transition layers in the starting stacking to try to model more accurately the diffusion of Ni and Co towards the surface.

Recent SIMS profiles could be obtained on these two samples (Figure 149). Even if these latter cannot be taken quantitatively from the elemental point of view, they also prompt for different signatures of Ta, Ni and O elements through the thickness with sharper interfaces when H* is not used during deposition. The sensitivity to H of SIMS might be questionable, but it nevertheless is detected by one order of magnitude more in the H* + O* treated sample. Whether this could be real or not, it looks also coherent with previous observations. It however launches new debates (i.e. formation of H₂ increasing porosity, formation of hybrids or other species) that could be targeted by future investigations using complementary techniques.

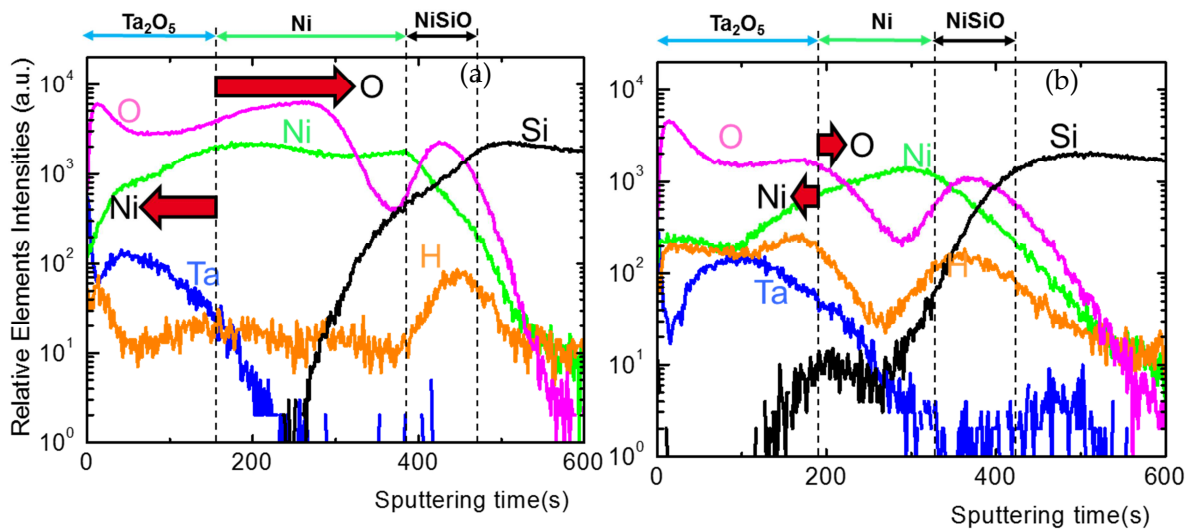


Figure 149 : SIMS measurements of (a) the sample deposited with the O^* PEALD process (b) the sample deposited with the $H^* + O^*$ PEALD process.

The study of these samples puts in light one of the current limitation of GIXRF and should be the starting point in order to improve the technique. Some solutions could be considered. One could create a starting structure for the simulation with a lot more layers in order to have a better depth resolution at the $Ta_2O_5 / NiCo$ interface. On the other hand, one could also try to simulate a depth profile for the various elements of interest (as demonstrated in Section 4.1.4) in order to perform the elemental quantification and depth-profiling. However, both these solutions are time consuming and will require a preliminary improvement of the available analysis software.

4.4. Bibliography

- [1] L. Shon-Roy, A. Wiesnoski, R. Zorich, et Integrated Circuit Engineering Corporation, *Advanced semiconductor fabrication handbook*. Scottsdale, Ariz.: Integrated Circuit Engineering, 1998.
- [2] J. . Ziegler, *Ion Implantation Science and Technology*. Burlington: Elsevier Science, 2012.
- [3] F. Le Cœur, J. Pelletier, Y. Arnal, et A. Lacoste, « Ion implantation by plasma immersion: interest, limitations and perspectives », *Surf. Coat. Technol.*, vol. 125, n° 1-3, p. 71-78, mars 2000.
- [4] A. Anders, *Handbook of Plasma Immersion Ion Implantation and Deposition*, Wiley-Interscience. 2000.
- [5] W. Ensinger, « Semiconductor processing by plasma immersion ion implantation », *Mater. Sci. Eng. A*, vol. 253, n° 1-2, p. 258-268, sept. 1998.
- [6] G. Gillen, Éd., *Secondary ion mass spectrometry: proceedings of the Eleventh International Conference on Secondary Ion Mass Spectrometry, SIMS XI, Orlando, Florida, September 7 - 12th, 1997*. Chichester: Wiley, 1998.
- [7] W. Vandervorst, J. Bennett, C. Huyghebaert, T. Conard, C. Gondran, et H. De Witte, « On the reliability of SIMS depth profiles through HfO₂-stacks », *Appl. Surf. Sci.*, vol. 231-232, p. 569-573, juin 2004.
- [8] G. Pepponi, D. Giubertoni, M. Bersani, F. Meirer, D. Ingerle, G. Steinhauser, C. Strelì, P. Hoenicke, et B. Beckhoff, « Grazing incidence x-ray fluorescence and secondary ion mass spectrometry combined approach for the characterization of ultrashallow arsenic distribution in silicon », *J. Vac. Sci. Technol. B Microelectron. Nanometer Struct.*, vol. 28, n° 1, p. C1C59, 2010.
- [9] P. Hönicke, B. Detlefs, M. Müller, E. Darlatt, E. Nolot, H. Grampeix, et B. Beckhoff, « Reference-free, depth-dependent characterization of nanolayers and gradient systems with advanced grazing incidence X-ray fluorescence analysis: Characterization of nanolayers and gradient systems », *Phys. Status Solidi A*, vol. 212, n° 3, p. 523-528, mars 2015.
- [10] Z. Essa, F. Cristiano, Y. Spiegel, P. Boulenc, Y. Qiu, M. Quillec, N. Taleb, A. Burenkov, M. Hackenberg, E. Bedel-Pereira, V. Mortet, F. Torregrosa, et C. Tavernier, « BF₃ PIII modeling: Implantation, amorphisation and diffusion », *AIP Conference Proceedings*, 2012, p. 237-240.
- [11] K.-A. B.-T. Meura, F. Torregrosa, A.-S. Robbes, Seoyoun Choi, A. Merkulov, M. P. Moret, J. Duchaine, N. Horiguchi, Letian Li, et C. Mitterbauer, « Characterization of arsenic PIII implants in FinFETs by LEXES, SIMS and STEM-EDX », *20th International Conference on Ion Implantation Technology*, 2014, p. 1-4.
- [12] S. Amelinckx, D. van Dyck, J. van Landuyt, et G. van Tendeloo, *Handbook of Microscopy, Handbook of Microscopy: Applications in Materials Science, Solid-State Physics, and Chemistry. Methods II*. John Wiley & Sons, 2008.
- [13] A. Benninghoven, « Surface investigation of solids by the statical method of secondary ion mass spectroscopy (SIMS) », *Surf. Sci.*, vol. 35, p. 427-457, mars 1973.
- [14] « SIMS Theory: Secondary Ion Yields - Elemental Effects ». Evans Analytical Group (EAG), 2015.
- [15] R. G. Wilson, « SIMS quantification in Si, GaAs, and diamond - an update », *Int. J. Mass Spectrom. Ion Process.*, vol. 143, p. 43-49, mai 1995.
- [16] D. Ingerle, M. Schiebl, C. Strelì, and P. Wobrauschek, "Combination of grazing incidence x-ray fluorescence with x-ray reflectivity in one table-top spectrometer for improved characterization of thin layer and implants on/in silicon wafers," *Rev. Sci. Instrum.*, vol. 85, no. 8, p. 083110, Aug. 2014.
- [17] E. Demenev, D. Giubertoni, J. van den Berg, M. Reading, et M. Bersani, « Calibration correction of ultra low energy SIMS profiles based on MEIS analyses for arsenic shallow implants in silicon », *Nucl. Instrum. Methods Phys. Res. Sect. B Beam Interact. Mater. At.*, vol. 273, p. 192-194, févr. 2012.

-
- [18] H. Hosono, « Recent progress in transparent oxide semiconductors: Materials and device application », *Thin Solid Films*, vol. 515, n° 15, p. 6000-6014, mai 2007.
- [19] C. G. Granqvist, « Transparent conductors as solar energy materials: A panoramic review », *Sol. Energy Mater. Sol. Cells*, vol. 91, p. 1529-1598, 2007.
- [20] D. R. Sahu, S.-Y. Lin, et J.-L. Huang, « ZnO/Ag/ZnO multilayer films for the application of a very low resistance transparent electrode », *Appl. Surf. Sci.*, vol. 252, n° 20, p. 7509-7514, août 2006.
- [21] « Low resistance and highly transparent ITO–Ag–ITO multilayer electrode using surface plasmon resonance of Ag layer for bulk-heterojunction organic solar cells », *Sol. Energy Mater. Sol. Cells*, n° 10, p. 1801-1809, 2009.
- [22] M. Fahland, T. Vogt, W. Schoenberger, et N. Schiller, « Optical properties of metal based transparent electrodes on polymer films », *Thin Solid Films*, vol. 516, n° 17, p. 5777-5780, 2008.
- [23] C. Guillén et J. Herrero, « TCO/metal/TCO structures for energy and flexible electronics », *Thin Solid Films*, vol. 520, n° 1, p. 1-17, oct. 2011.
- [24] D. Giubertoni, G. Pepponi, S. Gennaro, M. Bersani, M. A. Sahiner, S. P. Kelty, R. Doherty, M. A. Foad, M. Kah, K. J. Kirkby, J. C. Woicik, et P. Pianetta, « Correlation of local structure and electrical activation in arsenic ultrashallow junctions in silicon », *J. Appl. Phys.*, vol. 104, n° 10, p. 103716, nov. 2008.
- [25] V. A. Solé, E. Papillon, M. Cotte, P. Walter, et J. Susini, « A multiplatform code for the analysis of energy-dispersive X-ray fluorescence spectra », *Spectrochim. Acta Part B At. Spectrosc.*, vol. 62, p. 63-68, janv. 2007.
- [26] D. Ingerle, F. Meirer, G. Pepponi, E. Demenev, D. Giubertoni, P. Wobrauschek, et C. Strelt, « Combined evaluation of grazing incidence X-ray fluorescence and X-ray reflectivity data for improved profiling of ultra-shallow depth distributions », *Spectrochim. Acta Part B At. Spectrosc.*, vol. 99, p. 121-128, sept. 2014.
- [27] R. Storn et K. Price, « Differential Evolution - A Simple and Efficient Heuristic for Global Optimization over Continuous Spaces », *J Glob Optim*, p. 341-359, 1997.
- [28] K. N. Stoev et K. Sakurai, « Review on grazing incidence X-ray spectrometry and reflectometry », *Spectrochim. Acta Part B At. Spectrosc.*, vol. 54, n° 1, p. 41-82, 1999.
- [29] A. Prakash, D. Jana, et S. Maikap, « TaOx-based resistive switching memories: prospective and challenges », *Nanoscale Res. Lett.*, vol. 8, n° 1, p. 418, 2013.
- [30] F. Pan, S. Gao, C. Chen, C. Song, et F. Zeng, « Recent progress in resistive random access memories: Materials, switching mechanisms, and performance », *Mater. Sci. Eng. R Rep.*, vol. 83, p. 1-59, sept. 2014.
- [31] T. Diokh, E. Le-Roux, S. Jeannot, C. Cagli, V. Jousseau, J.-F. Nodin, M. Gros-Jean, C. Gaumer, M. Mellier, J. Cluzel, C. Carabasse, P. Candelier, et B. De Salvo, « Study of resistive random access memory based on TiN/TaOx/TiN integrated into a 65nm advanced complementary metal oxide semiconductor technology », *Thin Solid Films*, vol. 533, p. 24-28, avr. 2013.
- [32] L. Zhao, H.-Y. Chen, S.-C. Wu, Z. Jiang, S. Yu, T.-H. Hou, H.-S. P. Wong, et Y. Nishi, « Multi-level control of conductive nano-filament evolution in HfO₂ ReRAM by pulse-train operations », *Nanoscale*, vol. 6, n° 11, p. 5698, 2014.
- [33] M.-J. Lee, C. B. Lee, D. Lee, S. R. Lee, M. Chang, J. H. Hur, Y.-B. Kim, C.-J. Kim, D. H. Seo, S. Seo, U.-I. Chung, I.-K. Yoo, et K. Kim, « A fast, high-endurance and scalable non-volatile memory device made from asymmetric Ta₂O_{5-x}/TaO_{2-x} bilayer structures », *Nat. Mater.*, vol. 10, n° 8, p. 625-630, juill. 2011.
- [34] R. W. Johnson, A. Hultqvist, et S. F. Bent, « A brief review of atomic layer deposition: from fundamentals to applications », *Mater. Today*, vol. 17, n° 5, p. 236-246, juin 2014.

5. Conclusion and perspectives

This work has shown that GIXRF is a promising alternative depth-profiling characterization technique by applying it to different systems. Indeed, by performing measurements on commercial, homemade as well as synchrotron experimental setups, the methodologies, the possibilities and the limits of XRR and GIXRF combined analysis have been presented.

In this work, the development of this non-destructive innovative characterization technique has been performed via two distinct research approaches.

The first approach has consisted in performing the GIXRF-XRR combined analysis on samples of technological interest. Therefore, we have studied ultra-shallow dopant profiles developed specifically to answer the continuous need for miniaturization of electronic components. The use of this combined approach has put in evidence significant improvements compared to standard in-depth characterization techniques such as SIMS. Indeed, it has been shown that GIXRF can overcome some limits of SIMS by providing information on the total fluence and the distribution of the implanted atoms. PIII As implants in Si were also characterized by GIXRF using a priori no knowledge on the sample. The results of our analyses have proved the capabilities of the technique in terms of in-depth characterization with a resolution in the nanometer range, with refined values very closed to the ones obtained with SIMS. Then, with the goal to better describe components for optoelectronic and photovoltaic applications, an IO/Ag/IO multilayered structure has been investigated combining XRR and GIXRF measurements, using different excitation energies and experimental setups. The complete characterization of the stacking has been then possible. Moreover, the combined characterization has demonstrated the influence of the excitation energy on the accuracy of the results and also evidenced the presence of an annealing induced inter-diffusion throughout the material. Finally, new RAM technologies and especially ReRAM have been used to test the possibilities of the combined XRR and GIXRF analysis. Even if the complete in-depth characterization of the concentration profiles have not been fully determined, GIXRF has allowed to observe qualitative structural differences between samples treated with different deposition conditions.

The second approach developed in this work concerns the improvement of the methodology and more especially the development of combined analysis software. Indeed, in order to perform quantitative GIXRF analyses, it is necessary to compare the experimental results

to simulation based on the modelling of a sample structure. Recently, four dedicated analytical software have been developed each with their own specificities using the expertise of the laboratories of our collaborative international group. In this frame, the comparison and the test of these software has been necessary and has allowed better understanding of the various functions and of fundamental parameters that must be taken into account before performing a combined XRR and GIXRF analysis. An important part of this work has been then dedicated to the description of the instrumental geometrical function. In particular, it has been put in evidence the necessity to introduce a dependent angle factor in this geometrical function. This latter takes into account various effects such as the size of the beam, the position of the detector, the distance between the elements of the optical path, etc. on the fluorescence intensity. A focus has also been done on the quantification methods as well as their advantages and their limitations. We have demonstrated that the complete metrology of the instrumental setup was necessary in order to perform accurate XRR and GIXRF measurements. However, its time consumption and non-practicality makes this method not suitable in most situations.

Therefore, a simple quantification that requires less knowledge on the experimental setup has been presented and used in all applications. However, the simple quantification approach has its limitations as it require the GIXRF measurement of a reference sample prior to analysis and may not be perfectly accurate. This limitation is demonstrated in the study of the Ta₂O₅/NiCo/Si samples where the elemental quantification has not been possible. Moreover, the implanted sample modelling in the four current analysis software has also shown its limits as it may not be accurate enough to represent a depth-profile by a layer arrangement and as the depth-profile characterization by GIXRF is not straightforward. The improvement of GIXRF will thus be linked with an improvement of the combined analysis software (*i.e.* the way they handle the geometrical effects and the layer arrangement construction). New solutions are being considered and developed now in the different laboratories of our collaborative international group.

Finally, in this work, we have shown that the combination of two characterization techniques reduces strongly the uncertainties of the individual methods. One other axis for the development of GIXRF is then to combine GIXRF with other characterization techniques (two or more). Considering the applications presented in this work, the combination with SIMS seems obvious but other X-ray methods could be considered such as grazing exit X-ray fluorescence (GEXRF), extended X-ray absorption Fine structure (EXAFS) or X-ray Diffraction (XRD). In particular, as sometimes the polycrystalline studied films for microelectronic applications exhibit also preferential orientations, GIXRF and XRR techniques can be also coupled with XRD. The new developed combined GIXRF-XRR-XRD analysis approach (through the MAUD program) has already been tested on the transparent conducting oxides multilayered samples (IO/Ag/IO

heterostructures). With this approach, we have determined the different layer thicknesses and their crystallographic preferred orientations (Figure 150) and we have put in evidence the presence of a gradient profile for the chemical composition as well as for the films density for the annealing samples. However, if these first results are encouraging, additional work in this direction and especially for annealing samples presenting a gradient profile has to be pursued.

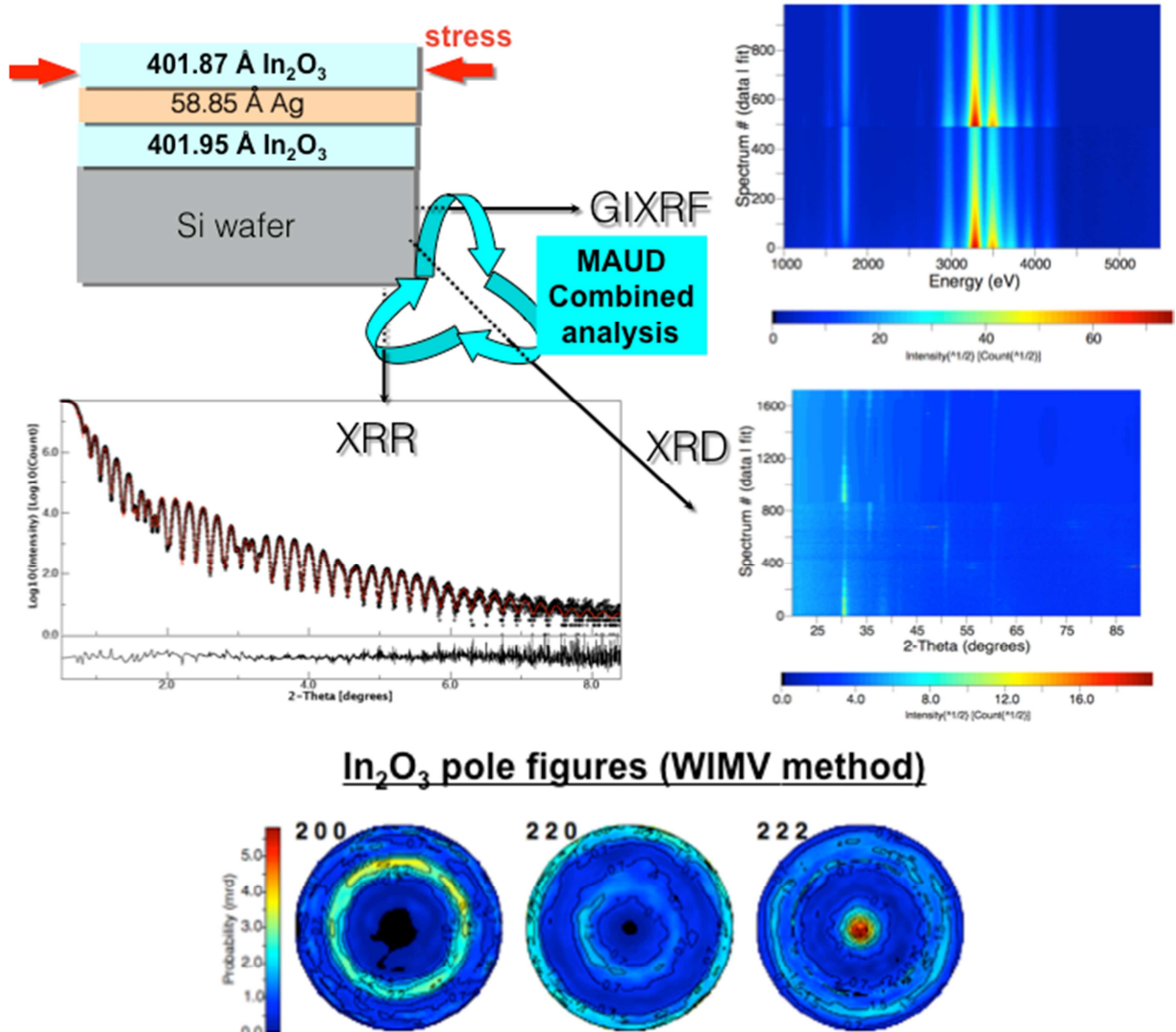


Figure 150: First results of GIXRF-XRR-XRD combined analysis approach on IO/Ag/IO heterostructures.

List of figures

Figure 1 : Spectrum of a tungsten (W) tube.

Figure 2 : Mechanism of pair production.

Figure 3 : Coherent scattering of an X-ray photon by an atom.

Figure 4 : The Compton scattering process.

Figure 5 : Plot of the mass attenuation coefficients versus the primary energy. It highlights the absorption edges of the different shells of a high Z element [3].

Figure 6 : Relative importance of the three major interactions. Solid lines show the boundary where the two neighboring effects are equal [1].

Figure 7 : Schematic principle of X-ray fluorescence.

Figure 8 : Atomic allowed electronic transitions.

Figure 9 : Fluorescence yield versus atomic number for K and L.

Figure 10 : Incident, reflected and refracted beam at an interface between two media with different refractive index.

Figure 11 : Penetration depth of Mo-K α X-ray radiation for silicon, nickel and platinum versus the incidence angle. It depends strongly on the incidence angle. Penetration depth is defined as the depth at which the intensity of the radiation inside the material falls to about 37%. Below the critical angle θ_c only a shallow surface is penetrated [3].

Figure 12 : Illustration of the X-ray standing wave field (XSW) created by the interference between the incident and the reflected wave. The planes in which constructive interference takes place are parallel to the sample surface. The periodicity varies with the incidence angle.

Figure 13 : Intensity above and below the interface between the air and a thick Si substrate considering a Mo-K α striking the sample with different glancing angles [3].

Figure 14 : Angular dependence of X-ray fluorescence intensity for different types of samples [8].

Figure 15 : Reflectance and transmittance of the electromagnetic radiation on a substrate.

Figure 16 : Reflectance and transmittance of electromagnetic radiation through a layer within a stack of N layers.

Figure 17 : Calculation of the primary X-ray fluorescence intensity from an atom in a layer j .

Figure 18 : Counts versus concentration from various matrix compositions of a FeNiCr alloy [29].

Figure 19 : Schematic illustration of secondary excitation in a sample containing Fe and Ni.

Figure 20 : The Ti-K α fluorescence intensity for a Si/Ti/Ni/Ti/Si (sub) multilayer sample as a function of incident angle [40].

Figure 21 : Schematic set-up of a TXRF experiment. Radiation emitted from the X-ray tube passes a filter and a mirror that act as a bandpass to eliminate radiation of undesired wavelengths. Fluorescence radiation is detected by an ED-XRF detector located at 90° above the sample.

Figure 22 : Schematic configuration of a TXRF setup using a Mo/W alloy anode emitting variable excitation energies [3].

Figure 23 : Detection limits of the TXRF instrument using a Mo/W alloy anode and a tunable double multilayer monochromator [3].

Figure 24 : Comparison of detection limits reached with various excitation and spectral modification devices. Values are extrapolated to 1000s and obtained from aqueous solutions pipetted on the sample then evaporated [5].

Figure 25 : Power density and optical properties of a line-focus and a micro-focus X-ray tube [6].

Figure 26 : Different excitation schemes for TXRF analysis;(a) Low-pass filter using a quartz mirror; (b) bandpass filter using a single multilayer mirror; (c) combination of a multilayer and quartz mirror; (d) double multilayer arrangement [9].

Figure 27 : Working principle of a Si(Li) detector. The voltage applied to the device allows the drift and collection of the charge carriers created by the ionizing radiation.

Figure 28 : Working principle of a SSD detector [12].

Figure 29 : Scheme of Hoefler TXRF spectrometer for low-Z elements [20].

Figure 30 : XRF spectrum of the studied biofilm. Excitation conditions: Cr tube at 30 kV and 20 mA [20].

Figure 31 : Pre-treatment process for TXRF measurements [21].

Figure 32 : Three possibilities of arranging wafer and detector for SR-TXRF [5].

Figure 33 : Comparison of TXRF spectra of (a) a 5 nm Mg layer excited with a standard Cr fine focus X-ray tube and (b) 500 pg Mg sample excited with a 1.77 keV synchrotron excitation [25].

Figure 34 : Spectrum of 100 pg of Ni on a Si wafer excited with a 17 keV radiation during 60 s. The DL was found to be 8 fg [27].

Figure 35 : Comparison of Al₂O₃ powder fluorescence spectra measured with laboratory TXRF (Atomika 8030C) and SR-TXRF [27].

Figure 36 : Spectra of Hf containing high-k layers taken in different energy regions. (a) Excitation energy = 10.5 keV and (b) Excitation energy = 1.75 keV. The green and the blue line show background components (green: Bremsstrahlung, blue: resonant Raman scattering of silicon), the red lines are the fluorescence lines convolved with the detector response function to deduce their intensity and the purple line shows the fit to the experimental spectrum [28].

Figure 37 : TXRF spectrum of In₂O₃/Ag/In₂O₃ sample excited by a standard Cu tube. The energy of Ag-L₃ and In-L₃ lines cannot be separated by ED-XRF detectors.

Figure 38 : TXRF spectrum of a wafer containing 1012 cm⁻² of various transition metals and 1013 cm⁻² of Na and Al (low-Z elements). The spectrum is fitted by detector response functions at the energies of fluorescence lines. The background includes Bremsstrahlung and resonant Raman scattering contributions [30].

Figure 39 : TXRF spectrum of the residue of a multi-element standard solution containing equal concentrations excited by Mo-K radiation.

Figure 40 : Set of relative element sensitivities measured under total reflection of X-rays.

Figure 41 : Relative fluorescence count rate as a function of the incident angle. The shift of GIXRF signals towards larger angles indicates the position of the layers in the stacking [43].

Figure 42 : Cu-K α GIXRF intensities of two different Cu(In,Ga)Se₂ films synthesized by three-stage co-evaporation process at 430 °C and 530 °C [44].

Figure 43 : Flow chart depicting the algorithm implemented for fitting GIXRF experimental data by correcting the SIMS profile given as initial best estimate [46].

Figure 44 : Comparison of the implantation profile for one of the As wafers (3 keV, 1.0×10¹⁵ cm⁻²) determined with various techniques and the respective SRIM profile [47].

Figure 45 : Determination of the layer thickness of a Pd layer on a silicon substrate. Measured fluorescence intensities of Pd and Si as a function of the incident angle result in a layer thickness of 132 nm. The manufacturer's value is 133 ± 3 nm [50].

Figure 46 : Analysis of a three-layer system by angle-resolved TXRF measurements. Both the thickness and the density of the layers have been determined [51].

Figure 47 : GIXRF fluorescence signal from Hf and Si from a HfSiO_x layer. The calculation was performed using only the GIXRF signal. Good fit results are obtained for a density of 6.1 g/cm³ using a thickness of 2.25 nm (a) as well as a density of 6.7 g/cm³ using a thickness of 2.05 nm (b), thus showing the ambiguity of the GIXRF data [53].

Figure 48 : How can a method (rows) help another method (columns) to improve or complement the results [54]

Figure 49 : Experimental setup for combined XRR and GIXRF analysis.

Figure 50 : Magnification of the L-edge range of silver [17].

Figure 51 : Conceptual scheme of the modeling of a multi-layered structure in the four used combined analysis software [31].

Figure 52 : Maud graphic interface of the material definition (in this case NiO). It lists the symmetry, the space group, the cell parameter, the number of atoms and their position in the crystallographic lattice.

Figure 53 : 2D schematic of the X-ray incident beam and the geometry for the fluorescence X-ray detection in a GIXRF experiment [28].

Figure 54 : 3D schematic of the X-ray incident beam and the geometry for the fluorescence X-ray detection in a GIXRF experiment.

Figure 55 : The inverse of geometrical function (*i.e.* the correction function) calculated for different widths L_d of the detectable area, where $L_s = 30\text{mm}$ and $b_0 = 0.15\text{ mm}$ and $I_0 = 1$. The short dotted line is a $\sin(\theta)$ function for a visual guide [28].

Figure 56 : Definition of the angles used in this work. The incidence angle θ , the detection angle φ_d is the angle between the X-ray detector and the horizontal plane and α is the angle between the detector and the sample will be used.

Figure 57 : Schematic of the geometry for the fluorescence X-ray detection in a GIXRF experiment with a X-ray fluorescence detector tilted compared to the sample surface.

Figure 58 : Schematic of the geometry for the fluorescence X-ray detection in a GIXRF experiment with a X-ray fluorescence detector tilted compared to a rotating sample.

Figure 59 : 2D schematic representation used for the calculation of the solid angle of detection $\Delta\Omega$.

Figure 60 : 3D schematic representation used for the calculation of the solid angle of detection $\Delta\Omega$.

Figure 61 : Comparison of the acceptance function in the case where the solid angle $\Delta\Omega$ is considered constant or not.

Figure 62 : Schematic of primary X-ray beam divergence.

Figure 63 : Comparison of the XRR simulation of a NiO (5nm) / Ni (50nm) / Si (sub) sample irradiated with a Cu-K α radiation.

Figure 64 : Comparison of the Si-K α GIXRF simulation of a NiO (5nm) / Ni (50nm) / Si (sub) sample irradiated with a Mo-K α radiation.

Figure 65 : Comparison of the Ni-K α GIXRF simulation of a NiO (5nm) / Ni (50nm) / Si (sub) sample irradiated with a Mo-K α radiation.

Figure 66 : Comparison of the Ni-K α GIXRF simulation of a NiO (5nm) / Ni (50nm) / Si (sub) sample irradiated with a 8400 eV radiation.

Figure 67 : Comparison of the XRR simulation of Table 4 sample irradiated with a Cu-K α radiation.

Figure 68 : Comparison of the Ni-K α GIXRF simulation of Table 4 sample irradiated with a Mo-K α radiation.

Figure 69 : Comparison of the XRR simulation of a NiO (5nm) / Ni (50nm) / Si (sub) sample with roughness irradiated with a divergent (HWHM = 0.3 mrad) Cu-K α radiation.

Figure 70 : Comparison of the Ni-K α GIXRF simulation of a NiO (5nm) / Ni (50nm) / Si (sub) sample with roughness irradiated with a divergent (HWHM = 0.3 mrad) Mo-K α radiation.

Figure 71 : Correction function $1/G(\theta)$ in Maud.

Figure 72 : Correction function $1/G(\theta)$ in jGIXA calculated for different widths L_d of the detectable area, where $L_s = 200\text{mm}$ and $b_0 = 50\text{ }\mu\text{m}$.

Figure 73 : Correction function $1/G(\theta)$ in the case of a rotating sample in jGIXA.

Figure 74 : Correction function $1/G(\theta)$ with various distance sample-collimator (d_1) in Medepy and GIMPY.

Figure 75 : Geometrical function $G(\theta)$ multiplied by the Ni-K α fluorescence intensity.

Figure 76 : Correction function $1/G(\theta)$ with various pinhole diameters (d_p) in Medepy and GIMPY.

Figure 77 : Geometrical function $G(\theta)$ multiplied to the Ni-K α fluorescence intensity.

Figure 78 : Correction function $1/G(\theta)$ with various pinhole height (d_2) in Medepy and GIMPY.

Figure 79 : Geometrical function $G(\theta)$ multiplied to the Ni-K α fluorescence intensity.

Figure 80 : Variation of the size of A (area seen by the X-ray detector on the detector side) with the incidence angle.

Figure 81 : Variation of the size of B (area seen by the X-ray detector on the source side) with the incidence angle.

Figure 82 : Comparison of the correction function for different detection angles in the case of an experimental setup with a rotating sample.

Figure 83 : Correction function $1/G(\theta)$ with various distance sample-collimator (d1) in Medepy and GIMPy.

Figure 84 : Geometric function $G(\theta)$ applied to the Ni-K α fluorescence intensity.

Figure 85 : Comparison of the Ni-K α fluorescence intensity corrected by various geometric functions $G(\theta)$.

Figure 86 : XRR measurements at 17479 eV (open circles) and fits (solid lines) of the Ni / Si sample by jGIXA.

Figure 87 : Ni-K α GIXRF measurements at 17479 eV (open circles) and fits (solid lines) of the Ni / Si sample by jGIXA.

Figure 88 : Schematic representation of a n-channel MOSFET (NMOS).

Figure 89 : Schematic representation of the ion beam (or beamline) implantation technique with mass separator.

Figure 90 : Schematic representation of the plasma immersion ion implantation (PIII) technique [3].

Figure 91 : Evolution of the plasma sheath with time when a negative voltage pulse $V(t)$ is applied to the substrate [3].

Figure 92 : The sputtering process, as a result of the collision cascade of the impacting primary ions, causes, neutral, positive and negative particles to be released from the surface [12].

Figure 93 : Schematic of a secondary ion mass spectrometer with mass selected primary ion beam [13].

Figure 94 : Logarithm of relative positive ion yields plotted as a function of ionization potential. The ion yields are relative to silicon in a silicon matrix with oxygen sputtering [14].

Figure 95 : Logarithm of relative negative ion yields plotted as a function of electron affinities. The ion yields are relative to silicon in a silicon matrix with oxygen sputtering [14].

Figure 96 : SIMS results for samples implanted at room temperature (25°C).

Figure 97 : SIMS results for samples implanted at (500°C).

Figure 98 : Schematic representation of the homemade GIXRF experimental setup [16].

Figure 99 : Detailed view of the GIXRF module of the homemade experimental setup [16].

Figure 100 : Fluorescence intensity extraction from a measurement at $\theta = 0.7^\circ$ with a Mo-tube.

Figure 101 : Ti-K α GIXRF signals of samples with various Ti thickness irradiated with a Cu-K α radiation.

Figure 102 : Linear relation between the expected thickness of Titanium deposited and the total fluorescence counts at angles larger than the critical angle of refraction (in this case 1°).

Figure 103 : As-K α GIXRF signals of the implanted samples irradiated with a Mo-K α radiation. The reference sample is a As beamline implant with a nominal fluence of 0.8×10^{15} .

Figure 104 : Si-K α GIXRF signals of the implanted samples irradiated with a Mo-K α radiation.

Figure 105 : TEM analysis of samples implanted at room temperature (25°C). The presence of a 13 nm amorphous layer can be noted.

Figure 106 : TEM analysis of samples implanted at 500°C.

Figure 107 : SIMS-As concentration depth profiles for samples implanted at room temperature (25°C) performed at FBK.

Figure 108 : SIMS-As concentration depth profiles for samples implanted at 500°C performed at FBK.

Figure 109 : XRR measurements at 17480 eV (open circles) and fit (solid lines) of the reference sample by jGIXA.

Figure 110 : As-K α GIXRF measurements at 17480 eV (open circles) and fit (solid lines) of the reference sample by jGIXA.

Figure 111 : XRR measurements at 17480 eV (open circles) and jGIXA fit (solid lines) of the implanted sample 1.

Figure 112 : As-K α GIXRF measurements at 17480 eV (open circles) and jGIXA fit (solid lines) of the implanted sample 1.

Figure 113 : XRR measurements at 17480 eV (open circles) and jGIXA fit (solid lines) of the implanted sample 2.

Figure 114 : As-K α GIXRF measurements at 17480 eV (open circles) and jGIXA fit (solid lines) of the implanted sample 2.

Figure 115 : Comparison of the As concentration depth-profiles obtained by GIXRF and by SIMS for the sample 1.

Figure 116 : Comparison of the As concentration depth-profiles obtained by GIXRF and by SIMS for the sample 2.

Figure 117 : Sheet resistance for IO/Ag/IO samples for various Ag thicknesses. 0 nm of Ag represents the R_s of a 80 nm In₂O₃ layer. For solar cells, an Ag thickness of 4 nm is required.

Figure 118 : Optical transmittance for IO/Ag/IO samples for various Ag thicknesses. For photovoltaic applications, an Ag thickness inferior to 8nm is required.

Figure 119 : Layer stack consisting of two 40 nm IO layers and a 6 nm Ag layer. The stack is deposited on a SiO₂ (500 nm)/ Si(100) substrate.

Figure 120 : Ag-L α GIXRF D8-Fabline measurements acquired at 8050 eV (Cu anode tube).

Figure 121 : In-L α GIXRF D8-Fabline measurements acquired at 8050 eV (Cu anode tube).

Figure 122 : Homemade combined XRR-GIXRF experimental setup (Atominstitut, Vienna, Austria) [16].

Figure 123 : Fluorescence intensity extraction from a measurement at $\theta = 1.2^\circ$ with a Cu-tube. Due to the correlation of Ag-L₃ and In-L₃ fluorescence peaks, the use of a third party software like PyMCA [25] is necessary.

Figure 124 : Fluorescence intensity from a measurement at 26400 eV with a synchrotron radiation at an angle of incidence $\theta = 0.12^\circ$. With this excitation energy, the fluorescence peaks of interest are not overlapping.

Figure 125 : GIXRF fit on JGIXA of a 50 nm Ni sample measured at 26400 eV at ESRF. Fitting of reference sample allows the determination of geometrical function $G(\theta)$.

Figure 126 : XRR measurements (open circles) and fits (solid lines) of the as-deposited samples A and C at 8.05 keV.

Figure 127 : Ag-L α GIXRF measurements (open circles) and fits (solid lines) of the as-deposited samples A and C at 8.05 keV.

Figure 128 : XRR measurements (open circles) and fits (solid lines) of the as-deposited sample A at 8.05 keV with and without the introduction of the LD-In₂O₃ top layer in the model. This top layer introduction is necessary in order to reproduce the experimental fringes around 1.5° .

Figure 129 : Ag-K α GIXRF Gilda measurements and fits of Sample A. The difference curve is represented at the bottom of the figure. Model 2 has been obtained by combining sets of data acquired at different excitation energies. It offers smaller differences between experimental and simulated data.

Figure 130 : Ag-K α GIXRF Gilda measurements and fits of Sample C. The difference curve is represented at the bottom of the figure. Model 2 has been obtained by combining sets of data acquired at different excitation energies. It offers smaller differences between experimental and simulated data.

Figure 131 : Ag-K α GIXRF measurement of the samples at 26400 eV. Differences in the GIXRF profile can be noted between the C (as deposited) and the D (annealed) sample.

Figure 132 : Ag-L α GIXRF measurements of the samples at 8050 eV. Differences in the GIXRF profile can be noted between the C (as deposited) and the D (annealed) sample.

Figure 133 : XRR measurements of the samples at 8050 eV.

Figure 134 : XRR and GIXRF measurements and fitting of the sample D with reflectivity measured at 8.05 keV and fluorescence at 26.4 keV.

Figure 135 : Metal-Insulator-Metal (MIM) structure of a Resistive RAM (ReRAM) cell. The top electrode is biased and the bottom electrode is grounded during electrical testing.

Figure 136 : Cross-sectional TEM image of the fabricated TiN/HfO_x/Pt ReRAM device [32].

Figure 137 : Schematic representation of the TaO_x device consisting of a thin Ta₂O_{5-x} insulating layer and a TaO_{2-x} base layer. The movement of internal oxygen ions or vacancies is used to model the switching [33].

Figure 138 : Chemical representation of the TertiaryButylimido,Tris(DiEthylamino)Tantalum (TBTDET).

Figure 139 : First PEALD experimental conditions. The precursor used is TBTDET and a O* plasma is used to remove the passivating atoms.

Figure 140 : Second PEALD experimental conditions. The precursor used is TBTDET. A H* and then a O* plasma are used to remove the passivating atoms with oxidizing the bottom layer.

Figure 141 : Fluorescence intensity extraction from a measurement at $\theta = 1^\circ$ at 10200 eV of the sample deposited with the O* plasma. Due to the overlaps of Co-KL₃, Ni-KL₃ and Ta-L₃ fluorescence peaks, the use of a third party software like PyMCA [25] was necessary.

Figure 142 : Ni-K α GIXRF fit on JGIXA of a 10 nm NiCo reference sample measured at 10200 eV at Elettra. Fitting of reference sample allows the determination of geometrical *function* $G(\theta)$.

Figure 143 : Comparison of the XRR measurements of the sample processed with O* plasma and the sample processed with the H* + O* plasma. The measurements have been performed at 10200 eV.

Figure 144 : Comparison of the Ta-L α GIXRF measurements of the sample processed with O* plasma and the sample processed with the H* + O* plasma. The measurements have been performed at 10200 eV.

Figure 145 : Comparison of the Ni-K α GIXRF measurements of the sample processed with O* plasma and the sample processed with the H* + O* plasma. The measurements have been performed at 10200 eV.

Figure 146 : Comparison of the Co-K α GIXRF measurements of the sample processed with O* plasma and the sample processed with the H* + O* plasma. The measurements have been performed at 10200 eV.

Figure 147 : (a) XRR (b) Ni-K α GIXRF (c) Co-K α GIXRF (d) Ta-L α GIXRF measurements (open circles) and fits (solid lines) of the sample deposited with the O* PEALD process. The measurements were performed at 10200 eV.

Figure 148 : (a) XRR (b) Ni-K α GIXRF (c) Co-K α GIXRF (d) Ta-L α GIXRF measurements (open circles) and fits (solid lines) of the sample deposited with the H* + O* PEALD process. The measurements were performed at 10200 eV.

Figure 149 : SIMS measurements of (a) the sample deposited with the O* PEALD process (b) the sample deposited with the H* + O* PEALD process.

List of tables

Table 1 : K and L X-ray lines in Siegbahn and IUPAC notations.

Table 2 : Detection limits and sensitivities at SSRL BL III-4 and with a standard X-ray tube (Cr fine focus X-ray tube) with 1000 s of counting time [25].

Table 3 : Model sample used for the simulation comparison.

Table 4 : Model sample used for the simulation comparison.

Table 5 : Starting sample model used for the simulation comparison.

Table 6 : Refined sample model.

Table 7 : Description of analyzed samples.

Table 8 : Comparison between the nominal fluence and the SIMS determined fluence.

Table 9 : Comparison between nominal, SIMS determined and GIXRF determined fluence.

Table 10 : Comparison between nominal and SIMS determined fluence.

Table 11 : Comparison between the nominal fluence, the SIMS determined fluence and the GIXRF determined fluence.

Table 12 : Description of analyzed samples.

Table 13 : Model 1 – Thickness and densities of the as-deposited samples obtained by comparison of jGIXA fitting and experimental results measured with Cu-K α energy.

Table 14 : Model 2 – Thickness and densities of the as-deposited samples obtained from correlating JGIXA fits of the experimental data measured at two different energies (respectively 26.4 and 8.05 keV).

Table 15 : Thickness and densities of the sample D obtained from correlating JGIXA fits of the experimental data measured at two different energies (respectively 26.4 and 8.05 keV).

Table 16 : Thickness and densities of the sample deposited with the O* PEALD process obtained from combined XRR and GIXRF fit in jGIXA correlating JGIXA fits.

Table 17 : Thickness and densities of the sample deposited with the H* + O* PEALD process obtained from correlating JGIXA fits of the experimental data measured at 10200 eV.

Development of X-ray Reflectometry (XRR) and Grazing Incidence X-ray Fluorescence (GIXRF) combined analysis for micro and nano-electronic applications.

Due to recent developments in microelectronics, new in-depth characterization techniques are needed. Combined Grazing Incidence X-ray Fluorescence (GIXRF) and X-ray Reflectivity (XRR) analysis is as a promising alternative technique. Indeed, this technique allows obtaining, in a non-destructive way, the depth-profile composition and density of multilayered samples. In the literature, only few works using the potentiality of the XRR-GIXRF technique have been reported. Therefore, in order to accelerate the development of its application in materials characterization, a collaborative international group has been set up between laboratories to share expertise, equipment and analysis software. The objective was to apprehend the methodologies for the XRR-GIXRF acquisition, measurements analysis as well as the physical principles along with the possible limitations of the technique. In this work, after a presentation of the analysis protocols and software, the solutions implemented in different software in order to handle instrumental effects and quantification problems, are discussed. Subsequently, applications of the combined XRR-GIXRF technique on samples of interest are presented. In particular, through the investigation of Ultra-Shallow junctions and various multilayers, the qualitative and quantitative depth-profiling capabilities are demonstrated and compared to classical characterization techniques. Finally, limitations of the technique and possible outlooks are discussed.

Développement de l'analyse combinée par Réflectométrie de rayons X (XRR) et Fluorescence des rayons X en Incidence Rasante (GIXRF) pour des applications micro et nano-électroniques.

En raison de récents développements en microélectronique, un besoin croissant de techniques alternatives de caractérisation est apparu. L'analyse combinée quantitative par réflectométrie de rayons (XRR) et Fluorescence X en incidence rasante (GIXRF) est une technique de caractérisation prometteuse. En effet, elle permet d'accéder de façon non destructive et avec une bonne résolution au profil de distribution en profondeur de composition et de densité d'échantillons multicouches. Dans la littérature, peu ou pas de travaux utilise les potentialités de cette analyse combinée. Pour accélérer le développement de cette dernière, un groupe international collaboratif a donc été mis en place afin de partager les expertises, les équipements et les logiciels d'analyse. Leurs objectifs étaient d'appréhender les méthodologies pour l'acquisition et l'analyse des mesures combinées XRR-GIXRF, mais aussi d'évaluer les principes physiques, les possibilités ainsi que les limites de cette technique. Dans ce travail, après une présentation des protocoles et logiciels d'analyse existant, les solutions mises en œuvre dans différents logiciels afin de résoudre les problèmes de quantification et de correction des effets instrumentaux sont décrites. Des applications de l'analyse combinée XRR-GIXRF sur des échantillons d'intérêt sont ensuite présentées. En particulier, via l'étude des jonctions ultra fines et diverses multicouches, les capacités qualitatives et quantitatives de profilage en profondeur de la technique sont détaillées et comparées aux techniques de caractérisation classiques. Enfin, les limites de la technique XRR-GIXRF et les perspectives possibles sont également discutées.